UNIVERSIDADE DE LISBOA
FACULDADE DE CIÊNCIAS

Understanding physical and dynamical processes in the atmosphere of the Solar System planets with ground and space based observations

“ Documento Definitivo”

Doutoramento em Astronomia e Astrofísica

José Eduardo Oliveira Silva

Tese orientada por:
Dr. Pedro Miguel Borges do Canto Mota Machado
Dr. Mário João Pires Fernandes Garcia Monteiro

Documento especialmente elaborado para a obtenção do grau de doutor

2021

UNIVERSIDADE DE LISBOA
FACULDADE DE CIÊNCIAS

Understanding physical and dynamical processes in the atmosphere of the Solar System planets with ground and space based observations

Doutoramento em Astronomia e Astrofísica

José Eduardo Oliveira Silva

Tese orientada por:
Dr. Pedro Miguel Borges do Canto Mota Machado
Dr. Mário João Pires Fernandes Garcia Monteiro

Júri:
Presidente:
- Doutor José Manuel de Nunes Vicente e Rebordão, Investigador Coordenador e Presidente do Departamento de Física da Faculdade de Ciências da Universidade de Lisboa

Vogais:
- Doutora Arianna Piccialli, Researcher Royal Belgian Institute for Space Aeronomy (BIRA-IASB), Bélgica, na qualidade de individualidade de reconhecida competência na área científica;
- Doutor Leigh Nicholas Fletcher, Associate Professor School of Physics and Astronomy da University of Leicester, UK;
- Doutor Aymeric Spiga, Senior Associate Professor Sorbonne Université, LMD, Paris;
- Doutor Ricardo Machado Trigo, Professor Associado Faculdade de Ciências da Universidade de Lisboa;
- Doutor Pedro Miguel Borges do Canto Mota Machado, Professor Auxiliar Convidado Faculdade de Ciências da Universidade de Lisboa, Orientador

Documento especialmente elaborado para a obtenção do grau de doutor

Colaboração com o Instituto de Astrofísica e Ciências do Espaço, financiada pelo Programa de Bolsas de Doutoramento da Universidade de Lisboa ao abrigo das Normas do Concurso 2017

2021

Acknowledgements

In science as in life, one should never face it alone. I was fortunate enough to have a network of support to guide and encourage me throughout this journey, on which people I truly cherish stand at the centre. So much has changed since the last time I wrote something like this at the end of my masters and, looking back it is a mix of sorrow, joy, and deep appreciation for this voyage.

I have always been curious. Before I could even stand up I would look curiously at all the strange figures in boards, papers, and drawings, trying to make sense of the world around me and almost greedily trying to absorb it all. Although a small astronomy spark was always there, it only exploded into a supernova before I enrolled in college and, after 8 years of studying physics and astronomy I am curious again for all things, and I believe that anything and everything can be interesting and exciting. Encouraging this behaviour from the start were my two loving parents, António Manuel Silva and Maria José Oliveira. Although I have trouble expressing my affection and appreciation for them, they are the ones who always have my back and made all of this possible, offering advice and supporting most of my decisions, often talking some sense into me when I act or think like a fool!

I also want to thank my brother, João Pedro Silva for being a connection to my family when I instinctively isolated myself from them, and for trying to make me see myself in a better light, something I continue to struggle with, and for being there in my darkest hours of fear and frustration.

From what I learned during my bachelors, it became natural for me to work hard to achieve my goals, and to push myself in achieving excellence, whatever that means. I later learned to pace myself but, it has been a challenge and an adventure to find new things that bring joy to my life, and fill the missing pieces. My flatmates and close friends in Lisbon have been an essential part in showing me a new world beyond what I was able to discover. With them I feel more confident and free, teaching me to be bold and share my ideas and crazy thoughts, and to keep me in touch with subjects completely outside the realm of science. With them I have learned much more about myself as both an adult, and an active member of society than what I could have hoped to do on my own. Although I strive for self-reliance, they continuously teach me the value of camaraderie and friendship. To Richard Peace, my brother, Joaquim Campos and Francisco Guerreiro, a huge thank you is not enough to express my gratitude towards what you have done for me!

Ever since I came to live in Lisbon (the big city by my standards) I have always tried to maintain a connection with my roots, especially my social circle growing up. Some of you have accompanied me to the city while others stayed in Tramagal, my hometown.

However, I'm glad that we were able to keep in touch and not loose such a close friendship. To Pedro Mendes, Duarte Valente, Bernardo Alegria, David Oliveira and many others, thank you for your welcoming arms and support. You make me realise the value of our roots together, and that long friendships deserve to be nurtured. It has been a dificult balance to achieve but you make it both easier, and I hope I deserve your patience since I'm not around as often as you would wish.

At last, I want to thank everyone within my professional circle, starting with the most important person throughout this PhD. I am forever grateful to my supervisor Dr. Pedro Machado. You have been a teacher, a mentor, a friend and dare I say my scientific stepfather. I could not have asked for a better person to guide me in the beginning of my career as an astrophysicist. Your devotion and love for science, your dedication to both your research and the team, your tireless work to make sure I had everything I needed to not only complete my journey at IA, but to spread my wings and brave the world equipped with the tools needed to become an accomplished scientist. You have opened more doors for me than I can count, exposing me to the best science being done at an international level, and the people behind it and have went above and beyond to help making sure I have a future career on this path I have chosen. I hope we can continue to collaborate and that in some years I am able to return and call you a fellow colleague, helping in making sure that the planetary sciences group in Lisbon thrives!
I also want to say a word to everyone I have ever met at the Institute of Astrophysics and Space Sciences. Thank you all for being a second home, a space of exciting ideas and loving people. I hope that my contribution has elevated IA in some form and that my presence has also been a boon to all my colleagues, aiding you in your projects.
And lastly I would also like to address all the folks at EPEC. It has been a truly enlightening experience meeting such a group of remarkable people who are invested in making our little academic corner a better place. I am glad to be part of this movement and I hope I can continue to contribute to our vision of a better world for all planetary scientists, where our research is not only exciting, but fun as well!

This project was supported by the University of Lisbon through the BD2017 program based on the regulation of investigation grants of the University of Lisbon, approved by law 89/2014, the Faculty of Sciences of the University of Lisbon and the Portuguese Foundation for Science and Technology (FCT) through the project P-TUGA with the code PTDC/FIS-AST/29942/2017. I also acknowledge the support of the European Space Agency and the associated funding bodies Centre National d'Etudes Spatiales (France) and Agenzia Spaziale Italiana (Italy) as well as the entire team behind the VIRTIS and VMC instruments onboard Venus Express space mission and the PSA archives. Additionally, I acknowledge the support and work of the entire Akatsuki team. Specifically I deeply appreciate the support of JAXA for enabling a short internship in their facilities which greatly contributed to this project. I also want to thank Joaquim Campos, João Silva, Pedro Abade and Daniela Paulo for offering their time as proofreaders of this thesis.

Abstract

The plan which gave purpose to this thesis was purposefully ambitious. Instead of focussing on a single theme, we chose to follow a path that would ultimately lead to a greater overall understanding of several ongoing processes within the atmospheres of planets in the Solar System. Our goal was to combine different techniques in a single project so that by the end of this PhD, not only did the candidate obtain valuable results and a worthy contribution to the scientific community, but also became proficient in multiple ways to study planetary atmospheres.

With images from multiple spacecraft, we employed the Cloud-Tracking technique to study the winds on multiple layers of Venus' cloud deck, and at the tropospheric level of Jupiter's atmosphere. We used the most modern instruments such as those onboard the japanese Akatsuki mission, retrieving multiple wind profiles to study the variability and evolution of the atmosphere across several altitude layers. Along with capturing winds, we set out to gather the most complete survey of atmospheric gravity waves on the lower clouds of Venus. This effort will help not only to understand their role in powering superrotation but also provide general circulation models valuable data on this previously under-explored feature.

From the ground we performed a unique Doppler velocimetry method to complement our analysis, proving that the wind results obtained from this method can be competitive with those gathered from spacecraft data at significantly lower costs and greater flexibility.

The capabilities of the team in which I am inserted have enabled multiple collaborations on other projects, further reinforcing that science is a joint effort. In this document, I attempt to provide further proof that my contribution is not only to academia but the larger society as well.

Keywords: Venus, Jupiter, Atmospheric Gravity Waves, Cloud-Tracking, Doppler Velocimetry.

Resumo em Português

O estudo de planetas do sistema solar tem já um longo percurso na história, desde as primeiras observações feitas com telescópios rudimentares até às mais modernas missões espaciais capazes de aterrar e operar remotamente em solo extraterrestre. Embora grande parte destas aventuras tenham como base as perguntas mais fundamentais da nossa existência (de onde viemos e para onde vamos?), na minha óptica o verdadeiro impulso para todos estes esforços é levado por algo bem mais simples: a curiosidade natural do ser humano. É ela que nos faz questionar o mundo que nos rodeia, além de procurar importância e significado em todas as coisas. Essa mesma curiosidade leva-nos a explorar mundos distantes dentro do nosso Sistema Solar e mais recentemente, a orbitar outras estrelas. Embora essa grande aventura do estudo de exoplanetas esteja em destaque nos dias de hoje, desde que percorro o caminho científico que considero absolutamente necessário o estudo detalhado dos objectos no nosso próprio 'quintal' cósmico. Não só são estes mais acessíveis a vários tipos de estudos mas, também motivado pelo facto de que num espaço tão pequeno, relativamente ao Universo, conseguimos encontrar uma enorme diversidade de realidades entre os vários planetas e os seus satélites naturais.

O plano para o desenvolvimento desta dissertação foi propositadamente ousado e ambicioso. O nosso objectivo era de oferecer à comunidade científica uma abordagem em vários temas de ciências planetárias num único trabalho. Ao combinar várias técnicas de observação e obtenção de dados, procurámos obter uma harmonia na ciência proveniente de todas elas. Para cumprir os nossos objectivos, tivemos em conta a equipa de investigadores na qual me insiro por forma a conduzir a minha investigação da forma mais eficaz possível. Por essa razão, este trabalho incide em dois planetas em particular: Vénus e Júpiter.

O segundo planeta a partir do Sol, Vénus é, em muitos aspectos, bastante semelhante à Terra. Ambos partilham a mesma origem, formaram-se sensivelmente ao mesmo tempo, têm dimensões e densidades muito próximas, também diferem pouco na sua composição química global e orbitam em torno do Sol a distâncias relativamente próximas no contexto das dimensões do Sistema Solar. Todavia, um olhar mais atento mostra um abismo entre os dois cenários, o paraíso em que vivemos e a paisagem queimada envolta em nuvens por onde chove ácido sulfúrico. A superfície de Vénus encontra-se a cerca de 460°C com uma pressão atmosférica 90 vezes mais intensa que a que sentimos ao nível do mar na Terra num perpétuo dia ou noite nublado que dura mais de 100 dias terrestres devido ao longo período de rotação do planeta. Estas características devem-se sobretudo ao papel da atmosfera de Vénus, em particular à sua massa e ao efeito de estufa descontrolado provocado pela abundância de CO_2. Esta situação extrema pode servir de exemplo para um possível futuro do nosso planeta, caso as alterações climáticas se agravem de forma catastrófica. Portanto o estudo do comportamento da atmosfera torna-se vital, não só

para compreender o que a levou ao seu estado actual, mas também conseguir identificar sinais de algo semelhante noutros corpos. Este aspecto torna-se cada vez mais importante na nossa era em que dezenas de 'exo-Terras' foram descobertas, algumas delas podendo, na verdade, ser mais semelhantes à nossa 'irmã gémea' no Sistema Solar.

Um dos aspectos mais importantes da atmosfera de Vénus é o facto desta estar num regime de super-rotação, circulando à volta do globo em cerca de 4.4 dias nas regiões superiores das nuvens, enquanto que o período de rotação da superfície do planeta está mais perto dos 243 dias. Isto faz com que os ventos adquiram velocidades superiores a 100 m/s embora este perfil não seja latitudinalmente uniforme nem constante em altura. Embora este fenómeno seja estudado há mais de 40 anos, os mecanismos que mantém tal velocidade ainda são desconhecidos. Apesar de ser provável que existam vários factores que contribuem para esta aceleração, o papel de ondas atmosféricas de gravidade neste cenário era, até agora ainda pouco estudado. O facto destas estruturas serem capazes de transportar energia e momento a várias camadas da atmosfera faz com que tenha surgido um novo interesse por estas ondas. É neste prisma que, com imagens obtidas por duas sondas espaciais (a missão europeia Venus Express e a missão japonesa Akatsuki) conduzimos possivelmente o maior estudo de ondas atmosféricas de gravidade nas nuvens baixas de Vénus alguma vez feito, analisando na sua totalidade a base de dados útil de ambos os instrumentos usados (VIRTIS e IR2). Com imagens de alta resolução em comprimentos de onda na zona do infravermelho foi possível observar a região das nuvens baixas de Vénus a cerca de 48 km de altitude, onde as nuvens formam padrões opacos em relação à emissão térmica mais intensa das camadas mais profundas da atmosfera. Neste estudo procurámos vestígios de actividade ondulatória e medimos as propriedades básicas das ondas identificadas, tais como o comprimento de onda horizontal e a largura do grupo ondulatório. Foi ainda possível, para parte dos grupos identificados, a caracterização dinâmica dos mesmos o que nos permite uma análise mais profunda da natureza e comportamento destas ondas. Os resultados deste estudo foram subsequentemente publicados em Silva et al. [2021].

No que toca à exploração de Júpiter, sendo o maior planeta do Sistema Solar e um gigante gasoso que suscita não só a nossa curiosidade geral, mas também um grande interesse científico devido aos muitos mistérios que circundam o planeta. Sendo um gigante gasoso, todo o planeta é um fluido em constante movimento, onde uma superfície como a compreendemos para os planetas terrestres não existe. Portanto, entende-se a existência de uma atmosfera com dimensões incomparáveis face à realidade que conhecemos nos planetas telúricos. Mais notório do nosso ponto de vista é a aparência visual das camadas superiores desta atmosfera, mostrando uma estrutura em bandas coloridas com ventos opostos que podem chegar aos 150 m/s. No meio destas bandas estão também centenas de sistemas de tempestades entre os quais se destaca a Grande Mancha Vermelha, uma tempestade com pelo menos mais de 180 anos. Entre os vários mistérios que rodeiam a dinâmica da atmosfera de Júpiter, destaca-se a circulação atmosférica entre as diferentes bandas bem como a manutenção das mesmas até vários quilómetros de profundidade.

O trabalho mais exploratório deste projecto consistiu em aplicar pela primeira vez nos gigantes, uma técnica de velocimetria Doppler, desenvolvida pelo orientador deste projecto, baseada na dispersão de radiação solar visível pelas camadas superiores de nuvens na direcção de observadores na Terra. O método de velocimetria Doppler explorado neste project foi inicialmente desenvolvido em Widemann et al. [2008] (técnica fiber-fed) e Machado et al. [2012] (técnica long-slit) e mais tarde refinado por Machado et al. [2014, 2017, 2021]. Este método tem sido aplicado com sucesso para o caso de Vénus e por esse motivo

a nossa equipa considerou que chegou agora o momento de expandir o alcance da mesma para outros alvos. O trabalho que visa estudar a dinâmica da troposfera superior de Júpiter com esta técnica, comparando com observações de sondas espaciais usando o método de seguimento de nuvens já amplamente utilizado, constitui uma parte desse esforço na qual mais directamente se insere este trabalho. Utilizámos o espectrógrafo ESPRESSO instalado no Very Large Telescope (VLT) para observar Jupiter em Julho de 2019, recolhendo o espectro da radiação solar dispersada pelas camadas superiores da troposfera de Júpiter, onde a profundidade óptica se aproxima da unidade. Tendo em conta o carácter exploratório destas observações, obtivemos perfis longitudinais dos ventos sensivelmente no mesmo nível da atmosfera através da técnica de seguimento de nuvens, usando imagens da sonda espacial Cassini. Os resultados deste estudo serão publicados num artigo que se encontra neste momento submetido à revista *Universe* [Silva et al., Submitted]
Embora ambos estes estudos sejam o foco desta tese de doutoramento a polivalência adquirida através da aprendizagem das diferentes técnicas abordadas neste trabalho, permitiram várias colaborações com outros membros da equipa. Estes incluem: o estudo de Saturno em comprimentos de onda já próximos do infravermelho, dando apoio às observações com o instrumento CARMENES no Calar Alto Astronomical Observatory (CAHA) com medições do vento zonal com dados Cassini; auxílio na recolha de medições dos ventos para várias altitudes na camada de nuvens em Vénus que permitiu a co-autoria em dois artigos [Goncalves et al., 2020, Machado et al., 2022]; e ainda apoio na discussão científica e redução de dados das observações a Marte durante a última tempestade global de poeira em 2018 bem como na detecção e caracterização de ondas atmosféricas no mesmo planeta. Durante a concepção deste trabalho também dei apoio como assitente às actividades de ensino na Faculdade de Ciências da Universidade de Lisboa, assim como uma participação activa em actividades de comunicação de ciência dinamizadas pelo Instituto de Astrofísica e Ciências do Espaço.

Palavras-chave: Vénus, Júpiter, Ondas Atmosféricas de Gravidade, Seguimento de Nuvens, Velocimetria Doppler.

Contents

Acknowledgements i

Abstract iii

Resumo em Português v

Figure index xii

Table index xii

List of Acronyms and Symbols xix

1 Overview 1

- 1.1 Project Context 1
- 1.2 Initial Workplan 2
- 1.3 Development and Achievements 4
- 1.4 Products of this PhD 5
  - 1.4.1 Personal Contributions 8
  - 1.4.2 Thesis Structure 9

2 Venus - Hidden behind Clouds 11

- 2.1 History and Exploration 12

2.1.1 The planet Venus in Human Culture 12
2.1.2 Early Scientific Observation of Venus 12
2.1.3 Space Age Exploration 13
2.2 Venus - State of the Art 20
2.2.1 Physical Characteristics 20
2.2.2 Atmosphere of Venus 21

3 Jupiter - Giant Swirling Vortex **33**
3.1 Exploring the largest gas giant 33
3.2 Origins of the Jovian System 36
3.3 Jupiter's Interior 38
3.4 Meteorology of Jupiter 41
3.4.1 Vertical Profile and Chemistry 41
3.4.2 Dynamical Processes 47
3.4.3 Storms and vortices and other features 51

4 Observations **57**
4.1 Venus Express 57
4.2 Akatsuki 58
4.3 VLT/ESPRESSO 59
4.3.1 Instrument Description 59
4.3.2 Observing Jupiter with ESPRESSO (July 2019) 61
4.4 Other Observations 63
4.4.1 Cassini ISS support for Doppler Velocimetry 63
4.4.2 Infrared observations of Venus with TNG/NICS 66
4.4.3 CARMENES infrared observations of Jupiter and Saturn 69

4.4.4 2018 Martian Global Dust Storm 69
4.4.5 Atmospheric Waves on Mars with MEx/OMEGA 73

5 Studying Atmosphere Dynamics of Solar System Planets 75

5.1 Image Processing 75
5.2 Cloud-Tracking 76
5.2.1 Cloud-Tracking with PLIA - PICV 77
5.2.2 Cloud-Tracking with ACT 80
5.3 Atmospheric Wave Characterisation 82
5.3.1 Morphological Characterisation 83
5.3.2 Atmospheric wave dynamics 85
5.3.3 Estimation of additional wave parameters 86
5.4 Doppler Velocimetry 89
5.4.1 Projected Radial Velocities 90
5.4.2 Young Effect 91
5.4.3 De-projection coefficients 92
5.4.4 Instrumental Spectral Drift 92
5.5 Error Estimation and Analysis 94
5.5.1 Cloud Tracking 94
5.5.2 Wave Characterisation Precision 95
5.5.3 Doppler Velocimetry 96

6 Results and Analysis 97

6.1 Atmospheric Circulation on Venus' Cloud Deck 97
6.1.1 Discussion 105
6.2 Atmospheric Waves on the Lower Cloud of Venus 105

6.2.1 Morphological properties 106

6.2.2 Dynamical properties 113

6.2.3 Characterisation precision 117

6.2.4 Interpretation of Characterised Packets 118

6.3 Analysis of the winds on Jupiter at the Troposphere 127

6.3.1 Doppler winds with VLT/ESPRESSO 127

6.3.2 Comparison with previous measurements 128

6.3.3 Multiwavelength Comparison 133

7 Conclusions **137**

7.1 Future Prospects and Closing Remarks 141

List of Figures

2.0.1 A full disk view of Venus from Akatsuki/UVI 11

2.1.1 The surface of Venus seen by the Venera 9 14

2.1.2 Global view of the surface of Venus from Magellan data 15

2.1.3 Venus Express instrument diagram 16

2.1.4 Akatsuki's main instruments diagram 18

2.2.1 Topography maps of Earth and Venus 21

2.2.2 Venus atmosphere seen by the Pioneer Venus Orbiter 22

2.2.3 Vertical structure of the cloud layer of Venus 24

2.2.4 Venus' cloud top altitude variability with latitude 25

2.2.5 Venus' atmospheric circulation diagram 27

2.2.6 Zonal wind profile of Venus 28

2.2.7 Meridional wind profile of Venus 29

2.2.8 Atmospheric gravity waves across the Solar System 30

3.1.1 Jupiter as seen from Voyager 1 34

3.1.2 The Juno spacecraft 36

3.2.1 Impact 'craters' on Jupiter after Shoemaker-Levy 9 comet collision 38

3.3.1 Jupiter's interior structure 40

3.4.1 Vertical structure of the atmosphere of Jupiter 42

3.4.2 Ammonia 'Mushballs' on Jupiter 43

3.4.3 Methane photochemistry paths 46

3.4.4 Jupiter's atmospheric banded structure 47

3.4.5 Jupiter's Zones and Belts diagram 49

3.4.6 Jupiter observed in the infrared 49

3.4.7 Model for atmospheric circulation in the bands of Jupiter 50

3.4.8 Variability of the Banded structure of the jovian atmosphere 51

3.4.9 Jupiter's Great Red Spot 52

3.4.10 Formation of the white Oval BA on Jupiter 53

3.4.11 The three longest lived ovals on Jupiter 54

3.4.12 Jupiter's northern hemisphere seen by Juno 55

3.4.13 Jupiter's North and South Polar regions 56

4.3.1 Optical path of the Coudé-train of ESPRESSO 60

4.3.2 A schematic of ESPRESSO 61

4.3.3 Observing plan of Jupiter with ESPRESSO, 2019 62

4.4.1 The Cassini spacecraft 65

4.4.2 Navigated image of Venus as seen from TNG/NICS on July 2012 68

4.4.3 Grid of fibre positions for the CARMENES observations strategy 70

4.4.4 Mars Global Dust Storm in 2018 71

4.4.5 Observing strategy with VLT/UVES of Mars during the 2018 Global Dust Storm 72

4.4.6 An atmospheric wave on Mars seen by MEx/OMEGA 73

5.2.1 Opening interface of PICV 78

5.2.2 PICV correlation options 78

5.2.3 PICV cloud tracking supervision 79

5.2.4 PICV - complete routine 80

5.2.5 Validation window when Cloud-Tracking with ACT 81

5.3.1 Image processing example for wave characterisation 82

5.3.2 Diagram of the Morphological Characterisation method 84

5.4.1 Diagram of the Doppler effect from backscattered solar radiation on Jupiter 90

6.1.1 Daily Zonal Wind Profiles during Akatsuki/UVI Observations 100

6.1.2 Average Profile of the Zonal Wind on Venus' Upper Cloud 101

6.1.3 Zonal wind variability with Latitude and Local Time 102

6.1.4 Mean Meridional Wind Profile from Akatsuki/UVI 103

6.1.5 Meridional wind variability with latitude and local time 104

6.1.6 Meridional Wind Profile of Venus' Upper Cloud across several years 104

6.2.1 Examples of detected waves on our study 106

6.2.2 Distribution of characterised wave packets 107

6.2.3 Distribution of distinct packets 107

6.2.4 Coverage of VIRTIS and IR2 and occurence of waves 108

6.2.5 Number of crests for the characterised waves 109

6.2.6 Morphological properties of characterised wave packets 110

6.2.7 Close-up of waves characterised in our systematic study 111

6.2.8 Distribution of morphological properties with latitude 112

6.2.9 Optical thickness drop provoked by the presence of characterised wave packets 112

6.2.10 Absolute phase velocity of wave packets against the zonal wind profile of Venus 114

6.2.11 Intrinsic phase velocity of characterised packets 115

6.2.12 Trajectory of characterised packets in Local Time 115

6.2.13 Trajectory of characterised packets above topography and their observed lifetimes 116

6.2.14 Vertical wavelength distribution of characterised packets 116

6.2.15 Dispersion diagram for dynamically characterised packets 118

6.2.16 Influence of wave properties on packet lifetime 122

6.2.17 Model of the vertical shear of the zonal wind at the lower clouds of Venus . 125

6.3.1 Panel of the Longitudinal Profiles of the Zonal Wind on Jupiter - Doppler 128

6.3.2 Jupiter's zonal wind profile from Cloud Tracking from 1995-2017 129

6.3.3 Cloud Tracking and Doppler Velocimetry results comparison 130

6.3.4 Doppler velocimetry results compared with JOVIAL-JIVE results 132

6.3.5 Multi-wavelength analysis of the zonal wind profile of Jupiter's troposphere 134

List of Tables

3.1 Chemical composition of Jupiter's Atmosphere 44

4.1 Summary of the ground-based observations of Jupiter 62

4.2 Scanning sequences for Jupiter VLT/ESPRESSO observing run on 21/22 July 2019. 63

4.3 Pointing geometry for VLT/ESPRESSO observations of Jupiter on July 2019. 64

4.4 Cassini ISS observations for Cloud Tracking - Global Profile 66

4.5 Cassini ISS observations for Cloud Tracking - Narrow Band Profiles 67

6.1 Upper Cloud Observations for Cloud Tracking with Akatsuki/UVI 98

6.2 List of Image Pairs when Cloud Tracking with Akatsuki 99

6.3 Morphological properties of characterised packets 110

6.4 Morphological characterisation precision 117

6.5 Variable values on the estimation of λ_z 121

6.6 Observed appearance/disappearance of wave packets 126

6.7 Averaged Doppler winds on each band of Jupiter observed with ESPRESSO 127

List of Acronyms and Symbols

ACT	Automatic Cloud Tracker
ADC	Atmospheric Dispersion Compensator (at ESPRESSO)
ARIEL	Atmospheric Remote-sensing Infrared Exoplanet Large-survey
ASPERA	Analyser of Space Plasma and Energetic Atoms
AT	Auxiliary Telescopes (at VLT)
AU	Astronomical Unit
CARMENES	Calar Alto high-Resolution search for M dwarfs with Exoearths with Near-infrared and optical Echelle Spectrographs
CCD	Charge-Coupled Device
CCL	Combined-Coudé Laboratory
CCS	Cross Correlation Surface
CFHT	Canada France Hawaii Telescope
CPESS	Reunion de Ciencias Planetarias y Sistema Solar
DE	Digital Electronics Unit
EGU	European Geosciences Union
ELT	Extremely Large Telescope
ENAA	Encontro Nacional de Astronomia e Astrofísica
EPEC	EuroPlanet Early-career Network
EPSC-DPS	EuroPlanet Science Congress - Division for Planetary Sciences
ESA	European Space Agency
ESPaDOnS	Echelle SpectroPolarimetric Device for the Observation of Stars
ESPRESSO	Echelle SPectrograph for Rocky Exoplanets and Stable Spectroscopic Observations
EUV	Extreme Ultraviolet
FCUL	Faculdade de Ciências da Universidade de Lisboa
FOV	Field-Of-View
GCM	General Circulation Model
GRS	Great Red Spot
GSFC	Goddard Space Flight Center
GUI	Graphic User Interface
HARPS-N	High Accuracy Radial velocity Planet Searcher - North
HPA	Half Phase Angle
HST	Hubble Space Telescope
IA	Instituto de Astrofísica e Ciências do Espaço
IAU	International Astronomical Unit
IDL	Interactive Data Language
INTA	Instituto Nacional de Técnica Aeroespacial

ISAS-JAXA	Institute of Space and Astronomical Science - Japan Aerospace Exploration Agency
IR	Infrared
IR1	1 μm Camera
IR2	2 μm Camera
ISS	Imaging Science Subsystem (onboard Cassini)
JIRAM	Jovian Infrared Auroral Mapper
JPL	Jet Propulsion Laboratory
LAC	Lightning and Airglow Camera
LIR	Longwave Infrared Camera
MARCI	Mars Color Imager (onboard MRO)
MEx	Mars Express
MODIS	Moderate Resolution Imaging Spectroradiometer
MRO	Mars Reconnaissance Orbiter
MWR	Microwave Radiometer (onboard Juno)
NAC	Narrow Angle Camera (onboard Cassini)
NASA	National Aeronautics and Space Administration
NICS	Near Infrared Camera Spectrometer
NIRPS	Near InfraRed Planet Searcher
NIMS	Near Infrared Mapping Spectrometer (onboard Galileo)
OMEGA	Visible and Infrared Mineralogical Mapping Spectrometer
PFS	Planetary Fourier Spectrometer
PhD	Doctor of Philosophy
PI	Principal Investigator
PICV	Planetary Image Correlation Velocimetry
PLIA	Planetary Laboratory for Image Analysis
PVOL	Planetary Virtual Observatory and Laboratory
RS	Radio Science
SEA	Sociedad Española de Astronomía
SMAA	Soft Matter in Astronomy and Astrophysics
SPICAV/SOIR	Ultraviolet and Infrared Atmospheric Spectrometer
SPICE	Spacecraft Planet Instrument C-Matrix Events Toolkit
SS-AS	Sub-Solar to Anti-Solar Circulation
SSAIL	Solar System Atmospheres' Investigation and exopLanets
SSI	Solid State Imaging instrument (onboard Galileo)
SWT	Science Working Team - Internal Akatsuki team Meeting
SZA	Solar Zenith Angle
TNG	Telescope Nazionale Galileo
USO	Ultra-Stable Oscillator
UT	Unit Telescope (at VLT)
UV	Ultraviolet
UVES	Ultraviolet and Visual Echelle Spectrograph
UVI	Ultraviolet Imager (onboard Akatsuki)
VERA	Venus Express Radio Science Experiment
VEx	Venus Express
VIRA	Venus International Reference Atmosphere
VIRTIS	Visible and Infrared Thermal Imaging Spectrometer
VMC	Venus Monitoring Camera

VLT	Very Large Telescope
WAC	Wide-Angle Camera (onboard Cassini)
WKB	Wentzel-Kramers-Brillouin approximation

a	Equatorial Planet Radius
$\mathbf{As_4}$	Arsenic Tetramer
$\mathbf{AsH_3}$	Arsine
$\boldsymbol{B}$	Atmospheric Static Stability
$\boldsymbol{berv}$	Correction from Earth's Rotation and Orbital Motion
$\mathbf{Br}\gamma$	Bracket Gamma Filter
$\mathbf{C_2H_2}$	Acetylene
$\mathbf{C_2H_6}$	Ethane
$\mathbf{CH_4}$	Methane
$\mathbf{CO}$	Carbon Monoxide
$\mathbf{CO_2}$	Carbon Dioxide
c_p	Phase Speed
c_S	Speed of Sound
ρ	Density
$D_\odot$	Diameter of the Sun
ω	Frequency
g	Gravity's Acceleration
$\mathbf{G}$	Gravitational Constant
$\mathbf{GeH_4}$	Germane
$\mathbf{GeS}$	Germanium Monosulfide
$\boldsymbol{h}$	Altitude above planet's surface
I_x	Radiance at x wavelength
I_x^{max}	Maximum Radiance at x wavelength
$\mathbf{NH_4}$	Ammonium
H_0	Density Scale-Height
$\mathbf{H}$	Hydrogen
$\mathbf{H_2}$	Molecular Hydrogen
$\mathbf{H_2S}$	Hydrogen Sulfide
$\mathbf{H_2O}$	Water
$\mathbf{He}$	Helium
$\mathbf{H_2SO_4}$	Sulphuric Acid
$\mathbf{J}_{2n}$	Gravitational Moments
ξ	Centrifugal Frequency when modified by the Meridional Shear of the Background Wind
$\boldsymbol{N}$	Brunt Väisälä frequency
$\mathbf{N_2}$	Dinitrogen
$\mathbf{N_2H_4}$	Hydrazine
$\mathbf{NH_2}$	Azanide
$\mathbf{NH_3}$	Ammonia
$\mathbf{NH_4}$	Ammonium
$\mathbf{NH_4SH}$	Ammonium Hydrosulfide
$\mathbf{O_2}$	Molecular Oxygen
P	Atmospheric Pressure
$\mathbf{P}_{2n}$	Legendre Polynomials

$\mathbf{P_2H_4}$	Diphosphane
$\mathbf{P_4O_6}$	Phosphorous Trioxide
$\mathbf{PH_2}$	Phosphanide
$\mathbf{PH_3}$	Phosphine
Ψ	Centrifugal Frequency
ϕ	Latitude
Φ	Phase Angle
$\bar{\phi}$	Average Latitude
ϕ_β	Latitude of sub-terrestrial point
φ	Inclination of the Solar Rotation Axis
λ	Longitude
$\Delta\lambda$	Displacement in Longitude
$\mathbf{R}_p$	Polar Radius
R_i	Richardson Number
$\boldsymbol{Rad}$	Distance from centre of planet
δs	Spatial Resolution error
$\mathbf{SO_2}$	Sulphur Dioxide
$\boldsymbol{T}$	Temperature
Th-Ar	Thorium-Argon Lamp
Δt	Time Interval
v_{rot}	Contribution of Doppler shift from differential planetary rotation
v_{topo}	Instantaneous velocity of planet's centre of mass in the topocentric frame
$v_\odot$	Equatorial velocity of the Sun
$\mathbf{V(r,}\theta\mathbf{)}$	Gravitational Potential
$\lambda_x, \lambda_y, \lambda_z$	Euclidean Components of Wavelength
(k, m, l)	Euclidean Components of Wavenumber
(u, v, w)	Euclidean Components of Wind
w_i	Radial Component of the Instantaneous Velocity
$w_{i,c}$	Projected wind velocity along the line-of-sight
$w_{i,c,ref}$	Reference projected wind velocity
δw_v	Wind velocity error
$\boldsymbol{Y}$	Young effect factor
ζ_x	Mean Standard deviation between measurements in the same packet for x property

Chapter 1

Overview

1.1 Project Context

Humankind is generally driven by curiosity. Ever since our time was not completely consumed by basic needs such as looking for food and shelter, our eyes gazed towards the beyond, in the starlit blackness of the night sky. I can only imagine what stories our ancestors told around the campfire of all the stars and planets that stood above. Many of these stories would include fantastical creatures or wonderful places where reality is much different than what we witness here on Earth. Fast forward several thousand years, and we have come to know millions of different creatures which populate almost every inch of this planet. And, although Earth also features a huge variety of landscapes, it is still only a tiny place in the cosmos. Our position in the grand scheme might put into perspective what are probably the most pressing questions that humanity has asked itself over the centuries: how did we get here and where will we go? Science has ever since tried to give clues so that we reach ever closer to an answer, understanding the world around us so that we might predict where we are headed, and find some meaning within our Universe. Its this quest that drives this PhD project, a thirst to understand worlds beyond our own, so different despite sharing a similar origin to Earth. Our planetary vicinity can function as a natural laboratory and proof that diversity can rise in such a small place in the cosmic scale. Though we can divide the planets in the Solar System as terrestrial or gas giants, no two planets are alike. However, comparative studies between bodies with the same origin can prove an illuminating exercise to further understand our place in the Universe, and the many evolutionary paths a planet might take throughout its development. Even more pressing is this subject with the discovery of thousands of planets orbiting other stars, which possibly have different birth conditions thus new and exotic features.

Of course, trying to understand all underlying mechanisms at work on all planets is a monumental task, well beyond an agreeable scope for a PhD project so we selected Venus and Jupiter to focus our analysis on, in particular their atmospheres.

Venus is the closest planet to Earth, not only in terms of distance but in physical similarities as well. With almost the same size, density and bulk chemical composition, it is often times regarded as Earth's twin. However, the massive atmosphere of Venus hides the bleak truth of the utter inhabitability of this planet, with scorching temperatures at the surface coupled with crushing atmospheric pressures. With similar origins to our home, we could ask how this has happened. How come we live in such a paradise while Venus is more akin to some hellish landscape? Continuous study of the atmosphere of Venus and the mechanisms that regulate its behaviour can hold the key to this question, and also gives us the tools to distinguish between Earth-like and Venus-like exoplanets for all those Earth-sized objects humans have discovered recently. Since many different mechanisms are at work and all contribute to the general atmospheric circulation, our plan was to select vital points on which we could concentrate our studies, so that they deepen our understanding of the targeted processes while also being useful for the planetary science community in general. Given our team's expertise and available data, we set out to analyse the wind flow of the atmosphere at two different levels in the cloud layer and research one less studied feature of Venus' atmosphere, atmospheric gravity waves which could have a significant impact in the atmosphere's general circulation.

Journeying from Venus to Jupiter, we find a very different planet. Jupiter's massive size and swirling cloud patterns lend it an uncommon majesty which caught the eye of astronomers since we started to peer into the outer Solar System planets (those beyond the Asteroid Belt). The strange nature of the gas giants, and the fact that they appear to be the most common type of exoplanet that has been found, makes its study of paramount importance. Our purpose now is to expand the tools which have been used for the study of Venus' atmosphere to other targets, being this exploratory work a second focus of this PhD project. Although Jupiter has been thoroughly observed from both the ground and space, atmosphere dynamics studies at cloud level have mostly relied on one technique or on modelling efforts. We hope to provide evidence that this task can be accomplished with other methods.

1.2 Initial Workplan

This PhD project was designed to provide an observational study with different techniques, using space and ground-based data coupled with model simulations, to improve our understanding of physical and dynamical processes in the atmosphere of Solar System planets, and use this acquired knowledge to pave the way for future studies of exoplanetary atmospheres.

For this project, we considered the present context of our team and the solid expertise of the candidate's supervisor on different observational techniques to measure winds on Venus' atmosphere, as well as our involvement in several international projects including ESPRESSO@VLT, NIRPS, Venus Express, Akatsuki, Cassini and ARIEL. The goal was to take advantage of both these features and our international collaboration network, for a comprehensive study on key mechanisms which can be dominant factors towards understanding the atmospheric general circulation of those planets and their climate's variability. Though this PhD project aims to study multiple targets in the Solar System, mainly through the network of collaborations mentioned, the available data in our team led us to focus on both Jupiter and Venus.

One crucial aspect of Venus' atmosphere which is yet to be fully revealed is its three-dimensional dynamical structure. The slowly rotating solid body of the planet enables the condition for a cyclostrophic regime, where atmospheric flow is considered frictionless and due to slow rotation of the planet, the Coriolis force can be neglected in the momentum equations [Sanchez-Lavega, 2011]. One piece of the puzzle of this complex circulation system is the behaviour of the wind at different levels in the atmosphere [Sanchez-Lavega et al., 2008]. Several methods allow us to retrieve these winds: Doppler shifts provoked by wind flow as observed from Earth-based spectrographs, can be used to infer atmospheric particle speeds [Goncalves et al., 2020, Machado et al., 2012, 2014, 2017, 2021]; cloud-tracking of moving features in ultraviolet [Horinouchi et al., 2018, Goncalves et al., 2020], visible and infrared wavelengths [Hueso et al., 2015] which are able to target from the top to the lower layers of the cloud deck, respectively; and thermal winds obtained from temperature fields and modelisation of cyclostrophic balance [Takagi et al., 2018, Gilli et al., 2021]. The mechanisms that control Venus' atmospheric superrotation, possibly the main distinguishing feature of Venus' circulation are yet to be fully understood. The techniques that we propose to explore during the course of this project aim to address this long standing challenge. As recently suggested by Bertaux et al. [2016] with Venus Express and Fukuhara et al. [2017] with Akatsuki data, the topographic landscape of Venus can have a measurable influence on cloud-top winds but, further confirmation of this influence and its degree still beg for additional research. Atmospheric gravity waves are proposed to be a way in which the topography influences the upper clouds, as air flow over mountains is a common source for these types of waves [Nappo, 2002]. These are frequently observed in planetary atmospheres [Peralta et al., 2014a,b] and because of their particular properties regarding energy transport within the atmosphere, a keen interest has been developed recently surrounding their analysis. Unfortunately, gravity waves are still poorly constrained for most targets in terms of their basic parameters, their spatial distribution, sources of excitation and vertical levels of dissipation.

Our initial goal was to investigate the temporal and spatial variability of winds at different heights on Venus' atmosphere using Doppler velocimetry and cloud tracking techniques. With these results it would be possible to constrain the vertical shear of the wind, and to investigate the lower branch of the meridional circulation, its temporal variability, and its influence on the superrotation of the atmosphere.

Regarding the exploration of atmospheric waves, Venus Express data explored in Peralta et al. [2008] and Piccialli et al. [2014] show an incredible variety in gravity waves that can be observed and measured however, only a fraction of the available data from this space mission has been used for this purpose. We planned to carry out an analysis of the complete Venus Express data set, complemented with images from the more recent japanese Akatsuki mission. New mathematical formulation allows us to infer on the vertical extent of these waves [Peralta et al., 2014a,b], and the gathered results from this survey could later be used to constrain Global Circulation Models (GCM) of Venus' atmosphere [Gilli et al., 2021].

Jupiter is a gas giant, a fluid planet much different from Venus where the permanent cloud veil obscures a rocky surface. Jupiter has no surface as we understand it and is made primarily of hydrogen and helium. Due to these characteristics, and the shear size of the planet, only a fraction of its huge atmosphere is accessible by remote sensing instruments ($\sim 0.05\%$ of its radius) [Irwin, 2009]. Clouds and hazes form at varying altitudes/pressure levels depending on their chemical composition, with upper tropospheric layers between 0.2-1 bar of pressure down to 20-50 bars for a mostly water cloud in the deep atmosphere [Seiff et al., 1998]. Dynamical phenomena in the weather layer shape different cloud patterns that define the visible appearance on the upper troposphere. The interplay between different circulation regimes and the many different features observed is still an enigma [Fletcher et al., 2020]. The high contrast between cloud morphologies permits their use as tracers of atmospheric motions in the weather layer, allowing cloud-tracking to be performed. So far, this has been the main tool employed to study winds in the troposphere of Jupiter [Porco et al., 2003, Hueso et al., 2017] however, with a fine-tuned Doppler velocimetry technique applied to Venus with success, we have within our reach another method. This adaptation to the giant planets was already producing promising preliminary results on Saturn at the start of this project, and our goal was to make use of our team's expertise in high resolution spectroscopy to retrieve Doppler winds of Jupiter for the first time.

Since the methane and ammonia absorption lines are expected to form in hazes above the tropospheric clouds where the Fraunhofer lines form, we expect to retrieve a profile of the vertical shear of the zonal wind on Jupiter when combined with cloud tracking results. With a successful adaptation of the Doppler velocimetry method for Jupiter, this project's results aim to provide the scientific community a case study in order to pave the way for the observation of similar exoplanetary atmospheres with modern technology, such as ESPRESSO and the upcoming Extremely Large Telescope (ELT).

1.3 Development and Achievements

Arguably, the biggest endeavour of this PhD project was the detection and characterisation of atmospheric gravity waves on Venus, in part due to our ambitious commitment to analyse the complete VMC and VIRTIS data sets looking for this feature, including posterior analysis. We intended to follow up on the previous gravity waves studies performed by Peralta et al. [2008] for the lower cloud, and Picciali et al. [2014] for the upper cloud so we could have the largest possible data base for the properties of these waves on Venus' atmosphere. However, we later realised the necessity to review the navigation of these images, since some of these waves could have dimensions of less than 10 km as evidenced in Picciali et al. [2014]. As such, an extremely high precision in navigation is mandatory for this kind of study. With close to 900 gravity waves detected with VMC, and since the revision of the navigation of the images would be both time-consuming and out of the scope of this project, we elected to leave such work in the context of another project where it could be fully addressed. Being able to use these detections with VMC in the future, will allow us to characterise waves on other layers of the atmosphere beyond the lower cloud.

In spite of this issue, we managed to compensate by completing the analysis of the entire VIRTIS data base for the wavelength windows that target the lower cloud (1.74 - 2.23 μm) [Peralta et al., 2017a], and complemented these images with all available data from the IR2 camera onboard the japanese Akatsuki spacecraft. Since both space missions orbited the planet at different times and with very different cruise characteristics (Venus Express had a highly elliptical polar orbit while Akatsuki's orbit period was longer but mostly equatorial), the data retrieved from each instrument could fill the gaps left by the other, helping to provide a complete picture of Venus' atmosphere. The results from this research were then published in Silva et al. [2021].

Regarding the second part of the project which involves the study of Jupiter, we used the planet-hunter VLT/ESPRESSO to perform high resolution spectroscopy on a Solar System gas giant in order to retrieve instantaneous Doppler winds. This would be a first time endeavour for this instrument. These observations were supported by an additional retrieval of winds on Jupiter with Cassini data for long term comparisons. Our Doppler velocimetry method, which has been proven successful for the case of Venus [Goncalves et al., 2020, 2021, Machado et al., 2012, 2014, 2017, 2021] was adapted to the Jupiter case, taking into account its fast rotation rate along with other particulars. Our goal was to explore the capabilities of the ESPRESSO instrument in studying the atmospheres of gas giants while also expanding the reach of our method to other targets. In Silva et al. [Submitted] we present the results from this exploratory work including our supporting analysis with Cassini and comparisons with previous works on Jupiter's troposphere dynamics.

During this project, our team became involved in the Atmospheric Remote-sensing Infrared Exoplanet Large-survey (ARIEL) space mission, dedicated on the characterisation of atmospheres of discovered exoplanets by examining the thermal structures and chemical compositions using spectra from about 1000 extrasolar targets. As planetary scientists dedicated to Solar System studies, our role is to form a bridge between our knowledge of the Solar System with what is being discovered on the exoplanets's side, with our group invited to be part of the scientific team leading one of the working groups of ARIEL "Synergies with Solar System". In this framework, we began to develop a tool which in essence takes average spectra from several planets of the Solar System to be used as proxies to compare with spectra retrieved from exoplanetary sources. This way, it might be possible to have a direct comparison between the natural laboratories present on our cosmic vicinity and the new results retrieved from ARIEL which would prove fundamental to, for example distinguish between Earth-like and Venus-like planets. I was involved in the early stages of development of this tool, testing average spectra of several Solar System targets. Although it is still a work in progress, our tool has been tentatively nicknamed 'PlanetWarp'.

Like so many of us, other possible avenues of exploration were cut-off by the sudden burst of the COVID-19 pandemic, which disabled the possibility of observations for a time, and limited the interaction between both members of the team and our international network of collaborators. Though not serious enough to jeopardize the delivery of this work, its impacts were felt not only at a professional level but at a personal one as well.

1.4 Products of this PhD

This project has contributed to a greater understanding of both Venus and Jupiter atmospheres, explored the boundaries of how we can study the atmosphere of gas giants with ground-based methods, and produced the most complete observational analysis of atmospheric gravity waves on Venus' lower cloud to date. A complete list of all productions from the work developed for this thesis is presented below:

As First Author / Presenter

- Principal investigator on a publication under the title: "Characterising Atmospheric Gravity Waves on the Night Side of Venus - A Systematic Analysis". Published in *Astronomy & Astrophysics* [Silva et al., 2021];
- Principal investigator on a publication under the title: "Jupiter's upper troposphere dynamics with reanalysed cloud-tracked data from Cassini and ground-based Doppler Ve-

locimetry with VLT/ESPRESSO". Submitted to *Universe* [Silva et al., Submitted];

• Oral presentation in Atmospheric Seminar at ISAS-JAXA(Institute of Space and Astronomical Science - Japan Aerospace Exploration Agency), Japan with title: "*Characterising Atmospheric Gravity Waves on Venus*". Invited contribution;

• Oral presentation at SWT 14 (Science Working Team) seminar of the Akatsuki space mission on February 2020 with title "*Characterising Atmospheric Gravity Waves on Venus*";

• Principal Investigator on an observing proposal for ESO's open call P105 to observe Jupiter with VLT/UVES;

• Poster and Oral presentations at EPSC-DPS (European Planetary Sciences Congress - Division for Planetary Sciences) 2019, EPSC 2020, 2021 (both virtual) with titles: "*Characterising Atmospheric Gravity Waves on Venus's lower and upper cloud banks using Venus Express VIRTIS and VMC data*"; "*Characterising atmospheric gravity waves on the lower cloud of Venus - A systematic study*"; and "*Final Results on Atmospheric Wave Characterisation on the Nightside Lower Clouds of Venus*";

• Poster presentation at EGU (European Geosciences Union - General Assembly) 2019 with title: "*Characterising Atmospheric Gravity Waves on the lower and upper cloud bank of Venus using Venus Express VMC and VIRTIS images*";

• Oral presentation at SSAIL (Solar System Atmospheres' Investigation and exopLanets) 2019 in Lisbon with title: "*Characterising Atmospheric Gravity Waves on the lower and upper cloud bank using Venus Express VMC and VIRTIS images*";

• Oral presentation at SMAA (Soft Matter in Astronomy and Astrophysics) on December 2018 with title "*Characterising Atmospheric Gravity Waves on the lower and upper cloud bank using Venus Express VMC and VIRTIS images*";

Oral presentation at CPESS-VI (VI Reunion de Ciencias Planetarias y Sistema Solar) at INTA with the title: "*Characterising Atmospheric Gravity Waves on the lower and upper cloud bank of Venus using Venus Express VMC and VIRTIS images*";

• Oral presentation at SEA 2018 in Salamanca with title: "*Characterising Atmospheric Gravity Waves on the lower and upper cloud bank of Venus using Venus Express VMC and VIRTIS images*";

• Oral presentations at ENAA XXIX in 2019, ENAA XXX (2020 - Virtual) and ENAA XXXI (2021 - virtual) in Lisbon with titles: "*Characterising atmospheric gravity waves on Venus*"; "*Characterising atmospheric gravity waves on the Night side of Venus - A Systematic Analysis*"; and *Final Results on Nightside small scale Waves on Venus*";

• Oral presentation at Jornadas Doutorais on March 2020 under the title: "Characterising Atmospheric Gravity Waves on Venus" at FCUL, Lisbon;

• Oral presentation at scientific workshop/meeting between the solar system group in IA and a select team of scientists from JAXA, under the title: "Characterising Atmospheric Gravity Waves on Venus";

• Poster presentation in Encontro com a Ciência e Tecnologia em Portugal (2020, 2021).

• Outreach article published on National Geographic Portugal with title: "O que esconde uma bola de gelo? Eis Europa." available at: (https://www.natgeo.pt/ciencia/2021/02/o-que-esconde-uma-bola-de-gelo-eis-europa);

As Co-author

- Goncalves et al. [2020] published on *Icarus* in 2020;

- Machado et al. [2021] published on *Atmosphere* in 2021;
- Machado et al. [2022] submitted to *Atmosphere.* Expected acceptance and publication in 2021.
- Machado et al. [in prep.] in preparation. Expected submission to *Icarus* by the end of 2021.
- Three observing proposals, one to observe Jupiter with VLT/ESPRESSO, one observing Jupiter and Saturn with CARMENES and one observing Venus with VLT/ESPRESSO. Both observations of the gas giants were accepted and performed but the Venus proposal unfortunately was not accepted.
- Two Oral presentations on the International Venus Conference held in Hokkaido, Japan 2019 with titles: "*Akatsuki (cloud-tracking) and TNG/HARPS-N (Doppler velocimetry) coordinated wind measurements of cloud top Venus atmosphere*" by Ruben Gonçalves, et al., and "*Meridional and Zonal winds at Venus atmosphere from Cloud tracking, Doppler techniques and comparison with modelling*" by Pedro Machado, et al.
- Oral presentations on EPSC 2018 held in Berlin, Germany with titles: "*Akatsuki and TNG/HARPS-N coordinated wind measurements of cloud top Venus' atmosphere*" by Ruben Gonçalves, et al, three Poster presentations at EPSC-DPS 2019 with titles: "*Venus' cloud top wind measurements with TNG/HARPS-N and coordinated Akatsuki observations*", by Ruben Gonçalves, et al., "*Venus' atmosphere cloud tracked winds (283 and 385 nm): comparison with Doppler winds and GCM simulations*", by Pedro Machado, et al., and "*Adaptation to infrared of Doppler Velocimetry applied to Saturn with CARMENES*" by Miguel Silva, et al and another four oral presentations at EPSC 2021: "*Final Results of Doppler Velocimetry Winds on Mars' Atmosphere*" by Pedro Machado et al.; "*Characterising Atmospheric Gravity Waves on Mars using Mars Express OMEGA images - a preliminary study*" by Francisco Brasil; "*Assembling aliens to explore the Solar System*" by Catarina Leote et al.; "*Venus Dynamics on the framework of Bepicolombo flyby to Venus and Akatsuki UVI coordinated observations with TNG HARPS-N observations*" by Daniela Espadinha;
- Three Oral presentations on SMAA with titles "*Comparative study of circulation regimes on planetary atmospheres*", by Pedro Machado, et al., "*Venus' cloud top wind measurements with TNG/HARPSN (Doppler velocimetry) and coordinated Akatsuki observations*"by Ruben Gonçalves, et al., and "*Ground-based Doppler Velocimetry: wind measurements in Saturn's atmosphere with UVES/VLT*" by Miguel Silva, et al;
- Oral presentation at CPESS-VI with title: "*Atmospheric Dynamics of Venus using Akatsuki's space-based observations and cloud tracking techniques*", by Daniela Espadinha, et al;
- Three Oral presentations on S-SAIL 2019 with titles: "*Meridional and Zonal winds at Venus' atmosphere from Cloud tracking, Doppler techniques and comparison with modelling*", "*Akatsuki (cloud-tracking) and TNG/HARPS-N (Doppler velocimetry) coordinated wind measurements of cloud top Venus' atmosphere*", by Ruben Gonçalves, et al., "*Adaptation to infrared of Doppler Velocimetry applied to Saturn with CARMENES*", by Miguel Silva, et al;
- Oral presentation at the EnVision Conference in Paris on February 2020 with title: "*Venus' Meridional and Zonal winds from: Akatsuki/UVI, Venus Express/VIRTIS, TNG/HARPS-N and CFHT/ESPaDOnS*" by Pedro Machado, et al;
- Oral presentation at the Communicating Astronomy with the Public Virtual conference with the title: "A board game about the Solar System in times of a pandemic" by Catarina Leote et al.;

- ARIEL Consortium Supporting Member for the ARIEL space mission and part of the working group: "Synergies between Solar System and exoplanets";
- Member of three working groups on EPEC (Europlanet Early Career Network): EPEC-EPSC, EPEC Outreach and EPEC Communications;
- Officer of the Spain & Portugal regional hub committee of the Europlanet Society as an EPEC representative of Portugal.

In addition to all research related activities, I also gave the Department of Physics of the University of Lisbon some support in the form of teaching duties. I was an assistant to physics classes concerning subjects related to electricity and magnetism to computer engineering and geophysics students, serving for three academic terms.

Since I consider outreach an essential part of every scientific career, I'll take this opportunity to highlight some activities in which I have been involved with. I have collaborated with the science communication department of IA on various events such as "Planetália - A Festa dos Planetas", and the Ignite IASTRO tours, as well as part of the scientific council on the development of a board game called "ET - A Solar System Adventure" designed to stimulate interest in planetary sciences on children and youngsters in Portugal. The project was in development for five months and with a later testing phase of seven months, delayed by the pandemic situation, is now being prepared for a first *Print & Play* version scheduled to be available very soon. Other activities include participation as an astronomer in public star-gazing events in various parts of the country, and scientific revision of IAU (International Astronomical Unit) translated content into Portuguese. Although more communication opportunities have been scarce in pandemic times, I was able to offer other forms of support to the science communication team at IA regarding education activities, such as short internships at IA which included interviews with researchers.

The techniques applied throughout this project are also valuable for other investigations, allowing me to participate in collaboration with other projects within our planetary sciences team. These include support on Doppler velocimetry results of Saturn with cloud-tracking data, model Solar System planets' spectra as it would be seen if it came from an exoplanetary source, and atmospheric waves studies on the atmosphere of Mars, the reason why my co-authorship on multiple talks and productions is possible.

1.4.1 Personal Contributions

I will use this section to clarify my specific involvement on all projects presented in this thesis.

I am the Principal Investigator (PI) of the research line related to atmospheric waves search and characterisation on Venus, which resulted in the publication Silva et al. [2021]. I led all aspects from data acquisition, which was on public archives, detection and characterisation of waves, interpretation and manuscript concept and writing.

I am also the PI on the work developed for the publication of Silva et al. [Submitted]. I led the cloud tracking effort, interpretation of results and writing of the manuscript.

Regarding my first co-authored publication in Goncalves et al. [2020], I contributed to the cloud tracking effort to retrieve wind velocity measurements from Akatsuki data.

My co-authorship of Machado et al. [2021] is justified by my participation in the writing of the manuscript, data handling and interpretation as well as assistance in the cloud tracking effort to retrieve the wind measurements used in the study.
Regarding the work on 2018 Mars global dust storm [Machado et al., in prep.], I gave support in the observing proposal and, for the project related to the detection and characterisation of atmospheric waves on Mars, I am counselling in the detection and characterisation effort of these waves and expect to be involved in the interpretation of results.
For the work developed in Machado et al. [2022] I participated in the cloud tracking effort to retrieve wind velocities in the lower cloud with TNG/NICS images, gave writing support on the navigation sections of the manuscript and was also involved in the interpretation of the results.
As for the project regarding near infrared and visible wavelength observations of both Jupiter and Saturn with CARMENES, I contributed with comparative cloud tracking results from Cassini/ISS observations and also supported the ground-based observing proposal.

1.4.2 Thesis Structure

The contents of this thesis are organized as follows:

- Chapter 2 introduces Venus to contextualize the work developed for this project with all previous knowledge relevant to our work. In this chapter we include the history of Venus' exploration, a detailed description of space missions to Venus, namely Venus Express and Akatsuki, and the current knowledge on the structure and behaviour of both the planet and its atmosphere;
- Chapter 3 documents important concepts to understand our framework when studying Jupiter, including current major questions regarding the gas giant. We explore its observation and exploration history, current knowledge of the planet's interior and an analysis of ongoing processes at cloud level;
- Chapter 4 provides a description of the observations performed to retrieve the scientific data used in this project. Each section focuses on a single mission or ground-based facility, with a final section (Other Observations) focussing on other projects which were not the primary subject of this thesis, but contributed with several co-authorships and were vital support for other members within our team;
- Chapter 5 explains all the methods used to retrieve the scientific results reported on this thesis. Since image processing is necessary for both cloud-tracking and atmospheric wave characterisation, we include it first in a separate section. In 'Error Estimation and Analysis' we detail the inherent errors involved when analysing data through the different methods used, even if contributions to the errors can be brought by the data itself and not the methods. We explore how these errors have affected our observations.
- Chapter 6 exposes all results from the data retrieved during observations described in chapter 4 using the methods explained in chapter 5. We separated each section focusing on the different topics where I was directly responsible for retrieving and analysing the data. Each section in this chapter incorporates the discussion of the results retrieved, and their interpretation in the context of earlier observations and models.
- Chapter 7 includes the final remarks and conclusions of this project. It also mentions

possible extensions for the work pursued during this thesis, and future collaborations and projects.

Chapter 2

Venus - Hidden behind Clouds

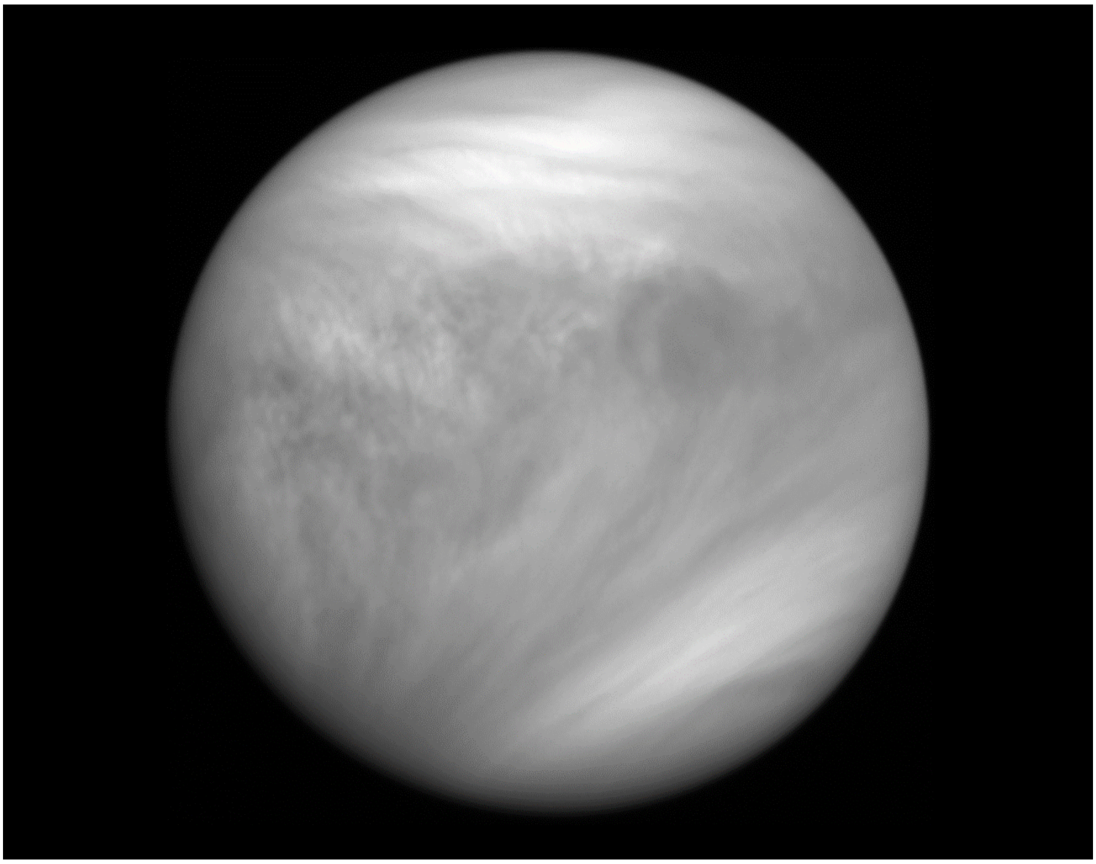

Figure 2.0.1: A full disk view of Venus as seen by the Akatsuki's UVI instrument at 365 nm on January 2016. The cloud layer visible in this image is at approximately 68-70 km of altitude above the surface of the planet, which is completely hidden by the atmosphere.

2.1 History and Exploration

2.1.1 The planet Venus in Human Culture

Venus is the third brightest object in the sky after the Sun and Moon. As such, it has been known and admired since pre-historic times, revered as a goddess or divine symbol of of primal importance to many cultures and religions, and is the subject of hundreds of myths and legends.

Known as the morning and evening star, it was believed to be two separate objects by several cultures including the ancient Egypt and classical Greece, since it seemed to disappear due to its proximity towards the Sun in the celestial sphere, only to rise again after a few days on the other side of it on the opposing horizon. This peculiarity would grant it either a dual aspect to divine entities it would represent, such as the summerian goddess Inanna, presiding over birth and death [Littleton, 2005], or representing the separation of ill-fated lovers according to folk tales from the vietnamese [Ravier, 1880]. The dual nature of the planet was known as *Phosphoros* and *Lucifer* for the morning star and *Heosphoros* or *Vesper* for the evening star before Pythagoras attributed both stars to a single object [Piccialli, 2010], even though previous texts already postulated this hypothesis.

The movements of this celestial object were also studied and revered by the Mayan civilization, timing important events such as wars, according to Venus' position and their celestial calendars [Milbrath, 1999]. Other cultures such as the Yolngu people of the Australian Aboriginals see Venus as *Banumbirr*, the origin of animals and other lands as she travels the sky. The Yolngu still hold a "Morning Star Ceremony" to communicate with their ancestors in the island of the dead, for guidance on their current lives [Norris, 2007].

2.1.2 Early Scientific Observation of Venus

Even though our ancestral cultures studied the celestial sphere and its objects in great detail, leading to a higher understanding of its mechanics, further details would elude ancient scientists until the advent of modern age astronomy, with the arrival of the telescope at the beginning of the 17th century. In 1610 Galileo Galilei, with the help of his refracting telescope, was the first man to observe the phases of Venus which could not be explained by the classical Ptolemaic geocentric model. A final unquestionable argument for Copernicus theory of *heliocentrism* came with the observation of Venus passing behind the Sun's disk [Grinspoon, 1997]. Other observations by Galileo, include the periodic variability of Venus's disk size and albedo fluctuations, later detected from Cassini observations [Marov and Grinspoon, 1998].

Transits of Venus on the Sun's disk have also provided valuable new insights on the majesty of the morning/evening star, the first recorded in 1761 by Mikhail Lomonosov, giving evidence of the presence of an atmosphere on Venus when he observed a glowing aureole that surrounded the planet during transit events. A following transit event in the 19th century would also allow better observations of parallax which made a much more accurate determination of the distance between Earth and the Sun possible [Grinspoon, 1997]. The most recent transit event occurred in 2012, upon which an international team of planetary scientists joined in a coordinated effort to analyse with modern instruments,

the aeroule effect on the atmosphere of Venus. This international campaign named Venus Twilight Experiment [Widemann et al., 2012] delivered a multitude of data, some of which is still under research.
As Venus is roughly the same size as Earth, its rotation was for long thought to be similar as well ($\sim$ 24 hours), until Schiaparelli proposed that Venus was tidally locked, conferring upon it a much slower rotation rate. Although such an orbital configuration is not present in Venus, the slow rotation would later be confirmed with radio observations, at the dawn of the space age in the 1960's. Before these observations, due to the number of characteristics that made Venus similar to Earth, along with the increasing number of observations that led to the conclusion that Venus was completely covered by clouds, scientists speculated that Venus housed a lush jungle-like environment hidden beneath the cloud cover. This would possibly be caused by enormous quantities of water vapour akin to what happens in tropical forests on Earth, only on a much larger scale. Microwave observations performed by Mayer et al. [1958] started first to challenge this idea, indicating a temperature source on Venus on the order of 600 K. Contrasting these findings, in millimetre data the temperature would be much lower, resulting in two competing ideas regarding the origin of the high temperature source. This debate only came to a close with the arrival of the *Mariner 2* robotic space probe, the first successful mission towards another planet, measuring high surface temperatures ($\sim$ 700 K) before getting crushed by the hostile environment of Venus [Sonett, 1963].

2.1.3 Space Age Exploration

During the cold war which prompted a race towards technological and scientific development, a large number of space missions were built with the goal of exploring our closest 'twin' neighbour. Over 30 different spacecraft have 'sailed' towards Venus since the dawn of the space age. The first of these missions was launched in 1961 (Venera 1), but contact with the spacecraft was lost before its closest approach to Venus. Success came with the American Mariner 2 probe, coming within 35.000 km from the planet and, equipped with its magnetometer was able to verify the lack of an intrinsic field on the planet. Other fly-by missions followed, including Mariners 5 and 10, the latter being noteworthy for its journey to Mercury and our first view of Venus in ultraviolet light, showing sharp contrasting features from a still unknown absorber. These observations also revealed the high velocity winds of the upper clouds of Venus' atmosphere in early 1974 [McFadden et al., 2007]. Despite the achievements from these missions, landing on the surface of another planet was also a major goal for both superpowers at the time, and after the moon landings of the 60's, we set course towards our closest planetary neighbours. The soviet *Venera* program (1961-1984) was the first successful set of missions to be able to reach the surface, gather atmospheric data during entry, and take the first picture of the surface of another planet (see Fig. 2.1.1). Beyond the obvious breakthroughs in technological capability, they were able to gather surface data that would greatly improve Venusian maps, and enable the analysis of physical and chemical conditions on Venus' rocky landscape. Data from these missions confirmed the existence of superrotation in the atmosphere, verifying that the contrasting UV absorbing clouds would complete a revolution around the planet in about 4 days, whereas its rotation was known to be much longer [Dollfus, 1975].

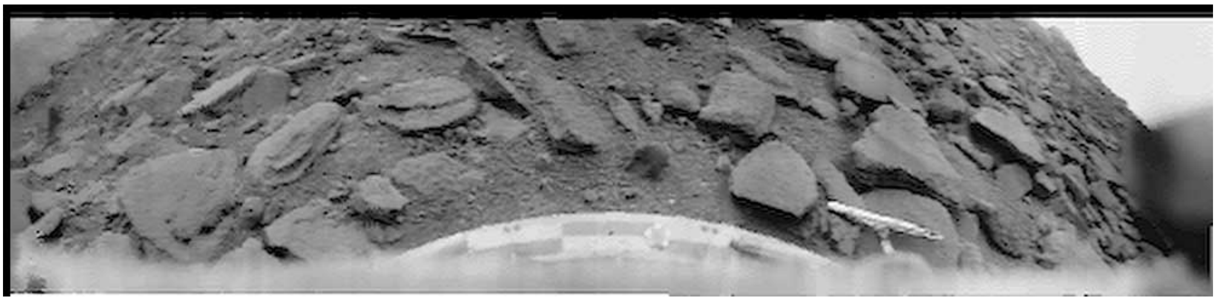

Figure 2.1.1: Panorama of the surface of Venus taken by the camera onboard the Venera 9 space probe, the first image of a planetary surface outside Earth in 1975. Credits: Soviet Space Program, `http://www.russianspaceweb.com/venera75.html`.

For competition's sake, NASA issued the *Pioneer* program with two spacecraft, the *Pioneer Venus Orbiter* and the *Pioneer Venus Multiprobe* launched in 1978. A special mention to the orbiter is warranted due to its long commission time of almost 13 years, enabling huge improvements on the scientific understanding of the planet. The orbiter retrieved the chemical distribution of the atmosphere and its clouds, its ionosphere and characterised several geological features on its surface [Kasprzak, 1990]. The following soviet space program for Venus were the *Vega* missions in 1984, which used a similar design for probes and landers but also deployed atmospheric balloons, that could survive inside the atmosphere of Venus for longer periods than landers, whose conditions were less severe than on the surface. This extended lifetime enabled more comprehensive measurements of temperature and pressure profiles of the thick atmosphere of Venus, including its dynamical behaviour [Blamont, 2008]. The Vega 2 mission was particularly successful, with its balloon being operational for 46.5 hours, travelling more than 11.000 km within the atmosphere [Wilson, 1987].

The Magellan probe was the last dedicated space mission to Venus before the turn of the century. Launched in 1989 and after a previous attempt to build such a mission, its primary goal was to map the entire surface of Venus with enhanced resolution using radar instrumentation, and to obtain a global gravity field of the planet to improve the current understanding of the planet's geological structures and their evolution. The mission was such a success that its high resolution topographical maps are still used today, thanks to its 4 year global survey of Venus leading to a final 'windmill' experiment before the spacecraft entered the atmosphere, being completely destroyed by entry friction.

Our 'evil' twin would be visited twice before its next dedicated mission, by both *Galileo* and *Cassini* spacecrafts, bound to the outer planets of the solar system, Jupiter and Saturn respectively, using Venus for a gravitational slingshot manoeuvre, to propel the spacecraft to the far reaches of the Solar System. Though scientists took advantage of both opportunities to analyse the atmosphere of Venus, retrieving some useful data, it was not until the Venus Express (VEx) mission from the European Space Agency that a greater scientific revolution was brought upon the study of our neighbouring planet.

Venus Express - First European Mission to Venus

Venus Express symbolized a revival in scientific interest around Venus, returning to explore the planet after 10 years without any dedicated mission. As pointed above, the

Figure 2.1.2: Global view of the surface of Venus. This image was constructed using the radar mapping data from Magellan with a computer generated globe. The image is color coded to enhance geological features such as the enormous equatorial highland of Aphrodite Terra in bright yellow. Credits: Magellan Mission Images, JPL, `https://www2.jpl.nasa.gov/magellan/images.html`.

Pioneer and Magellan spacecraft made important discoveries regarding Venus' geology and geophysics and the former, paired with the atmospheric balloon from Vega 2, provided extraordinary insights on the chemical composition and dynamics of the atmosphere. However, key questions remained such as a global temperature profile, the nature of the lower cloud and thermosphere, the underlying mechanisms that support atmospheric superrotation, the dynamics of the polar vortices, the origin of the unknown ultraviolet (UV) absorber, the processes responsible for the energy balance and runaway greenhouse effect on Venus and many other mysteries [Svedhem et al., 2007a]. The mission was also finished in record time thanks to ESA's strategic play to scavenge Mars Express and Rosetta's heritage, along with using the same industrial and scientific teams. These efforts allowed for Venus Express to be ready for launch in just 4 years since approval [Svedhem et al., 2007a]. In an attempt to answer some of these questions the payload of the mission is listed as follows, giving greater emphasis to the Visible and Infrared Thermal Imaging Spectrometer (VIRTIS) and the Venus Monitoring Camera (VMC):

- **ASPERA** - Through its five sensors, the ASPERA-4 investigated the plasma environment around Venus, the interaction between this and the induced electromagnetic field around the planet and its consequences to the atmosphere;
- **PFS: Planetary Fourier Spectrometer** - A spectrometer operating in the thermal infrared (IR) range to study the atmospheric composition in the mesosphere and upper clouds (between 60 and 100 km);
- **SPICAV/SOIR** - An UV and IR spectrometer to study the atmosphere of Venus in solar and stellar occulations, limb and nadir geometry [Bertaux et al., 2007]. The main goal of this experiment was to study the vertical structure and composition of the upper atmosphere between 70 and 180 km approximately, specifically looking for the spectral

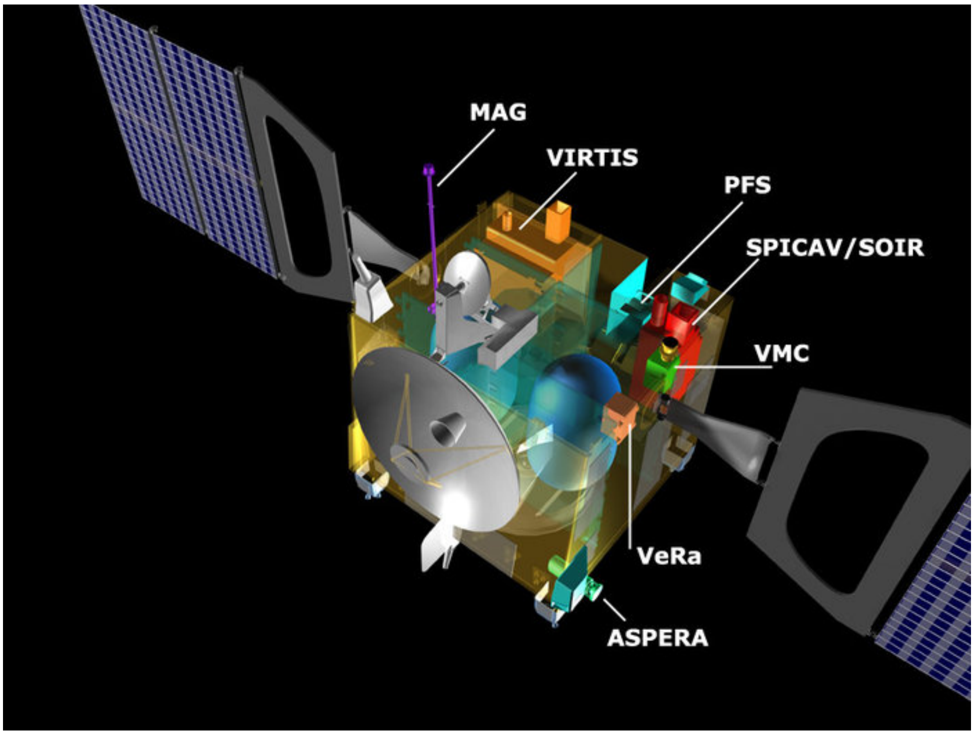

Figure 2.1.3: A diagram of all the instruments on board Venus Express. Credits to ESA.

features of semi-heavy water (HDO) in this atmospheric region, as well as study the haze above the clouds and the microphysical properties of aerosols;

- **VERA: Venus Express Radio Science Experiment** - An instrument which uses radio occultations to investigate the vertical structure of the atmosphere and ionosphere. Aimed at giving vertical profiles of both temperature and pressure from 40 to 100 km with a resolution of a few hundred meters, and profiles of the electron density from about 80 km to the ionopause, close to 600 km of altitude;
- **VIRTIS: Visible and IR Thermal Imaging Spectrometer** - An instrument equipped with two separate telescopes which work on two channels: VIRTIS-M a mapping spectrometer that operates in two wavelength ranges (VIRTIS-M-VIS from 0.3 to 1 μm and VIRTIS-M-IR from 1 to 5 μm); and VIRTIS-H, a high-resolution spectrometer focused on the infrared [Drossart et al., 2007]. On imaging mode, VIRTIS extracts cubes of images, dividing its spectral range in hundreds of wavelength slits. This setup allows the visualization of different layers of the atmosphere at the same time [Sanchez-Lavega et al., 2008]. This experiment had a very broad range of scientific objectives thanks to its design. Through the near infrared spectral 'windows' it allowed the study of chemical abundance and dynamics of the lower cloud (between approximately 44-49 km) on Venus' nightside, while beyond the morning terminator into daylight, it could study these same properties in the upper clouds. Since VEx featured a highly elliptical orbit during its mission, with an apocenter of 60,000 km and a pericenter as close as 350 km above the clouds, imaging with VIRTIS at its closest approach becomes problematic. The large integration times of the hyperspectral cubes prove to be an obstacle as the spacecraft speeds past its pericentre around Venus. For this reason, data coverage from this instrument concerns mostly the southern hemisphere while its northern counterpart consists of only scattered points, which give it only a statistical coverage [Piccialli, 2010]. Along with studying the atmosphere at various levels, the 1 μm 'window' was also in reach of VIRTIS' sensors,

allowing it to map the surface of Venus on the nightside.

- **VMC: Venus Monitoring Camera** - This instrument consists of a wide-angle camera designed for observation of the atmosphere through four narrow band filters centred at 365 (UV), 513 (VIS), 935 (NIR1) and 1010 (NIR2) nm. Camera specifications allow images with a spatial resolution between 0.2 and 50 km, at pericentre and apocentre respectively. Each of these wavelengths were chosen for specific science goals. The UV channel targets the upper clouds, as it demonstrates an absorption feature belonging to an unknown compound. The variation in the spatial and vertical distribution of this unknown UV absorber produces markings on Venus' observable atmosphere, allowing scientists to track these features to study the atmosphere dynamics at the cloud tops along with the observations of atmospheric waves [Piccialli et al., 2014] and other small-scale phenomena. The channel centred at visible wavelengths (513 nm) observes the O_2 nightglow which enables an analysis on the circulation of the upper atmosphere. The first IR channel studied the water vapour at the cloud top, and was also used in search of lightning, and the other IR channel attempts to take advantage of a spectral window at 1010 nm to look for 'hot-spots' in the surface brightness of Venus' nightside. Another important task reserved for VMC is to provide an imaging context for other instruments onboard VEx as it can operate along the entire orbit, taking about 100 images for each.

As can be seen from the payload described above, this mission employed a very diversified set of observation techniques over a broad spectrum, designed to cover the full globe of Venus at various wavelength ranges, sounding its atmosphere and surface over its planned mission. While VEx terminated operations due to fuel exhaustion in December 2014 and a more recent mission is still in orbit today, its data is still under exploration and responsible for major scientific breakthroughs concerning Venus.

Akatsuki - The Venus Climate Orbiter

As its old name implies, Akatsuki (japanese word meaning 'dawn') aimed to unveil the global climate brought upon by the circulation of the atmosphere of Venus and its thick layer of clouds. Equipped with sophisticated imaging instruments, Akatsuki is poised for meteorological studies of the atmosphere of Venus, in a complementary way to Venus Express. The mission was launched on May 21, 2010 and orbit insertion was planned for December of the same year, but the orbit insertion manoeuvre was unsuccessful due to a malfunction of the propulsion system [Nakamura et al., 2016]. The spacecraft would orbit around the Sun for another 5 years before a new opportunity came to get back in touch with Venus. This second attempt was fortunately successful however, its originally planned 30-hour elliptical orbit near the ecliptic plane was jeopardized and the new orbit became much longer and elongated, with a period of 10 and half days, an apocentre of 360,000 km and a pericentre between 1000 and 8000 km. In spite of this significant change, it did not force any major alteration on the observation strategy that was to be employed by mission scientists.

The now larger time span that the spacecraft is further away from Venus allows for a more continuous global monitoring, with the full disk being observable about 96% of available time within an orbital revolution, opposed to the original 60% planned. Another advantage is that the observation geometry is also stable over several days allowing us to track the evolution of large cloud features and the development of global scale atmospheric

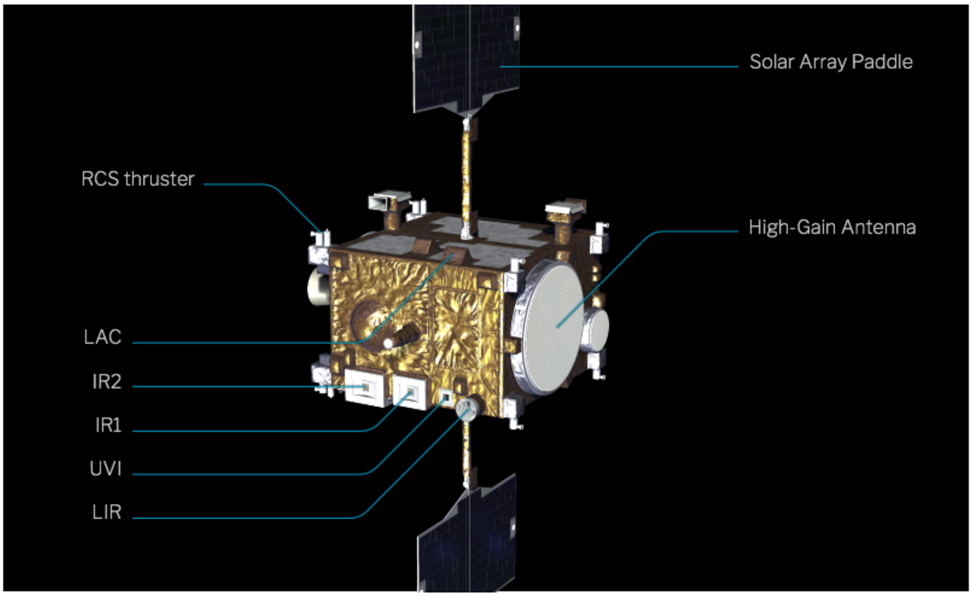

Figure 2.1.4: JAXA's Akatsuki spacecraft instrument payload. This image shows the placement of all imaging instruments of which the UVI and IR2 were extensively used in this project. Credits to ISAS (Institute of Space and Astronautical Science)/JAXA.

structures, at the cost of a lower spatial resolution [Nakamura et al., 2016].

Since the primary mission of Akatsuki is to analyse the global circulation mechanisms of Venus' atmosphere, its scientific payload is sensitive to multiple altitude levels, in order to properly model its three dimensional structure and dynamics:

- 1-μm Camera (IR1) - This camera was designed to mostly operate on the nightside at wavelengths which penetrate the whole atmosphere. By measuring thermal radiation which comes mostly from the surface at the target wavelengths (0.90; 0.97 and 1.01 μm), the data retrieved yields information on surface materials and possibly hot lava ejected from active volcanic sources. The 0.97 μm channel is also sensitive to absorption by water vapour, allowing to estimate its quantity and distribution below the cloud. A more detailed description of the instrument can be found in Iwagami et al. [2011];
- 2-μm Camera (IR2) - This instrument targets the lower cloud region and the section below, between 35 and 50 km of altitude using the atmospheric windows at wavelengths 1.73, 2.26 and 2.32 μm. These windows are subject to CO_2 absorption, with the last one is also being subject to a CO absorption band. Since the latter chemical species is expected to be produced above the cloud and then sink to the deeper atmosphere, its distribution can give information on the vertical circulation of the atmosphere in this region [Nakamura et al., 2011]. Another goal of this camera is to track cloud motions on the lower cloud region and to characterise an instability region within the cloud deck between 50 and 55 km of altitude [Belton et al., 1991];
- Ultraviolet Imager (UVI) - Designed to map the ultraviolet (UV) contrast from scattered solar radiation present in the upper cloud, brought by the absorption of SO_2 at 283 nm and the enigmatic unknown absorber at 365 nm. Tracking these UV markers has yielded wind vectors at the cloud top [Horinouchi et al., 2018] and studying spatial distribution of both absorbers could lead to a better understanding of vertical motions in the upper clouds;
- Longwave Infrared Camera (LIR) - A thermal imager equipped to detect the emission from the cloud top at longer wavelengths (8-12 μm), mapping the temperature in

the upper clouds, which can be translated to cloud height distribution. Images taken by LIR can illustrate convective cells and various types of waves within the cloud deck, and can do so on both day and nightside without losing image quality, unlike other imagers onboard. A complete description of this camera can be found in Taguchi et al. [2007] and Fukuhara et al. [2011];

- Lightning and Airglow Camera (LAC) - An instrument employed to conduct a search for lightning on the atmosphere of Venus [Takahashi et al., 2008], so far having never been confirmed before, even though it has already offered a good list of candidates [Takahashi et al., 2020]. If it exists, lightning distribution should reflect the microphysics of clouds and mesoscale convection.
- Radio Science (RS) - An instrument to perform the radio occultation experiment to determine the vertical structure of Venus' atmosphere [Imamura et al., 2011]. This sophisticated experiment yields temperature and pressure profiles of the neutral atmosphere accessible by this technique, which for Venus ranges between 32 and 90 km of altitude. The RS instrument is equipped with an ultra-stable oscillator (USO) which provides a stable reference for the signal used in the radio occultation experiment, and is also unique when compared to other occultation experiments for Venus since Akatsuki's orbit allows low latitudes to be sensed much more with this technique than in previous missions.

The four cameras dedicated to broad climatology studies (IR1, IR2, UVI and LIR) are controlled by a special Digital Electronics Unit (DE) which facilitates handling operations when observations with these four instruments are consistently repeated.

The most recent heritage of Venusian space exploration comes from VEx and the Japanese mission, with its set of complementary instruments, was expected to overlap with the European mission, allowing for coordinated observations. The fact that both missions have very different orbits (VEx has a polar orbit with periapsis near the north pole while Akatsuki has an equatorial orbit) and their scientific payload was distinct, meant that a full coverage of Venus' atmosphere and surface would be possible in great detail, due to the different spatial and temporal coverage of both missions. One such example would be the interaction between data from IR1 and VIRTIS both yielding information from the surface of the planet, where IR1 would be able to easily distinguish between cloud and surface features due to continuous monitoring, while VIRTIS having an extended wavelength range would provide better spectroscopic data to determine surface material.

Alas, with the initial failure of Akatsuki's orbit insertion manoeuvre, this joint endeavour became only possible in a desynchronised fashion, making planned coordinated observations void. However, opportunities to take advantage of the different temporal and spatial coverages of both spacecraft were taken to full effect, as in the characterisation of gravity waves on the lower clouds of Venus which is described in greater detail in Silva et al. [2021]. At the time of writing of this document, Akatsuki still orbits around Venus and leads the front-line of Venus's space exploration, continuing our efforts to uncover our mysterious twin.

2.2 Venus - State of the Art

2.2.1 Physical Characteristics

At a first glance, Venus could be seen as a very similar planet to Earth, with nearly the same mass (0.815 Earths), density (less than 5% relative difference), size (0.866 Earth's volume), and bulk chemical composition. Both have substantial atmospheres and relevant cloud systems [Bengtsson and Grinspoon, 2013]. Both planets seem to have formed at approximately the same time and under similar conditions yet, they evolved in drastically different ways [Svedhem et al., 2007b]. While we might know Earth to be our home and the only paradise we have, Venus could be more easily compared with several versions of Hell from different human cultures.

Venus travels around the Sun in a nearly circular orbit, taking 224.7 days for a complete revolution [McFadden et al., 2007]. However, it also features a 243-day retrograde rotation, effectively making a venusian year shorter than a single day. However, given present day orbital conditions for Venus, we should expect that the solid globe of Venus would synchronize with its orbital period due to solid body tides raised by the Sun. Thus, there should be other forces that maintain the current regime [Margot et al., 2021]. Venus' orbital eccentricity is also the lowest in the Solar System, although it has been theorized that it might not have always been this way. The evolution of the atmosphere of Venus, mainly its loss of water and current runaway greenhouse effect, might be tied to how orbital characteristics of the planet have changed since its formation. Jupiter and Saturn migrating from the inner Solar System to their present orbits could have had a long lasting impact on the evolution of Venus' atmosphere, by provoking drastic changes to the orbit of the planet [Kane et al., 2020].

The lack of surface probes that survive for long on the surface of Venus as presented in Sec.2.1.3, as well as its thick layer of clouds presents a challenge in investigating the surface and the interior structure of our close neighbour. The size of the core and its global physical nature are still uncertain [Margot et al., 2021] and while there is no evidence of present global plate tectonics, there are signs of some tectonic processes [Nimmo and Mackenzie, 1998], and recent data from VEx suggests the presence of active volcanism on Venus today [Stofan, 2016].

Most surface data we have on Venus comes from the Magellan orbiter, with its almost global radar maps along with VIRTIS/VEx and IR1/Akatsuki observations. Since both Venus and Earth are of such a similar size and we expect that their formation processes were mostly identical, the energy available for geological evolution would be comparable. This is because it mostly comes from the heat generated during the accretion phase of planet formation and decay of radiogenic isotopes. Over time, the decay becomes more significant than accretion heat in generating internal energy for rocky planets [McFadden et al., 2007]. However, despite both having a large topographic range, Venus and Earth show a very different distribution and types of geological features.

Figure 2.2.1 shows that the surface of Venus is dominated by plains, populated by regional highlands that can be understood as continents. One, such as *Ishtar Terra* forms in the northern hemisphere and houses the tallest mountain range on Venus, Maxwell Montes which rises to almost 11 km above the average surface elevation. Also, *Aphrodite Terra* near the equator is the largest highland on Venus featuring a greater number of what appear to be ridges or fractures, possibly caused by compression forces from mantle

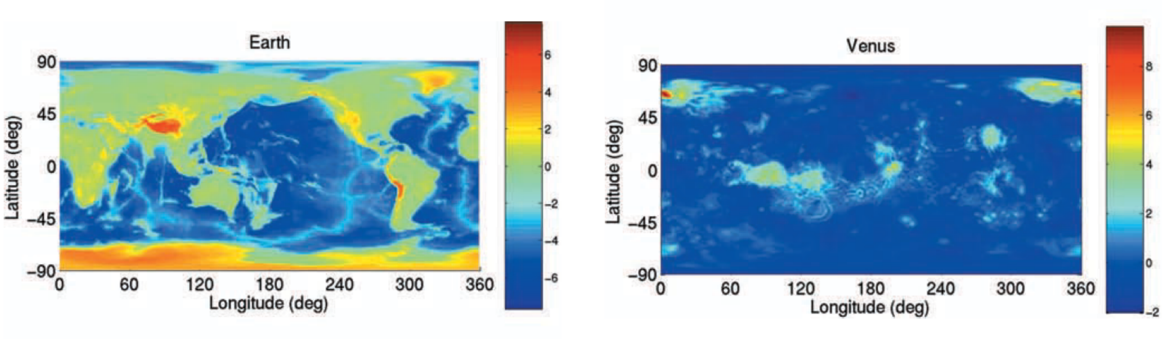

Figure 2.2.1: Topography map of Earth and Venus at a 1 pixel/degree resolution. From [McFadden et al., 2007].

activity below the surface [Hansen and Lopez, 2018]. Contrary to Earth whose plate tectonics help a continuous recycling of the lithosphere with its rifts and subduction zones, geological activity on Venus lacks such a system, even though it shows complex topographical features and evidence of recent surface evolution.

Compared to Mars, Mercury and the Moon, Venus shows a very reduced number of impact craters distributed seemingly randomly across the surface. Being consistent with a strong immobile lithosphere, these inner Solar System objects feature surfaces that show no signs of recent activity, with impact craters accumulating overtime while Venus' surface seems have been subjected to periods of tectonic activity in recent history. This has led to the general hypothesis that Venus surface is very young because it has suffered a major resurfacing event, which essentially 'erases' most craters present in the plains by filling them with volcanic lava. This leads to the conclusion that the surface ought to be globally of the same age with the exception of the highest regions. However, less catastrophic models where smaller areas are resurfaced asynchronously are also consistent with the random distribution of craters observed in Venus while providing a more straightforward explanation to the existence of a great number of geologically complex features [Uppalapati et al., 2020]. A detailed study on the geological features of Venus by Hansen and Lopez [2018] further supports the more regionally constrained resurfacing events, reinforcing that several features on Venus indicate a very long record of geological activity that could date back to billions of years, unaffected by erosion mechanisms unlike Earth.

2.2.2 Atmosphere of Venus

Genesis

Planetary atmospheres form if the gravitational pull of the body is high enough to retain gases, that are either formed as a by-product of accretion or captured from its environment, against a number of mechanisms that favour their escape [Sanchez-Lavega, 2011]. A primordial atmosphere usually forms by 'outgassing'. As the proto-planetary body heats up from accretion, gases are released and then trapped by the gravitational force of the accreted body. The internal differentiation of the proto-planet can also be a secondary source of volatiles through early surface vents and volcanism. When the proto-planet ac-

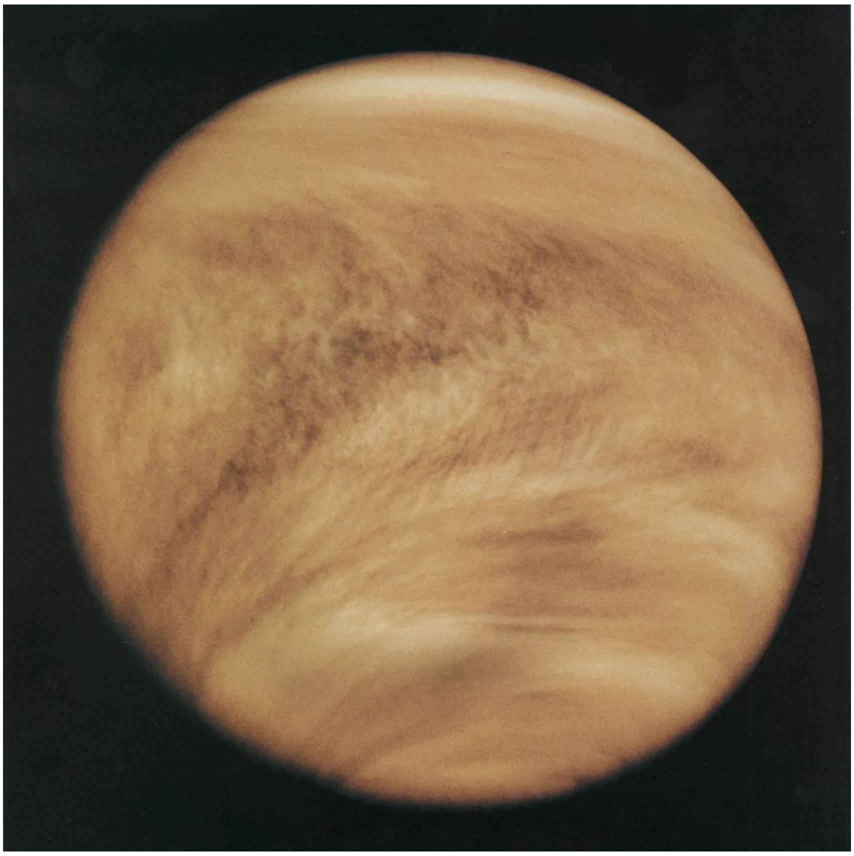

Figure 2.2.2: A colour enhanced image of Venus in the ultraviolet, taken by the Pioneer Venus Orbiter in 1979. Credits: NASA/JPL website.

quires enough mass, this infant atmosphere can become thick enough to increase surface temperatures by a blanketing effect, to levels at which most materials vaporize [Sanchez-Lavega, 2011]. As the proto-planet gradually cools down, this degassing process eventually stops. However, the atmosphere continues to evolve by feeding on collisions with smaller asteroids and comets which are rich in volatiles. Further interaction with the surface, interior, and in the case of Earth, chemical reactions caused by living organisms, lead the atmosphere to its current conditions.

It is noticeable though that the key lies in the evolution process of each atmosphere, the reason why Earth and Venus are so different from each other. As the atmosphere of Venus matured, it endured escape processes from the atmosphere, either through simple thermal escape in which particles in the atmosphere gather enough energy through random collisions to reach the escape velocity of the atmosphere, photochemical escape or the effects of solar wind. The latter would be particularly effective on Venus since it lacks an interior generated magnetic field which could shield it against atmospheric depletion, with hydrogen being the most significant specie to be eroded by this effect [Bougher et al., 1997, Sanchez-Lavega, 2011]. This mechanism would also be partially responsible for the present lack of water on Venus, with an early extreme ultraviolet (EUV) flux which could have driven a rapid vaporization of water. This could generate a positive feedback mechanism in which surface temperatures would increase, from which more vaporization followed [Bengtsson and Grinspoon, 2013]. This water was inevitably lost to space, but the timescale in which this occurred is still highly uncertain. This is in part due to our poor understanding of the effects of clouds that were already formed by this time and

their role in a moist greenhouse environment.
Interactions between the atmosphere and surface also played a major role in the distinct evolutionary paths from the primordial atmosphere, which would be similar to the early terrestrial one. As the bulk chemical composition of both planets is very similar, one could ask where all the CO_2 which makes up approximately 96% of Venus' atmosphere [McFadden et al., 2007] is present on Earth. This marks the crucial role of early life forms on Earth as well as the presence of a vast ocean, both of which encouraged CO_2 absorption, keeping it from accumulating in the atmosphere which supposedly led to a runaway greenhouse effect on Venus. Extensive volcanism coupled with a lack of a reliable absorbing mechanism as on Earth's oceans also contributed to increased concentrations of SO_2, another greenhouse gas, which is still present on Venus as a primary component of its clouds. However, the real evolutionary path that led to current conditions on Venus, as well as the possibility that the atmosphere of Venus is not exactly stable as we know it [McFadden et al., 2007] remains unclear.

Structure and Composition

The atmosphere of Venus is almost 100 times more massive than Earth's [Marov et al., 1973] and through different paths, both evolved to attain very different structures. Because of these conditions, we observe a very high pressure at the surface, similar to what could be felt at a depth of almost 1 km underwater, only at temperatures capable of melting lead ($\approx$ 735 K), in an environment of dark basalt rock under a hazy shadowed horizon [Bengtsson and Grinspoon, 2013]. In fact, thermodynamically speaking, the properties of the lowest part of the atmosphere make it closer to the liquid phase than the gaseous one, the surface being a cauldron for some kind of hellish soup. Interestingly, the major compound of the atmosphere (CO_2) has its critical point at a temperature of 304° and pressure of 73 bars, so at about 15 km of altitude where these conditions can be met, CO_2 is a supercritical fluid [Kasting, 1988].
It is this molecule, aided by SO_2 and water vapour, that is very effective at blocking infrared radiation, which is mostly emitted thermally by the surface as well as the relatively few rays of sunlight that are able to reach it. As this energy from both sources becomes trapped below the clouds it produces a runaway greenhouse effect and the scorching temperatures we observe [McFadden et al., 2007]. Because of this effect and the slow rotation of the planet, combined with probably an ineffective transport of energy across the globe, atmospheric conditions close to the surface are more or less static and independent of latitude, local time or seasons since there appear to be none in Venus. Below the cloud layer, whose top altitude lie between 67 and 70 km, the atmosphere is generally stable with the exception of two altitude ranges [Zasova et al., 2007], one within the cloud layer somewhere between 50 and 55 km and another in the lower atmosphere between 15 and 30 km. On these intervals, the orderly structure of Venus's atmosphere is thought to be disturbed by convection or turbulence. The role of these unstable regions can be of great importance to the circulation of the atmosphere and dynamics of smaller scale features such as atmospheric waves.

As can be seen from Fig. 2.2.3, the cloud layer of Venus can be divided in four sections, two haze layers and between them the cloud deck with the middle and lower cloud grouped together due to the uncertain nature of their boundary [Titov et al., 2018].

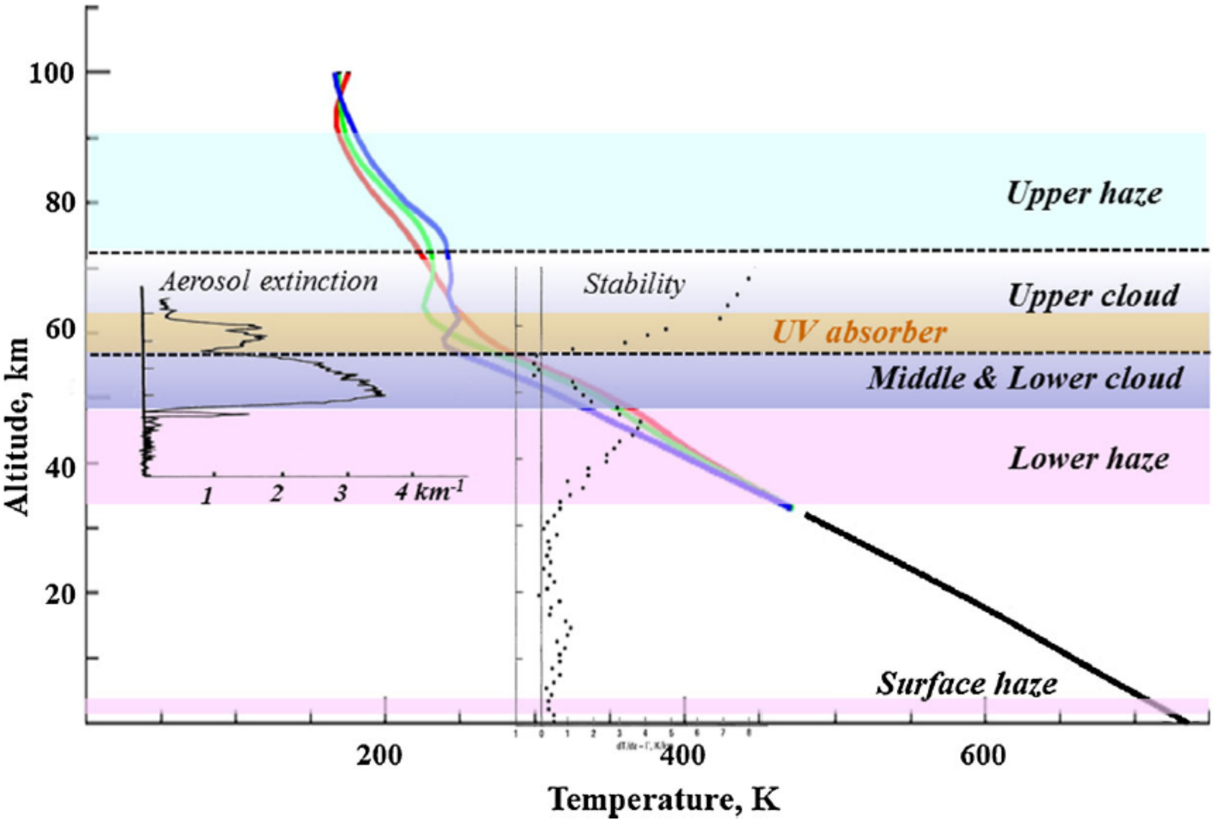

Figure 2.2.3: Vertical structure of the cloud layer of Venus as derived by space missions prior to the arrival of Venus Express and Akatsuki. The coloured lines show the mean temperature profile at low (red), middle (blue) and high (green) latitudes and a black line representing the temperature evolution below 30 km. A typical profile of aerosol extinction as can be found in Ragent et al. [1985] is shown on the left and in the middle represented as a dotted line is the static stability profile featured in the VIRA model [Seiff et al., 1985].

Clouds form when gases in the atmosphere are able to condense thanks the variable temperature-pressure conditions with altitude and several factors that contribute to their generation. If small particles of micron or submicron size can be found where conditions for cloud formation are met, gas can condense around these particles by a process known as nucleation [Sanchez-Lavega, 2011]. The formation of clouds on Venus is maintained through a chemical cycle involving H_2S0_4 (sulphuric acid) as its central compound. Raining down towards the lower atmosphere, this molecule is broken down into water vapour, SO_2 and oxygen, possibly due to the higher temperatures and pressure. With atmospheric circulation and mixing, for example through the convective layer between 15-30 km of altitude, these gases are brought back upward, which are then absorbed by the cloud deck. On the top of the clouds, SO_2 and water vapour molecules are bombarded by heavy UV solar radiation, which feeds the process that converts it back to H_2SO_4 [McFadden et al., 2007]. Another component in the upper cloud which is responsible for near-UV absorption seen in high contrasting cloud features on Venus, such as the noteworthy Y-wave shape observable in Fig.2.2.2 is still a mystery. Favourable candidates include iron chloride, sulphur allotropes or other related species. It is also possible that there is more than one UV absorber responsible for the high contrast in this wavelength range on the upper clouds [Krasnopolsky, 2013].

Above the turbulent region putatively stabilising at $\sim$ 30 km [Ando et al., 2020] lies a fine haze layer with supposedly different composition than the clouds, thanks to sulphuric acid being unstable under the conditions found at these altitudes. At approximately 47 km lies the base of the lower cloud, accessible by the infrared windows explored with the VIRTIS instrument and later with the IR2 camera. This region is characterised by low stability hence difficult to study, with observations limited to the nightside hemisphere of Venus. Also, the height of this layer also seems dependent on latitude, its base going down to 42 km at latitudes higher than 75°. However, the challenges to observe unambiguous data regarding the lower cloud leave many questions of its nature unanswered [Titov et al., 2018].

The cloud top remains the most observed atmospheric region of Venus, highly accessible from space in a broad spectral range from UV to thermal IR. It is also home to the photochemically produced clouds of sulfuric acid, which make Venus a highly reflective planet and the reason why it shines so brightly in the sky. The most recent accounts claim it extends from approximately 64 km to 72 km of altitude [Haus et al., 2014] but the upper boundary of this layer is difficult to trace at low and middle latitudes, melding with the upper haze layer which can extend to ~ 110 km. Spectroscopic observations by VIRTIS and SPICAV instruments have given a reliable tool which traced the thickness and height of the upper cloud layer as well as its variability over time and wavelength. According to Fig. 2.2.4 the cloud top altitude can vary considerably from the equator to the poles with a difference of up to 10 km starting its descend near a region known as the 'cold collar' where temperature can decrease by about 25° from the equator [Piccialli, 2010]. Interestingly, the middle cloud doesn't seem to be subject to this latitudinal variability

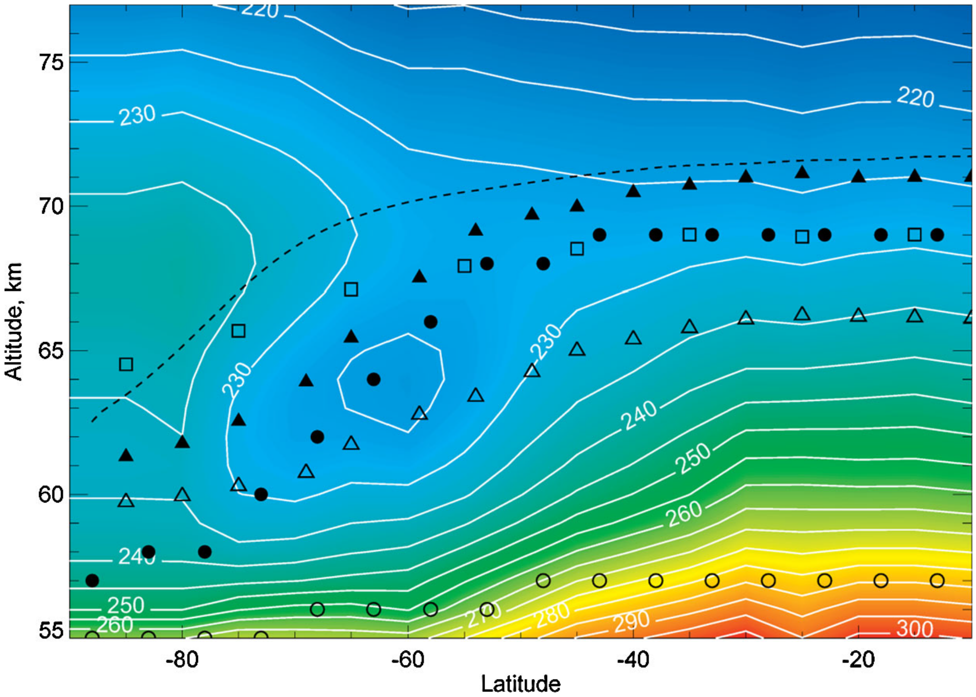

Figure 2.2.4: Latitude dependence of the upper cloud altitude with a background contour of the temperature field derived from data from the VIRTIS instrument [Haus et al., 2014]. Each plot represents a different absorption band used to probe the layer's height. The dashed line represents the 1.5 μm band [Ignatiev, 2009, Cottini et al., 2012] and the squares the 2.5 μm band [Cottini et al., 2015], both from CO$_2$. Filled and empty triangles represent the 1 μm and 5 μm wavelengths respectively, derived for the northern hemisphere and mapped here to the southern hemisphere symmetrically with respect to the equator [Haus et al., 2013] and the circles, filled and empty stand for the 8.2 and 27.4 μm band respectively [Zasova et al., 2007]. More details can be found in [Titov et al., 2018].

in height[Titov et al., 2018].

Atmospheric Circulation and Dynamics

The huge depth and mass of Venus' atmosphere makes it a challenging observational and modelling target to study its circulation and dynamics. Different techniques provide only a limited analysis of the atmosphere, and all are hampered by several constraints posed by the Venusian environment. Also, the very different regimes of circulation between Venus and Earth somewhat restricts the application of techniques used to study our atmosphere on Venus, while also making it more challenging to predict several atmospheric movements such as meridional flow due to the prevailing cyclostrophic balance caused by the slow rotation of the solid globe of Venus [Limaye and Rengel, 2013]. Contrastingly, for the case of Earth or even Jupiter, due to their faster rotation speeds the balance of wind flow is altered by the influence of the Coriolis force. This would lead to a geostrophic regime if only atmospheric friction did not play a role in the circulation as well. An empirical consequence of both contrasting regimes would be existence of a single *Hadley* cell, as in the case of Venus

The most striking feature of the dynamics of Venus' atmosphere is its superrotation. The cloud top level can circle the planet more than sixty times faster than the solid globe, blowing at speeds that can reach more than 100 m/s. This rapid flow is weakly directed towards the respective pole in each hemisphere, building up into a mid-latitude jet at $\sim$ 45° latitude and a sharp reduction in wind speed at $\sim$55° latitude [Sanchez-Lavega et al., 2008], compatible with the location of the 'cold collar', leading to a swirling polar vortex. Though it has been more than 40 years since the first detection of this remarkable zonal flow, its source and support mechanism remain largely unknown.

Paired with this motion is the *Hadley cell* circulation associated to each hemisphere. There seem to be a relation between the existence of a single *Hadley* cell on Venus and the cyclostrophic balance endured by the atmosphere, especially when compared to fast rotators such as Earth or Jupiter that feature multiple atmospheric circulation cells of this kind, thanks to another kind of balanced flow [Sanchez-Lavega, 2011]. With an axial tilt of approximately 2.6° with its orbital plane acknowledging Venus' retrograde rotation, the sub-solar point at noon never strays too far from the equator causing the heated gases to rise, travelling from the equator to the poles until it cools and descends, returning to equatorial latitudes at lower height [Read et al., 2013]. Above the cloud deck at approximately 100 km and beyond, the much more tenuous atmosphere exhibits a sub-solar to anti-solar point (SS-AS) circulation, taking gas heated by the sun onto the nightside. However, the global circulation in this region is difficult to characterise in detail because few tracers can be used to monitor the dynamics of this region. Additionally, the transition from the retrograde superrotation regime in the cloud layer to the SS-AS circulation above is still a mystery, with winds and temperature rapidly changing through unexplained mechanisms which several models attempt to predict [Gilli et al., 2021, Navarro et al., 2021]. Recombination of chemical species on the nightside can produce a noticeable airglow at select wavelengths, which can tentatively be monitored to study atmospheric circulation, such as the 1.27 μm O_2 emission [Gorinov et al., 2018]. However, how these tracers are used to interpret the variability within the altitude region, in which it is estimated that airglow is produced, is still poorly constrained. Moreover, assumptions in the most recent models can lead to limitations such as the propagation and role of waves in atmospheric

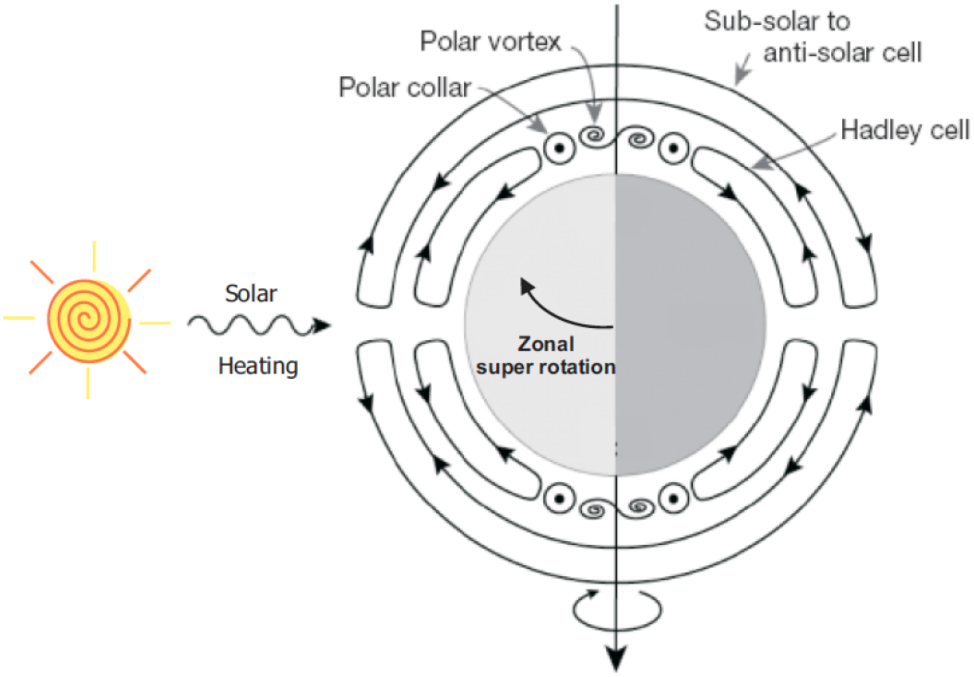

Figure 2.2.5: Atmospheric global circulation regimes on Venus. From Taylor and Grinspoon [2009]

circulation and the influence of the 11-year solar cycle which could impact the extreme ultraviolet heating above 130 km of altitude, which powers SS-AS circulation [Gorinov et al., 2018, Gilli et al., 2021, Navarro et al., 2021].

As presented in Fig.2.2.4, VIRTIS data indicates that the altitude of the cloud top observed in the UV gradually changes from equator to the south pole [Ignatiev, 2009]. The winds in the cloud deck at latitudes $< 55°$ seem predominantly constant but show significant vertical wind shear from the base of the cloud, with velocities between 60-70 m/s to the already discussed 100 m/s zonal in the cloud top. This wind shear is not constant within the cloud layer, being significantly stronger in the upper clouds (8 m/s per km) than in the lower cloud ($<$ 1 m/s per km). The winds within the cloud deck also show variability with time. According to [Hueso et al., 2015], during six years of observations by VIRTIS-M and VMC, the observable clouds in visible and UV wavelengths showed increased levels of turbulence along with a stronger wind in the afternoon hours however, its causes and true temporal scales of change are unknown. Other oscillations in the zonal wind flow have been registered from various earlier missions to Venus, which according to Genio and Rossow [1990] point to the possibility of cyclic changes to the cloud's dynamics on a 5-10 year timescale.

Recent studies by Horinouchi et al. [2018] and Goncalves et al. [2020] revealed that the cloud top wind profiles can show asymmetries in their flow on the order of a 10-15 m/s decrease (see Fig. 2.2.6). These might be caused by a persistent vertical shear effect and the results on the meridional wind in the upper cloud presented in Goncalves et al. [2020] feature an asymmetry for the northern hemisphere showing increased speed in relation to the south hemisphere (see Fig. 2.2.7). Hence, there's the possibility of an anti correlation between both flow regimes. This study also reveals some day-to-day variability of wind velocity, showcasing complex dynamics at play on the top of the cloud deck.

As explained previously, the lower cloud has weaker winds than the cloud top and it is also subject to variability, with results from VEx suggesting greater instability at sub-polar latitudes when compared to the mid-latitudes. A long term study performed by Peralta

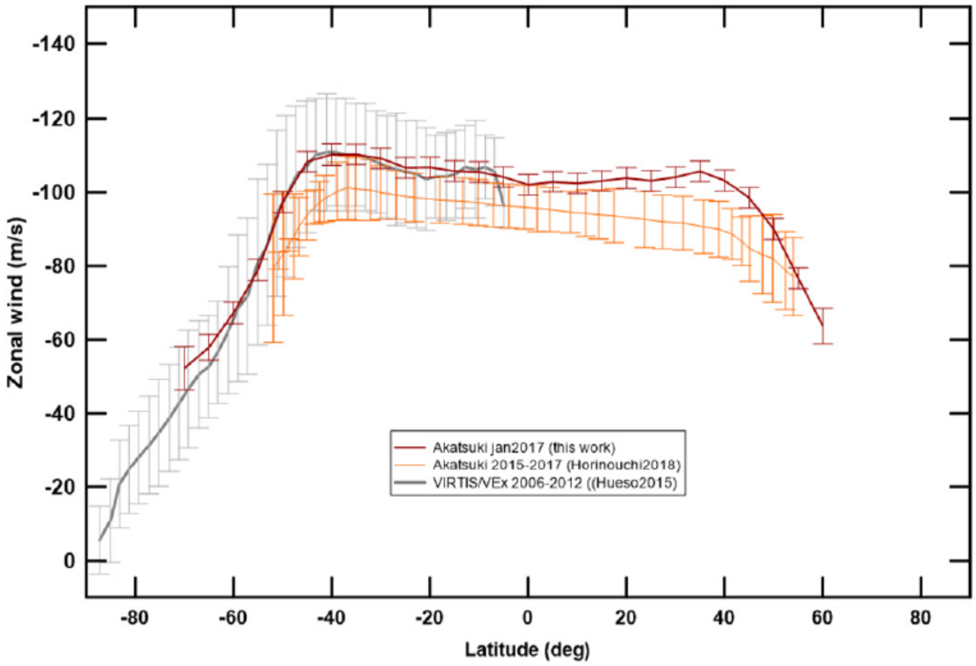

Figure 2.2.6: Zonal wind profile of the upper clouds of Venus at approximately 70 km of altitude from the latest space observations with Akatsuki in red [Goncalves et al., 2020], orange [Horinouchi et al., 2018], and VEx in grey [Hueso et al., 2015].

et al. [2018] demonstrates decadal wind variability at lower latitudes (30°S - 30°N), with data from many different missions across a period of 40 years, suggesting that an oscillating disturbance with an amplitude of $\sim$ 15 m/s and a period of 30 years causes large scale variations on the speed of the zonal wind in the lower cloud.

Below the cloud deck, the atmosphere is modelled to be in a constant state of turbulence with a low wind speed near the surface which increases with height [Morellina et al., 2020].

Waves and Periodic Structures

Since the mechanism behind atmospheric superrotation on Venus is still not well understood, great efforts have been made to continuously monitor its evolution and variability of winds across multiple timescales. With more recent observations, it has become possible to study in greater detail how different cloud morphologies can affect the circulation. One of the most famous of these is the so-called Y feature, first observed in the 1960s, an enormous cloud that periodically appears with a life cycle of approximately 30 days that according to most interpretations is the combination of two different planetary-scale waves: a Rossby wave at mid-latitudes and a Kelvin wave at low latitudes. Both would have an appreciable impact on the wind flow of Venus' atmosphere dynamics [Hueso, 2019]. Such large scale features can also manifest in the form of stationary bow-shaped waves [Fukuhara et al., 2017] or a recently discovered sharp disruption in the lower cloud [Peralta et al., 2020] which displays cyclical behaviour while reportedly not being related to Venus' topography.

Other forms of periodic structures exist, especially on smaller scales such as atmospheric gravity waves. An atmospheric gravity wave is an oscillatory disturbance on a layer of the atmosphere in which the buoyancy of the displaced air parcel acts as the restoring force.

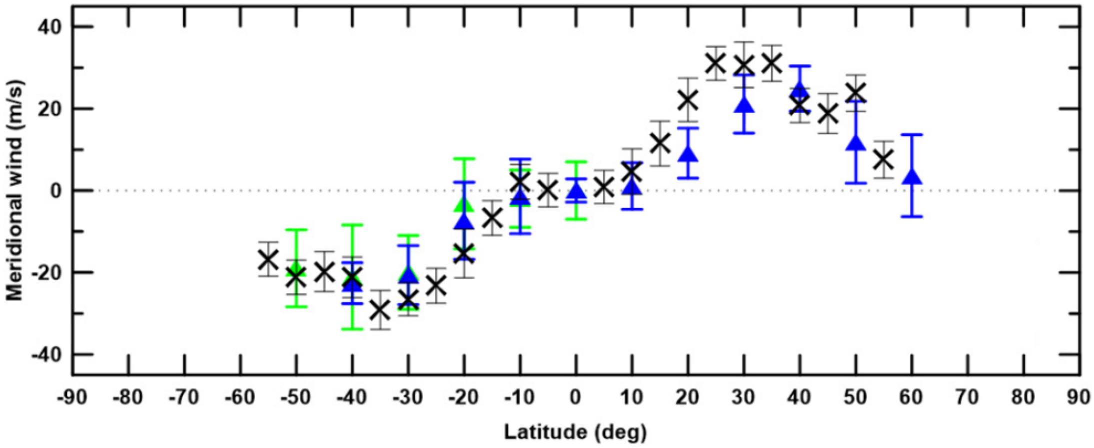

Figure 2.2.7: Profile of the meridional wind on the cloud tops of Venus. This data was retrieved from ground-based observations with both CFHT/ESPaDOnS in blue [Machado et al., 2017], green [Machado et al., 2014], and HARPS-N in black [Goncalves et al., 2020].

As such, this kind of wave can only exist in a continuously stably stratified atmosphere, that is, a fluid in which the static stability is positive and horizontal variations in pressure (within the atmospheric layer) are negligible when compared to the vertical variations (in altitude) [Sutherland, 2010].

These waves represent an efficient transport mechanism of energy and momentum which can dissipate at different altitudes and force the dynamics of several layers of the atmosphere. This dissipation or wave breaking can dump the transported momentum and energy to the mean flow, contributing to an acceleration, thus significantly altering the thermal and dynamical regime of the atmosphere [Alexander et al., 2010]. Such attributes are particularly useful for the case of Venus since these features can be another key towards understanding Venus' general circulation mechanics, particularly the superrotation of the cloud layer [Silva et al., 2021]. In fact, these types of features have been observed on other locations besides Venus such as Earth's atmosphere [Sanchez-Lavega, 2011], Mars' atmosphere in cloud formations [Määttänen et al., 2010, McConnochie et al., 2010], on Jupiter's temperature profile [Young et al., 2005] and cloud level [Arregi et al., 2009](See Fig.2.2.8).

Venus' atmosphere displays an incredible variety of waves, which are detected at different wavelengths ranging from the ultraviolet to the near-infrared. The periodic structure of the waves observed in the ultraviolet can be seen as differences in the reflected light at the top of the clouds while waves in the infrared appear through opacity patterns to the thermal radiation under the cloud layer where they propagate [Belton et al., 1976, Rossow et al., 1990, Peralta et al., 2008, Piccialli et al., 2014]. Observations of waves in the upper cloud with the Venus Monitoring Camera (VMC) instrument onboard the European Space Agency (ESA) Venus Express (VEx) space mission lead to the detection of periodic structures interpreted as gravity waves whose activity was mostly limited to the cold collar region (60° - 80°) and concentrated above a high topography region on the northern hemisphere (Ishtar Terra) [Piccialli et al., 2014]. This would suggest that these waves are generated by a Kelvin-Helmholtz instability or that waves are excited by the interaction of the lower atmosphere with the surface topography. However, a need for improving the statistics of wave analysis to further develop these and other hypotheses has been expressed [Piccialli et al., 2014]. Additional observations of the upper clouds using VIRTIS images at target wavelengths 3.9 μm and 5 μm reveal the presence of a large

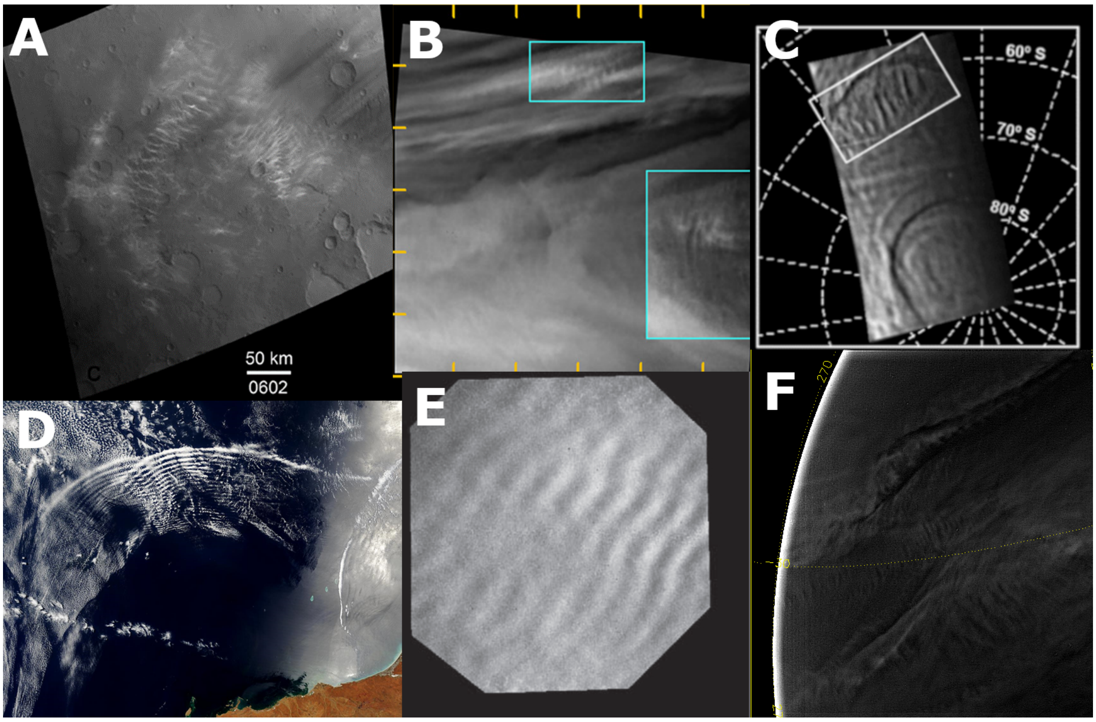

Figure 2.2.8: Atmospheric gravity waves across the Solar System. Panel A shows an atmospheric wave in the faint clouds of Mars [Määttänen et al., 2010]; panel B shows two wave packet propagating at cloud level on Jupiter [Arregi et al., 2009]; panel C shows a mesoscale wave orbiting around the south pole of Venus in the lower clouds [Peralta et al., 2008]; panel D shows a pair of crescent-shaped gravity waves moving away from Australia on Earth (Credits to MODIS/Terra - NASA/GSFC); panel E shows part of a wave system visible on the top of the clouds of Venus [Piccialli et al., 2014]; and panel F illustrates several wave packets propagating on the nightside of Venus' lower cloud as seen from the IR2 camera onboard Akatsuki [Silva et al., 2021].

number of stationary mesoscale (between 5 to hundreds of kilometers, but smaller than synoptic scales that consider global atmospheric formations with dimensions larger than 1000 km) waves [Peralta et al., 2017b]. For the case of Venus, mesoscales comprehend dimensions of atmospheric features between 5-10 km and hundreds of km, but smaller than synoptic scale where formations with dimensions beyond 1000 km come into play. More stationary features were also observed in Kitahara et al. [2019], with observations at 283 nm, which the authors conclude are the result of mountain generated gravity waves. Interestingly, even though gravity waves are generally related to high relief structures from the surface and it is the best understood mechanism by which these types of waves form [Sutherland, 2010], the same structures are mysteriously missing on the nightside lower clouds. On the other hand, waves detected in the lower cloud of Venus show a large diversity of properties and morphologies at an extended latitudinal and longitudinal range, and their presence seems uncorrelated to any notable topographical feature on the surface of Venus [Peralta et al., 2008, Silva et al., 2021].

Radio occultation data also allow direct detection of waves through small-scale temperature fluctuations, the latest studies of which reveal significant wave activity in the cold collar region favouring the northern hemisphere [Tellmann et al., 2012]. With these results, Tellmann et al. [2012] concludes that waves are generated by either convection or topographical forcing, supporting other wave studies using different observation techniques [Peralta et al., 2008, Piccialli et al., 2014]. The results presented in this thesis and published in Silva et al. [2021] aim to expand this discussion to the lower clouds of Venus, pointing out that these types of waves might have multiple sources that generate the great variety of waves observed. Further global studies of atmospheric waves on other atmospheric layers such as the upper cloud, would be most useful in answering current open questions related to these structures and their true role in Venus' atmospheric circulation.

Chapter 3

Jupiter - Giant Swirling Vortex

3.1 Exploring the largest gas giant

With the exception of the Sun, Jupiter is the largest and most massive object in the solar system, with more than twice the mass of all other planets combined [Irwin, 2009]. This makes it an important gravitational influence within the solar system, playing a noticeable role in the orbits and rotation periods of other planets. It also makes it a significant gravity well, capturing or forcing the orbits of thousands of small objects, such as the *trojans*, a group of asteroids that share Jupiter's orbit around the Sun [Jewitt et al., 2004]. Despite its massive size, Jupiter is the fastest rotating planet in the solar system, with a period of 9.84 h [Sanchez-Lavega, 2011], and supports a colossal magnetic field that if visible from Earth, would appear five times larger than the full Moon in the sky, despite being much farther away [Russel et al., 1993].

The general understanding of Jupiter and its system of large moons and other satellites has increased immensely over the years with both ground and space-based exploration. With the detection of thousands of Jupiter-like exoplanets, all acquired knowledge can be used as a proxy for the new targets orbiting other stars.

Earliest observations of the giant planet date back to at least the first Babylonian dynasty of the 7^{th} or 8^{th} century BC, following the movement of this 'wandering star' across the sky [Sachs, 1974]. Though a prominent body in the night sky, its more detailed recorded study was brought by the arrival of telescopic observations, first made by Galileo Galilei, discovering the four Galilean moons in 1610: Io, Europa, Ganymede and Callisto. Still in the 17^{th} century, Giovanni Cassini made other observations of Jupiter which revealed the coloured banded structure of its cloud layer and that the planet was apparently oblate [O'Connor and Robertson, 2003]. One of the most conspicuous features of Jupiter's atmosphere, the Great Red Spot (GRS), may have been first observed as early as 1664 by Robert Hooke, most notably known for being the first person to observe a microorganism under a microscope of his own design [Hooke, 1664]. Though a disputed claim, since it is difficult to confirm if a spot seen in roughly the same region of Jupiter's atmosphere was in fact the GRS or some other storm that preceded it, it is remarkable that instruments from this age were able to glimpse the GRS. Nevertheless, it is a very long-lived structure, with continuous observations since 1830, making it at least more than 170 years old

Figure 3.1.1: This close-up image of Jupiter with its prominent Great Red Spot was taken by Voyager when it flew past the gas giant in 1979. Also in this picture, in the bottom left corner is Jupiter's largest moon Ganymede. Credits to NASA's Goddard Space Flight Centre

[Irwin, 2009].

A true revolution for the exploration of giant planets came as the space age developed, encouraging scientists and engineers to attempt journeys to planets beyond the asteroid belt. However, electronic equipment cruising the jovian system would face a potentially hazardous radiation zone around Jupiter. Such radiation belts were already discovered earlier around the Earth, but strong radio emissions from Jupiter suggested the presence of high energy electrons trapped in the planet's strong magnetic field [Burke and Franklin, 1995]. The first of these spacecrafts to fly past Jupiter were the Pioneer probes 10 and 11, launched in 1972 and 1973. They gave the first detailed pictures of cloud structures within the atmospheric bands and measured much stronger radiation fields near the planet than what was expected, aiding on the planning of future missions [Bagenal, 2019]. Following the early success of the Pioneer probes, a plan for a great tour of the outer solar system (beyond the asteroid belt) formed with the realization that Jupiter, Saturn, Uranus and Neptune would be in the same quadrant of the solar system during the 1980s. Thus, the Voyager mission was born, comprised of two spacecrafts, Voyager 1 and 2, which sailed

across the solar system capturing turbulent eddies and swirling clouds around the GRS (as in Fig. 3.1.1) as they flew past Jupiter. These observations led to a first characterisation of the movement of clouds and a deeper understanding of the behaviour of eddies on the turbulent jovian environment at cloud level. One of the most successful space missions to date, the Cassini-Huygens mission, on its journey towards Saturn, made its closest approach to Jupiter on December 30, 2000 for a gravity assist manoeuvre. Although brief, the images taken during approach were most useful to update the zonal wind profiles, revealing east-west alternate bands extending to polar latitudes. Observations of the rings were able to further constrain the particle size distribution present on the system, along with other discoveries concerning the great number of moons orbiting the gas giant [Bagenal, 2019]. Another more recent passage into the jovian system was performed by New Horizons, an interplanetary probe on a journey to the dwarf planet Pluto in 2007. It gave important contributions to the analysis of little red spots and magnetic field sampling as it drifted away from the sun following Jupiter's magnetic field's tail [Beisser, 2015].
Though each fly-by mission, gave important contributions to our knowledge of the Jupiter system, orbiting spacecraft have the obvious advantage of a much extended period of observations, the ability therein for various observing campaigns throughout the mission's duration. The Galileo program was the first space mission specifically designed to place a spacecraft into orbit around a giant planet and the first effort to deploy an entry probe into the atmosphere of such a planet [Irwin, 2009]. The orbiter was active from 1995, when it reached the Jovian system, until 2003, when it was purposefully crashed into Jupiter's atmosphere. The idea was to prevent possible contamination from any organic matter that might have clung to the spacecraft, should it collide with the Galilean satellites. This is specially relevant for Europa, whose mounting scientific evidence support the possibility of the presence of life forms beneath the ice sheet that covers the moon [Kanik and de Vera, 2021]. Thanks to its entry probe, Galileo was responsible for the only *in-situ* measurements we have on a gas giant, retrieving relative abundances, pressure and temperature profiles down to a depth of 22 bars (or roughly 150 km below the cloud level where the atmospheric pressure matches the surface pressure on earth). Continuous studies of atmosphere dynamics, chemical composition and lightning activity were also major results from Galileo data, as well as the discovery of an internally-generated magnetic field on Ganymede. Another important discovery concerning magnetic fields was the detection of perturbations, which revealed the likely presence of subsurface oceans on some of the galilean moons [Bagenal, 2019], such as Europa as previously mentioned.

Juno is the most recent mission to Jupiter, arriving at the system on the 4^{th} of July, 2016 and is currently navigating around the planet in a highly elliptical polar orbit, avoiding the highest radiation regions and capturing the poles in full splendour for the first time. This orbit lets Juno pass very close to Jupiter, at altitudes below 8000 km, allowing unprecedented close observations of Jupiter's interior, deep atmosphere and the polar magnetosphere. The goal of this mission was to measure water abundance in the deep atmosphere, and to finally determine the nature of Jupiter's core, directly addressing the planet's origin and thereby that of the solar system. The polar orbit has also allowed Juno to study the powerful auroras which, up until now, complete observations were limited, due to the geometry of the orbits of previous missions. [Bolton et al., 2017a]. During its running time, Juno has offered a plethora of new evidence regarding Jupiter's magnetic field, particularly its irregularity in the northern hemisphere [Connerney et al., 2018]. Through gravity measurements, it has revealed that the core has indeed heavy elements (heavier than hydrogen and helium) but they continuously mix with the internal liquid

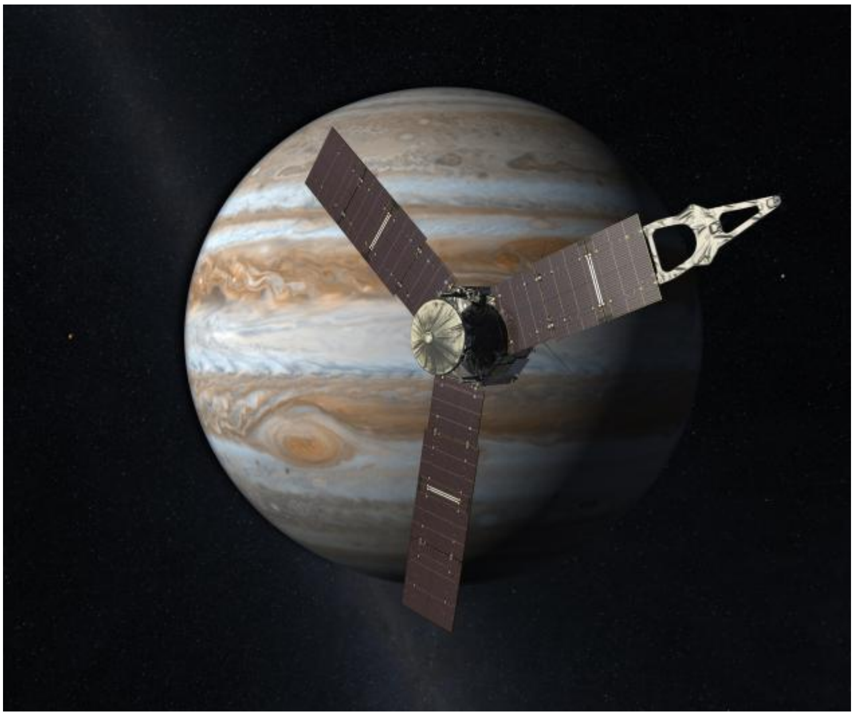

Figure 3.1.2: Artist's depiction of Juno spacecraft with Jupiter on the background. Credits to NASA/JPL.

metallic hydrogen [Wahl et al., 2017], spreading to $\sim 40\%$ of Jupiter's radius. Also, microwave data has also enabled scientists to infer that atmospheric convection observed in the cloud region can extend down to 3000 km [Kaspi et al., 2018]. The Juno mission has been extended a second time, now to explore the full jovian system with 42 additional orbits, continuing exploration until September 2025.

3.2 Origins of the Jovian System

The most commonly accepted theory for planet formation is the core accretion model, by which a planet grows from the concentration of solid material in a proto-solar nebula, distributed on a disk plane orbiting a gestating star [Sanchez-Lavega, 2011]. The concentration of solid material is made in sheets to increase the chances of collision for smaller particles in similar orbits, which stick together thanks to small forces such as Van der Waal's force, in a process known as coagulation from which *planetesimals* can form. Over time these proto-planets can reach sizes on the order of 10 km, when their gravitational pull starts to become significant in relation to its neighbours in the disk, leading to a runaway process where several of these larger bodies form at the expense of smaller ones. Once these embryos reach a mass on the order of 10 Earth masses, they are able to trap the nebula gas along with any remaining planetesimals until a critical mass is reached, when any gas in the region of the planet's orbit hydrodynamically collapses onto it. Hence, the embryo becomes the planet's solid core encased in a huge envelope of gas. This process elegantly explains the bulk composition differences between the giant planets of the solar system and explains the presence of a 'metallic' (elements heavier and helium) core or at least a planetary centre enriched in heavy elements if the core has eroded [Sanchez-Lavega, 2011, Irwin, 2009]. However, this model appears to form planets too slowly to be compared with the lifetime of circumstellar disks observed around other stars, and doesn't account for planetary migration. These big changes in the orbits of planets seem to be commonly occurring, thanks to the growing number of observations of so called 'Hot Jupiters', which are gas giants orbiting close to their host star at distances less than 1 AU, which are difficult to explain if the planet formed at that distance to its host star. An alternate view that attempts to tackle the long formation times of the accretion model is one in which a protostellar disk of sufficient density may become gravitationally unstable, with giant planets collapsing directly from the nebula disk much earlier. The speedy formation of the proto-planet permits more interaction with the disk which can make the planet migrate within the circumstellar disk, accounting for the existence of hot Jupiters. However, this model entails a similar composition between all gas giants formed within the system, something not observed for the case of the Solar System. Indeed, migration of the gas giants, at least of Jupiter and Saturn, seems essential to explain the small mass of Mars in relation to Earth and Venus. The migration of the gas giants could also catalyse the Late Heavy Bombardment, a cataclysmic event which brought a large number of asteroids on a collision path with the terrestrial planets. When Jupiter migrated inward, it could have shepherded a lot of material to the inner Solar System thanks to its great size. This migration is explained in two mechanisms known as the Grand Tack and Nice models. The Grand Tack model, initially suggested by Walsh et al. [2011], proposes that Jupiter was the first gas giant to form and once it accreted enough mass, it carved an annular gap in the protoplanetary disk and migrated inward. Saturn also grew alongside Jupiter but achieved a significant mass at a slower rate and farther away from the Sun. Once Saturn achieved appropriate mass, it joined Jupiter in its migration to the inner Solar System, catching up to its giant cousin as its migration was faster, until it reached an exterior 3:2 mean motion resonance with Jupiter. This would shift the balance of disk torques acting on the planets' orbits, causing them to migrate outwards together. This second migration would them be slowed and eventually stopped as the protoplanetary disk dissipated, leaving the giant planets on still resonant orbits at approximately their current locations in relation to the Sun. From this configuration it is possible that a much later instability takes place as explained by the Nice model [Gomes et al., 2005] provided enough material remains in the disk [Raymond et al., 2014].

Since the giant planets seem to form first and at a faster rate than terrestrial ones, the processes by which the atmosphere forms and evolves is also slightly different. Due to the increased size of the proto-planet (10 earth masses), these bodies are able to directly capture gas from the protoplanetary disk, rapidly forming the atmosphere with chemical compositions comparable to the Sun, in terms of hydrogen and helium. These atmospheres suffered few modifications in their composition as they evolved [Sanchez-Lavega, 2011]. As such, the giant planets cooled gradually from their formation stage, which kept their interiors at sufficiently low temperatures so that some chemical components started to differentiate within the planet's interior. This process is still believed to be happening today on the interior of Jupiter, with helium raining down towards the centre of the planet amidst a large swathe of metallic hydrogen [Stevenson, 2020]. The large mass of Jupiter also attracts other transient bodies of the Solar System, resulting in significant impact events that temporarily alter the atmosphere such as the "Shoemaker-Levy 9" collision in 1994 and another of a smaller scale in 2009, suggesting that these events are quite frequent [Sanchez-Lavega, 2011].

Figure 3.2.1: This image from the Hubble Space Telescope shows several dark spots that mark the impact sites from the shard of the Shoemaker-Levy 9 comet in 1994. Each of this features evolved in a timescale of days after the collisions. Credits to NASA.

3.3 Jupiter's Interior

Since Jupiter is almost entirely composed of hydrogen and helium (more than 85% hydrogen and close to 14% helium as well as other minor components), it is a fluid planet in which there is no surface as we understand it on terrestrial planets. In fact, Jupiter and Saturn are closer to what we could call a 'failed star' in which not enough mass was reached to ignite deuterium fusion in its interior [Guillot and Gautier, 2014]. As we dive into the planet, temperature and pressure rise to levels in which exotic physical state transitions occur, such where hydrogen changes to an electron-degenerate state of ionized protons and electrons we call *metallic hydrogen* [Irwin, 2009]. Since there is no reason for the interior to be homogeneous and static, it is likely that this transition is gradual rather than having a sharp boundary (like a solid surface) [Stevenson, 2020].

Knowledge of the interior structure and conditions of a fluid planet, such as Jupiter, relies mostly on accurate measurements of the gravitational field as well as an estimation of the moments of inertia among other factors [Irwin, 2009]. Contrary to the shape of most terrestrial planets, where it is possible to reasonably approximate them to a sphere, such that the gravitational acceleration all over the surface points almost exactly to the centre of the planet, Jupiter's fast spinning motion coupled with its fluid character introduces a noticeable bulge of the poles. This effect interferes with the normal shape of the gravitational field we are accustomed to on Earth. Thus, the gravitational field at the 'surface' of the planet is displaced by a small angle from the radial direction, which varies with latitude. This led to the usage of alternative latitude and longitude coordinates, the planetographic system, defined as the inclination of the local normal to the equatorial plane. This gravitational field (without the dynamical influence of convection or tides) can be described with:

$$V(r,\theta) = \frac{GM}{r}\left[1 - \sum_{n=1} J_{2n}\left(\frac{a}{r}\right)^{2n} P_{2n}(cos\theta)\right] \tag{3.1}$$

where G is the gravitational constant, M is the mass of the planet, a, r are the equatorial and some arbitrary radii respectively, the J_{2n} coefficients are the gravitational moments which can be useful to describe the distribution of mass in the interior, P_{2n} are the Legendre polynomials, and θ is the co-latitude (90° - Latitude). Different parameters of J describe several conditions in the interior of the planet and since some of them can be retrieved through gravitational analysis by orbiters such as Galileo and Juno, their values can be used in models of the interior of Jupiter. One of these parameters (J_2) can be used as proxy for the moment of inertia, which for the case of Jupiter is indicative of a significant concentration of mass towards the centre of the planet. However, the distribution of most species beneath the deep cloud of Jupiter is very much uncertain, given the difficulty to model how a particular composite interacts with the temperature and pressure conditions theorized for the interior of Jupiter. One such species is helium, the second most abundant component of Jupiter which is generally mixed with hydrogen although, it is expected to separate as pressure increases inside Jupiter. While separated, since helium is denser than the surrounding hydrogen dominated environment, most models theorize that helium atoms gather as droplets, which then rain down to deeper levels in the planet's interior. However, the temperature also rises along with pressure which makes it impossible for helium to be immiscible from the metallic hydrogen at greater depths, where it redissolves [Stevenson, 2020].

Giant planets, in particular Jupiter and Saturn, provide a natural laboratory for the chemical conditions of the protosolar nebula, since these planets ought to have formed first and at a relatively fast pace when compared to the other inhabitants of the Solar System. Their distribution of heavy elements (elements other than H and He) can be effective indicators of the conditions of the Solar System at the time of its genesis. The most abundant of these in the gas giants are carbon (C), nitrogen (N), oxygen (O), and sulphur (S) and they are all found in higher concentrations relative to solar composition, increasing from Jupiter to Neptune. One of the most puzzling components of the gas giants is the abundance of H_2O, which is an effective proxy for the oxygen content on the deep atmosphere of these planets. However, it is difficult to measure with available techniques as its condensation is quite deep (presumably 5 bar level [Guillot and Gautier, 2014]). Even Galileo's entry probe, which was able to gather data up to depths where the pressure reaches 22 bars, fell into a 5-μm hotspot, believed to be exceptionally dry and governed by downwelling motions [Ingersoll et al., 2004] thus, extracting at most a lower limit for water abundance on Jupiter's atmosphere.

The knowledge of the internal composition of Jupiter and respective ratios to solar abundance can have drastic implications in the way we perceive the giant planets to have formed. Since Jupiter is probably the first born planet of the Solar System, its interior encloses several mysteries surrounding the genesis of our planetary system. One such that challenges current formation models is the gathered evidence by the Juno spacecraft that Jupiter most likely houses a diluted core of heavy elements, as opposed to the classical three layered structure supported by standard formation models. In fact, it seems very challenging to reproduce the present conditions of Jupiter's interior, suggesting more complex formation mechanisms in the planet's early history [Muller et al., 2020]. Figure 3.3.1

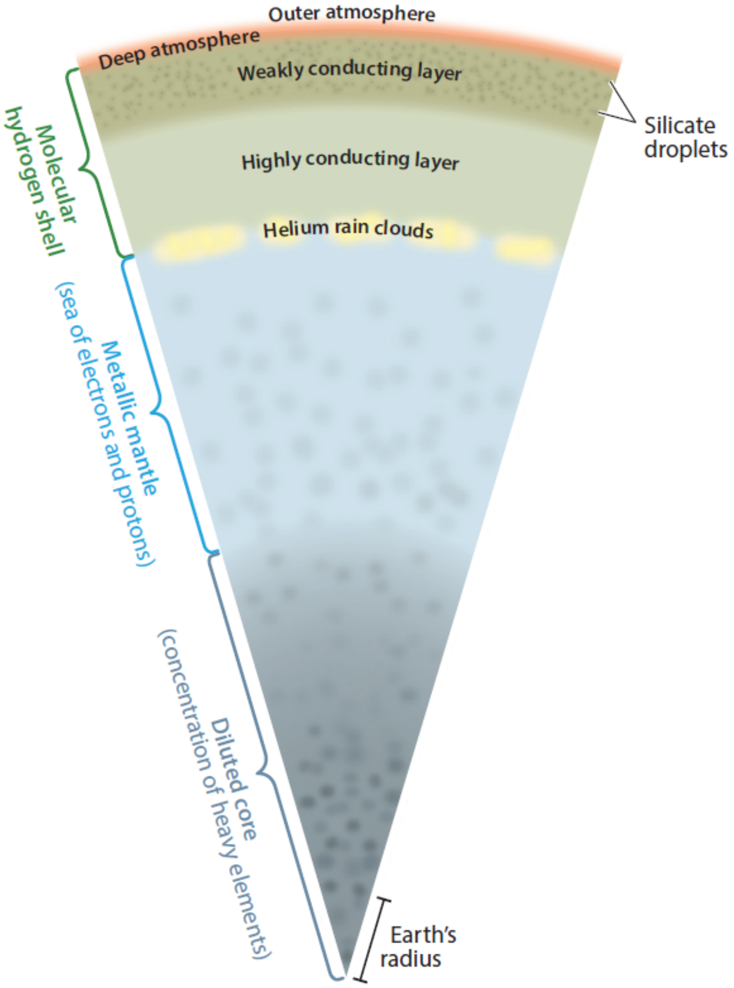

Figure 3.3.1: Currently favoured model of Jupiter's interior structure. The commonly observed atmosphere of Jupiter is characterised mostly by ammonia clouds followed in depth by water and silicate clouds presumed to form at tens of kilobars of pressure. Notice the conducting layers and the region where putative conditions are met for the formation of metallic hydrogen. The dynamical regime theorized for this region is the proposed origin for Jupiter's massive magnetic field. At greater depths we find a concentration of heavy elements which forms the diluted core of Jupiter. Figure taken from Stevenson [2020].

shows our current picture of the interior structure of Jupiter.
Since the deep interior of Jupiter is fluid, as the planet gradually contracts it releases heat via the Kelvin-Helmholtz mechanism. Due to the modelled conditions of the interior, the most effective means of energy transport inside the gas giant is convection, although at certain depths other forms of transport such as conduction or even radiation can become important as well [Irwin, 2009]. However, current evidence of the heavy element distribution inside the planet show that despite being internally hot and therefore convective as previously pointed out, it is unable to fully mix such elements. Possible reasons might lie in the initial conditions during planet formation or some kind of giant impact early in its history [Guillot and Fletcher, 2020].

3.4 Meteorology of Jupiter

Easily the most striking feature on Jupiter's atmosphere, the contrasting bands of clouds which continuously swirl around the planet. Despite having been heavily studied for decades, and with new insights from the still running Juno mission, a few mysteries still lay shrouded beneath the surface.

3.4.1 Vertical Profile and Chemistry

Recent efforts to probe the deep atmosphere of Jupiter in order to understand its visible structure and behaviour, have been concentrated mainly on the detailed measurements performed by Juno, as well as the heritage from the only *in situ* data we have on the gas giant, provided by Galileo's entry probe.
Although the concept of Jupiter's atmosphere can be somewhat broad given the lack of hard boundaries between regions as previously established, we can understand its structure by dividing the atmosphere in three different sections:

- The thermosphere which forms the upper boundary between the lower layers and interplanetary space, where powerful auroras form by interacting with the extreme ultraviolet radiation from the Sun and the charged particles in the magnetosphere [Yelle and Miller, 2007];
- The stratosphere which is located above the temperature minimum in the tropopause and dominated by radiative process to transport energy [Moses et al., 2007];
- The troposphere where the weather layers and clouds reside, characteristic for the banded structure on most visible light images.

A model of the vertical structure of the atmosphere of Jupiter is illustrated on figure 3.4.1.
Most of our understanding of the deeper atmosphere of Jupiter has been predicted through the use of thermochemical equilibrium models, since it is difficult to measure directly the composition and location (in depth) of cloud layers. Current predictions put different species condensing at separated levels in the atmosphere, with the water (H_2O) cloud at approximately 6 bars, the ammonium hydrosulfide (NH_4SH) cloud at 2.2 bars and ammonia (NH_4) clouds at 0.7 bars [Dahl et al., 2020]. These locations are usually taken as the starting point for interpreting observations of Jupiter's atmosphere however, these

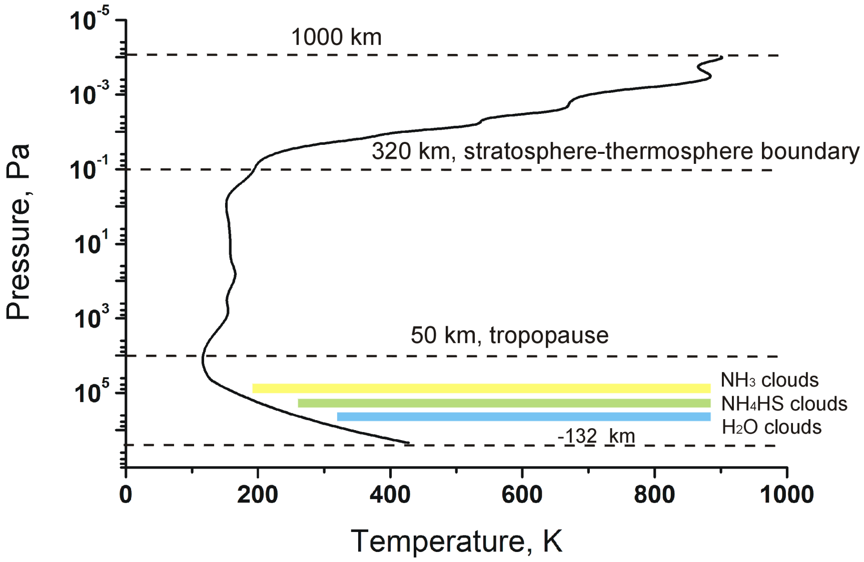

Figure 3.4.1: Vertical structure of the jovian atmosphere. This profile contains the gathered data from the Galileo entry probe during its descent into the atmosphere of Jupiter, reaching the approximately 22 bar level before data transmission ceased. From [Seiff et al., 1998].

assumptions should be taken with precaution [R. West et al., 2007]. Contrary to what happens in terrestrial planets, condensates which form clouds on Jupiter tend to sink into the planet since the bulk chemical composition is primarily H and He, which are lighter gases. From this peculiarity, we can expect that cloud formation on the gas giants is very different from the situation seen on Earth or observed on Venus [Irwin, 2009].

Much of the uncertainty in how these cloud layers are distributed in Jupiter is the way chemical species circulate in the deep atmosphere, and how each layer interacts with its surrounding environment. According to our general understanding of the behaviour of most atmospheres, if it is mostly convective such as is assumed for Jupiter, the mixing ratio of a condensible should be uniform up to the level at which its partial pressure matches the locally determined vapour pressure [Stevenson, 2020]. At higher altitudes than this level, where the pressure is lower, we expect clouds of the condensible to form and the reduced temperatures lead to lower mixing ratios. For example, before the Juno era, observations and models suggested that ammonia would be uniformly mixed at depths greater than 4 bar however, Microwave Radiometer (MWR) results show that concentrations of ammonia remains variable down to pressures of tens of bars [Bolton et al., 2017b], showing a non-uniform distribution. An interesting explanation to this phenomenon lies in the noticed absence of lightning storms in the equatorial region which allows small scale convection to maintain near homogeneity in this region [Stevenson, 2020]. As with the other giant planets in the Solar System with the exception of Uranus, significant internal heat is emitted, surpassing the absorbed solar radiation. This offers a nice explanation to why convection is the prevalent source of energy transport in the interior of the planet, even if in some situation other mechanisms can also become significant [Sanchez-Lavega, 2011].

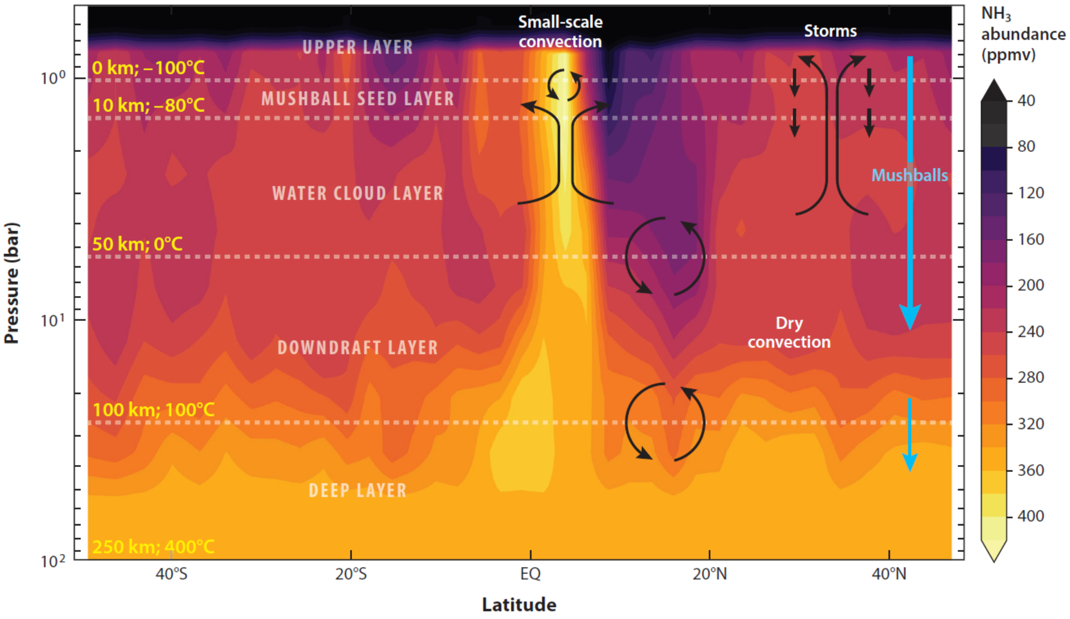

Figure 3.4.2: A possible explanation for the heterogeneous distribution of ammonia on Jupiter from MWR Juno results [Bolton et al., 2017b]. This schematic shows the average map of ammonia abundance on Jupiter retrieved during several perijove passes as a function of latitude and pressure. This figure also illustrates temperature and altitude levels from the reference level (where atmospheric pressure is equal to surface air pressure on Earth), along with layer categorization and dynamical processes occurring in this region of the atmosphere. From [Stevenson, 2020].

Atmospheric Chemistry of Jupiter

The structure of the atmosphere of Jupiter and its interior elemental distribution are heavily intertwined with how different molecules interact in the jovian landscape, and what chemical processes are prevalent within and below the clouds.

Table 3.1 lists the abundance of chemical elements in the atmosphere of Jupiter. These values, as stated before, point to a heavier element abundance than initial models for Jupiter, which brought it closer to Sun-like values. We see values between 3 to 5 times higher on most chemical compounds that are not H or He. Some of these molecules become the main components to form clouds (condensibles), while other are unstable depending on temperature and pressure conditions, which becomes an useful tracer of atmospheric circulation. Such species are called *disequilibrium species*. Other processes such as photolysis by solar ultraviolet radiation are responsible for transforming other species in the upper parts of the atmosphere, affecting the chemical abundance of several molecules. Knowledge of the chemical reactions and the boundary conditions in which they occur can prove critical to understand the vertical circulation of air parcels between the deep atmosphere and the top of the clouds on Jupiter. To further illustrate how some of these processes can be relevant, we follow with some important chemical reactions between elements present in the atmosphere of Jupiter:

$$CH_4 + H_2O \rightleftharpoons CO + 3H_2 \tag{3.2}$$

$$2NH_3 \rightleftharpoons N_2 + 3H_2 \tag{3.3}$$

Above the temperature of approximately 1000°K, the right-hand side of these reactions dominates, whereas the other is prevalent at lower temperatures. In this case, it becomes

Table 3.1: Chemical composition of Jupiter's Atmosphere

Species	**Mole Fraction**
H_2	0.864
He	0.136
H_2O	2-20$\times10^{-9}$ (P<50 mbar)
	0.29 $\times10^{-4}$ (19 bar, *cond*)
CH_4	3.27$\times10^{-3}$
NH_3	2.6$\times10^{-4}$(P)(*cond*)
	2.96$\times10^{-4}$(8 bar)
H_2S	2.75$\times10^{-5}$(16 bar) (reac)
^{20}Ne	(2.3$\times10^{-5}$)
^{36}Ar	(1.5$\times10^{-5}$)
^{84}Kr	(5$\times10^{-9}$)
^{132}Xe	(2.3$\times10^{-10}$)
PH_3	6$\times10^{-7}$ (*dis*)
GeH_4	7$\times10^{-10}$(*dis*)
AsH_3	2.2$\times10^{-10}$(*dis*)
CO	2$\times10^{-9}$(*dis*)
CO_2	Detected
C_2H_2	3-20$\times10^{-8}$(*phot*)
C_2H_4	7$\times10^{-9}$ (*phot*)
C_3H_4	2.5$\times10^{-9}$ (*phot*)
C_3H_8	Detected
C_4H_2	9 $\times10^{-11}$ (*phot*)
C_6H_6	2 $\times10^{-11}$ (*phot*)

All chemical abundances are given as volume mixing ratios. Some species abundance is variable with altitude (pressure level, P). Condensible species are marked with (*cond*), disequilibrium species are marked with (*dis*), chemical reactive species are marked as (*reac*) and photochemical species are marked as (*phot*). This table was taken from [Sanchez-Lavega, 2011] however, further details can be found on Atreya et al. [2003].

unlikely that significant concentrations of CO or N_2 are present at cloud level, where direct observations can be made unless vertical transport is strong enough to feed these molecules to the upper layers before they are all transformed into methane and water. Carbon monoxide can also react with water to form CO_2 in the upper troposphere, although it has not been detected further down in the atmosphere of all giant planets. This might indicate that more than one process can be responsible for breaking down CO_2 or that its detection is simply more difficult for deeper layers.

$$CO + H_2O \rightleftharpoons CO_2 + H_2 \tag{3.4}$$

Other important disequilibrium species include germane, arsine, and phosphine, as their abundances are higher than would be expected should Jupiter's atmosphere be in chemical equilibrium. Generally, these gases are produced deep in the atmosphere where temperatures reach $1000°K$ and pressure up to 1 kbar, and then through a multitude of chemical processes convert, at the upper reaches of the atmosphere, into the chemical species below in equations 3.5,3.6,3.7 on a timescale of 100 days. More details on the intermediate steps to reach some of these species can be found in Atreya [1986]:

$$GeH_4 + H_2S \rightleftharpoons GeS + 3H_2 \tag{3.5}$$

$$4PH_3 + 6H_2O \rightleftharpoons P_4O_6 + 12H_2 \tag{3.6}$$

$$4AsH_3 \rightleftharpoons As_4 + 6H_2 \tag{3.7}$$

Measurements of the vertical profiles of these species provide constraints in the eddy-mixing coefficient. Products from photodissociation of molecules by solar UV radiation are also important when considering the composition of the upper atmosphere, more exposed to sunlight. Given that photolysis is reliant on the radiation that reaches certain species, *Rayleigh scattering* must be considered as it modulates the dispersion of radiation in air particles, depending on their size and wavelength of inbound radiation [Irwin, 2009]. Some of these reaction are highlighted here:

$$\begin{gathered} NH_3 + h\nu \rightleftharpoons NH_2 + H \\ NH_2 + NH_2 + M \rightleftharpoons N_2H_4{+}M \end{gathered} \tag{3.8}$$

Here, **M** is any other molecule and $h\nu$ represents solar radiation. When ammonia reaches the upper atmosphere, at pressures around 100 mbar, it can be broken down to form hidrazine (N_2H_4). Hydrazine is then expected to condense at temperatures found in Jupiter's upper troposphere, and the resultant ice particles are a component of the haze layer on Jupiter's upper atmosphere. At even higher altitude levels, unbroken ammonia molecules can also freeze to form ice particles, thus become a constituent of hazes found on Jupiter.

Another interesting molecule to look into is phosphine whose photolysis can be described by these reactions:

$$\begin{gathered} PH_3 + h\nu \rightleftharpoons PH_2 + H \\ PH_2 + PH_2 + M \rightleftharpoons P_2H_4 + M \end{gathered} \tag{3.9}$$

As with ammonia, photodissociation is expected to occur at the 100 mbar pressure level and if temperatures get low enough, diphosphine condenses and becomes another haze material in the upper troposphere. Looking at Table 3.1, we can see that methane is also relatively abundant in the atmosphere and, although the type of radiation capable of performing photolysis on methane can not penetrate further than 10 mbar due to Rayleigh scattering, the ability of methane to absorb radiation is very high. With this, the main region for methane photodissociation is at higher altitudes than the previous two cases, which leads to decreased pressures, making subsequent reactions less efficient. The complicated chemistry revolving around this compound and its interaction with solar radiation is showed in Fig. 3.4.3.

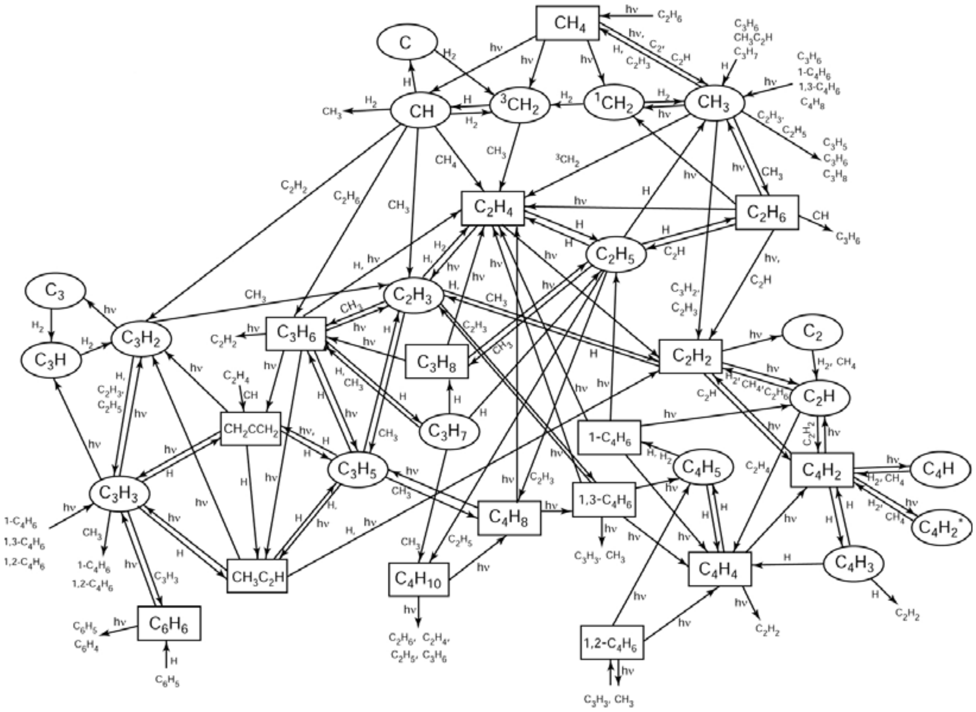

Figure 3.4.3: Methane photochemistry paths. From [Moses, 2000].

Photolysis of methane happens predominantly at higher levels in the atmosphere, with a peak level of photodissociation between 0.1 μbar and 0.1 mbar. While this may be the main region for methane photodissociation, to produce the observed hydrocarbons, other reactions are needed which are only efficient at higher pressures ($>$ 0.1 mbar). The main products of photodissociation are C_2H_2, C_2H_6, along with several other molecules of the form $C_{2n}H_2$. Some products of these reactions will compose stratospheric hazes which spread vertically through eddy mixing. Some of these species will then eventually descend into the atmosphere to warmer areas, where they are transformed back into methane again, possibly starting another cycle if methane is brought to higher layers of the atmosphere [Irwin, 2009].

Not only are these chemical studies relevant to analyse the composition of Jupiter's atmosphere and infer its vertical distribution and air circulation, but also to unravel another enigma of the gas giant: its colourful display between zones, belts and storms, particularly the reddish colour of the GRS. Although it is widely accepted that the white colour of most bands is a manifestation of ammonia ice clouds, which result from upwelling of gas, the darker colour of the belts does not have a clear single source, possibly being a combination of chemical species. However, a recent study by Carlson et al. [2016] proposes a solution based on laboratory generated compounds which could also form on the environment surrounding the GRS. The suggested process has ammonia photolyzed at high tropospheric altitudes and, through vertical circulation within the storm, its photoprod-

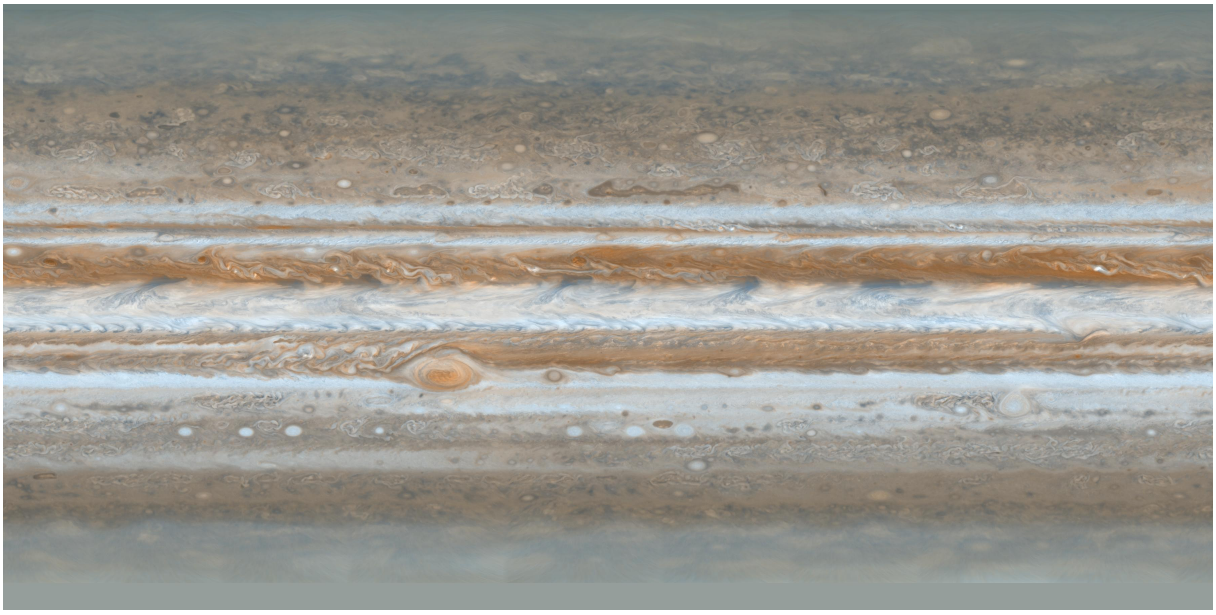

Figure 3.4.4: A cylindrically projected map of the atmosphere of Jupiter built with multiple images from the narrow angle camera of the Cassini spacecraft. Although the original data was taken at just two wavelengths in the near-infrared and blue part of the spectrum, they have been coloured to match what the human eye would see should it gaze upon Jupiter. Credits to NASA/JPL/Space Science Institute.

ucts NH_2 and H react with downwelling C_2H_2 and begin a chemical chain reaction which generates a solid residue that shows a colour that matches the observed visual spectrum of the GRS. This applies if the chromophore is distributed in a thin film at the top of the GRS tropospheric cloud (Crème Brûlée model) [Baines, 2019]. Furthermore, since this red colouration is not exclusive to the GRS, Sromovsky [2017] studied other cloud regions on Jupiter, verifying that their visual spectrum is also a good fit for the chromophore suggested by Carlson et al. [2016], using the crème brûlée model for its particles [Baines, 2019]. This leads to the possibility that this chromophore is quite universal in Jupiter, responsible for the various shades of red/orange observed on multiple cloud regions on the gas giant. Using more recent data from Juno, Dahl et al. [2020] find that this model and chromophore, while giving reasonable results for Jupiter's cloud bands, does not seem to be a safe assumption for more unique weather events such as the 2016-2017 Southern Equatorial outbreak.

3.4.2 Dynamical Processes

The Banded Structure

The mesmerizing banded structure of Jupiter's clouds is easily observed on Earth with a small telescope, with the bright regions traditionally called "zones" and the darker bands called "belts". This structure is populated by dozens of jet streams and storms that can last for centuries. Zones and belts feature jets that flow in different directions, with the former being anticyclonic (clockwise rotation in the northern hemisphere and counter-clockwise in the southern one) while the belts are cyclonic (opposite rotation). Although much more noticeable in the gas giants, planetary banding is not unique to the giant planets beyond the Asteroid Belt. Earth's circulation is also subdivided in three distinct regimes: a tropical Hadley cell characterised by moist convective activity at small scales; extra-tropical Ferrel circulation characterised by large scale baroclinic waves, and the polar circulation cell. However, the boundary between different dynamical regions is often blurred. Additionally, it seems that the size of the equatorial Hadley cell depends on planetary rotation, from almost planet wide tropical cells for slow rotators like Venus, to a narrow Hadley cell and multiple Ferrel-like extra-tropical cells in fast rotators such as Jupiter [Fletcher et al., 2020].

Despite zones and belts being recognized mostly by their albedos, which refer to the top most clouds in the troposphere, they can also be differentiated through temperature, and as mentioned earlier, by their dynamical regime. Beyond the condensed clouds, the atmosphere is stably-stratified above the region where radiative energy transfer processes become more significant than convection, somewhere between 300-500 mbar. The "weather layer" where clouds form, is in a moist sub-adiabatic regime due to release of latent heat during cloud formation [Fletcher et al., 2020]. This location is likely to be where primary meteorological features give rise to eddies that power the zonal jet system. However, there is evidence that these zonal jets can extend to great depths, up to 3000 km below the cloud level where it is hypothesized that *Lorentz* drag becomes an important force that counters this jet stream [Kaspi et al., 2018].

The magnitude of these jets and evolution in time have been studied extensively over decades, in part using cloud-tracking techniques further described in section 5.2. Observations revealed that eastward and westward winds have very similar magnitudes with the exception of the equatorial zone which favours an eastward wind velocity that can reach 150 m/s. Additionally the jets don't appear to be symmetric in relation to the equator: A stronger jet at 24°N that has no southern counterpart; the GRS in the southern hemisphere, and even within the equatorial jet there is also an apparent asymmetry from the presence of a trapped Rossby wave between the equatorial zone and the North Equatorial Belt [Asay-Davis et al., 2011]. Another difference between zones and belts is the presence and altitude of thick clouds, with white zones bearing clouds which darken the region at infrared wavelengths, while belts show an absence of clouds and increased temperature, evidenced by the enhanced emission in the infrared. The altitude difference between regions in the banded structure can also point to particularly interesting dynamics pertaining the boundary regions between zones and belts. Several observations of eastward jets consistently reveal that the equatorward flanks are colder than the poleward ones throughout the upper troposphere from 700 - 1000 mbar (top-most clouds), to at least the tropopause near 100 mbar [Conrath et al., 1998, Simon-Miller et al., 2006, Fletcher et al., 2016]. The latitudes of these zonal jets seem to be correlated with the locations of the strongest meridional temperature gradients. Thus, these boundary regions are characterised by a maximum in vertical wind shear. It has been further verified that cloud-top winds decay with altitude above the troposphere, probably by means of meridional circulation and drag force. These dynamical processes imply that air is generally upwelling and adiabatically cooled in zones, flows polewards and sinks, warming adiabatically in the belts[Fletcher et al., 2020]. However, the reason why jets seem to slow down from the upper troposphere to the tropopause remains unclear. It is possible that some form of wave drag from gravity wave dissipation is responsible [Ingersoll et al., 2004] however, this effect has not been reproduced naturally from GCMs, which don't feature this observed decay in wind velocity.

This wind velocity decrease is contrasted at cloud level by an observed acceleration of the

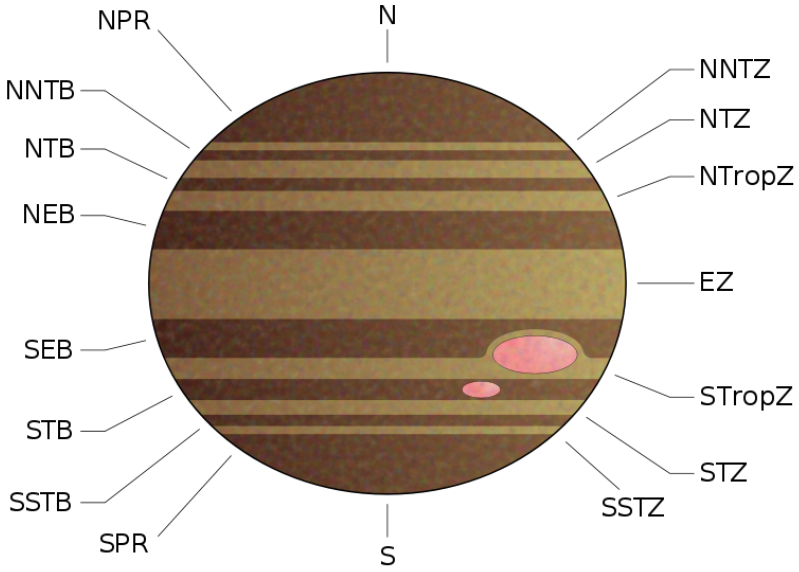

Figure 3.4.5: Nomenclature of the banded structure of Jupiter. On the centre is the Equatorial Zone (EZ) neighboured by the northern and southern equatorial belts (NEB, SEB). Above and below we find the tropical zones (NTropZ, STropZ) and further polewards we reach the temperate zones and belts (NTZ, NTB, STZ, STB). The remaining areas are occupied by the north-north/south-south temperate zones/belts and onto the polar regions.

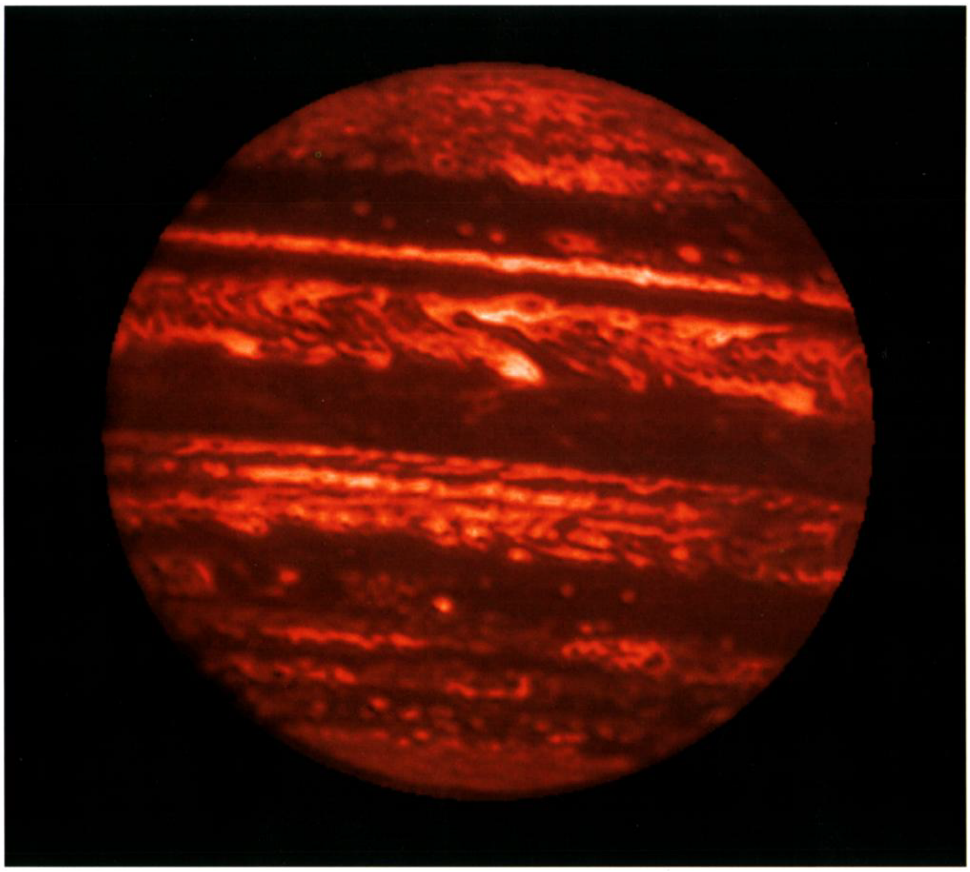

Figure 3.4.6: The Jupiter's disk in the M narrowband ($\sim 5\ \mu$m). This image is shown in false colour and logarithmically stretched to better observe pixel contrast. It shows Jupiter as a prominent emitter in the IR, particularly in the belts which are located in warmer deeper layers of the atmosphere [Ingersoll et al., 2004].

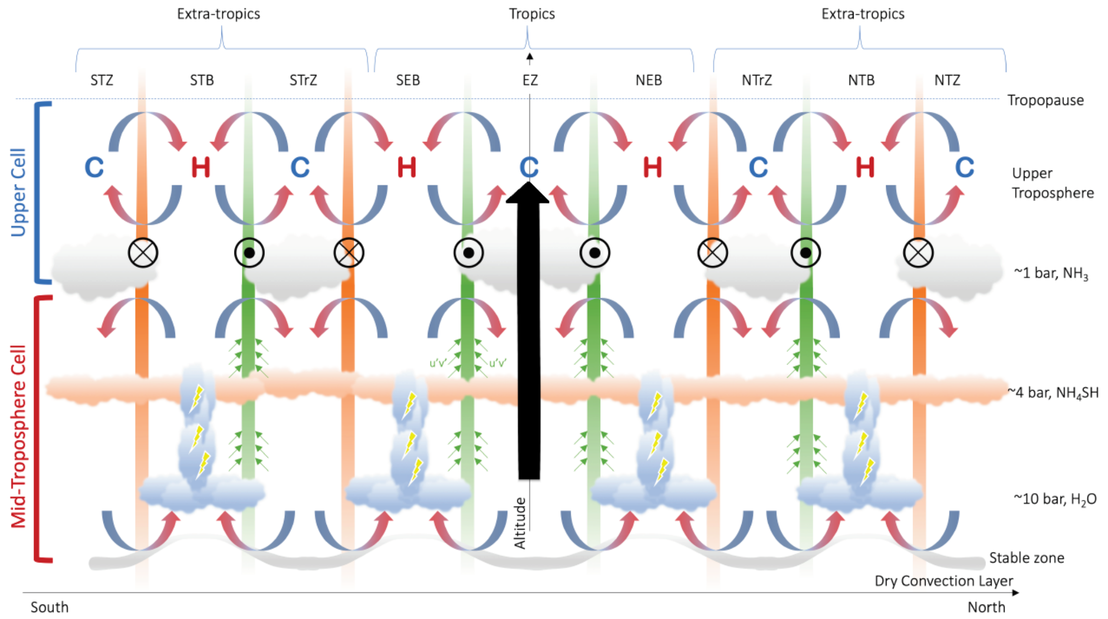

Figure 3.4.7: Diagram of the stacked cells model for the troposphere of a gas giant. This model can be applied to Jupiter and Saturn with varying number of Ferrel-like cells and the altitude in which different cloud layers settle. Strong equatorial upwelling which penetrates both cells is indicated by the thick black arrow. The transition point between the upper and mid-troposphere cells is placed somewhat arbitrarily near the top of the clouds. This results in divergent flow over the belts and convergent flow over the zones. Taken from Fletcher et al. [2020] which expands upon the models by Ingersoll et al. [2000] and Showman and de Pater [2005].

zonal jets, possibly caused by some eddy forcing and turbulence which include thunderstorms in moist-convective complexes (for example in the belts), and natural instabilities arising from gradients in temperature and zonal wind velocity. The energy that powers these processes could come from the planet's internal heat, which has already been established as quite substantial, or from the potential energy stored within the thermal gradients themselves. On this level, turbulences associated with moisture can also provoke the thunderstorms observed predominantly in the belts, although other causes for lightning are possible [Fletcher et al., 2020]. A conundrum then exists on how these regimes transit from one another within the troposphere since the latter forces belt-to-zone meridional circulation by eddy acceleration.

Figure 3.4.7 attempts to model the circulation in the troposphere, which regulates the stability of the banded structure visible on Jupiter's atmosphere. It shows two apparently competing dynamical regimes whose respective transition is still not clear. Production of atmospheric waves at depth in Jupiter and their dissipation higher in the atmosphere might hold the key to the transition between the two circulation regimes described above [Fletcher et al., 2020].

Although already a complicated model, it has trouble explaining the ever-changing nature of the belt-zone activity cycle. Even if the disposition of bands is somewhat stable on the visible atmosphere of Jupiter, the structure of the bright zones and darker belts can evolve over variable time periods in response to obscured meteorological activity within and/or below the main cloud decks. The changes can be so profound as to encircle the entire planet, provoking changes in band colouration such as reddening, which can be related to aerosol changes via photochemical processes, possibly associated with accumulation of the reactions described in Carlson et al. [2016] and expanded upon in Sromovsky [2017].

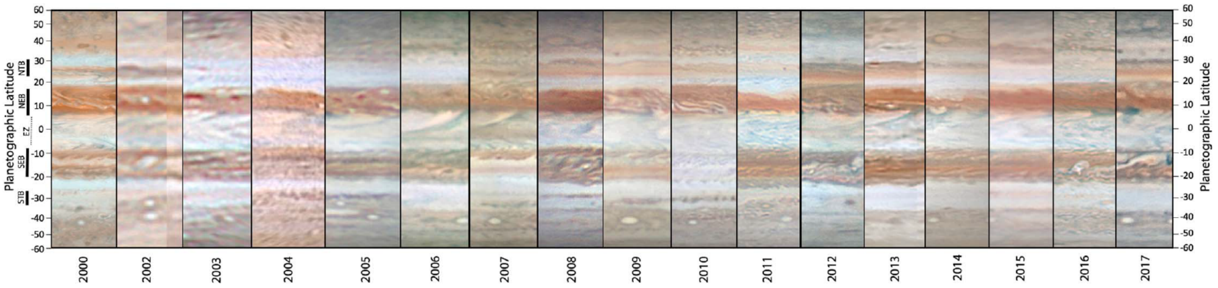

Figure 3.4.8: Jupiter belt/zone variability between 2000 and 2017 with observations from Cassini, Juno and amateur astronomers. This sequence features several examples of NTB revivals, NEB expansions, EZ colouration changes, and SEB revivals. Taken from Fletcher [2017].

Other sources of variability include sudden outbreaks and convective plumes which rise to the top of the clouds, leading to some revival events [Fletcher, 2017] as can be observed in Fig. 3.4.8.

The causes for these drastic changes in appearance are possibly many, as their character is highly variable however, disturbances of the NTB band on Jupiter (see Fig. 3.4.5) seem associated with moist convective plumes rising from the depths of the water cloud in the deep atmosphere. Although many of these events appear cyclic, it is currently difficult to predict when and what provokes such changes. Due to Jupiter's small axial tilt, it is unlikely that seasonal variations play a significant role but, the 4.4 year cycle of Jupiter's quasi-quadrennial oscillation (an equatorial temperature oscillation in the stratosphere) can cause secondary circulation patterns which can lead to favourable conditions for belt/zone variability. However, more long term observations and refined numerical simulations are required to disentangle the possible origins of these upheavals [Fletcher, 2017].

3.4.3 Storms and vortices and other features

Along with its characteristic banded structure, vortices at cloud level are one of the most ubiquitous presences in Jupiter's atmosphere, including the long-lived GRS. They can be visually distinguished by their albedo contrast relative to their surroundings and by their oval shape. Vortices can be classified according to their relative vorticity as cyclones or anticyclones depending on their location in relation to the equator and the direction of their rotation as explained in the previous section.

Anticyclonic vortices appear in greater number and are generally more stable than cyclones, except at polar latitudes where the situation is reversed. A vortex can be understood through its vorticity distribution (how the fluid in the vortex rotates) and the relation with its neighbouring flow shear. Temporal changes in the vortex morphology can also be relevant as well as interaction with other structures, including other vortices which can lead to a merger, forming a bigger storm or their destruction with eddies. Since the powering and support mechanisms for the zonal jets of Jupiter are yet to be fully understood, it is likely that these discrete features, their interactions with each other, and the mean flow, play an important role in the atmosphere's global dynamics [Ingersoll et al., 2004, Barrado-Izagirre et al., 2021].

Figure 3.4.9: Jupiter's Great Red Spot as captured by NASA's Juno spacecraft. This image has enough resolution to show intricate feature inside the gigantic storm system along with surrounding turbulent areas along with multiple eddies in the boundaries between belts and zones. Credits to NASA.

These type of vortices form in multiple ways. Smaller ovals ($<$ 1000 km) can be generated in updrafts whose spreading motion produces anticyclonic vorticity or when an anticyclonic zone suffers some disturbance. Other forcing mechanisms include moist convection or solar heating according to shallow-water models [Yadav et al., 2020]. Their overlying hazes have generally increased altitudes with lower temperatures at upper levels, suggesting moderate upwelling. White ovals can also sometimes change colour, with a similar appearance to the GRS, with the same UV absorber that is present in that storm [Ingersoll et al., 2004].

Great Red Spot

Jupiter's GRS (example in Fig. 3.4.9) is the most dominant and long-lived feature on the atmosphere, an anticyclonic storm more than 170 years old and almost twice the diameter of the Earth. Interestingly, frequent observations from the Hubble Space Telescope (HST) and views from Galileo, Cassini, New Horizons and Juno have established a monitoring record which confirms that since it was first observed, the GRS is shrinking. Additionally, it has been observed that this storm drifts slightly westward within its latitudinal range and that its orange/red colour has intensified recently. These changes are possibly tied to variations in the background relative vorticity [Simon et al., 2018]. Despite its strong morphological changes in the last 140 years, the wind field surrounding and within the GRS has suffered only modest modifications albeit in a shorter time interval (almost 40 years), which implies a deeply rooted dynamical circulation. This presents a contrast with earlier depictions of the structure of the GRS along with current models of other anticyclonic vortices [Irwin, 2009]. Indeed, recent results presented in Li et al. [2020]

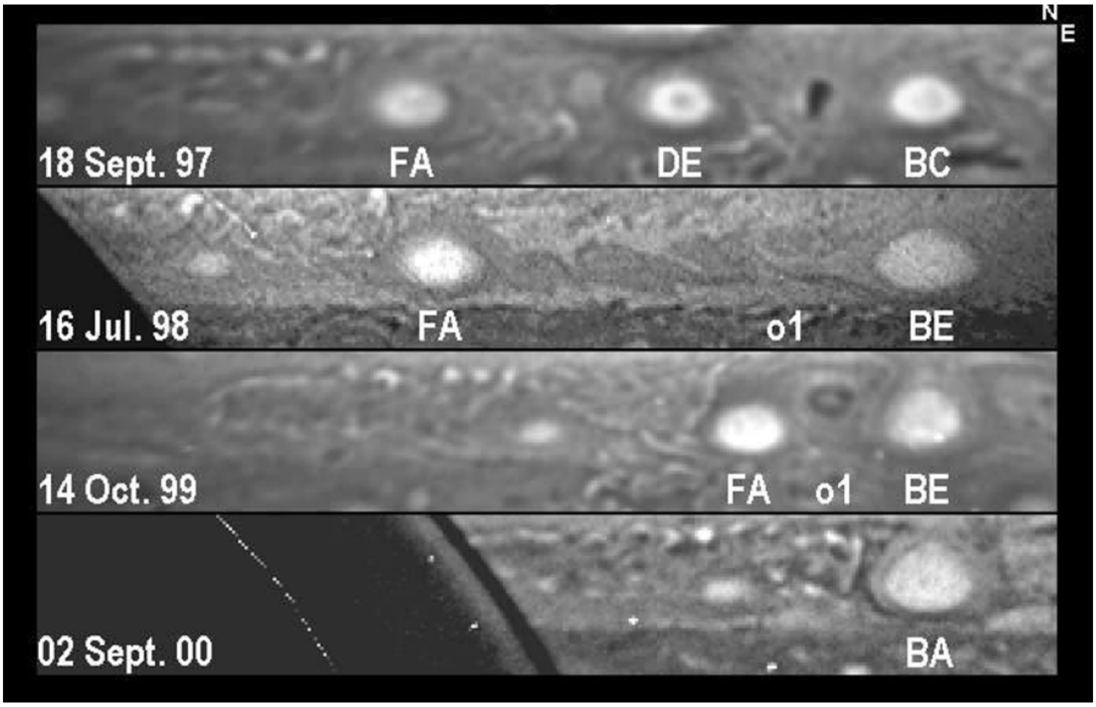

Figure 3.4.10: The merger of the white ovals which gave birth to the second largest storm in Jupiter, Oval BA. These images were obtained from observations from 1997 to 2000 by HST. Taken from Irwin [2009] and credits to NASA.

suggest that the GRS extends dynamically down to pressures greater than 100 bars (230 km down from the 1-bar level in Jupiter), possibly reaching even deeper levels. The winds in the outer annulus can reach 150 m/s according to recent observations, decreasing towards the nucleus of the storm. Within the GRS it is possible for other structures to form, such as mesoscale waves (found with dimensions of 75 km in wavelength) whose presence signals the existence of static stability within the confines of the storm, and internal spiralling vortices that share the GRS anticyclonic rotation [Sanchez-Lavega et al., 2018].

Other Important Ovals

Though not as impressive as the GRS, the jovian atmosphere harbours many other long lived vortices (years of monitored existence), usually with white clouds whose interactions with other atmospheric phenomena and the general zone/belt dynamics lend them different and interesting properties to compare with the GRS. Currently known as Oval BA, this vortex is the result of a merger of six different storms between 1997 and 2000 (see Fig. 3.4.10).

The rotation of this and other large white ovals is defined by their interior cloud texture. Like the GRS, rotational velocity increases with radial distance from the center until the visual boundary of the storm and its temperature is slightly subdued at upper tropospheric levels [Ingersoll et al., 2004]. Amateur observations in 2005 detected a change in colouration of this oval to the familiar red of the GRS, but later observations with Juno show the Oval BA in its familiar white colour, suggesting that whatever mechanism maintains the chromophore of GRS stable, it is not present in smaller ovals.

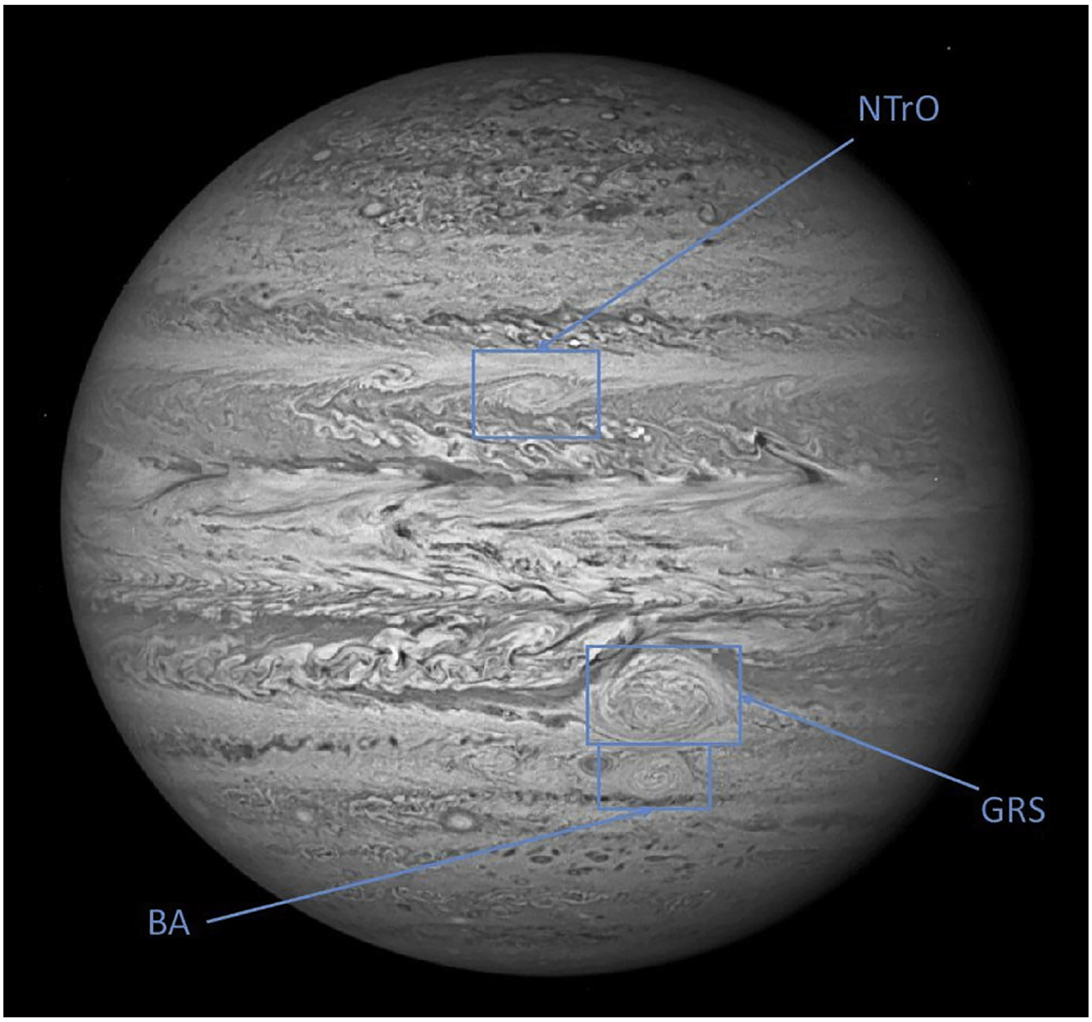

Figure 3.4.11: The three longest-lived and largest ovals in Jupiter's atmosphere. Observation from HST on the 20th of September 2012 with the F763M filter. Taken from Barrado-Izagirre et al. [2021].

Another interesting long-lived anticyclone manifests between the NTropZ and the NEB (see Fig. 3.4.11) being the third largest storm of its kind in Jupiter (after the GRS and Oval BA). The region where it is located is also interesting because it is home to the formation of several other white ovals of the same kind, cyclonic features and other peculiar cases. The fact that it also grew far from the influence of the GRS, unlike Oval BA lends it an interesting case for the development of a large vortex not influence by the presence of such a big storm system. Like Oval BA, it has experienced vortex mergers and colour changes, as well as vertical cloud structure and upper cloud content modifications over 10 years of observations. Contrarily to the two other bigger storm systems, this oval approximately shares its vorticity with the zonal jet at the main latitude in which it is embedded, which entails that this oval is mainly sustained by the zonal jets confining it. The life-span of this vortex and the stability of its drift rate and vorticity are more clues that these long-lived system are sustained by the atmospheres at deeper levels in contrast to the traditional shallow-water models [Barrado-Izagirre et al., 2021].

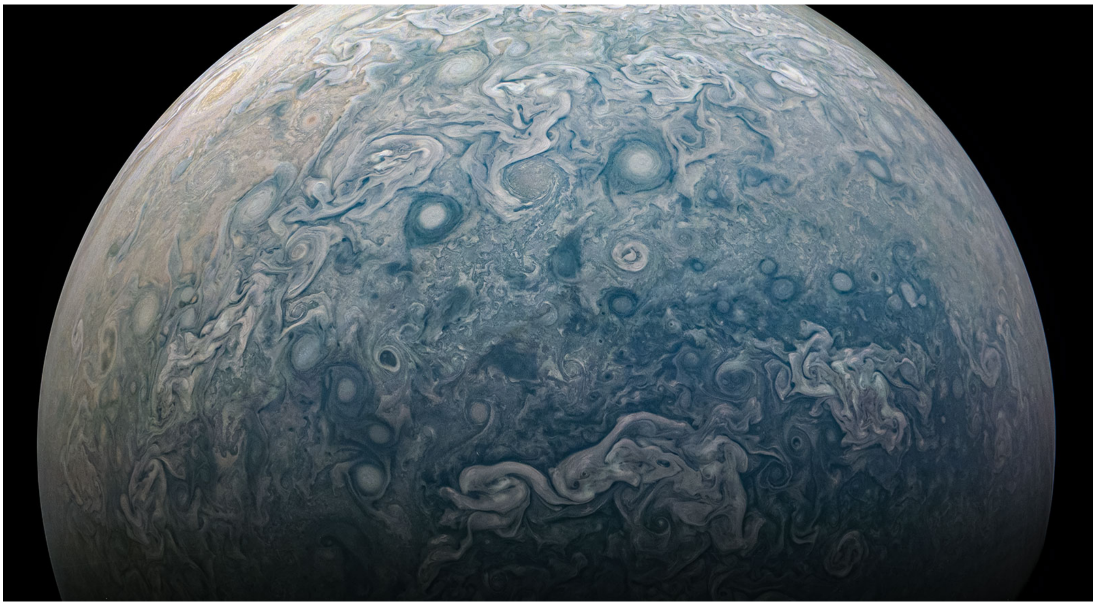

Figure 3.4.12: During its 24^{th} close fly-by, Juno captured this image of the northern hemisphere of Jupiter. At higher latitudes, the banded structure gives way to a sprawling chaos of vortices and turbulence until the poles. Credits to NASA.

Cyclonic Features

Regions of cyclonic activity tend to be more spread out and chaotic than their anticyclonic counterparts. Most of these feature have a filamentary structure and evolve rapidly. Like the belt regions on Jupiter, closed cyclonic features are warmer than their surroundings at upper tropospheric levels, consistent with downwelling [Conrath et al., 1981, Ingersoll et al., 2004].

Some stable cyclones do exist, the best example being the brown barges, dark elongated features at visible wavelengths that brighten up at 5 μm, suggesting reduced cloud cover and subsidence [Irwin, 2009].

There's an observed asymmetry between the prevalence of anticyclonic features over cyclonic ones. It is possible that this difference arises from the fact that anticyclones are generally vertically thicker, or that the belts are sites of moist convection which makes anticyclones possibly last longer and lends more turbulence to the medium respectively [Ingersoll et al., 2004].

The atmospheric structure of Jupiter's polar regions changes dramatically from the belt/zone structure at lower latitudes to a concentration of swirling clouds and closed vortices (see Fig. 3.4.12). Juno's unique orbit has enabled the observation of the polar region of Jupiter for the first time, revealing persistent polygonal patterns of large cyclones around both poles [Adriani et al., 2018]. Both poles feature a cyclonic vortex close to the polar point enclosed by eight circling cyclones (North) in an hexagonal pattern and by five cyclones (South) in a pentagonal pattern. Their stability and internal dynamics are possibly linked with atmospheric exchange with deeper layers and vigorous vertical circulation [Adriani et al., 2020].

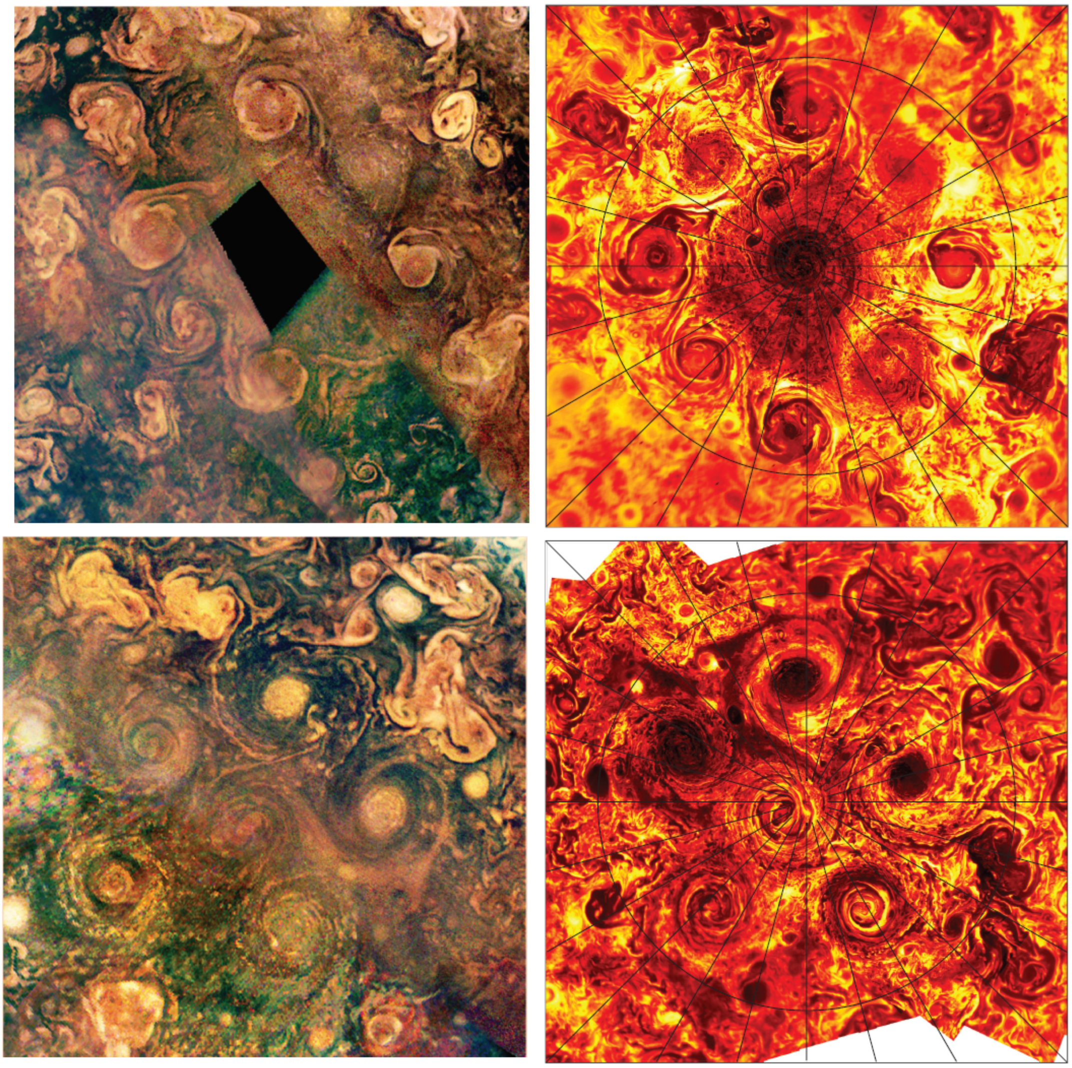

Figure 3.4.13: The North (Upper images) and South (Lower images) poles as they appear in visible wavelengths (left) and infrared wavelengths with both the JunoCam and JIRAM instrument onboard Juno. The visible images are obtained with several perijove passes as different areas of the poles are on the nightside due to the small axial tilt of Jupiter. Taken from Adriani et al. [2018].

Chapter 4

Observations

In this chapter lies a detailed description of the observations performed for the purpose of this thesis. The bulk of the scientific data used is in the form of images taken from orbiting spacecraft such as VEx and Akatsuki. Given the nature of this project, thousands of images were used to retrieve the necessary data. Additionally, our team made observations with ground-based telescopes to analyse the winds on Jupiter with a unique Doppler velocimetry method. Though I personally did not conduct the observing runs with ESPRESSO, I later became involved with data reduction and analysis, making this another part of this project. We compare the ground-based data with the legacy of observations made by the Cassini and Hubble spacecrafts of the troposphere of Jupiter, including a cloud-tracked winds retrieved by our team as part of the effort for long-term comparisons. Although I could not physically undertake any observing campaign due to the current pandemic, other projects in which I am actively involved make use of data from observations made by several members of our team.

4.1 Venus Express

On a first approach, to conduct our intended research we used mostly imaging data from VEx instruments VIRTIS and VMC, both described in chapter 2.1.3. All images used for the studies conducted for this thesis were taken from ESA's Planetary Science Archive, a public data library.

While VIRTIS-M possesses a very large number of wavelength filters on both channels, only a few are useful for our purposes, specially the ones which narrowly target the cloud deck at varying heights with good enough contrast between features. Within the IR channel there are four useful wavelength ranges: 1.74 μm and 2.2-2.3 μm which allow the tracking of features on the lower cloud deck at approximate altitudes between 44-49 km. Atmospheric features appear as opacity patterns against a brighter background which represents the thermal emission from lower areas of the atmosphere of Venus; 3.9 μm and 5 μm which sense thermal emission of the upper clouds, close to 70 km of altitude. Note that observations of the lower clouds with the first two wavelengths must be performed on the nightside of the disk, as the dayside hemisphere provides little to no features and targets the upper clouds' reflected light. We also browsed through the visible channel of VIRTIS, selecting wavelengths which target the top of the clouds ($\sim$ 365 nm), and the middle clouds between 55-65 km (575-680 nm and 900-955 nm), observing the dayside hemisphere of Venus [Peralta et al., 2017a].

Though we used VEx images for cloud-tracking in previous works, for the purpose of this thesis, exploration of this data set was primarily for atmospheric gravity waves research. In this sense, our goal was to conduct the most complete survey on atmospheric waves on the lower cloud, observable through VIRTIS-M-IR wavelengths 1.74 and 2.25 μm. We set out to follow up on the analysis performed in Peralta et al. [2008], and conducted our search for waves over 13 months of VIRTIS data starting in August 2007 until the unfortunate malfunction of the infrared (IR) channel of VIRTIS-M in October 2008, which disabled its use for the rest of the mission [Hueso et al., 2012]. In the results section below, we also include the data from Peralta et al. [2008], who observed the lower cloud from April 2006 to March 2007, in order to present the data set in its most complete format. A total of 239 orbits were examined, each image at the four target wavelength ranges (1.74, 2.25, 3.9 and 5 μm).

Images from VMC target a narrower range of wavelengths, with a selection of four filters available, two of which (UV and VIS) would be useful for our studies. Being simpler data than the hyperspectral cubes from VIRTIS, and the fact that these wavelengths target mostly the upper cloud region with high contrasting features provoked by the presence of the unknown UV absorber, browsing and treatment of these images was more streamlined for our purposes. The shorter integration times of this instrument allow observations close to the pericenter of the spacecraft's orbit around Venus, which entails in some cases very high resolutions ($\sim$ 0.2 km/pixel). These allow the observation of atmospheric features in finer detail such as gravity waves as those studied in Piccialli et al. [2014]. To complement this study, we set out to analyse the remainder of VMC data set from where the observations performed by Piccialli et al. [2014] left off, which meant browsing through approximately 270,000 images. So far we have analysed over 63,000 images, comprised in approximately 300 VMC orbits which cover a year of observations in 2013, detecting almost 900 signatures of wave activity in the upper and middle clouds. As we later acknowledged the need for a revision of the geometry of observations due to the high spatial resolution demands of our study, in order to complete the work plan of this project, we chose to leave this line of research for the future.

4.2 Akatsuki

The japanese space mission, which is still in orbit, brings modernized instruments specifically suited for climatology studies of the planet. Though the initial plan of observations carried out by Akatsuki was modified, some interesting advantages rose from the new orbit.

After orbit reinsertion, observations of the full apparent disc of Venus for longer time intervals than was possible for VIRTIS, opened up equatorial latitudes for exploration in both UV and IR, enabling a more comprehensive look into the atmosphere of Venus. We used the UVI and IR2 cameras for both cloud-tracking and atmospheric wave characterisation purposes.

Observations of the upper cloud were made between 26 and 31 of January 2017, during orbit 39 after reinsertion [Goncalves et al., 2020]. This specific period was selected for coordinated observations with Telescopio Nazionale Galileo (TNG) HARPS-N (High-Accuracy Radial-velocity Planetary Searcher - North) to perform doppler velocimetry, later described in this chapter. We had 3 images for each day of observation suited for cloud tracking, each separated by a time interval of two hours, using the 365 nm centre wavelength filter of the UVI instrument [Yamazaki et al., 2018].

To observe the lower cloud we used all available data from the IR2 camera to complement our search for waves. The wavelength filters available with this instrument target the lower cloud during nightside hemisphere observations. The data from the first orbits after reinsertion contained a very high level of noise and aberrations, rendering them without any use for our purposes. The IR2 camera possesses an extra filter at 2.02 μm although, it is most effective on the dayside hemisphere as it captures CO_2 absorption at the top of the clouds [Peralta et al., 2017a], outside our area of interest. Hence, we did not make any use of those images.

We browsed through the three available IR2 wavelength filters however, images at 2.26 μm were predominantly used for the search of waves because they presented the sharpest view of the lower cloud, crucial to unambiguously detect and characterise cloud shapes, and more importantly minimised light pollution from the dayside of the disc of Venus caused by multiple reflections of infrared light on the detector [Satoh et al., 2017]. Although this effect partially constrained the characterisation of some features, image processing techniques described in section 5.1 were employed to curb these image artefacts. We inspected all IR2 data along 30 orbits, from March 2016 to December 2016, before the acquisition of images was indefinitely interrupted due to a malfunction of the electronics [Iwagami et al., 2018]. In total, 1255 VIRTIS-M images, each at the target wavelengths mentioned above, and 1639 IR2 images were analysed to detect atmospheric waves during the periods selected.

4.3 VLT/ESPRESSO

4.3.1 Instrument Description

Situated atop *Cerro Paranal* in the Atacama Desert, Chile, stands the Very Large Telescope array (VLT), one of the leading facilities for European visible light astronomy at the Paranal Observatory. Composed of four 8.2 metre Unit Telescopes (UT) and an additional four 1.8 metre Auxiliary Telescopes (AT) which can be moved on tracks to fit specific observing positions, with its broad instrumentation program it is one of the most powerful telescope suites in the world [ESO]. One such instrument is the Echelle SPectrograph for Rocky Exoplanets and Stable Spectroscopy Observations (ESPRESSO), a fibre-fed, cross-dispersed, high-resolution echelle spectrograph located in the Incoherent Combined-Coudé Laboratory (ICCL), where it can be fed the light of either one or all four UTs. In each configuration, light journeys to the instrument via a so-called Coudé-train optical system which separates the light from the science target and background (7 arcseconds away from the target) into two fibres, which combined form the slit of the spectrograph [Pepe et al., 2014].

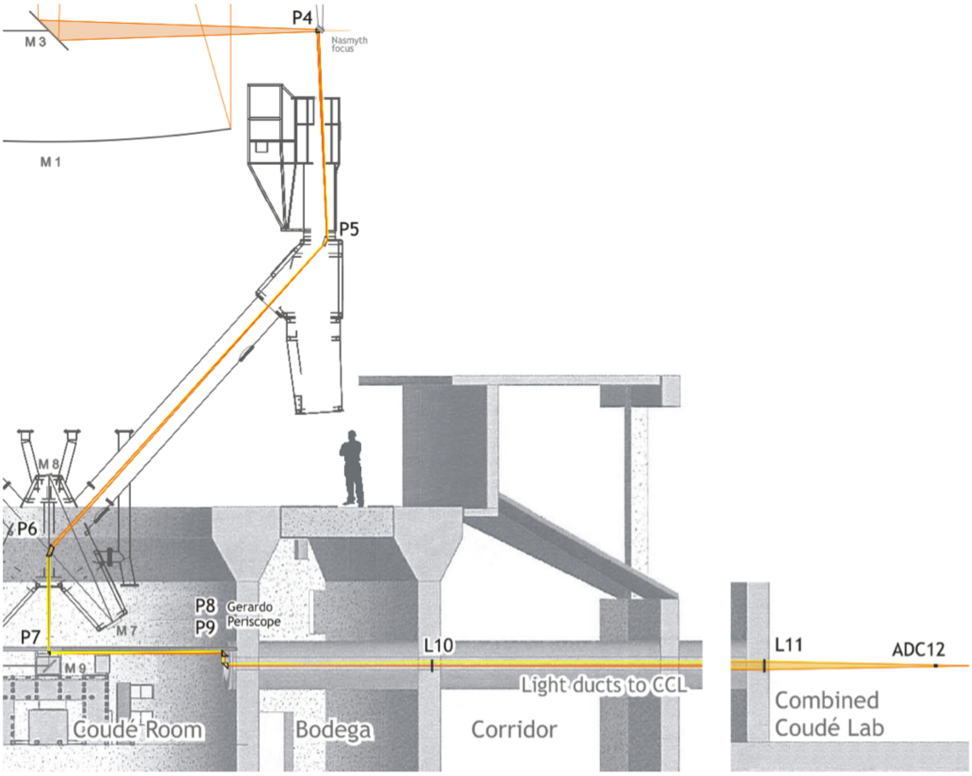

Figure 4.3.1: The structure of the Coudé-train of ESPRESSO showing the optical path that light takes from the telescope through the use of several prisms (P4-P9), large lenses (L10, L11) and an Atmospheric Dispersion Compensator (ADC). This schematic also includes several mirrors (M1,M3, M7, M8 and M9) that are part of the telescope and Coudé-train. This figure is taken from Pepe et al. [2014].

The Coudé-train is composed of 11 optical elements as shown in figure 4.3.1. It picks up light from the telescope through one of the Nasmyth focus, and guides the beam down through tunnels in a path that can reach 60 m in length until it reaches the CCL, where the spectrograph is located. As light reaches the CCL, it passes through the Front-end (FE) unit, which is responsible for field stabilization and collecting light from additional calibration sources in order to perform for example spectral flat-fielding, wavelength calibration and drift measurement. A toggling system in the FE carries six fibre heads, used to select between resolution modes (Medium (MR), High (HR) and Ultra-High Resolution (UHR)). The four MR fibres can be used simultaneously to function in the 4-UT configuration while, when using a single UT, either HR or UHR fibres can be positioned at the output of the operating FE unit assigned to the UT in use. Each of these fibres carries a pierced mirror through which relay optics re-image the light onto the two fibres mentioned earlier, one that targets the science object and another for background or reference point. The light from these fibres is then finally dispersed when it enters the spectrograph and the spectra is imaged through two different camera arms, a red and a blue one with two distinct detectors. Light is sent to each of these channels (red and blue) by a dichroic beamsplitter, a type of colour filter that separates radiation of different wavelength on a light beam. Two camera lenses then separately focus the blue and red portion of the cross-dispersed echelle spectra onto a large CCD detector each. Each of these CCDs are different in thickness and their sensitivity is optimized for each of their respective channels [Pepe et al., 2021]. Figure 4.3.2 shows a schematic of the spectrograph and its optical design.

Through the use of a pupil slicer, we get two simultaneous spectra of light from both fibres

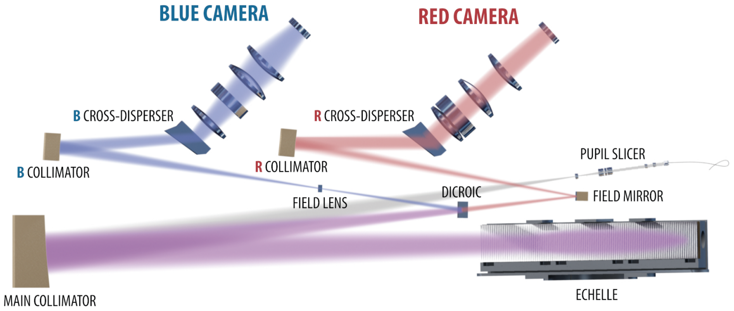

Figure 4.3.2: The optical design of the ESPRESSO spectrograph and its components. Schematic taken from Hernández et al. [2018]

in a wavelength range between 378.2 and 788.7 nm with a resolving power that ranges from 70,000 in the MR mode to more than 190,000 in the UHR mode a resolution never before reached with any other instrument at these wavelengths. Since for the particular Doppler Velocimetry technique used in this work we require the instrument to be as stable as possible, ESPRESSO also offers in this regard. As with many instruments of its kind, the spectrograph is sealed into a vacuum chamber that is located inside a thermally controlled room. These conditions ensure that temperature and air pressure remain constant, minimizing their impact on the stability of the instrument. Additionally, the setup of the spectrograph is symmetric relative to the vertical plane, to counter any unbalance provoked by gravity, and no alignment mechanisms or movable components exist inside the vacuum chamber. ESPRESSO was originally designed for exoplanet hunting and atmospheric characterisation. However, just as was demonstrated in Goncalves et al. [2020] for HARPS-N, using these very high resolution spectrographs on solar system atmospheres can open new horizons on what is possible to achieve with ground-based instruments.

4.3.2 Observing Jupiter with ESPRESSO (July 2019)

We were granted an observing period with ESPRESSO between the 21^{st} and 22^{nd} of July 2019, being the first time the instrument would be used to study a solar system planet. The goal of these observations was to retrieve zonal wind measurements in the banded structure of the planet, taking advantage of the unprecedented resolution of ESPRESSO which allows us a precision that can go lower than 1 m/s with our Doppler Velocimetry method.

With ESPRESSO, Jupiter was observed a little more than 5 hours between the late hours (23:00 UT) of 21^{st} of July and the early morning (04:20 UT) of the 22^{nd}, 2019. The first hour of observations was mostly used for calibration efforts and pointing accuracy verification, hence no science data is taken from that period. At the time of observation, the planet presented an apparent magnitude of -2.61, an angular diameter of 45.92 arc seconds and an illuminated fraction close of 99.986%, a high percentage as is expected from planets beyond Earth's orbit form the Sun. Together they correspond to a surface brightness as seen from Earth on the order of 5.44 mag/arcsec^2. Observations were carried out as a time series of 60 second exposures at predetermined positions on Jupiter's visible disk, making an effort to align the sequences with the latitudinal bands. One minute exposures guaranteed an S/N ratio above 100 for the central spectral orders of the echellogram of ESPRESSO. The UHR mode was used for the best possible resolution, thus

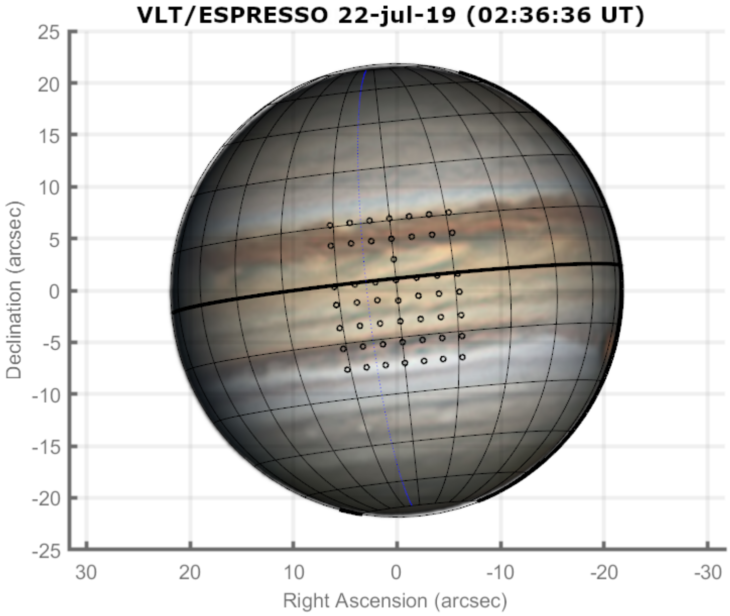

Figure 4.3.3: Schematic of the observing routine on Jupiter by VLT/ESPRESSO on the 22nd of July 2019. The small circles represent the FOV of the fibre proportional to the size of Jupiter's disk in the context of these observations (0.5 arc seconds in diameter for the size of the FOV). We also included a grid to tentatively map the relative position of each observing position in latitude and longitude. Grid lines have intervals of 15° on both coordinates. The solid black line on the right side of the spherical grid represents the morning terminator while the blue dotted line marks the location of the 12 h local time meridian. The picture of the planet's disk was taken from the Planetary Virtual Observatory and Laboratory. Picture credits go to Gary Walker.

the most precise measurements of the Doppler shifts. For these observations, the FOV of the instrument was approximately 0.5 arc seconds, represented as small circles on figure 4.3.3, which also shows the placement of the fibre's FOV on the visible disk of Jupiter. The strategy of observations was designed to target individual bands of Jupiter. As the retrievals are sequential, with a return to the reference point after each exposure, because our observing time was limited, we chose to observe points closer to the reference, along different latitudinal bands.

We summarise the observing conditions and geometry of the target during observations on table 4.1. The observing routine employed was similar to previous efforts to retrieve Doppler shifts on Venus with both the HARPS-N [Goncalves et al., 2020] and the CFHT/ESPaDOnS [Machado et al., 2017] in the sense that scanning was made in

Table 4.1: Summary of the ground-based observations of Jupiter

(1) Date	(2) Time (UT)	(3) Φ(°)	(4) Ang.Diam.(")	(5) Sub-Obs.Lat (°)	(6) Air-mass
21/22 July	23:03 - 04:20	7.7	45.92	-3.05	1.003 - 1.254

The Date and Time-Interval refer to the value registered by the instrument during observations; (3) is the Phase Angle; (4) is the size of the disk of Jupiter in the sky in arc seconds; (5) is the sub-observer latitude on Jupiter's frame; and (6) represents the air-mass at the target's location in the sky during observations.

Table 4.2: Scanning sequences for Jupiter VLT/ESPRESSO observing run on 21/22 July 2019.

[1] Seq. Number	[2] Location	[3] Time-Interval (UT)	[4] Position Order
(1)	Equator	00:18 - 01:02	1-5-6-7-1-2-3-4
(2)	S Lat 10°	01:06 - 02:28	9-36-33-34-1-37-38
(3)	N Lat 10°	02:33 - 03:01	1-13-24-25-21-22
(4)	N Lat 15°	03:05 - 03:17	14-31-28
(5)	S Lat 15°	03:20 - 03:43	1-42-43-39-10
(6)	S Lat 15-20°	03:47 - 04:20	48-49-45-46-11-40

[1] sequence number; [2] location on disk; [3] Time Interval of the beginning and end of sequence (in UT); [4] Points acquisition order. All positions were observed twice with a 60 second exposure each.

sequences based on the same planetary latitude, which was particularly important due to the nature of the contrasting wind flow between each band at cloud level. To ensure stability during the observing run, our method relies on repeated observations of the reference point at the beginning and end of each sequence. However, because ESPRESSO proved to be remarkably stable and observing time was limited, the team chose to maximize the number of points on Jupiter's disk that could be observed, observing each position fewer times than usually performed. We carried out two 60 second exposures for each position to ensure consistency between retrievals in the same position.

4.4 Other Observations

4.4.1 Cassini ISS support for Doppler Velocimetry

The Cassini/Huygens mission was one of the longest and most successful space adventures of this century. Launched from Cape Canaveral on October 15, 1997, the Cassini spacecraft would go on a seven year cruise on route towards Saturn, with multiple gravity-assist manoeuvrers which took it to Venus and Jupiter before reaching its final target in 2004.

The Cassini spacecraft is a three axis-stabilized probe which stands over 6.7 m tall, weights more than two tons and its high gain antenna has a 4 m diameter. Cassini was powered by three Radioisotope Thermoelectric Generator, providing an output of 630 W of power. Although its main mission was to study Saturn and its moon, specially the changes brought to the atmosphere and ring system with the seasons, its passage through Jupiter has permitted access to valuable high spatial resolution images of the troposphere of the gas giant.

This data was retrieved by the Imaging Science Subsystem (ISS), an instrument built with two cameras: a narrow-angle camera (NAC) and a wide-angle camera (WAC). Each of these focus images of Jupiter in a 1,024 squared CCD array. The WAC and NAC's FOV differ by up to 10 times, with NAC being 6.1 × 6.1 mrad ($6 \times 6 \mu$rad per pixel) and WAC

Table 4.3: Pointing geometry for VLT/ESPRESSO observations of Jupiter on July 2019.

[1] Position	[2] $\lambda - \lambda_{SO}(^\circ)$	[3] $\phi(^\circ)$
1	0	0
2	5.24	0
3	10.53	0
4	15.92	0
5	-5.24	0
6	-10.53	0
7	-15.92	0
8	0	-5.24
9	0	-10.53
10	0	-15.92
11	0	-21.45
12	0	5.24
13	0	10.53
14	0	15.92
15	5.24	-4.59
16	10.53	-4.59
17	15.92	-4.59
18	-5.24	-4.59
19	-10.53	-4.59
20	-15.92	-4.59
21	5.24	10.53
22	10.53	10.53
23	15.92	10.53
24	-5.24	10.53
25	-10.53	10.53
26	-15.92	10.53
.	.	.
.	.	.
27	5.24	15.92
28	10.53	15.92
29	15.92	15.92
30	-5.24	15.92
31	-10.53	15.92
32	-15.92	15.92
33	5.24	-10.53
34	10.53	-10.53
35	15.92	-10.53
36	-5.24	-10.53
37	-10.53	-10.53
38	-15.92	-10.53
39	5.24	-15.92
40	10.53	-15.92
41	15.92	-15.92
42	-5.24	-15.92
43	-10.53	-15.92
44	-15.92	-15.92
39	5.24	-15.92
40	10.53	-15.92
41	15.92	-15.92
42	-5.24	-15.92
43	-10.53	-15.92
44	-15.92	-15.92
45	5.24	-21.45
46	10.53	-21.45
47	15.92	-21.45
48	-5.24	-21.45
49	-10.53	-21.45
50	-15.92	-21.45

[1] Point nomenclature (also present in Figure 4.3.3); [2] planetocentric longitude of point relative to sub-observer meridian (sub-terrestrial in this case); [3] Latitude of the point's center.

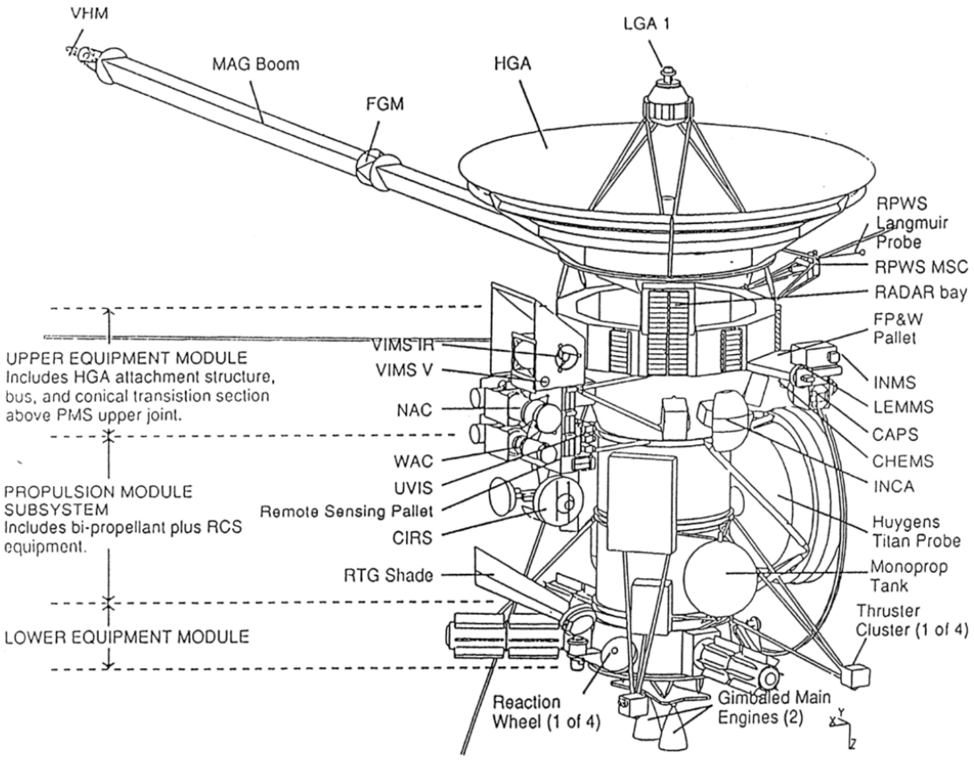

Figure 4.4.1: The Cassini spacecraft diagram.

significantly larger. Each camera has several filters available with NAC covering a larger wavelength range from 200 to 1100 nm with 24 filters. This extended coverage allows the study of composition, distribution and physical properties of clouds and aerosols across multiple heights within the cloud layers thanks to observations near methane absorption bands. The extended filter wheel combined with continuous observations also permits the visualization of the same location at multiple illumination and viewing angles, although such feat was limited for Jupiter's fly-by. Nonetheless, this opportunity revealed organized flow towards the poles on Jupiter [Irwin, 2009].

To complement our ground-based observations we performed a deeper analysis of suitable Cassini images with the ISS of Jupiter at visible wavelengths, not only to retrieve a global profile of the zonal wind, but also for a more detailed retrieval of the wind on each observed Jupiter band with ESPRESSO. Using the Planetary Virtual Observatory and Laboratory tool (PVOL), we extracted images from Cassini/ISS during the fly-by period targeting Jupiter. Wavelength range and filter combination choice were made with emphasis on the best possible contrast to distinguish different cloud features and the boundaries between zones and belts. The filters chosen include a broad-band colour filter centred at 450 nm and a methane continuum band filter centred at 750 nm and two methane filters for observations of the atmosphere at slightly higher levels. The broad band filter covers Jupiter's tropospheric region between 0.5 and 1 bar [Sanchez-Lavega, 2011], while the methane band should cover regions slightly higher (300-450 mbar) due to the risen methane hazes in Jupiter's atmosphere when compared to the ammonia cloud at approximately 0.7 bar. We purposefully did not chose images were the GRS is within line-of-sight of Earth observations to match the ESPRESSO observing runs which were taken when the giant storm was on Jupiter's nightside. We made two sets of observations: one to obtain the global profile, using a wider range of filters and covering the largest possible area in Jupiter (Table 4.4); and another to track moving features within each band already observed with ESPRESSO (Table 4.5).

Table 4.4: Cassini ISS observations for Cloud Tracking - Global Profile

Data Volume	Image pairs	Filters	Date (yyyy-mm-dd)	Time Int.	Latitude Range
1004	N1354886098_1 N1354921390_1	CL1;CB2	2000-12-07	9h48m	75°S - 15°N
1004	N1355237264_1 N1355275124_1	CL1;MT2	2000-12-11	9h31m	20°S - 90°N
1004	N1355298277_1 N1355332351_1	CL1;MT3	2000-12-12	9h32m	80°S - 40°N
1004	N1355328495_1 N1355362570_1	CL1;CB2	2000-12-12	9h28m	30°S - 10°S
1004	N1355328458_1 N1355362532_1	BL1;CL2	2000-12-12	9h28m	80°S - 25°N

The name of each image file in the ISS catalogue has a letter where 'N' refers to the narrow angle camera. With each image, NAC combines two filters to create images for specific purposes. In this case clear filters (CL1, CL2) offer high sensitivity which can be combined with the broad-band colour filters, methane or continuum band filters to maximise the contrast between cloud features in the images.

The second set of observations described in Table 4.5 was valuable to complement the Doppler Velocimetry results, taking wind tracers on the same latitudes and cloud bands of Jupiter as the ESPRESSO observations, despite being almost 20 years apart.

4.4.2 Infrared observations of Venus with TNG/NICS

Continuous ground-based observations of Solar System targets, such as Venus is crucial if we aim to monitor the evolution of the atmosphere since space missions, which generally offer greater spatial resolution for many dynamical studies of the winds, are not always available and are, in most cases, a costly enterprise.

The nightside lower clouds of Venus have been a possibility for exploration ever since a radiative window was discovered for the lower clouds of Venus, which captures the opacity of this layer against the deeper and warmer atmospheric emission [Allen and Crawford, 1984]. Early attempts to explore the nightside lower clouds at the infrared transparency windows (1.74 - 2.3 μm) with ground based instruments were carried out by Crisp et al. [1991] and Chanover et al. [1998]. First space-based contributions to analyse winds in the lower clouds came with the Pioneer Venus entry probe and infrared observations performed by Galileo/NIMS [Carlson et al., 1991]. From 2006, this atmospheric layer was then thoroughly explored in the southern hemisphere by VEx, gathering wind profiles with never before seen accuracy [Sanchez-Lavega et al., 2008, Hueso et al., 2012].

As a result of VEx's orbit around Venus, the lower cloud dynamics were poorly charac-

Table 4.5: Cassini ISS observations for Cloud Tracking - Narrow Band Profiles

Image pairs	Filters	Date (yyyy-mm-dd)	Time Int.	Latitude Range	Longitude Range
N1355275054_1 N1355309128_1	BL1;CL2	2000-12-12	9h28m	20°S - 40°N	150° - 270°
N135527168_1 N1355309528_1	BL1;CL2	2000-12-12	10h31m	50°S - 20°N	150° - 300°
N1355275087_1 N1355309161_1	CL1;CB2	2000-12-12	9h28m	20°S - 40°N	180° - 300°
N1355271705_1 N1355309565_1	CL1;CB2	2000-12-12	10h31m	50°S - 20°N	150° - 300°
N1355282659_1 N1355316733_1	CL1;CB2	2000-12-12	9h28m	20°S - 40°N	250° - 360°
N1355283063_1 N1355317137_1	CL1;CB2	2000-12-12	9h28m	50°S - 20°N	250° - 360°
N1355294017_1 N1355328091_1	CL1;CB2	2000-12-12	9h28m	20°S - 40°N	0° - 180°
N1355294421_1 N1355328495_1	CL1;CB2	2000-12-12	9h28m	50°S - 20°N	0° - 180°
N1355301589_1 N1355335663_1	CL1;CB2	2000-12-12	9h28m	20°S - 40°N	70° - 230°
N1355301993_1 N1355336067_1	CL1;CB2	2000-12-12	9h28m	50°S - 20°N	70° - 230°

All images come form the same data volume COISS 1004.

terised in the northern hemisphere. The more recent and ongoing Akatsuki mission has provided the possibility to study northern latitudes, targeting the bottom clouds with remarkable detail and discovering new kinds of features [Peralta et al., 2019, 2020]. Unfortunately, both IR1 and IR2 cameras, which are capable of surveying the atmosphere at the appropriate wavelengths that peer through the upper atmosphere and can see opacity patterns at lower altitudes, stopped working in December 2016 [Iwagami et al., 2018]. A similar malfunction occurred for the VIRTIS-IR channel, shortening its potential interval of operations as has been referred previously. Due to these setbacks, ground-based observations of the lower cloud become more relevant as the only way to continue to study the lower cloud and its features.

Techniques for ground-based observations have recently seen new developments which can make them a reliable substitute to spacecraft observations in times when these are unavailable. Increased precision in the images' navigation and geometry information with NASA SPICE kernels [Acton et al., 2017] and an improved cloud-tracking method based on phase correlation between images [Peralta et al., 2018] (described in chapter 5.2), similar to the one used for dynamical characterisation of waves in the lower cloud [Silva et al., 2021], all improve our retrieved results.

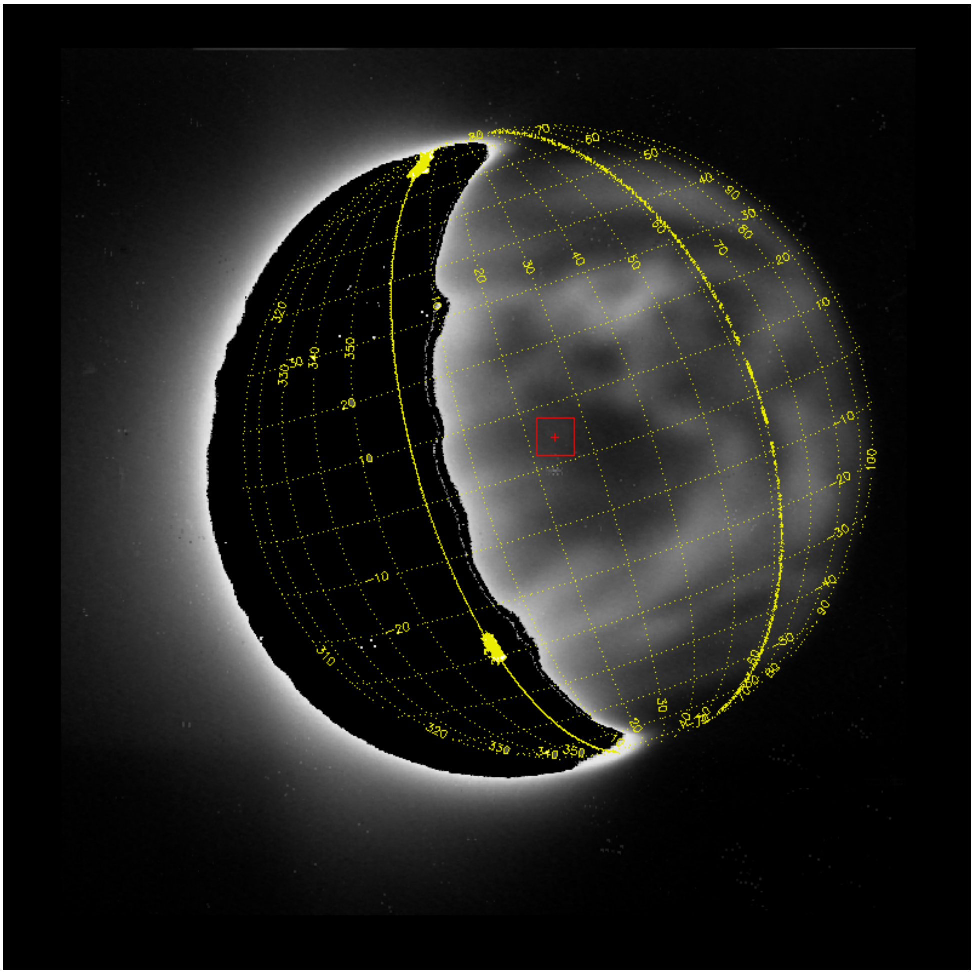

Figure 4.4.2: The navigation grid on Venus' disk at the time of the TNG/NICS observations showing a precise allocation of geographical coordinates to each pixel in the disk. In this image we can see the clouds forming opacity patterns against the brighter background on the nightside (right) of the disk, while the black crescent shape represents the subtracted part from an another observation taken with the Br γ filter, which removes the contribution from the saturated dayside of Venus.

These enhanced methods were applied to observations performed with the Near Infrared Camera and Spectrograph (NICS) of the *Telescopio Nazionale Galileo* (TNG), in La Palma Observatory on July 2012. Venus was observed just before dawn for periods of 2.5 hours on three consecutive nights. The nightside was observed with a continuum K filter centred at 2.28 microns, which is sensitive to opacity patterns made by clouds at approximately 48 km of altitude against the deeper and brighter atmosphere.

Since the K continuum observations feature an excessive contribution from the dayside of Venus, a correction in the form of a set of observations with a Bracket gamma (Br γ) filter were made, as cloud features on the lower cloud are not visible with this filter, and it is possible to subtract the Brγ image with the original K continuum to obtain the image illustrated in Fig. 4.4.2.

The main objective of this study is to use ground-based infrared observations to retrieve wind measurements and a cloud distribution map in the lower clouds of Venus, complementing spacecraft scientific observations. Full analysis and results from this research are presented in Machado et al. [2022].

4.4.3 CARMENES infrared observations of Jupiter and Saturn

The gas giants are overall harder to explore with space missions, in large part because of the long distances, and consequently longer travel times for the spacecraft to get there. Although Jupiter and Saturn have seen their fair share of dedicated missions, from Galileo to Cassini, relying only on data from onboard instruments leaves us with significant gaps in monitoring the dynamical regimes and evolution of the atmospheres of these planets. Continuous ground-based observations give us a way to tackle this problem and also gives a number of advantages when compared to sending spacecraft to the planet, namely the overall greater stability of Earth-bound telescopes.

The complex dynamical nature of the cloud cover of Jupiter has been amply observed and studied by both ground and space based instruments however, as proven in Chapter 3 many questions remain unanswered. Wind velocities have been determined on Jupiter's troposphere mainly through cloud-tracking with a precision that ranges between 5-15 m/s, using several correlation techniques [Hueso et al., 2017]. Although this technique has proven reliable, it provides only averaged winds over a time interval, which for the case of Jupiter often ranges between 9-10 hours due to its rapid rotation. Given the success in its application on Venus, our team has made recent efforts to expand the Doppler velocimetry method to other targets such as Jupiter as presented in this project and Mars.

Observations were made with the Calar Alto high Resolution search for M dwarfs with Exoearths with Near-infrared and optical Echelle Spectrographs (CARMENES) in May 2019 to perform high resolution spectroscopy, applying our Doppler velocimetry method to Jupiter. The novelty in this application is that we also used specific methane lines to retrieve zonal winds on several layers of the jovian atmosphere, targeting both the cloud tops and upper hazes.

Our observing strategy led us to retrieve spectra all over the disk in a similar manner as represented by Fig. 4.4.3. We are currently analysing the data from this observing run, as adaptation to wavelengths other than the visible part of the spectrum lends to new challenges for our pipeline.

4.4.4 2018 Martian Global Dust Storm

Dust storms on Mars occur with moderate frequency, ranging from small-sized whirlwinds to gigantic, global scale storms, capable of encircling the planet. One such storm was recently observed in 2018, one of the largest in recorded history. These storms can persist for several months, drastically affecting the atmosphere of Mars [Rajendran et al., 2021]. However, these events are rare and unpredictable and as such, are still poorly understood. Because of its tenuous atmosphere, measuring winds on Mars poses a real challenge for most methods used to study the dynamics of the atmosphere, namely the popular cloud-tracking method. But global dust storms provide a unique opportunity to apply our Doppler velocimetry method, where we measure the Doppler effect of solar Fraunhofer lines back-scattered on dust particles being carried by Martian winds.

Mars' atmosphere is much less dense than Earth or Venus' to the point that dust has a huge impact on its conditions and characteristics [Gierasch and Goody, 2020]. The increased dust load warms the atmosphere as a consequence of the greater optical depth of the

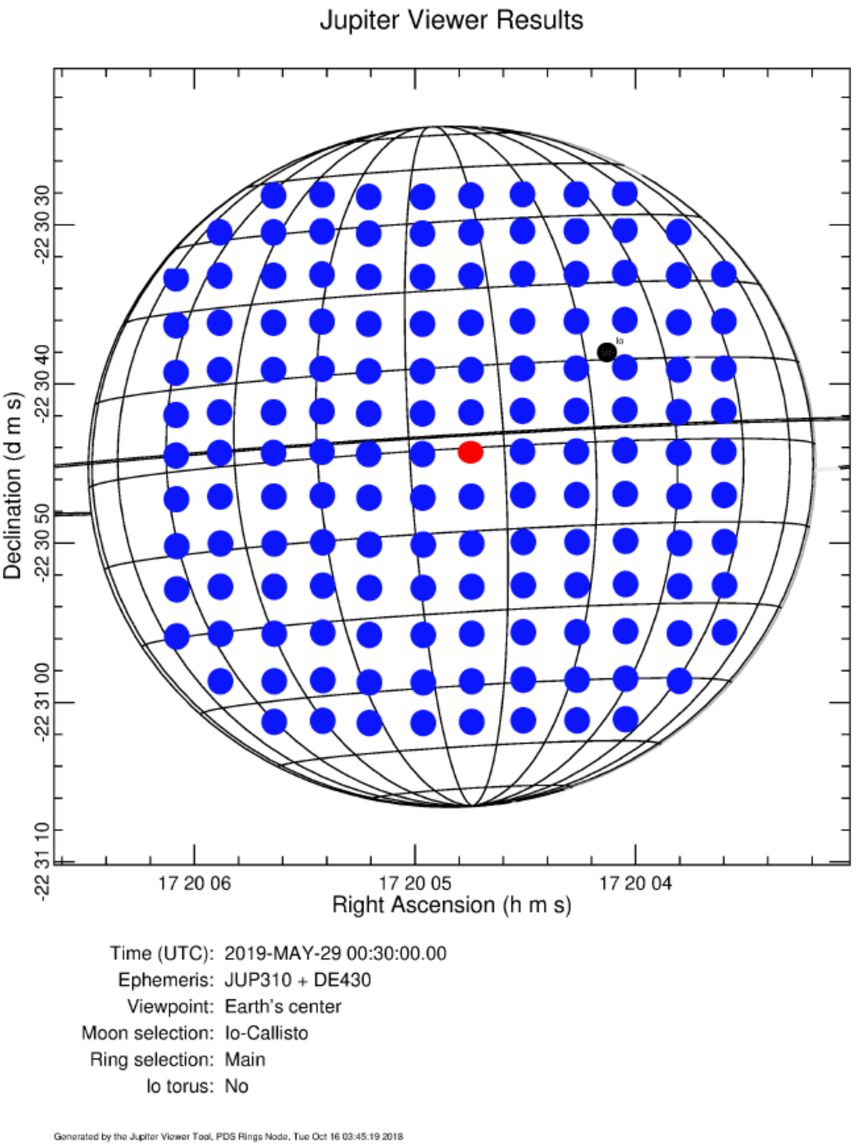

Figure 4.4.3: Observing strategy for the CARMENES observations conducted on May 29, 2019. The black dot is the satellite Io, the red dot is the reference point and the blue dots are the FOVs of the spectrograph on top of Jupiter disk with apropriate angular diameter at the time of observation.

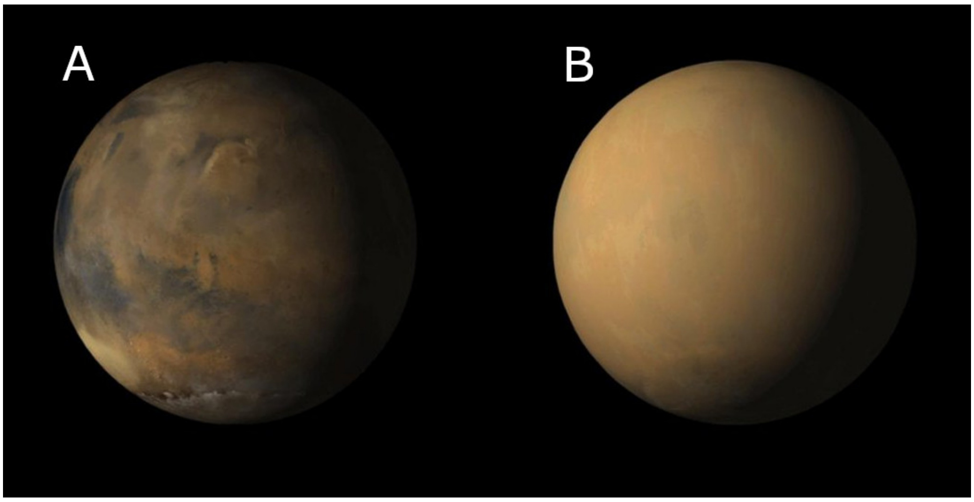

Figure 4.4.4: Side-by-side view of Mars in May (A) and July (B) of 2018, as seen from Mars Color Imager (MARCI) camera onboard NASA's Mars Reconnaissance Orbiter (MRO). Both views differ drastically due to a sudden global dust storm, encircling the planet and blocking the view of most surface features. Credits to NASA - https://www.jpl.nasa.gov/images/mars-before-and-after-dust-storm.

suspended particles. Airborne dust particles absorb and scatter radiation in the visible part of the spectrum which inevitably leads to temperature increase of the particles, which transfers to the surrounding environment through heat. Since concentrations of airborne dust on Mars do not tend to be homogeneous, the heating provoked by their presence, and interaction with sunlight, leads to pressure gradients which can power winds. In fact, the dusty season on Mars features a much more vigorous circulation, with the mass flux of circulatory patterns doubling for some cases [Haberle et al., 1993]. However, given that the Martian atmosphere has a low mass when compared with other terrestrial planets, the winds carry little momentum. But knowledge of these winds is vital to study the role of global dust storms on the energy budget of atmospheric circulation while they are in suspension. We made use of director discretionary time to perform observations with the Ultraviolet and Visual Echelle Spectrograph (UVES) at the VLT. The high resolution achieved by the instrument (R $\sim$ 100,000) allows the velocity of dust particles to be measured with our Doppler velocimetry method with an average error of approximately 5 m.s^{-1}. As with the Jupiter case presented in this work, the contribution from the rotation of Mars to the overall Doppler shift was significant, hence it required correction in much the same way as for our Jupiter Doppler retrievals. These observations also share their novelty with the ones made by ESPRESSO on Jupiter, being the first time that Doppler velocimetry based on spectroscopic observations at visible and ultraviolet wavelengths is used to study Mars' atmosphere.

Results on the winds on Mars with this technique contribute to a better understanding of these phenomena and of Mars' atmosphere in general, by measuring the wind velocity and its spatial variability through a latitudinal wind profile and a wind map of the storm as a function of latitude and local time. Should this method prove valid to retrieve winds on Mars, this can be a new tool to investigate the Martian atmosphere during dust storms. The details of this campaign and its results will be included in Machado et al. [in prep.].

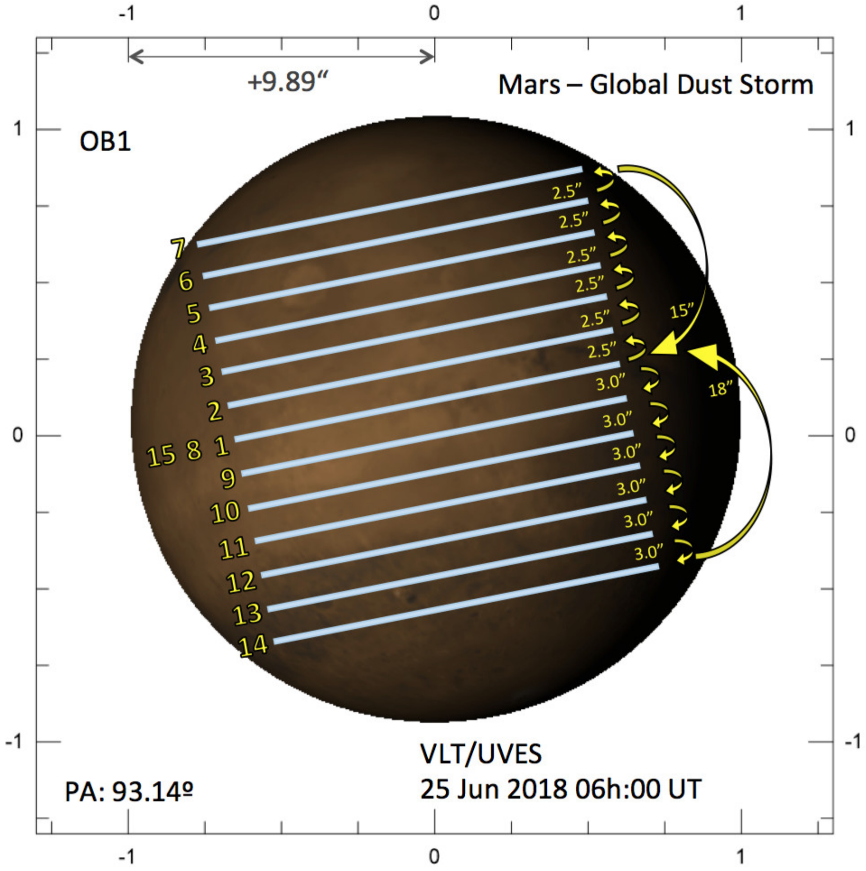

Figure 4.4.5: The diagram with the VLT/UVES slit positions on Mars' disk at the time of observation.

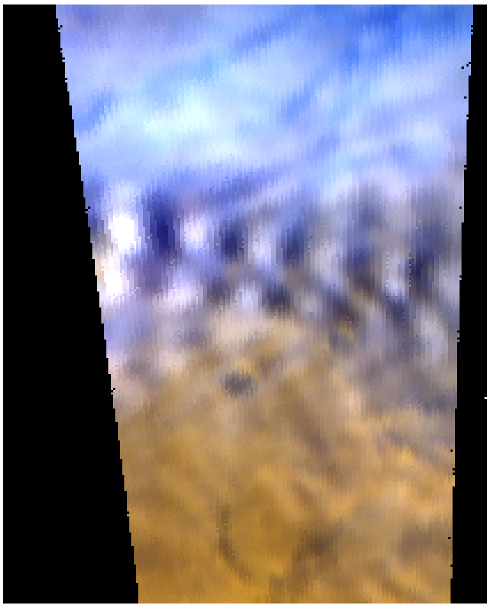

Figure 4.4.6: An atmospheric wave on Mars observed by the OMEGA instrument on board the Mars Express orbiter. This colour-enhanced image shows the contrast between the orange-brown surface of Mars with the white-blue faint clouds in its thin atmosphere. Credits to Francisco Brasil.

4.4.5 Atmospheric Waves on Mars with MEx/OMEGA

Given that atmospheric waves also manifest themselves on most Solar System planets with an atmosphere in equilibrium, in many cases such features and their roles in the atmospheric circulation of their host planets remain poorly understood. As demonstrated throughout this work, such an analysis is possible, which can provide an in depth view on the occurrence, characteristics and dynamics of waves. Moreover, much of these techniques are transferable to other planets. With extensive amounts of data from Mars Express' (MEx) Visible and Infrared Mineralogical Mapping Spectrometer (OMEGA) for atmospheric characterisation purposes, we began conducting observations to identify and characterise these waves manifesting on the thin Martian atmosphere.
Mars Express, one of the longest surviving missions in operation, the first European mission bound towards another planet, arrived on Mars on the 25th of December 2003. It included an orbiter which still revolves around the planet after more than 17 years on a highly elliptical (quasi-polar), with an apocentre at 10,530 km from the planet and a pericentre as close as 330 km, and the small lander Beagle 2 [Wilson, 2004]. The OMEGA instrument is a mapping spectrometer on board the Mars Express which consists of two co-aligned grating spectrometers: the visible and near infrared (VNIR), and the short wavelength infrared (SWIR) spectrometers. OMEGA produces cubes of images, dividing its spectral range into 352 spectral channels from 0.38 to 5.1 μm with 7 to 20 nm wide. The spatial resolution varies from ~300 m to 5 km per pixel depending on the spacecraft altitude at the time of acquisition. With seven extensions of the standard mission, OMEGA has acquired 14,512 spectral qubes along its 20,000 orbits. Since August 2010, with the subsequent failure of the C spectrometer, only the VIS and/or L spectrometer remain operational for observation. My collaborations on this endeavour lies mostly in previous knowledge of wave identification and characterisation, as well as familiarity with VIRTIS data, of which OMEGA is quite similar. So far, a few waves have been identified,

with an example in Fig. 4.4.6.

Chapter 5

Studying Atmosphere Dynamics of Solar System Planets

For obvious reasons, the first atmosphere that was and continues to be studied is our own on Earth. Something as common as weather forecasting is recognised as useful in our everyday lives however, a deep understanding of atmosphere dynamics that drive climate locally and globally is crucial to the survival of our species. This is especially in current times with the present threat of climate change, which challenge long established mechanisms of atmospheric circulation. However, ours is but one case in the Universe and within our Solar System many planetary scale objects are able to sustain atmospheres that endure different processes, and show wildly distinct characteristics and evolutionary paths. The dynamics of each atmosphere can reveal a plethora of information on the processes that drive its evolution, and looking beyond our own planet we have access to a laboratory of different environments, which can help us understand the behaviour of nature on Earth. Though science studies, in their simplest form, aim to understand the inner workings of the cosmos for their own sake, revealing the mechanisms behind Venus' atmospheric evolution for example, can hold the key to understand what it takes to evolve a planet with similar initial conditions as our own, to the world described in section 2.
A huge variety of tools are used to study atmospheres of solar system planets, from imaging to spectroscopy, chemical analysis, atmospheric modelling and more, all giving part of the answers to reveal the mysteries behind each system. Here, I focus on three different techniques employed throughout this doctoral program: Cloud Tracking, Atmospheric Wave Characterisation and Doppler Velocimetry. Each of these methods was used to study the dynamics of Venus and Jupiter.

5.1 Image Processing

A significant component of this PhD involved handling a large number of images from space based observations. As with any other observational study, raw data cannot provide the necessary information to produce useful science results and in our particular case, the processing of images used either for cloud tracking or atmospheric wave analysis was crucial to extract useful features for our research. Each type of image (either from VIRTIS-M/VEx or IR2/Akatsuki for example) required a different approach however, all of them start with proper navigation of the image. An image of a planetary atmosphere is, in its most basic form, a collection of pixels whose stored information builds the image at an appropriate wavelength depending on the instrument and filter that targets the planet used to retrieve the data that is made visible in the image. Without any reference system, it becomes impossible to tell where each atmospheric feature is located with respect to the planet's geography, especially on a target where the surface is permanently behind clouds (Venus), or there isn't any (Jupiter). Image navigation becomes the first crucial step by establishing a latitude and longitude coordinate to each pixel in the image, effectively mapping every observable point within the visible area of the planet. This is accomplished through the use of the Spacecraft Planet Instrument C-matrix Events (SPICE) toolkit, a collection of data from a multitude of observations, geometrical calculation of the spacecraft's movement and instrument attitude, and information on the target planet, which allows for the best navigation precision possible [Acton et al., 2017]. However, there are edge cases for which some fine-tuning is needed to get satisfactory results. One example is the case of images from the Akatsuki spacecraft, on which IR2's pointing was subject to uncertainties due to thermal distortion among other factors which required additional corrections [Ogohara et al., 2017, Satoh et al., 2017]. Even though an algorithm was developed for automatic fitting of the navigation grid by detecting planetary limb pixels [Ogohara et al., 2017], it would not perform adequately for some of the images used for this thesis, due to photometric issues of IR2 images as well as frequent darkening of the planetary limb [Peralta et al., 2018]. Thus, we used an interactive tool as described in [Peralta et al., 2018] which allows a manual adjustment of the grid using as a reference several locations near the limb of the planet. Through image navigation, computing distances between points on the atmosphere of a planet, for example the size of a storm system, becomes possible.

Our next task then is to enhance any useful features on the observable disk of the planet, either to search and characterise any kind of morphology such as waves, or to have sufficient tracers to retrieve the dynamics of that specific region. The processing routine differed between instruments and specific images required additional adjustments for the best possible result.

First, we would employ a *Minnaert* and *limb darkening* corrections to simulate an homogeneous illumination between different locations on the atmosphere, independently from their local time. Then we would adjust the brightness/contrast while sharpening the features present in the image through *unsharp masking* techniques and adaptive histogram equalization. Each processing step was interactively controlled for the best possible results, often times some of the steps being repeated, while also avoiding loosing information to *overprocessing*.

5.2 Cloud-Tracking

Though a powerful method to study the winds of planetary atmospheres at cloud level, cloud-tracking is in principle very simple. If you have two images at different times that show cloud features, provided the images are navigated, it is possible to record the displacement of such features between both images. Since we have knowledge of the time interval between the images and the distance by which the features were displaced, we can obtain a mean velocity of the clouds on that region at that particular time. Optimal time intervals between images will depend on the target since for this method to function properly, the same feature needs to be correctly identified on both images. With thousand of tracers across several latitudinal regions and within few days of observation, it is possible to build a global wind profile at cloud level. Combining this with multiple observing periods across months or years of data, along with observations of clouds at multiple wavelengths which can target different altitudes within a cloud layer, we can obtain a three-dimensional profile of the dynamics of the clouds on a planet, and possibly capture seasonal variations and trends. The tools used for cloud-tracking allow us to retrieve two components of wind velocity: a zonal wind with orientation parallel to the equator ($\mathbf{u}$) and a meridional wind with north-south orientation ($\mathbf{v}$). This technique is often performed with the aid of specialized software with either manual or automatic methods. Although automatization can potentially yield more wind tracers in less time, it is harder to control the quality of the wind tracers retrieved, which can lead to a less reliable wind profile. Thus, our methods rely on either supervised or completely manual procedures that evaluate tracers calculated by the tools we use.

5.2.1 Cloud-Tracking with PLIA - PICV

One of the software suites used by our group is the Planetary Laboratory for Image Analysis (PLIA) [Hueso et al., 2010], an integrated set of programs supported by Interactive Data Language (IDL) with a fully operational Graphic User Interface (GUI), developed at the University of the Basque Country in Bilbau. This tool was generously shared with our research group in Lisbon by the Bilbao research team as part of our collaboration in studying the atmospheres of Solar System planets. It runs on any operating system supported by IDL, although it has only been tested thoroughly on Windows XP, and was already extensively used to analyse images retrieved by the Galileo Solid Stage Imaging (SSI) instrument [Belton et al., 1992] of Jupiter and Venus, Cassini Image Science Subsystem (ISS) [Porco et al., 2004] of Jupiter and Saturn, and hyperspectral cube images obtained by VIRTIS-M [Drossart et al., 2007] onboard Venus Express.
The main focus of this software is the study of atmosphere dynamics by processing astronomical images. This includes, to some extent, planetary navigation and a number of image correction and processing tools as described above, some dedicated to certain instruments like VIRTIS/VEx, photometric scans, and is also able to compute geometric projections of images into polar or cylindrical maps, which are necessary for cloud-tracking. More details on this tool can be found in Hueso et al. [2010].

One such software is an auxiliary tool within PLIA's repertoire, the Planetary Image Correlation Velocimetry (PICV) program. As the name implies, this tool uses image correlation to identify similar cloud patterns between two images within a known time interval to perform cloud tracking. An example of the software interface at startup after loading an image pair is illustrated in Fig. 5.2.1. The images must be navigated and encoded in a way that the program can read the time interval between both images, which can range typically from 0.5 to 2 hours for Venus to 9 or more hours for Jupiter (approximately a full rotation period) as its fast rotation makes the selection of two images showing the same

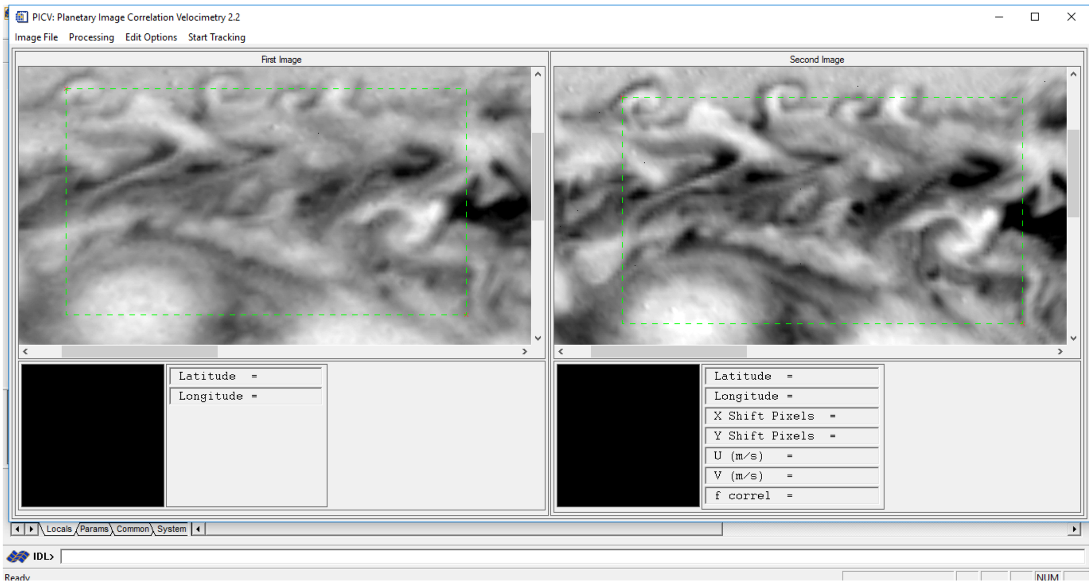

Figure 5.2.1: The interface of PICV after loading an image pair. A light green outline is also visible which is the area box selected in which cloud tracking will be performed. The images selected are close-ups of Jupiter's atmosphere by Cassini ISS during its flyby in 2000.

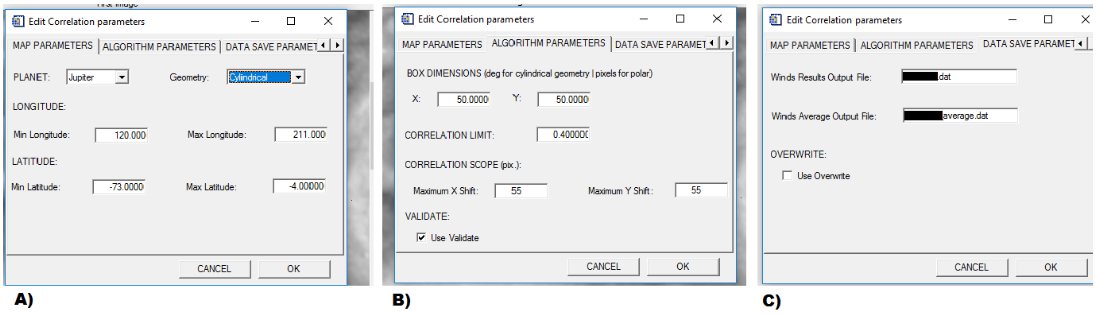

PLANET: Jupiter
Geometry: Cylindrical
LONGITUDE:
Min Longitude: 120.000
Max Longitude: 211.000
LATITUDE:
Min Latitude: -73.0000
Max Latitude: -4.00000

BOX DIMENSIONS (deg for cylindrical geometry | pixels for polar)
X: 50.0000
Y: 50.0000
CORRELATION LIMIT: 0.400000
CORRELATION SCOPE (pix.):
Maximum X Shift: 55
Maximum Y Shift: 55
VALIDATE:
☑ Use Validate

Winds Results Output File: [redacted].dat
Winds Average Output File: [redacted]average.dat
OVERWRITE:
☐ Use Overwrite

Figure 5.2.2: Showcase of PICV correlation options before performing cloud-tracking. Each parameter is adjusted before every run for the best possible results. Panel A is where the user provides data on the geometry of both images; panel B allows a fine-tuning of the parameters of the algorithm whose best values will depend on the location where the correlation box was selected and cloud features present there; panel C manages data export where two files will be generated as a result of cloud-tracking, one with every wind vector and another with the statistical average along the same latitude.

cloud features challenging. Since PICV relies on image correlation, both images within the selected pair must be processed in a way that the system can adequately identify different atmospheric patterns in the clouds, to allow the image correlation algorithm to associate the features appropriately. This software measures the pixel displacement of the correlated features between both images. To correctly calculate the wind vectors, mapped boundaries of the images must be provided, along with the desired algorithm parameters that will be used for cloud-tracking (see Fig.5.2.2). PICV uses this information to then calculate the zonal and meridional components of the winds and draw wind vectors in the second image.

The area box (green outline in Fig. 5.2.1) will be filled with correlation boxes with a customisable size that should be appropriate for the cloud features present in the area selected during cloud tracking, until all available space in the area is occupied. For PICV to produce reliable values, we must provide the cartographic limitation of the image (latitude and longitude range of the image) and if the images are projected in a cylindrical

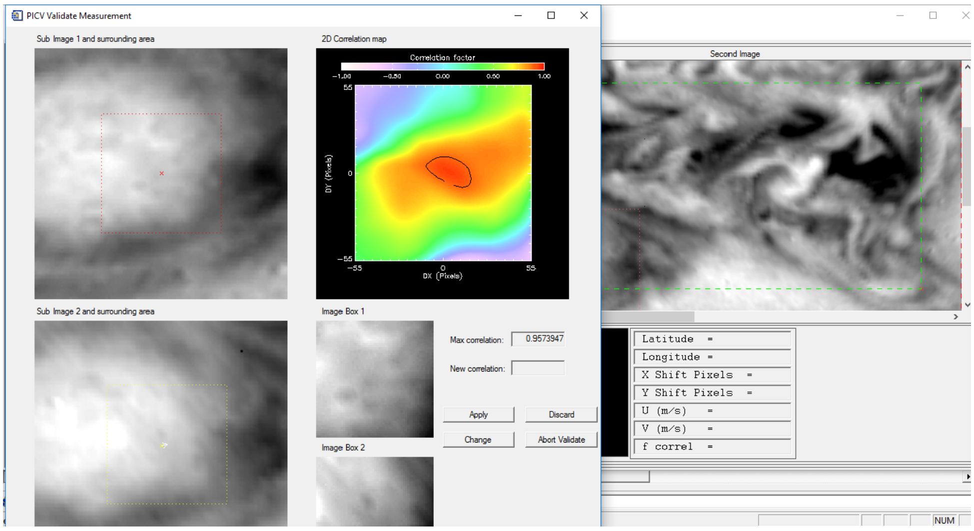

Max correlation: 0.9573947
New correlation:

Latitude =
Longitude =
X Shift Pixels =
Y Shift Pixels =
U (m/s) =
V (m/s) =
f correl =

Figure 5.2.3: PICV interface during cloud-tracking. Each wind vector calculated by the program can be validated by the user based on the quality of the correlation between perceived cloud formations (through close-ups of the image box and the highest correlation value found.

or a polar perspective as this changes how the software's algorithm works. As the study area is filled with correlation boxes we must be sure that their sizes are suitable for the shapes present in the images. For example, if the cloud features in the selected area have mostly elongated shapes, we ought to establish horizontally stretched boxes to completely capture such cloud features. Also, depending on the typical wind velocity of the target we can select the correlation scope for cloud tracking by applying limits to the horizontal and vertical displacement that is recognized as cloud movement (see panel B in Fig. 5.2.2). Note that the values inserted have different meanings depending on the geometry chosen, where we selected the size of the boxes in degrees if we are taking the cylindrical projection, and in pixels if we are dealing with images with polar projections. The results are then stored in data files, one of which presents a latitudinal average of the wind vectors retrieved.

After selecting all parameters, we would employ a supervised run which allowed us validation of every wind vector that is measured by PICV. Through the interface shown in Fig. 5.2.3, which shows the relative correlation boxes on each image and their surrounding areas, we can evaluate which cloud features are being compared by the algorithm and where. Along with a cropped section of the images, there is also a colour map showing how the correlation values vary within the images. A good wind measurement is obtained when this correlation map shows a sharply localized zone where the correlation values are high (at least 0.7 depending on the images' quality). With this information on the wind vector suggested by the program, we can accept the wind vector measurement or decline depending on the parameters above. Either way, the process may continue with our supervision in every measurement, or we can hand the controls to the automatic algorithm within PICV, validating measurements based on our previous supervision and parameters selected before cloud tracking (see Fig.5.2.2).

As cloud tracking in the selected area is finished, the GUI can look similar to Fig. 5.2.4. The wind results are stored in the appointed data files and it is possible to perform cloud tracking again in the same image pair, focusing on different zones to cover other features in more locations, or on the same area with different parameters selected for cloud tracking.

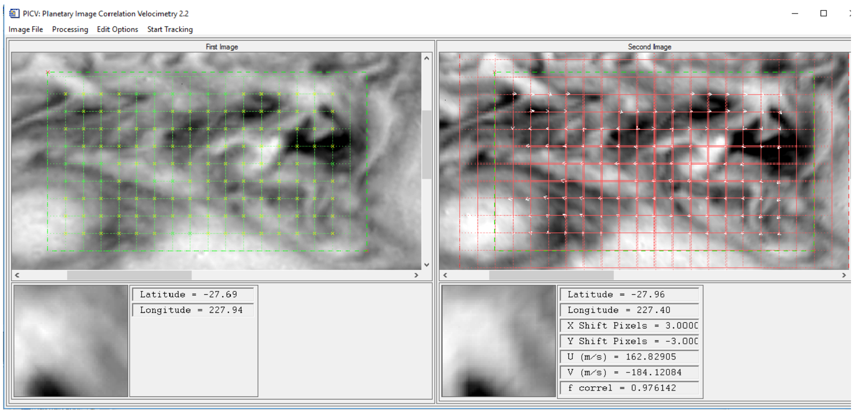

```
Latitude = -27.69
Longitude = 227.94
```

```
Latitude = -27.96
Longitude = 227.40
X Shift Pixels = 3.0000
Y Shift Pixels = -3.000
U (m/s) = 162.82905
V (m/s) = -184.12084
f correl = 0.976142
```

Figure 5.2.4: PICV when one cloud-tracking routine is complete. The small white arrows in the red grid on the right panel represent the calculated wind vectors.

5.2.2 Cloud-Tracking with ACT

Also using IDL, we performed cloud-tracking with a different set of tools provided by Dr. Javier Peralta, jointly called *Automatic Cloud Tracker*. Originally tailored to work with images from the Akatsuki space mission, it has been adapted to also interpret VIRTIS-M images, and provides more control over the processing routine than PLIA. This comes with the limitation that ACT is currently suited to work on Venus only, though it might be possible to expand its use to other targets in the future depending on the type of data used.

In line with PLIA, image navigation is performed before we use the program for processing and cloud tracking. After correcting the navigation through limb fitting and adequately process the images with the routine described above, images are usually geometrically projected onto cylindrical geometry with the best resolution possible, similar to the original images. ACT offers three methods by which cloud-tracking can be performed: a *manual method*, a *supervised method* and a fully *automatic method*.

The main aspect of this program is its application of phase correlation between two images that are displaced by a known time interval, reliant on a frequency-domain representation of the images calculated with a Fast Fourier Transform that enables the deduction of the displacement from the location of a peak in a *cross-correlogram* [Peralta et al., 2018].

The automatic tool is based on this correlation method and uses a relaxation labelling technique to better identify peaks in the *correlogram*. As explained in Horinouchi et al. [2017a], the displacement vectors proposed by the program when template matching are associated with local peaks on the Cross-Correlation Surface (CCS), and their selection is based on the evaluation of the proximity of the vectors over neighbouring grid points in the CCS to the local peaks of correlation. For the reasons stated at the beginning of Sec. 5.2, we did not employ automatic cloud-tracking for the purpose of our studies.

The supervised technique functions in a similar manner to PICV in the sense that wind vectors are suggested by the program and the user has control over which measurements are accepted. However, instead of selecting a large correlation box between both images and adjusting algorithm parameters beforehand, the user can select any desired location on the first image, after which the program will attempt to recognize the same feature after displacement on the second image based on the computed *cross-correlogram*. For every measurement a window like Fig. 5.2.5 appears so that the user can validate the

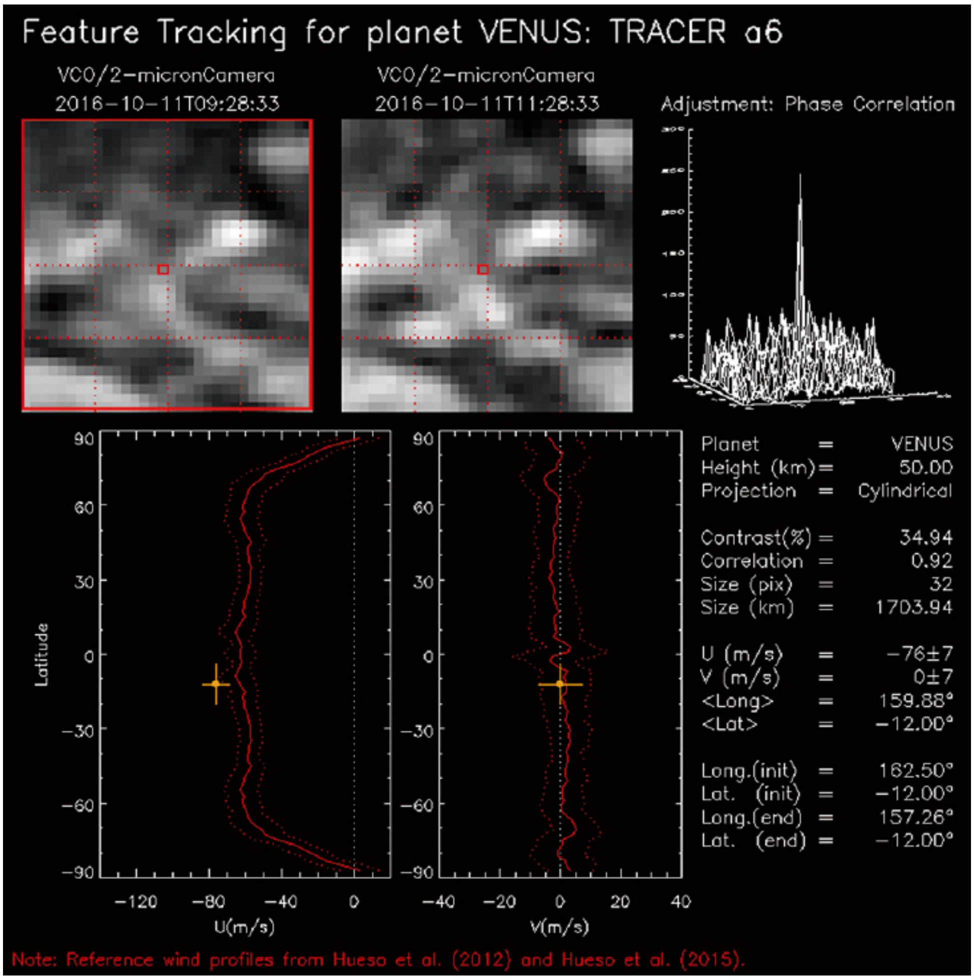

Planet = VENUS
Height (km) = 50.00
Projection = Cylindrical

Contrast(%) = 34.94
Correlation = 0.92
Size (pix) = 32
Size (km) = 1703.94

U (m/s) = −76±7
V (m/s) = 0±7
<Long> = 159.88°
<Lat> = −12.00°

Long.(init) = 162.50°
Lat. (init) = −12.00°
Long.(end) = 157.26°
Lat. (end) = −12.00°

Figure 5.2.5: Example of the validation window during cloud-tracking with ACT. It is visible here the positive identification of a cloud tracer in a pair of IR2 images using phase correlation, with two panels on the top-left showing the cloud identified on both images and the cross-correlogram on the right with a single clear peak, indicating a successful match. The proposed wind speed of the tracer can be readily compared with a reference wind profile, in this case from VEx/VIRTIS-M [Hueso et al., 2012] in the two plots below along with detailed information on the tracer. Image from Peralta et al. [2018].

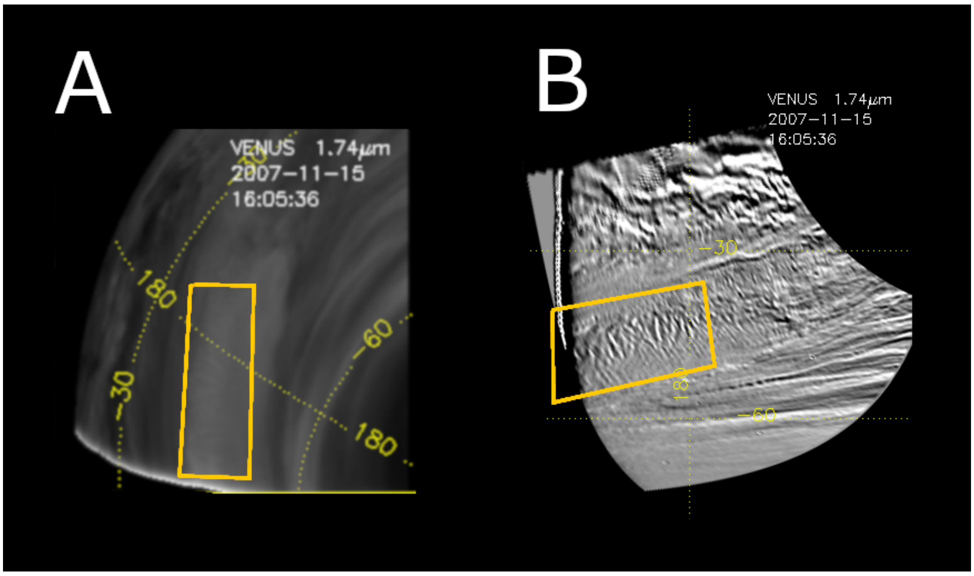

Figure 5.3.1: Example of a navigated VIRTIS-M-IR image from Venus Express archive (A) and after image processing and application of a cylindrical projection (B). From Silva et al. [2021]. The wave packet present in this image is highlighted with a yellow frame.

wind tracer or not, based on the presence of a clear peak in the correlogram, the similarity between clouds on both images, and how the wind speed compares with reference wind profiles such as those reported in Hueso et al. [2012] and Hueso et al. [2015].
The technique we used in our work, despite taking advantage of the template in Fig.5.2.5 was completely manual, as we had to select a cloud feature on the first image and carefully look for the same shifted feature on the second in order to produce reliable tracers. We used the validation template for comparison with the reference wind profiles, and then repeated the process for as many tracers as possible for each image pair.

5.3 Atmospheric Wave Characterisation

Atmospheric waves are visible on images of most planets as quasi-periodical sequences of bright crests and darker troughs, usually limited by other atmospheric structures or environmental conditions, forming a wave packet. Our goal was not only to detect the presence of waves on a planetary atmosphere (Venus in this case), but to also characterise them in terms of their morphology, basic parameters such as wavelength, size and orientation, and study the waves' dynamics, including how they travelled within the atmosphere and evolved. We focused our analysis on mesoscale gravity waves, which are waves with spatial scales between tens to hundreds of km however, our methods could also be used to study other types of waves like those described in Fukuhara et al. [2017].

Using a similar image processing routine than the one used for cloud-tracking as described in Sec.5.1 we would systematically search for these periodic features at several wavelengths from our available data. Though the degree of image processing might differ between instruments, the method to identify waves is almost always identical. With the cloud features present in the enhanced image, we look for at least three consecutive light and dark stripes that signal the presence of a wave, searching each image individually 'by eye'. Although a time consuming task, a manual search remains the most reliable way to detect these structures, given their wide range of shapes, sizes, and orientations. Each positive detection was confirmed after checking the presence of the wave packets on images taken with different filters sensing the same altitude region (performed with VIRTIS-M data), eliminating spurious detections from image defects. Confirmation through the identification of identical wave packets between images of the same area on the disc of Venus at short time intervals (1–2 h) was also performed where possible. In Fig. 5.3.1 we show an example of a VIRTIS-M image with a wave before and after the processing routine.

5.3.1 Morphological Characterisation

After the manual search, each detected packet is analysed for its morphological properties and position on Venus' atmosphere. Properties such as horizontal wavelength, packet width and length are extracted by calculating the distance between an origin and destination target points in the wave packet using the expression:

$$Dist = \frac{\pi\sqrt{(\lambda_2-\lambda_1)^2 cos^2\left(\bar{\phi}\frac{\pi}{180}\right)+(\phi_2-\phi_1)^2}}{180}(a+h) \tag{5.1}$$

This calculation is applied between two pixels on top of the visible disk of the atmosphere on a navigated image. The values of λ_1, λ_2 and ϕ_1, ϕ_2 are the longitudinal and latitudinal coordinates of the origin and destination points, $\bar{\phi}$ is the average latitude between measured points, a is the planet radius and h is the altitude of the observed cloud layer. Each of these measurements was repeated several times, particularly horizontal wavelength retrievals, which were taken between each visible crest to assess possible wavelength variability within the packet. The orientation of the packet is the angle between the general axis perpendicular to the wave front alignment and the local parallel at the origin point. Angles in this calculation are in degrees.

$$\theta = arctan\left(\frac{\Delta\phi}{\Delta\lambda}\right) \tag{5.2}$$

Since all that is required to characterise wave packets is a navigated image, both tools described earlier (PLIA and ACT) can be used to compute this data. Through PLIA we could target individual pixels with ease, choosing the points of origin for the distance measurement between the navigated pixels in the planetary image. However, to guarantee an accurate retrieval of morphological properties we marked several points on the vicinity in each observable crest and made sure that from one crest to the other, perpendicularity between oscillations was maintained. Then all marked points in the same crest within a 5-pixel square area are averaged to eliminate possible outliers. Horizontal wavelength, packet length and width are retrieved from the average values of marked points on each end. This process is repeated for several locations (depending on the size and morphology of the wave) within the wave packet, to examine the consistency of measurements. Some of these waves were either very close to the boundaries of the image or partially missed by the instrument's Field-Of-View (FOV), so packet length and width measurements were not possible for all detected waves thus, when retrieved, these were often minimum values for those properties.

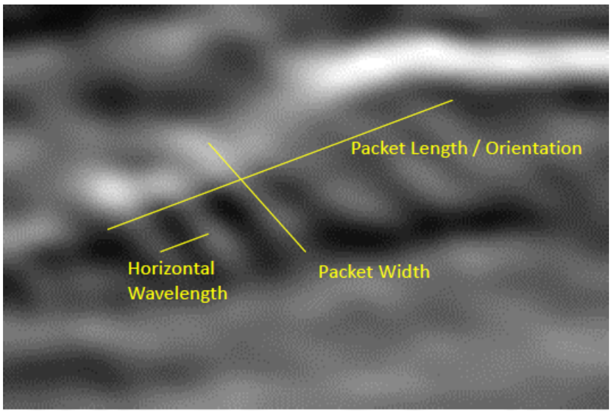

Figure 5.3.2: Schematic of the characterisation of morphological properties of waves. Yellow lines show how property is retrieved for an example wave packet.

A more sophisticated semi-automatic method from ACT allows the simultaneous retrieval of several morphological and geographical properties of detected waves, which speeds up characterisation. The distance between two chosen points on the planet's surface is calculated within the program, which streamlines the characterisation routine by giving the user a faster read on the property being measured, as well as the position and error associated with the measurement, given by the spatial resolution at that point. By performing this several times between each crest, on two ends of one crest perpendicular to the orientation, and the points that range between the first and last crest of the wave train, horizontal wavelength, packet width, length and orientation are calculated faster than with PLIA. A schematic of morphological characterisation performed in ACT can be seen on Fig.5.3.2. Since this program gives more control over processing techniques and each measurement, we can adapt more easily to challenges that might rise from the processing of some images or other issues, which ultimately improves the quality of the data extracted.

Although wave amplitude would be extremely useful to infer the energy transported by the waves, its estimation is often difficult. For waves in the lower clouds of Venus, atmospheric parameters such as density and pressure obtained through nadir observations at this altitude are subject to large uncertainties [Silva et al., 2021]. However, other parameters could potentially be used indirectly to give clues on wave amplitude. One of these could be the evaluation of the perturbation provoked by waves on the optical thickness of the clouds. The degree of this perturbation can then used as a 'proxy' for normalised wave amplitude [Tselioudis et al., 1992]. To study the effect of waves on the optical depth of the nightside lower clouds, we used only images from VIRTIS/VEx, as images from the IR2 camera present a light contamination problem [Satoh et al., 2017]. The optical depth was calculated at a wavelength of 1.74 μm using the expression:

$$\tau = log\left(\frac{I^{max}_{1.74\mu m}}{I_{1.74\mu m}}\right) \tag{5.3}$$

Where $I^{max}_{1.74\mu m}$ and $I_{1.74\mu m}$ are the maximum value of radiance and the radiance at every pixel in VIRTIS images, respectively [Peralta et al., 2020]. Optical depth values were extracted on both crests and troughs of waves, taking the highest and lowest possible value respectively. From several retrievals, the optical thickness drop ratio between crests and troughs could be calculated. Even though we would take a mean result of the drop ratio between consecutive crest/trough sequences to have one value of the optical thickness drop for each wave-packet, we also registered the highest drop ratio measured. Besides the before mentioned light contamination problem, this method is subject to lingering artefacts that survived the image processing and correction routine, as well as non-negligible variations of radiance close to the dayside terminator, which limits the number of cases where the optical thickness drop can be retrieved with good quality results.

5.3.2 Atmospheric wave dynamics

The detection of the same wave packet across several images provided an opportunity to study the movement of this feature on its planetary atmosphere in a way akin to the cloud tracking technique. However, this pursuit had its own challenges presented by observational constraints, specially with VIRTIS data since we found that it generally was not possible to observe the same region of the disc continuously for more than 6 hours within the same orbit of VEx. In spite of this limitation, we used the detected waves eligible for dynamical characterisation to retrieve their phase velocity, a limited trajectory during propagation, and their dynamical relation with the background wind flow.

Because of Akatsuki's longer equatorial orbit around Venus, this task was better accomplished for waves detected with IR2 images since we were able to monitor larger areas over longer periods of time than with VIRTIS. This in turn allowed more wave packets to be followed, some for extended periods of time compared to VIRTIS observations and, on some occasions before they became apparent or after they vanished in the images, possibly witnessing wave generation and/or dispersion.

To track the displacements of each crest from a wave packet between two images separated by a known time interval, the procedure was similar to what is described in Peralta et al. [2018], taking several wind tracers on recognizable features of each wave packet. We also retrieved the local background wind at similar latitudes using methods identical to cloud tracking, also applied in Goncalves et al. [2020], though now in the lower cloud. Background wind retrieval served to evaluate the intrinsic phase velocity of these waves and how they compare with the general atmospheric circulation.

Phase velocities of wave packets and background wind velocity were measured individually using wind tracers and the following equation:

$$U = \frac{cos(\bar{\phi}) a \frac{\pi}{180} \Delta\lambda}{\Delta t} \tag{5.4}$$

where U is the zonal velocity of the tracked tracer (wave crest for phase velocity or any cloud feature for the background wind), $\bar{\phi}$ is the latitude average as in equation 5.1, $\Delta\lambda$ is the zonal displacement of the tracked feature between images A and B, and Δt is the time between the considered images. Wave phase speed is measured by tracking individual recognizable structures that belong to the wave packet (mostly wave crests) between one or more pairs of images, depending on the lifetime and visibility of the packet. In addition to the above-mentioned constraints on the dynamical characterisation of waves, wave dispersion also plays a role in their visual classification and characteristics, as a single wave packet can break into two or more separate ones.

5.3.3 Estimation of additional wave parameters

The waves detected by our study show many similarities with other features that were interpreted in the past as atmospheric gravity waves such as in Peralta et al. [2008] and Piccialli et al. [2014]. Assuming that our atmospheric waves are of the same type, it is possible to extract additional characteristics by employing analytical models, which aid in their interpretation. To this end, we made use of temperature profiles obtained from radio-occultation data from the Ultra-Stable Oscillator (USO) [Imamura et al., 2011], onboard the Akatsuki space mission, to infer the Brunt Väisälä frequency. This atmospheric quantity is essential to estimate the vertical wavelength of atmospheric gravity waves, among other properties.

For mesoscale waves of this kind, we can use linear theory to describe wave phenomena, where the amplitude of the disturbance is small when compared to the mean state of the atmosphere. This consideration makes it possible to apply the perturbations method, where the disturbances are small enough to neglect cross terms in the equations of the general motion of the atmosphere [Peralta et al., 2014a]. With this approximation, all field variables are divided into two parts: a reference state and a perturbation state as a local deviation from the basic state [Sanchez-Lavega, 2011]. We can then consider Venus' atmosphere to be in a cyclostrophic regime, where the equatorward component of the centrifugal force of the zonal wind is balanced by a meridional pressure gradient [Piccialli, 2010]. Further including an approximation of the atmosphere to an ideal gas with adiabatic atmospheric motions where friction is negligible, we can have a system of equations that describe atmospheric motions [Peralta et al., 2014a]:

$$\frac{\partial u}{\partial t} + u\frac{\partial u}{\partial x} + v\frac{\partial u}{\partial y} + w\frac{\partial u}{\partial h} = -\frac{1}{\rho}\frac{\partial P}{\partial x} + \frac{uv}{a}tan\phi \tag{5.5a}$$

$$\frac{\partial v}{\partial t} + u\frac{\partial v}{\partial x} + v\frac{\partial v}{\partial y} + w\frac{\partial v}{\partial h} = -\frac{1}{\rho}\frac{\partial P}{\partial y} - \frac{u^2}{a}tan\phi \tag{5.5b}$$

$$\frac{\partial w}{\partial t} + u\frac{\partial w}{\partial x} + v\frac{\partial w}{\partial y} + w\frac{\partial w}{\partial h} = -\frac{1}{\rho}\frac{\partial P}{\partial h} - g \tag{5.5c}$$

$$\frac{\partial \rho}{\partial t} + u\frac{\partial \rho}{\partial x} + v\frac{\partial \rho}{\partial y} + w\frac{\partial \rho}{\partial h} = -\rho\left(\frac{\partial u}{\partial x} + \frac{\partial v}{\partial y} + \frac{\partial w}{\partial h}\right) \tag{5.5d}$$

$$\frac{\partial \Theta}{\partial t} + u\frac{\partial \Theta}{\partial x} + v\frac{\partial \Theta}{\partial y} + w\frac{\partial \Theta}{\partial h} = 0 \tag{5.5e}$$

$$P = \rho RT \tag{5.5f}$$

where equations (5.5a)-(5.5c) are the momentum equations, (5.5d) is the continuity equation, (5.5e) is the thermodynamic equation and (5.5f) is the equation of ideal gases. In these equations, (u, v, w) are the zonal, meridional and vertical components of the wind; P is the atmospheric pressure; ρ is the density of the medium; g is the gravity acceleration; ϕ is the latitude; h is the altitude above the planet's surface; a is the planetary radius; and Θ=lnθ, with θ being the potential temperature.

Introducing perturbations in the X-Z plane into equations (5.5), discarding terms from the product of perturbations and defining a centrifugal frequency Ψ=(u_0/a)tan(ϕ) we have:

$$\frac{\partial u'}{\partial t} + u_0\frac{\partial u'}{\partial x} + \frac{\partial}{\partial x}\left(\frac{P'}{\rho_0}\right) - \Psi.v' + \frac{\partial u_0}{\partial y}v' = 0 \tag{5.6a}$$

$$\frac{\partial v'}{\partial t} + u_0\frac{\partial v'}{\partial x} + 2\Psi.u' = 0 \tag{5.6b}$$

$$\frac{\partial w'}{\partial t} + u_0\frac{\partial w'}{\partial x} + \frac{1}{\rho_0}\frac{\partial P'}{\partial z} + \frac{\rho'}{\rho_0}g = 0 \tag{5.6c}$$

$$\frac{\partial \rho'}{\partial t} + u_0\frac{\partial \rho'}{\partial x} + w'\frac{\partial \rho_0}{\partial z} = -\rho_0\left(\frac{\partial u'}{\partial x} + \frac{\partial w'}{\partial z}\right) \tag{5.6d}$$

$$\frac{\partial \Theta'}{\partial t} + u_0\frac{\partial \Theta'}{\partial x} + w'\frac{\partial \Theta_0}{\partial z} = 0 \tag{5.6e}$$

$$\frac{P'}{P_0} = \frac{\rho'}{\rho_0} + \frac{T'}{T_0} \tag{5.6f}$$

where each variable with a subscript or superscript such as X_0 and X' corresponds to its respective reference state and perturbation. Note that one of terms in the momentum equation 5.6b has been cancelled out by the gravitational force, when the coordinate system is rotated around the X-axis so that the Z-axis lies along the vector sum of g and Ψ [Peralta et al., 2014a]. Then, assuming that the perturbations due to waves are oscillatory, with the form $u'(x,z,t) = \hat{u}(z).exp[i.(kx - \omega t)]$, where the periodic behaviour in the vertical direction is contained in $\hat{u}(z)$, with ω as the frequency and defining $\hat{\omega} = \omega - ku_0$ as the intrinsic frequency, we obtain a set of equations for the amplitude of the disturbances: $\hat{u}(z), \hat{v}(z), \hat{w}(z), \hat{P}(z), \hat{\rho}(z)$, and $\hat{\Theta}(z)$:

$$-i\hat{\omega}.\hat{u} + \left(\frac{\partial u_0}{\partial y} - \Psi\right).\hat{v} + ik.\frac{\hat{P}}{\rho_0} = 0 \tag{5.7a}$$

$$-i\hat{\omega}.\hat{v} + 2\Psi - \hat{u} = 0 \tag{5.7b}$$

$$-n_4.i\hat{\omega}.\hat{w} + \frac{d}{dz}\left(\frac{\hat{P}}{\rho_0}\right) - n_3.B\frac{\hat{P}}{\rho_0} - g.\Theta = 0 \tag{5.7c}$$

$$-n_2.i\hat{\omega}.\frac{\hat{\rho}}{\rho_0} + ik.\hat{u} + \frac{d\hat{w}}{dz} - n_1.\frac{\hat{w}}{H_0} = 0 \tag{5.7d}$$

$$-i.\hat{\omega}.\hat{\Theta} + B.\hat{w} = 0 \tag{5.7e}$$

where $1/H_0 = -\partial ln(\rho_0)/\partial z$, $B = \partial ln(\theta)/\partial z = \partial\Theta/\partial z$ is the atmospheric static stability [Holton, 2004]. Additionally, the values (n_1, n_2, n_3, n_4) are parameters to apply approximations for the atmosphere under various conditions, such as n_1, n_2, and n_3 representing terms related to an incompressible atmosphere while n_4 is related to the hydrostatic approximation. Using the procedure explained in detail in [Peralta et al., 2014a], in which the equations in (5.7) are combined and solved, we can arrive at a generic dispersion relation for multiple kinds of atmospheric waves:

$$m^2 = n_3 B.\left(\frac{n_1}{H_0} - n_2 B\right) + (n_4\hat{\omega}^2 - gB).\left(\frac{n_2}{c_S^2} - \frac{k^2}{\hat{\omega}^2 - \xi^2}\right) - \frac{1}{4}\left[B(n_2 - n_3) - \frac{n_1}{H_0}\right]^2 \tag{5.8}$$

where c_S^2 is the speed of sound and $\xi^2 = 2\Psi(\Psi - \partial u_0/\partial y)$ represents the centrifugal frequency when it is modified by the meridional shear of the background zonal wind. For the case of gravity waves, following on Peralta et al. [2014a] extensive analysis, all tracer parameters (n_1, n_2, n_3, n_4) are set to 1 and applying appropriate approximations based on the planet studied, in this case Venus, and trading the frequency for the phase velocity $c_p^x = \omega/k$ we reach the dispersion relation for gravity waves used in our study [Silva et al., 2021]:

$$(c_p^x - \bar{u})^2 = \frac{N^2.k^2 + \xi^2.(m^2 + \frac{1}{4H_0^2})}{k^2 + m^2 + \frac{1}{4H_0^2}} \tag{5.9}$$

where c_p^x is the zonal component of the phase velocity, ū is the average zonal wind, N is the Brunt Väisälä frequency, and k and m are the horizontal and vertical wave numbers with the form:

$$k = \frac{2\pi}{\lambda_x} \tag{5.10a}$$

$$m = \frac{2\pi}{\lambda_z} \tag{5.10b}$$

with λ_x and λ_z being the horizontal and vertical wavelengths. We are not including the meridional component of the phase velocity of waves in this discussion because the best spatial resolution achieved on these images is of the same order of magnitude as the error in meridional wind flow in the lower cloud, as already discussed by Hueso et al. [2012]. Using the aforementioned results from the radio occultation experiment with Akatsuki and published by Ando et al. [2020], we can compute the Brunt Väisälä frequency from the static stability profiles of the lower cloud during the period of observation:

$$N = \sqrt{\frac{g\ .\ B}{T}} \tag{5.11}$$

Since the static stability and consequently the Brunt Väisälä frequency can both vary with altitude and latitude, values of N were calculated for different altitude levels within the expected vertical region of the lower cloud. The Brunt Väisälä frequency, is used along with the retrieved horizontal wavelengths and phase velocities to compute the vertical wavelength of the characterised packets. Inserting expression (5.10b) in equation (5.9) and solving for the vertical wavelength yields:

$$\lambda_z = \frac{2\pi\sqrt{\hat{c_p^x}^2 - \frac{\xi^2}{k^2}}}{\sqrt{N^2 - \hat{c_p^x}^2.k^2 + \frac{1}{4H_0^2}\left(\frac{\xi^2}{k^2} + \hat{c_p^x}^2\right)}} \tag{5.12}$$

where $\hat{c_p^x}$ is the intrinsic zonal component of the phase speed resulting from c_p^x - ū. We calculated the value of λ_z for each wave packet at the altitudes within the lower cloud range, using the previously obtained values of the static stability from radio occultation data.

The calculations briefly discussed above, assume that the vertical wind shear can be neglected, as it does not significantly influence wave propagation and that the static stability is constant with altitude. It has been proposed by Iga and Matsuda [2005] that if the intrinsic phase velocity is higher than the change in zonal wind in a vertical wavelength, the vertical wind shear that would affect these calculations can be discarded.

We also understand that the static stability also changes with altitude, even within the lower cloud layer which would necessarily change these equations. Though we account for variations of the static stability with altitude when calculating λ_z, we shall expand on this issue further in Section 6.2.4.

5.4 Doppler Velocimetry

This method, which uses spectroscopic data to retrieve wind velocity measurements from planetary atmospheres, employs a completely different set of skills than described in previous sections. Contrary to the cloud-tracking technique, where we gather averaged winds over a set time interval (determined by the temporal distance between the two images in the pair) for large cloud structures, the Doppler velocimetry method provides instantaneous wind velocity measurements. The method developed within our team in particular, uses Fraunhofer lines (characteristic absorption lines from gas in the Sun's photosphere when interacting with continuum radiation emitted from warmer and deeper layers of our host star) in the visible part of the spectrum, scattered by cloud particles of the target atmosphere (in our case Jupiter). The spectral information we receive with ground observations, is the result of sunlight being absorbed by the particles in upper layers of the cloud level of a planetary atmosphere, and then re-emitted in Earth's direction. For this reason, we use a single backscatter approximation as the gas particles in this region are usually far enough from each other so that we can mostly ignore multiple scattering considerations. The crux of this method comes from the Doppler shifts manifested in the Fraunhofer lines of the back-scattered sunlight from particles on the atmosphere, which move with some relative velocity with respect to our frame of reference [Widemann et al., 2008].

One of the great challenges pertaining ground-based observations of planetary winds lies in maintaining a stable velocity reference when acquiring data. Several different techniques that use high-resolution spectroscopy to retrieve planetary winds in the visible part of the spectrum have all addressed this issue [Civeit et al., 2005, Luz et al., 2005, 2006, Widemann et al., 2007, 2008, Machado et al., 2012, 2014, 2017, Goncalves et al., 2020]. The reason for this challenge is that radiation dispersion laws and inherent instrumental uncertainties have constrained absolute reference rest frames with accuracies no better than about 100 m/s. Global winds on most planetary targets, can have wind amplitude variations or latitudinal gradients on the order of 5-10 m/s projected on the line-of-sight, so absolute reference frames become unreliable to use with most instruments. However, with recent instruments such as HARPS and ESPRESSO, primarily used for exoplanet search and characterisation, we can potentially retrieve radial velocities with extreme precision, lower than 5-10 m/s. However, applications of this kind are just being explored now.

Because of this difficulty, the Doppler velocimetry method used in this work, is based on an optimal weighting of the Doppler shifts of all the lines present in the spectrum, relative to some reference spectrum. This application was initially developed by Dr. Thomas Widemann, described in Widemann et al. [2008], and then refined by Dr. Pedro Machado, the supervisor of this work, for two types of instruments: long slit [Machado et al., 2012], and fibre-fed [Machado et al., 2014] spectrographs.

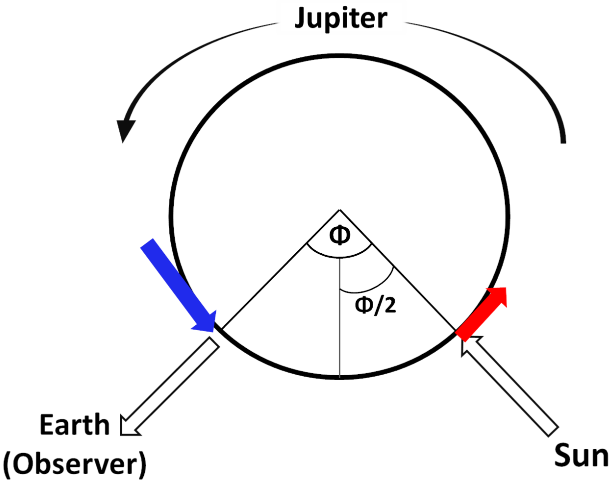

Figure 5.4.1: Diagram of the Doppler effect on backscattered solar radiation from particles on Jupiter. This model assumes a single scattering approximation. The solid white arrows represent radiation being absorbed (right) and then emitted (left) without Doppler effect. The coloured arrows represent the respective Doppler shifts provoked by the relative movements of particles with respect to Earth, when radiation is absorbed (red) or emitted (blue) by them. Φ is the phase angle between the Sun and Earth, centred on the planet.

5.4.1 Projected Radial Velocities

The Doppler shift present in the lines of the solar backscattered spectrum results from two instantaneous motions: one between the Sun and the planet's upper cloud particles, whose Doppler shift is minimal near the planet's sub-solar point and maximum at the sub-terrestrial point (observer); and another between the observer and the planet's atmosphere, resulting from the topocentric velocity of cloud particles in the target's atmosphere in the observer's reference frame, whose Doppler shift reaches its lowest value close to the sub-terrestrial point and highest at the sub-solar point. These combined motions add-up and contribute to a spatial variation of the Doppler shift as a function of latitude and longitude on the target. If Φ is the phase angle between the Sun and Earth centred on the target, at Half Phase Angle (HPA) $\Phi/2$ the sum of both Doppler shifts from the two instantaneous motions is zero. A diagram for these two motions is illustrated in Figure 5.4.1.

This is important since through this situation, we always have a null-Doppler shift meridian assuming a purely zonal wind field. As such, it can serve as a reference point and also a tool to measure any kind of spurious Doppler shifts that come from sources other than the particles' velocity. Additionally, this effect has been taken advantage of by using the whole null-Doppler meridian to study any shift present in the spectra at this location, which is presumed to be the result of meridional wind flow. This could be retrieved for the case of Venus, capturing the meridional wind with ground-based observations for the first time with high-resolution spectroscopy [Goncalves et al., 2020].

Since solar radiation is scattered from both the target planet and Earth's atmospheres and taking into account that some Fraunhofer lines are absorbed by our atmosphere, the contribution from telluric lines needs to be accounted for. To this end, the instrument registers both spectra and a least-squares deconvolution is applied to the pattern of Fraunhofer lines, using a mask that matches the Sun's stellar type (G2 type star), providing the radial velocity (along the line-of-sight) in the solar system barycentric frame (B). From the correlation function between Fraunhofer lines scattered from Venus and Earth, a double Gaussian fit is applied to extract the velocity h of the radiation scattered off of the target only.

However, to calculate this velocity other components are introduced to account for additional contributions to the Doppler shifts of the lines, and it is necessary to express these measurements in Jupiter's centre rest frame:

$$w_i = h - (berv + v_{topo} + v_{rot}) \tag{5.13}$$

Where w_i is the radial component of the instantaneous velocity of the planet's clouds in the observer's direction, expressed in the centre rest frame of the target (P); h is the absolute velocity of solar lines scattered off the planet's clouds expressed in the barycentric frame (B); $berv$ is the correction from Earth's rotation and orbital motion, i.e. the observer's movement in the barycentric frame (B); v_{topo} is the instantaneous velocity of the planet's centre of mass in the topocentric frame (T); and v_{rot} is the contribution of the Doppler shift from the differential rotation of the planet. The values for the velocities $berv$ and v_{topo} are taken from the ephemerides calculated by an online platform hosted by JPL/NASA (https://ssd.jpl.nasa.gov/horizons.cgi). The rightmost variable in equation 5.13 is usually missing on previous works of Doppler velocimetry [Goncalves et al., 2020, 2021, Machado et al., 2012, 2014, 2017, 2021] with this method, since they have targeted mostly Venus, a planet that rotates very slowly in relation to the zonal circulation of its atmosphere at the cloud tops. However, for Jupiter, its rapid rotation confers a non-negligible influence in the measured Doppler shifts that needs to be acknowledged. For this purpose we used the standard rotation velocities from System III definitions [Riddle and Warwick, 1976] for the gas giant, which give it a spin velocity at equator of approximately 12.6 km/s.

5.4.2 Young Effect

Due to the extended angular size of the Sun as seen from Jupiter ($\sim 0.1°$) and its fast rotation ($\sim$ 2 km/s), a differential elevation of the finite solar disk near the terminator (line that separates the day and night sides of a planet illuminated by a star), leads to an unbalance between the contribution of the approaching (blue shifted radiation) and receding (red shifted radiation) solar limbs. In this geometric configuration, the excess of one or the other has an effect on the apparent line Doppler shifts measured on the planet's atmosphere. This phenomenon is called the "Young effect". It has been shown [Young, 1975] that this effect can be derived through this calculation:

$$Y \sim \frac{v_{\odot} D_{\odot}}{sin\theta} \tag{5.14}$$

Where $v_{\odot}$ and $D_{\odot}$ are the equatorial velocity, $D_{\odot}$ the angular diameter of the Sun as seen from the observer, and θ is the angle in the planet between the observed point and the terminator. According to equations 5.14 this effect is more prominent as we get close to the terminator. A recent study by Gaulme et al. [2018] points out that equation 5.14 and an empirical relation deduced in Young [1975] applied for Venus ($Y = 3.2tan(\theta_{SZA})$ where θ_{SZA} is the solar zenith angle) are both limited to the equator of the planet in question and ignore the Sun's limb darkening. Thus, in the mentioned article, by performing sophisticated numerical simulations, a lower empirical factor between 2.7 and 3 is reached (as opposed to 3.2 in the original work by Young [1975]):

$$Y = C(\Lambda) sin(\varphi) cos(\theta_{SZA}) \tag{5.15}$$

Where $C(\Lambda)$ is a coefficient dependent on wavelength which varies between different planets of the solar system, and which can be applied within the visible range of the spectrum, and φ is the inclination of the solar rotation axis with respect to the local horizon on the target planet. In the context of this work which is applied to Jupiter, according to Gaulme et al. [2018], $C(\Lambda) = 0.4$ for the wavelength range of ESPRESSO. Taking into account the fact that from the observer's (Earth's) perspective, Jupiter's disk is almost always completely illuminated, as it is an outer planet of the Solar System, and given the low phase angle during acquisition, the calculated Young effect for these observations amounts to less than 0.1 m/s, rendering it irrelevant in relation to the expected wind velocities (100-150 m/s).
This correction can then be applied by means of equation 5.16

$$w_{i,c} = w_i + Y(\phi, \lambda) \tag{5.16}$$

where $w_{i,c}$ is the projected wind velocity along the line-of-sight (with the Young effect correction applied), w_i is the measured Doppler shift and $Y(\phi, \lambda)$ the correction term for the Young effect as expressed in equation 5.15. Notice that Y is a function of the latitude and longitude of the observed point on the disk which will dictate both φ and θ_{SZA}.

5.4.3 De-projection coefficients

The velocities retrieved through the Doppler shift from Eq. 5.13 are radial velocities, thus they are projected along the line-of-sight. To obtain the amplitude of the wind velocities on the planet at each point observed in the planetocentric frame of reference, we need to compute the local de-projection factor (F).

$$F = 2.cos(\Phi/2).sin(\lambda - \Phi/2).cos\phi_\beta \tag{5.17}$$

where Φ is the phase angle at which the observation was performed, λ is longitude of the point being measured on the disk, and ϕ_β is the latitude of the sub-terrestrial point. This factor is modulated by both the geometry of observations, and the planetary longitude as seen from the ground. In the case of a zonal circulation, as what is evaluated here, the line-of-sight Doppler shift is proportional to the projection of wind velocity on the bisector phase angle Machado et al. [2012]. For each location probed on the disk of Jupiter, as illustrated in Fig. 4.3.3, these coefficients were calculated and then used to convert the extracted Doppler shifts to instantaneous velocities of particles in the atmosphere.

5.4.4 Instrumental Spectral Drift

The spectral acquisition on Jupiter's bands by VLT/ESPRESSO is sequential, thus monitoring possible changes in spectral calibration with time is required to ensure measurement robustness. When the instantaneous velocity of the planet's centre of mass (v_{topo}) is subtracted from the calculated velocity of atmospheric particles with the Doppler shift on the spectra retrieved, spectral wavelength calibration is performed at both the beginning and end of the observing session. On this case, this calibration was performed with a Th-Ar lamp exposure. Since the absorption lines from Earth's atmosphere are well known, their putative superposition to the target planet's spectra can be used as additional on-sky calibration.

As mentioned earlier, global winds are, on most planets such as Jupiter, subject to wind amplitude variations or latitudinal gradients that can range between 5 to 40 m/s projected on the line-of-sight. Even though ESPRESSO can achieve a good enough spectral resolution, which can take into account such deviations with direct measurements, we take from previous experience [Goncalves et al., 2020, 2021, Machado et al., 2014, 2017, 2021] that better results can be achieved by measuring relative Doppler shifts between two sets of absorption lines. Choosing arbitrarily the first spectrum of each series of sequential acquisitions $w_{i,c,ref}$ as a velocity reference so that:

$$v_i = w_{i,c} - w_{i,c,ref} \tag{5.18}$$

where v_i represents the line-of-sight relative velocity, which results from the subtraction of the absolute velocity retrieved at some target point in the planet's disk ($w_{i,c}$), and the velocity in the reference point. With each return to the point of reference, a slow drift of the velocity retrieved from this point becomes apparent, which presumably occurs due to imperfectly corrected instrumental effects and measurement of absorption lines from the Sun with respect to Earth's ones [Widemann et al., 2007]. Using our Doppler velocimetry method on a fibre-fed spectrograph, such as ESPRESSO, relies on sequential spectral acquisition on Jupiter's disk. Since to compute relative Doppler shifts we use a reference point, during observations this point is returned to several times to correct the velocities retrieved from the instrumental spectral drift and/or spectral calibration variability with time. The reference point chosen is located in the meeting point between the equator and the HPA meridian, so that theoretically both meridional and zonal components (respectively) of the winds gathered from the Doppler shifts should be zero. Such properties make this point the ideal reference for the spectral drift by making several observations during sequence acquisition.

Since we assume that any variations of the Doppler shift measured on this reference point come from the spectral drift provoked by the instrument, we fit all the reference point velocities to a series of linear segments v_{trend}, taking the initial velocity from the reference point to have a zero offset. With this trend line, it is possible to compute the offset caused by the spectral drift at any point in time during observations, which is then used to further correct the velocities retrieved:

$$v_i' = v_i - v_{i,trend} \tag{5.19}$$

where each relative Doppler retrieval v_i is subtracted by the value of the drift trend $v_{i,trend}$ at the time v_i was observed, obtaining the spectral drift corrected velocity v_i'. In previous observing runs using other instruments such as CFHT/ESPaDOnS, this correction process required the observation of the reference point on both ends of each sequence however, since ESPRESSO is exceptionally stable this requirement is not so strongly enforced as can be seen on table 4.2.

5.5 Error Estimation and Analysis

5.5.1 Cloud Tracking

Since this method is heavily reliant on the quality of the images used to track cloud features, spatial resolution is one of the most important sources of error when retrieving wind velocity tracers. However, both cloud tracking methods used for the purpose of this work have different processing routines towards the calculation of velocity components, even if absolute error values vary with mostly the same quantities: spatial resolution and the time interval between both images.
Both the supervised cloud tracking method with PICV and the 'manual' process with ACT calculate wind vector components (zonal and meridional) by measuring the displacement of cloud features within the given time interval between an image pair:

$$u = Rad\ cos(\bar{\phi})\frac{\pi}{180}\frac{\Delta X\delta s}{\Delta t} \tag{5.20}$$

$$v = Rad * \frac{\pi}{180}\frac{\Delta Y * \delta s}{\Delta t} \tag{5.21}$$

where ΔX and ΔY are the horizontal and vertical pixel displacements of the feature, δs is the spatial resolution of the image, and Rad is the distance from the centre of the planet, which considers an oblate spheroid case such as Jupiter's:

$$Rad = \frac{R_{eq}R_p}{\sqrt{(R_{eq}sin\bar{\phi})^2 + (R_p cos\bar{\phi})^2}} \tag{5.22}$$

where R_p is the polar radius.
As becomes evident in equations 5.20 and 5.21, the errors associated with these tracers come mostly from the variable spatial resolution of the image and the time interval between the pair.
Navigation and geometric information on the size, orientation, latitude and longitude coordinates is mostly handled by SPICE, hence errors pertaining radius and coordinates in the planetary grid come mainly from the accuracy and stability of the spacecraft's attitude, the uncertainty in the spacecraft's position and the temporal precision on the time-tag attributed to each image. The attitude of spacecrafts such as VEx is usually stable with the largest deviations on the order of 10 mdeg, approximately five times smaller than the best spatial resolution achieved in all the images used for this study. The uncertainty in the spacecraft's position entails errors on the order of tens of meters with respect to navigation and size of planetary objects as analysed by [Rosenblatt et al., 2008], at least ten times lower than the best spatial resolution achieved. The accuracy in the temporal data of the images is on the order of miliseconds, more than five orders of magnitude smaller than the shortest time interval between two images used in any pair.
Considering that all other sources of error listed above are minor, the errors in wind velocity δw_v are computed as:

$$\delta w_v = \frac{\delta s}{\Delta t} \tag{5.23}$$

To better handle fluctuations between gathered results, we apply an appropriate latitudinal binning for the wind profiles produced with data from cloud tracking, through a weighted average of all relevant data points for that latitudinal range:

$$WA(V^{obs}) = \frac{\sum_{i=1}^{n} V_i^{obs}\sigma_i}{\sum_{i=1}^{n}\sigma_i} \tag{5.24}$$

where V_i^{obs} is the ith wind velocity result to be averaged, and σ is the individual error associated with that measurement.

Considering other possible sources of error, the PICV algorithm that recognizes similar patterns in the clouds, might suggest tracers that do not entirely correspond to the same moving cloud feature. Even though this step is supervised, for images with poor resolution or for very faint features it can become challenging to properly identify in which pixel has the feature moved into. Other incidental image artefacts can make the identification of features difficult, leading to fewer tracers, thus larger errors. Since with the 'manual' cloud tracking the user has more freedom to choose exactly which pixel to use as a wind tracer, it potentially leads to more retrieved tracers and consequently more robust results.

5.5.2 Wave Characterisation Precision

As in cloud tracking, a high spatial resolution is crucial concerning both wave detection and characterisation, both to distinguish between different crests of a wave-train, and to more confidently measure the packet. During morphological characterisation we are concerned with a high number of distance measurements between points on an atmospheric wave thus, the resolution defines our capability for precise data. As waves are generally small scale features, the highest possible spatial resolution was a much sought after quality of all the images gathered for this study, guiding our image selection towards pictures where the spacecrafts that targeted Venus (VEx and Akatsuki in this case) where as close as possible to the atmosphere without diminishing their capability to gather data. Hence, the highly elliptical orbits of both missions provided good windows of opportunity for such observations.

To ensure consistency between different measurements of the same wave packets and eliminating possible outliers, a simple average and standard deviation was used between measurements pertaining the same packet. Because of our technique to retrieve the orientation of packets, we achieved higher precision for longer packets. The measuring process for orientation was also sensitive to the packet width, although to a lesser degree.

Retrieved phase velocities are affected in much the same way as in cloud tracking since both methods are fundamentally similar.

Other predominant effects that compromise characterisation, especially optical thickness studies, is the light pollution from the dayside caused by multiple reflections of light inside the detector of IR2 [Satoh et al., 2017]. Not only did this influence detectability of crests closer to the terminator (or possibly entire wave packets), but it also made some optical thickness characterisation impossible, as this external light would eclipse the natural drop between crests of a wave. For this reason, we elected to discard the optical thickness measurements from IR2 images. Other sources of error include navigation and geometry errors from limb fitting, however these are generally less significant. Although in essence, navigation presents only marginal errors, IR2 images required more grid corrections because, for many nightside images, light contamination from the dayside mentioned earlier, along with other effects such as the high opacity of the lower clouds, which makes the limb more difficult to identify, led to significant misalignments of the navigation grid. As such, we used the same interactive limb-fitting method developed and detailed in [Peralta et al., 2018]. The precision of this correction can be estimated to range between 0.5 and 1 pixel, depending on the case at hand.

5.5.3 Doppler Velocimetry

The total error on a given velocity measurement $w_{i,c}$ is the sum of a combination of uncertainties of different origins. The spectral calibration performed using the Th-Ar lamp can be subject to uncertainties regarding the dispersion spectrum from the lamp itself, the least-square deconvolution of Fraunhofer lines, the additional fit to telluric lines, and unpredictability of weather conditions, as well as minor variations in temperature and pressure on the spectrograph. Additionally, guiding and pointing accuracy errors can provoke uncertainties which affect the Doppler shifts measured that will be used to compute the velocity of winds on Jupiter. Since the referenced multiple sources have errors of varying degree, and we repeat exposures on the same point in the disk as part of our observing routine, it is possible to test the internal consistency of the retrieved radial velocity (h) instead of estimating upper limits for each source of error. An estimate of the individual error on the velocity retrieved for each band of Jupiter, was made by simply calculating the standard deviation between two 60 second exposures for each point. This estimation was performed after all other sources of error exposed above were considered. Depending on the instrument and the observing time available, more exposures are usually preferred to ensure the consistency of the acquisition process. The velocities on each target point were obtained by weight-averaging the retrieved values from consecutive exposures. Taking σ_i as the error on the reference point velocity relative to the retrieval v_i, the statistical combined error for each point can be calculated using:

$$\sigma_i' = \sqrt{\sigma_{i,trend}^2 + \sigma_i^2} \tag{5.25}$$

where $\sigma_{i,trend}$ represents the linearly interpolated error from the deviations of v_i from $v_{i,trend}$ along the segment between two reference point exposures. The errors calculated for our Doppler velocimetry measurements with ESPRESSO, taking into account all factors exposed above, were on average 10.6 m.s^{-1} with the biggest error bar being around 19.3 m.s^{-1}. Even though all previously mentioned sources of error are important for the precision of the results obtained with this method, the error associated with the pointing accuracy of the fibre's FOV during exposure, was more important than all other contributors to the general error. One reason why is because this error will be propagated through the de-projection of line-of-sight drifts, into wind velocities of both zonal and meridional components. To monitor these fluctuations, the observer has the responsibility to control the fibre's FOV drift, verifying if it wanders by more than half the fibre's angular diameter from the targeted point. Should it do so, the observation is discarded and then repeated, a process that is limited by the total allocated time for the observation with the telescope. For the case of ESPRESSO two 60 second exposures were enough to guarantee a good S/N ratio, while the stability of this state-of-the-art instrument allowed such exposures to be made with confidence.

Chapter 6

Results and Analysis

6.1 Atmospheric Circulation on Venus' Cloud Deck

The observations with Akatsuki/UVI on January 2017, were made as part of a coordinated campaign with ground-based observations with the TNG/HARPS-N, whose main results were published in Goncalves et al. [2020]. From the six days of observations with Akatsuki, three were also covered from the ground, for a cross-validating analysis of the winds in the upper cloud with two different techniques. For the purpose of this document, I will only describe results from cloud tracking, on which I was directly involved, contributing in data retrieval and analysis.

For each day observed with Akatsuki data, we had 3 images, each separated by approximately 2 hours (henceforth codenamed A, B and C). Since the cloud tracking technique involves following the movement of cloud features between a pair of images, we were able to extract wind tracers from three different pairs (A-B, B-C and A-C). Two of the pairs share the same time-span between images, but the third one features a longer interval of 4 hours between pictures. The longer time intervals can reduce errors on wind velocity measurements however, depending on the atmosphere, some features that can be used as tracers can evolve and disappear in shorter time frames, which can make it more difficult to retrieve measurements from a greater number of features.

A total of 4035 cloud tracers were retrieved between all image pairs to gather results on the wind velocity at the upper cloud. These tracers were retrieved with the cloud tracking tool described in section 5.2.2. Details on the observations and image pairs used are illustrated on Tables 6.1 and 6.2.

In table 6.2 we can see that in most cases, the image pair with the longest time interval (A+C) has less wind tracers retrieved for the reasons explained previously. Each tracer has data on both the zonal and meridional component of the winds in the upper cloud of Venus. Figure 6.1.1 shows the latitudinal profile of the zonal wind in the upper clouds of Venus for each day of observation with Akatsuki/UVI, during the coordinated campaign with ground-based observations. All panels show the characteristic plateau of the wind profile at low and mid latitudes with wind speed values between 100-120 m.s^{-1} in the retrograde direction (hence the negative sign), with a sharp decrease in velocity near 50° towards the poles. Also noticeable in the panels is some day-to-day variability of wind

Table 6.1: Upper Cloud Observations for Cloud Tracking with Akatsuki/UVI

(1) Date-Time (UT)	(2) Res. (km/pix)	(3) Lat.	(4) LT	(5) Dis. (km)	(6) Ang.Diam.(")	(7) Code
26-01-2017 - 17:35	38.56	72°N - 88°S	7:30-18:00	139,281	5.04	A
26-01-2017 - 19:35	41.87	72°N - 88°S	7:30-18:00	150,410	4.67	B
26-01-2017 - 21:35	44.96	72°N - 88°S	7:30-18:00	160,935	4,36	C
27-01-2017 - 17:05	57.96	75°N - 85°S	8:00-18:00	241,464	2.91	A
27-01-2017 - 19:05	59.42	75°N - 85°S	8:00-18:00	248,056	2.83	B
27-01-2017 - 21:05	60.81	75°N - 85°S	8:00-18:00	254,403	2.76	C
28-01-2017 - 18:05	72.50	75°N - 85°S	8:30-18:00	308,741	2.27	A
28-01-2017 - 20:05	73.37	75°N - 85°S	8:30-18:00	312,904	2.24	B
28-01-2017 - 22:05	74.16	75°N - 85°S	8:30-18:00	316,909	2.21	C
29-01-2017 - 18:55	80.53	75°N - 85°S	9:00-18:00	350,172	2.00	A
29-01-2017 - 20:55	80.97	75°N - 85°S	9:00-18:00	352,612	1.99	B
29-01-2017 - 22:55	81.39	75°N - 85°S	9:00-18:00	354,927	1.98	C
30-01-2017 - 18:05	83.76	75°N - 85°S	9:15-18:00	371,094	1.89	A
30-01-2017 - 20:05	83.86	75°N - 85°S	9:15-18:00	372,172	1.88	B
30-01-2017 - 18:05	83.93	75°N - 85°S	9:15-18:00	373,138	1.88	C
31-01-2017 - 17:25	83.90	70°N - 80°S	9:50-18:00	376,765	1.86	A
31-01-2017 - 19:25	83.80	70°N - 80°S	9:50-18:00	376,553	1.86	B
31-01-2017 - 21:25	83.65	70°N - 80°S	9:50-18:00	376,23	1.86	C

Observations with Akatsuki UVI for the coordinated campaign with ground-based observations. The columns in the table are as follows: (1) Date and time in UT of observation; (2) Mean spatial resolution of the image; (3) Latitude range of Venus' visible disk; (4) Local time range of Venus' dayside; (5) Distance between Akatsuki and the centre of Venus; (6) Apparent angular diameter of Venus as seen by Akatsuki; (7) Codename attributed to the image for identification when pairing within the same day of observation.

Table 6.2: List of Image Pairs when Cloud Tracking with Akatsuki

(1) Date	(2) Image pair	(3) N^o Tracers
26-01-2017	A+B	284
26-01-2017	B+C	310
26-01-2017	A+C	164
27-01-2017	A+B	168
27-01-2017	B+C	255
27-01-2017	A+C	176
28-01-2017	A+B	252
28-01-2017	B+C	215
28-01-2017	A+C	201
29-01-2017	A+B	257
29-01-2017	B+C	264
29-01-2017	A+C	154
30-01-2017	A+B	288
30-01-2017	B+C	235
30-01-2017	A+C	170
31-01-2017	A+B	201
31-01-2017	B+C	262
31-01-2017	A+C	179

(1) Date of Observation; (2) Images used in the pair for Cloud Tracking; (3) Number of Wind Tracers retrieved.

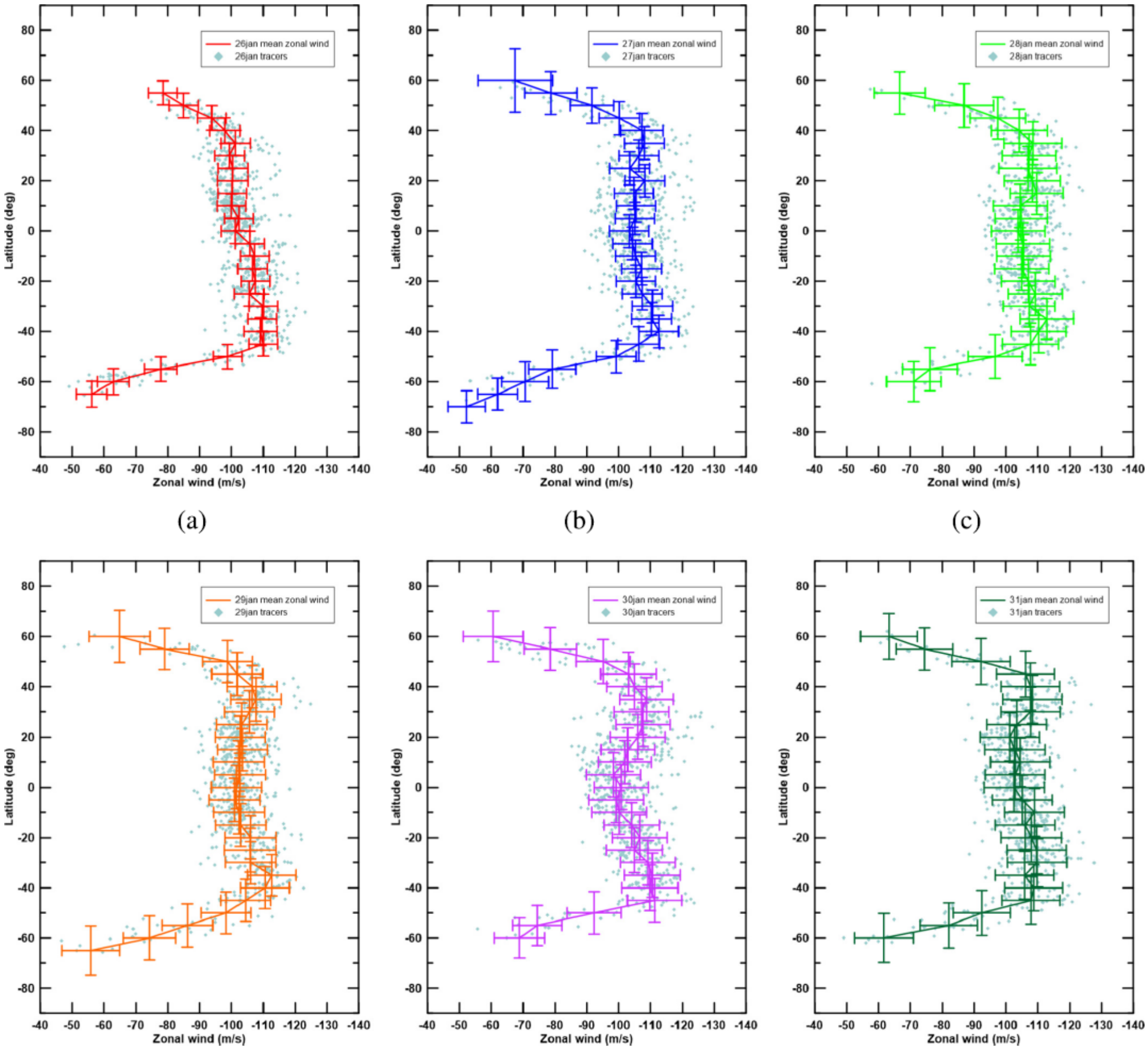

(a) (b) (c)

(d) (e) (f)

Figure 6.1.1: Zonal wind latitudinal profiles for each day of observation with Akatsuki/UVI images (26 to 31 of January, in panel a to f respectively). The coloured profile on each panel is built from a weighted average of individual zonal velocity results for each day, performed with a binning of 5°. Also shown on each panel is the cluster of individual measurements on the background of the mean profile, represented by light grey rhombuses. From Goncalves et al. [2020].

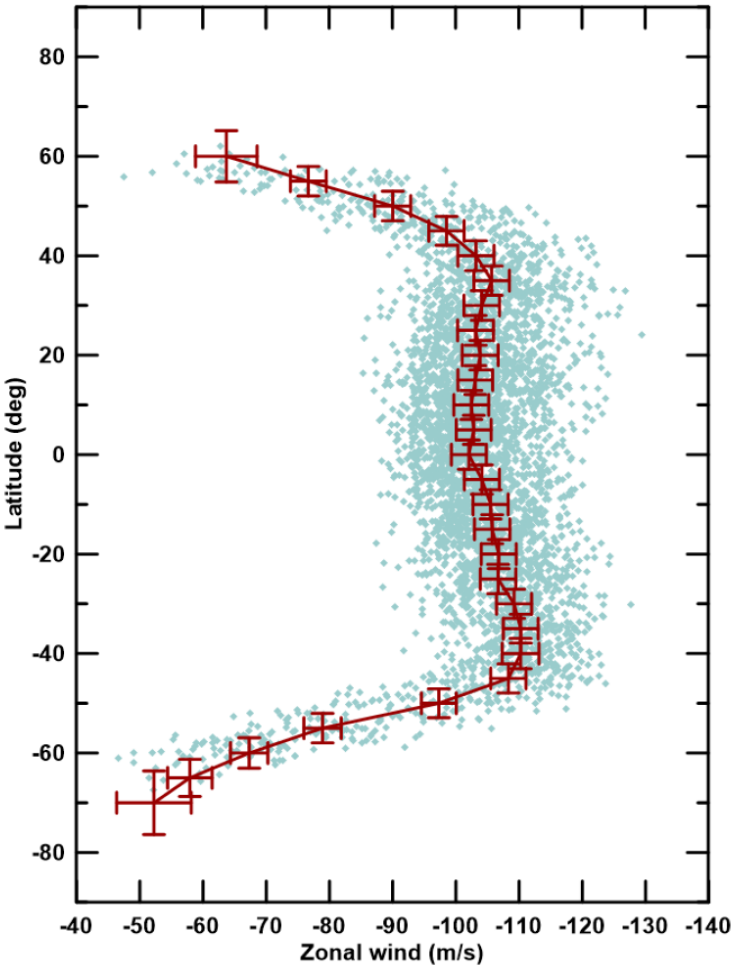

Figure 6.1.2: Mean zonal wind profile of the results from cloud tracking with Akatsuki/UVI images. The average was calculated using a latitude bin of 5° across all days of observation. The mean profile is represented by the red line, featuring the error bars from the weighted average and the grey rhombuses are all 4035 individual tracers. From Goncalves et al. [2020]

velocity specially on the 26th (panel A) where there is an apparent asymmetry in the profile between the north and south hemispheres.

The average wind profile in Fig 6.1.2 is consistent with previous cloud tracking results obtained by other authors with the same instrument such as Horinouchi et al. [2018] and earlier results with VEx/VIRTIS [Sanchez-Lavega et al., 2008, Hueso et al., 2015].

Spatial and temporal variability of the zonal wind can be analysed simultaneously in Fig 6.1.3. The contour plots show a general daily variability around 5-10 m.s^{-1} and evidence of the north-south asymmetry, more prevalent on the first day (26th of January) but also visible on other days and reflected on the averaged results. This equatorial asymmetry has also been observed in Horinouchi et al. [2018] - whose results were retrieved between October 2016 and March 2017 - using the same instrument onboard Akatsuki. Additionally, these results also show an acceleration of the wind towards the evening terminator, more noticeable on the 28th (panel c in Fig. 6.1.3). This increase in velocity by up to 10 m.s^{-1} has already been noticed with other instruments [Hueso et al., 2015] and techniques [Machado et al., 2017] however, its source is still an open question.

Regarding meridional wind, results from this study are illustrated in Figs. 6.1.4, 6.1.5, built in the same way as Figs 6.1.2, 6.1.3. As with the zonal wind, a day-to-day variability, in this case around 4-8 m.s^{-1} (already competing with our error bars which are around

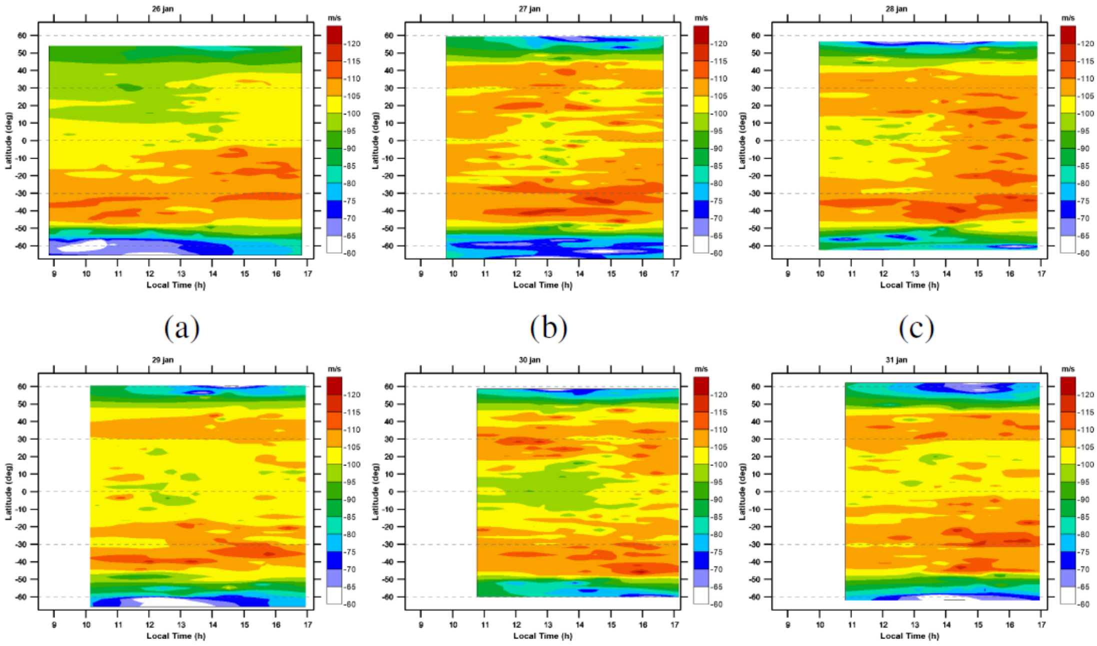

(a) (b) (c)

(d) (e) (f)

Figure 6.1.3: Contour plots of the zonal wind in the upper clouds of Venus in function of latitude and local time from Akatsuki/UVI data. The magnitude of the zonal wind is illustrated as a colour code, flowing in the westward direction. The polynomial interpolation which built this grid has a resolution of approximately 2° in latitude and 0.3 h in local time. From Goncalves et al. [2020]

5 m/s), is present between the six days of observation with a significant increase in the northern hemisphere on the first day (panel a Fig. 6.1.5).

Contrary to what was observed with the zonal wind, meridional winds pickup on the northern hemisphere on the first day, contributing to greater asymmetry than on the following days of observation.

It is interesting to notice that both asymmetries are mostly reserved for the first day only, which could suggest some type of correlation between both wind regimes. Furthermore, Goncalves et al. [2020] claim that there is evidence of a decrease in meridional wind velocity towards the evening terminator, possibly also a correlation with zonal wind speed increase towards the same local time.

Looking at the profile of zonal and meridional wind across several years in Fig. 2.2.6, we find that the equatorial orbit of the Akatsuki spacecraft offers a clear advantage since it is possible to gather wind velocities on both hemispheres, responsible for the discovery of this north-south asymmetry. Along the southern hemisphere, the latitudinal profile from our observations more closely matches the profile by Hueso et al. [2015] than Horinouchi et al. [2018], even though the latter was retrieved with the same instrument at the same wavelength. The main difference between our results and those shown in Fig. 2.2.6 from other authors are that both used an automatic cloud tracking routine whereas we employed a 'manual' approach, and both works feature much longer time-spans than our six days of observation. Although there is some variability as already shown, the profile remains stable over the years with almost constant zonal wind speed below 30° latitude with a steep decrease in velocity at higher latitudes on both hemispheres.

As for the meridional wind, our profile (Fig. 6.1.4) is consistent with previous observations with velocity peaks near 40°-50° latitude on both hemispheres reaching 15 m.s^{-1}. However, it is still difficult to properly interpret meridional wind results with cloud track-

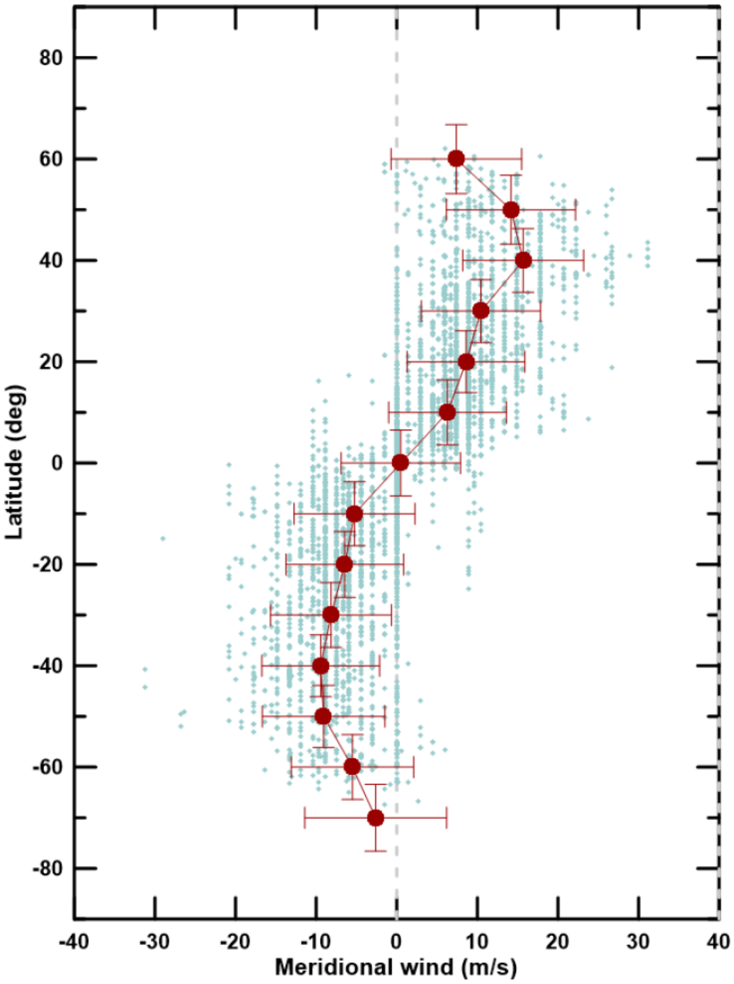

Figure 6.1.4: Latitudinal profile of the mean meridional wind. on the upper clouds of Venus. The red circles accompanied by the connecting line represent the weighted average profile with a 5° binning, while the grey circles are the individual tracers. Due to the lower values of the meridional wind, which in some cases approaches the resolution of the pictures used, we see more empty space between tracers, signifying the limit of resolution. From Goncalves et al. [2020].

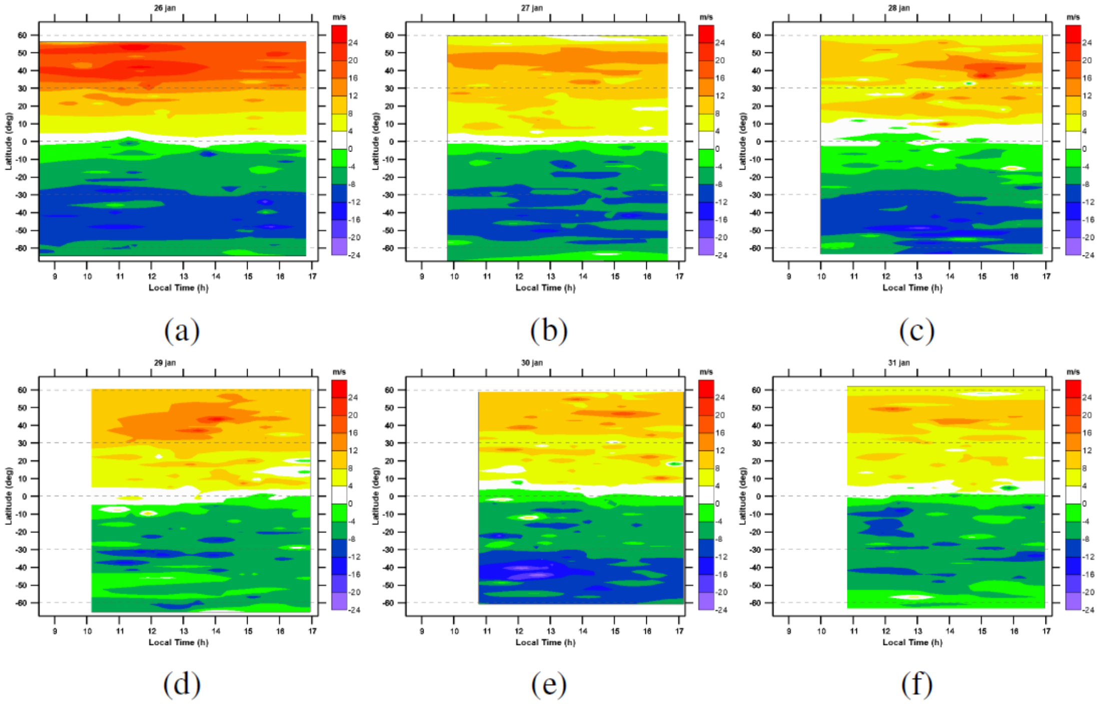

(a) (b) (c)

(d) (e) (f)

Figure 6.1.5: Contour plots of the meridional wind in function of latitude and local time across the six days of observation with Akatsuki/UVI. Panels a-f represent the results on each day from 26th-31st of January. Positive values (towards warmer colours) represent poleward velocity towards the north and vice-versa for bluer shades. The polynomial interpolation has the same resolution as in Fig. 6.1.3. From Goncalves et al. [2020].

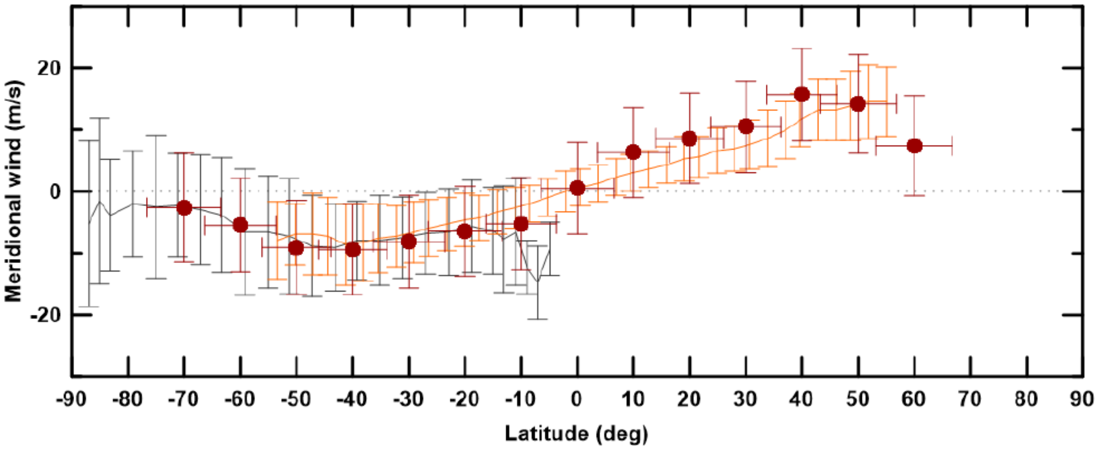

Figure 6.1.6: Meridional wind results from different cloud tracking studies. Red circles represent our profile [Goncalves et al., 2020]; the yellow line are the results from Horinouchi et al. [2018]; and the grey line represent the work by Hueso et al. [2015] using VEx/VIRTIS observations. From Goncalves et al. [2020].

ing data across several years, since most results have errors of similar orders of magnitude as the values of the meridional wind velocities.

6.1.1 Discussion

One of the most surprising aspect of these results is the before mentioned north-south asymmetry of the zonal wind profile, also reported in Horinouchi et al. [2018], whose observations include the dates we also used. However, previous data sets (observations of Akatsuki, prior to August 2016) fail to show any evidence of this asymmetrical profile, which suggests that some variable phenomena or episodic event might be responsible for this. As we also report an asymmetry of the meridional profile, although an increase in velocity instead, it seems that both asymmetries may be anti-correlated. According to Horinouchi et al. [2018], possible causes include the influence of vigorous vertical shear or some hemispherical asymmetry in the altitude of the upper clouds. Thermal tides could also play a role to generate this peculiar feature [Takagi et al., 2018]. Other features such as atmospheric waves, in particular the planetary scale Y-feature, could also contribute to this asymmetry but with our data alone it is not possible to attribute a proper cause for this dynamical behaviour. Additional measurements of the zonal wind on both hemispheres across a larger time interval are required to constrain this phenomenon, investigate its periodicity and amplitude variability, in order to postulate possible reasons for this asymmetry.

Regarding the local time variability of wind speed, namely the increase of the magnitude of the zonal wind and respective decrease of the meridional wind near the evening terminator, the combined effect of vertical wind shear, local time dependence of temperature and thermal tides could reflect these changes [Sanchez-Lavega et al., 2008, Hueso et al., 2015, Horinouchi et al., 2018, Takagi et al., 2018]. Although, relations between cloud top wind flow and topography have been studied in the past [Bertaux et al., 2016] and continue to be a topic of debate, our results do not show any kind of correlation with topographical features. Nevertheless, our observations are limited to a very short temporal interval, and a broader coverage might reveal such influence on the upper cloud dynamics. The next sections expand upon this topic with the influence of gravity waves, putatively generated by the presence of mountains or other rugged terrain.

6.2 Atmospheric Waves on the Lower Cloud of Venus

Examples of wave packets observed and characterised with both VIRTIS and IR2 night-side images are displayed in Fig. 6.2.1. A total of 277 wave packets were identified and morphologically characterised in images from both instruments, while for dynamics only 168 characterisations were retrieved. Of all retrieved wave packets, approximately 32% were dynamically characterised (phase velocities retrieved), with a significantly higher proportion of IR2 waves available for tracking than those from VIRTIS. Packets were characterised on every image in which they appeared, not only for completion but also to track the evolution of each packet over time. As such, we distinguish every wave packet

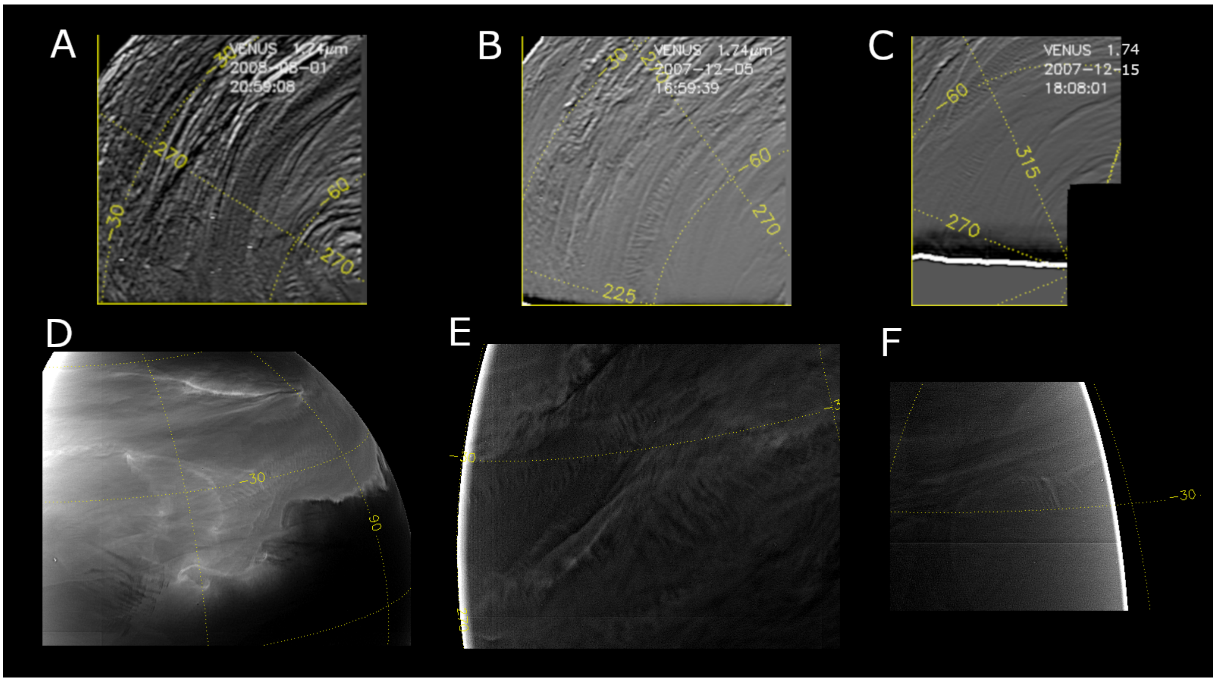

Figure 6.2.1: Examples of detected waves on navigated images. A-C: VIRTIS images processed with a directional kernel and unsharp masking; D-F: IR2 images processed with unsharp masking and histogram equalisation.

measurement with 'distinct' packet measurements, as the latter refers to a single wave packet propagating in the atmosphere, even if its properties are measured on more than one image. Regarding distinct packets, 94 were observed and analysed on VIRTIS images and 42 from IR2 data. With the addition of the data from Peralta et al. [2008], a total of 166 different wave packets are included in this study.

Our characterisation process is separated in two steps: morphological and dynamical characterisation. The first requires a single image of a wave packet and retrieves what we called morphological properties. The second evaluates the dynamical nature of the wave, given that we have access to at least two near-consecutive images of the propagating wave packet. We shall thus separate our exposure of the results from both processes of characterisation, followed by an analysis of the results obtained, all of which was published in Silva et al. [2021].

6.2.1 Morphological properties

For wave packet distribution, figure 6.2.2 shows every instance of wave characterisation, even if the same wave packet is being characterised across different images. In Fig. 6.2.3 we also show a more compact version of this map with distinct packets only. The large rows of points that represent the movement of the same wave packet characterised on different images are gone as a result. As illustrated by both Figs. 6.2.2 and 6.2.3, most of the wave activity was observed on the southern hemisphere of Venus.

Moreover, the large concentration of VIRTIS packets at 225°-315° longitude may be an observation bias, because during the observed period (August 2007 - October 2008) VIR-

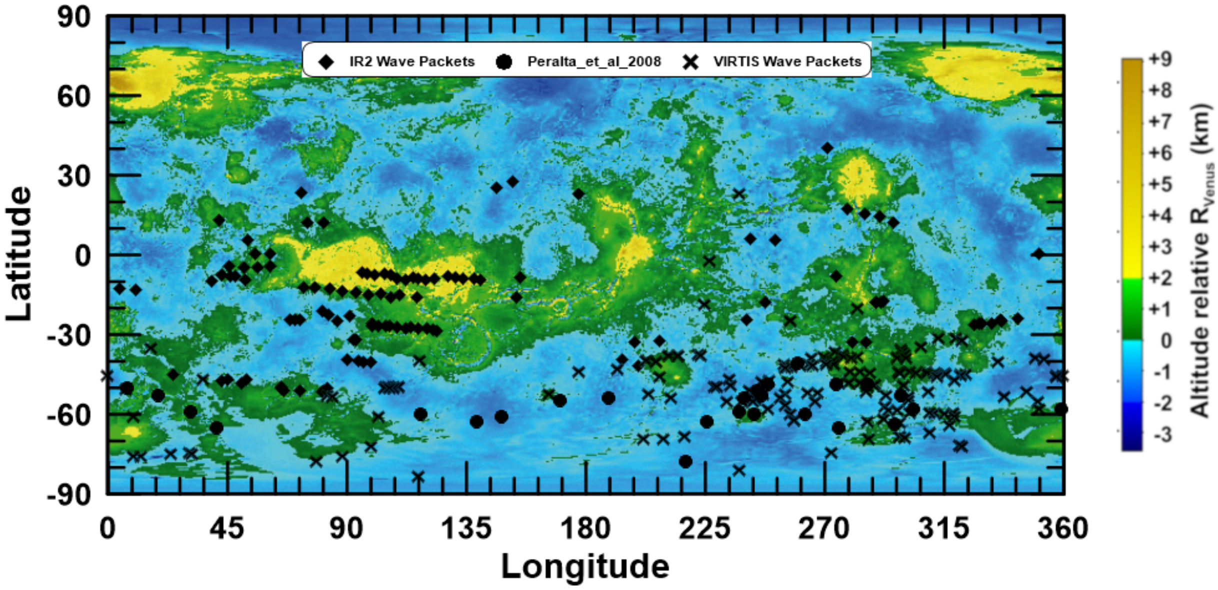

Figure 6.2.2: Distribution of characterised wave packets on the nightside of Venus during the period of observation. Wave packets from VIRTIS data are represented by crosses and from IR2 are represented by rhombuses. Additionally, represented by dark circles are wave packets featured in Peralta et al. [2008]. The topography map was made from data from VeRa onboard Venus Express [Hausler et al., 2006, 2007].

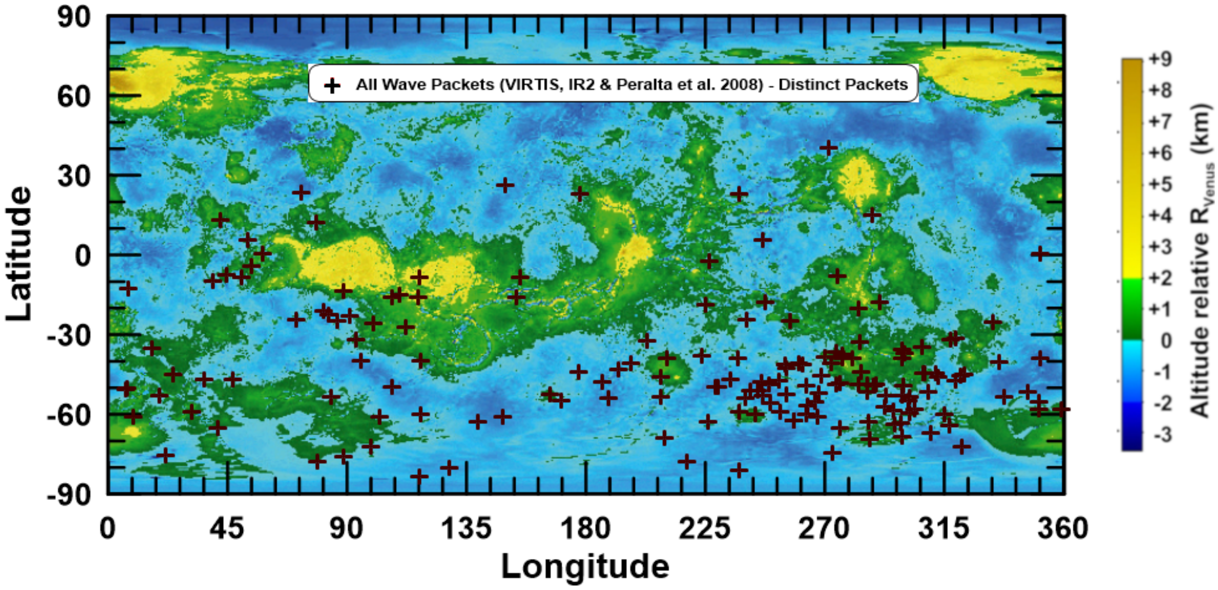

Figure 6.2.3: Distribution of characterised wave packets on the nightside of Venus in a latitude/longitude map. On this map, we represent only distinct packets from all three data sets: VIRTIS, IR2, and the data from Peralta et al. [2008].

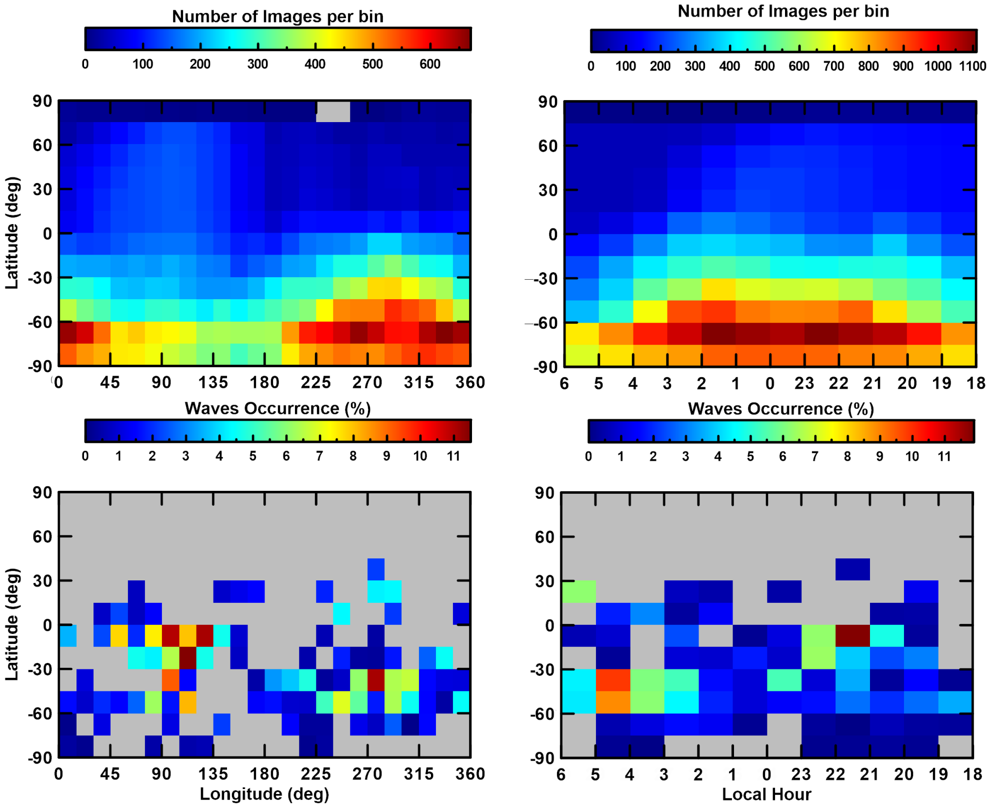

Figure 6.2.4: *Top* - Latitude/longitude and latitude/local time coverage maps of VIRTIS and IR2 images during the period of observation for both datasets. A greater number of images are shown for the southern hemisphere, particularly in regions between 60° and 90°S at 0°-45° and 195°-360° and slightly decreasing between both terminators. *Bottom* - Latitude/longitude and latitude/local time maps of the percentage of wave occurrence within the number of images analysed.

.

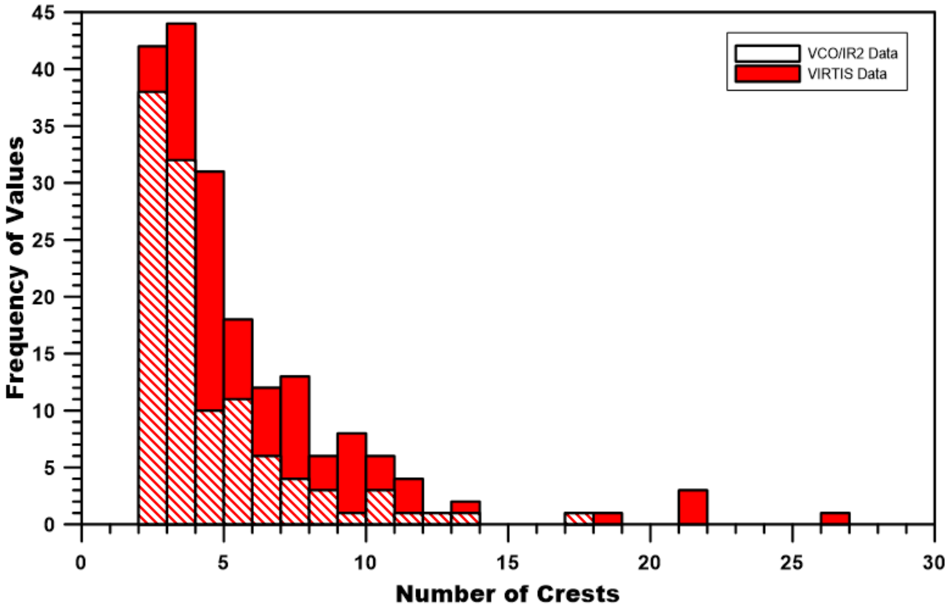

Figure 6.2.5: Histogram showing the number of crests on each characterised wave packet. Includes data from Peralta et al. [2008] which encompass VIRTIS data from July 2006 to March 2007.

TIS scanned this region much more frequently than other areas which is illustrated in Fig. 6.2.4 (Top-left plot). There are also a good number of images and detections at equatorial and 'subtropical' latitudes (0°-30°), as the orbit of Akatsuki enables the detection of wave activity in regions that were out of reach for VIRTIS during its orbit around Venus.
The occurrence maps in Fig. 6.2.4 combine the distribution of characterised waves with the number of images that target each sector on Venus to show the mesoscale wave frequency (number of observations with mesoscale waves to 'total number of observations' ratio) at different locations. Even though wave occurrence is never higher than 11%, an asymmetry in their distribution is clear as wave occurrence seems more concentrated in two different regions, between 45°and 135° at equatorial latitudes, and between 270°and 315° flanked by subtropical latitudes and the region where the cold-collar would be [Piccialli et al., 2012].

Figure 6.2.5 shows the number of crests of characterised wave packets. We established that a minimum of three crests for wave packet detection was required to distinguish a mesoscale wave from other cloud patterns that might share a similar morphology. According to our detections, shorter packets (3-4 crests) seem to be more common in both data sets with increasing rarity for packets with many more crests (>10). However, the causes of these observations are uncertain.

Figure 6.2.6 shows the results of the morphological properties of characterised packets. Waves characterised with VIRTIS data have the values of their properties, such as horizontal wavelength and packet width, more concentrated on narrower ranges than IR2 waves. Even though we have approximately 59% more wave characterisations with VIRTIS data when compared with IR2, the properties distribution is not proportional between both data sets. This is especially true for the case of the orientation of wave packets in Fig. 6.2.6 (Bottom right plot), where we can identify approximately the 10° orientation as the most frequent value for VIRTIS waves, whereas IR2 waves present two peaks regarding orientation, one at -10° and another at 20°.

The values retrieved for the morphological properties of wave packets on both VIRTIS and IR2 databases are summarised in Table 6.3. The spatial resolution of observations

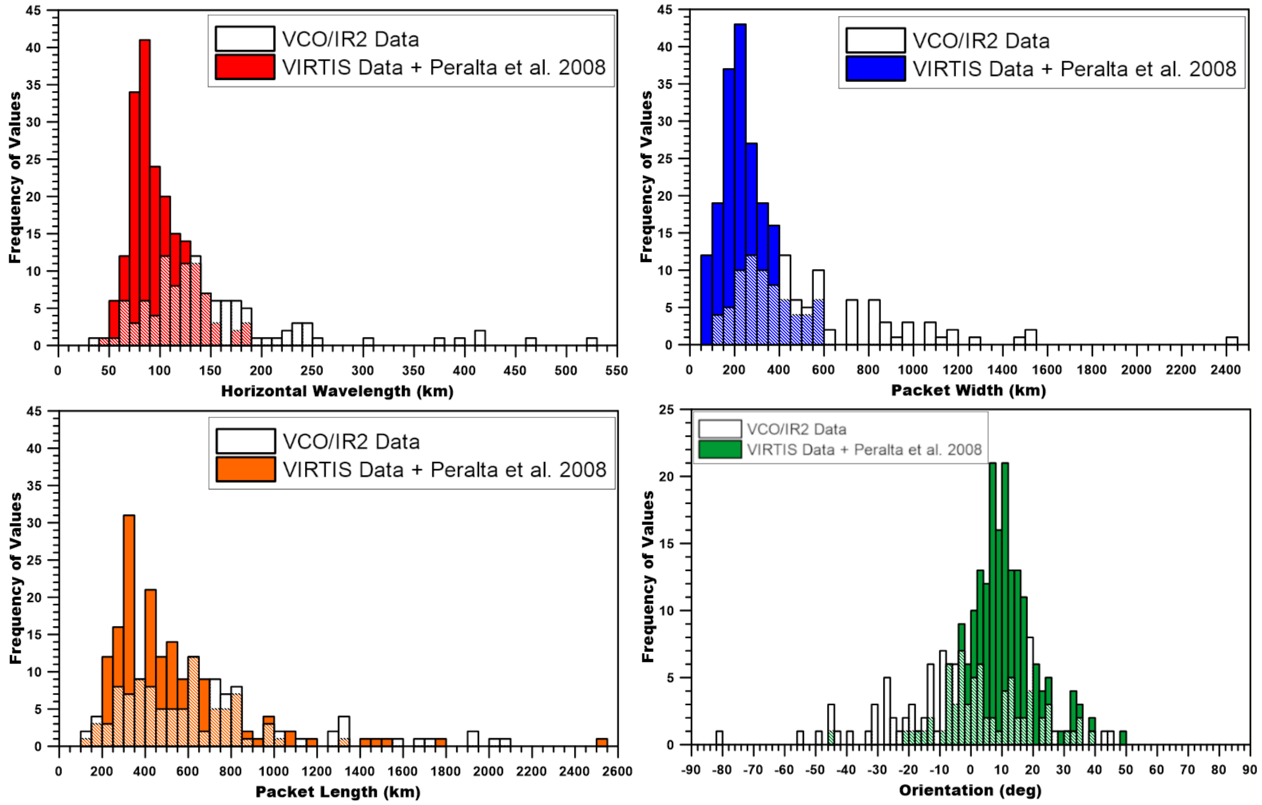

Figure 6.2.6: Histogram plots of the morphological properties of identified waves on nightside images of VIRTIS-IR and IR2. Also included are data from Peralta et al. [2008].

Table 6.3: Morphological properties of characterised packets

Instrument	λ_x	σ_{λ_x}	PW	σ_{PW}	PL	σ_{PL}	θ	σ_θ
			(Km)				(°)	
VIRTIS	100 (48 - 183)	27.07	250 (77 - 597)	115	486 (137 - 2512)	302.77	9 (-45 - 50)	11.61
IR2	158 (39 - 524)	82.79	527 (115 - 2340)	360.16	716 (107 - 2089)	412.24	-3 (-80 - 45)	21.78

λ_x is the horizontal wavelength, PW is the packet width, PL is packet length, and θ is the orientation of the packet. σ_{λ_x}, σ_{PW}, σ_{PL} and σ_θ are the standard deviations between all wave packets for its respective property. The first value of each of λ_x, PW, PL, and θ is the mean value and in brackets are the minimum and maximum values measured for that property.

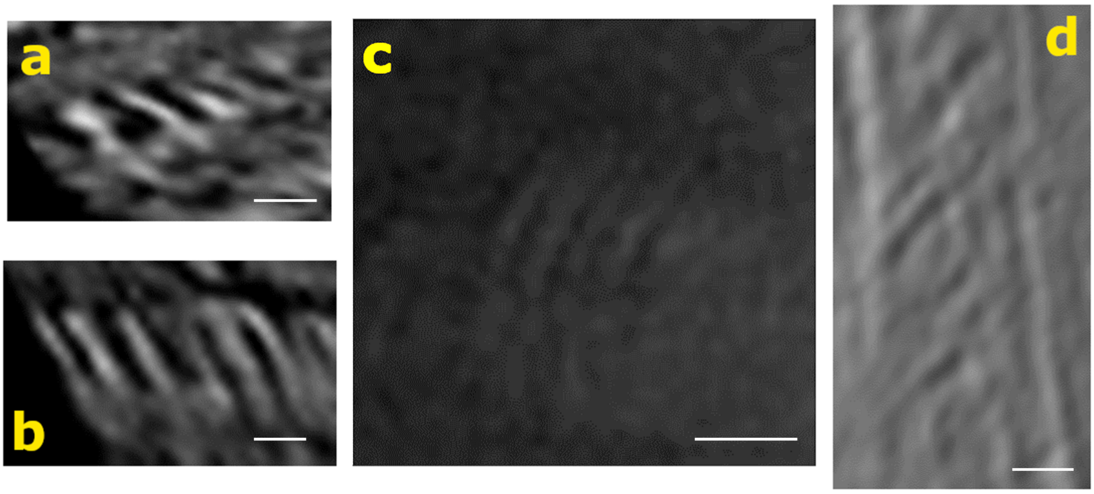

Figure 6.2.7: Examples of wave packets characterised with VIRTIS and IR2. The two images on the left (a(VI0834_04), b(VI0607_07)) show the crests and troughs very clearly, with a sharp contrast in comparison to the background atmosphere. The two images on the right (c(ir2_20160905_033333_226_l2b_v10), d(VI0588_05)) show that the boundary for the width of each different crest is not as clear. The white bars on each image represent a distance of 100 Km.

was limited (minimum of 12 km/pix on VIRTIS and 5 km/pix on IR2) and so there is the possibility of waves with shorter wavelengths that we were unable to characterise in our observations. In fact, such small packets have been detected in the upper clouds of Venus [Piccialli et al., 2014] and it is unclear if such waves also exist on the sounded atmospheric layer in this study. Also, the widths of some of these packets changed considerably within their extension (packet length), which lead to larger deviations from the mean value of the packet width. Furthermore, some of the packets did not have a clear boundary from where the crests emerged from the background atmosphere, and their width might be greater than what observing conditions would allow us to see during characterisation (see Fig. 6.2.7).

As IR2 data span wider areas on Venus's nightside, higher values for the packet length were expected. However, some of these characterisations offer only the minimum packet length, as putative crests blend into the background atmosphere or the packets extend beyond the image, especially for the VIRTIS case. Since the orientation is defined as the angle relative to the parallel (line of constant latitude parallel to the equator), values are positive when increasing to the north and negative otherwise, but proper direction of propagation for these waves can only be discovered if the same wave can be identified in two or more images. As previously stated, orientation values of VIRTIS and IR2 waves have the most contrasting distributions when compared with other morphological properties. Probable cause is attributed to the broader region where the packets are located when compared to VIRTIS waves, although an explanation as to why orientation seems more affected by this than other properties remains elusive.

Figure 6.2.8 shows how the morphological properties of waves are distributed across the geographical latitude of Venus. Waves detected closer to the equator exhibit a greater dispersion in their retrieved values, but not for all morphological properties. Distinct sources and greater variability of the dynamics of the lower cloud layer at these latitudes might contribute to the dispersion of these values, creating more diverse waveforms [Horinouchi et al., 2017b].

Figure 6.2.9 shows the range of values for the relative drop in optical thickness between

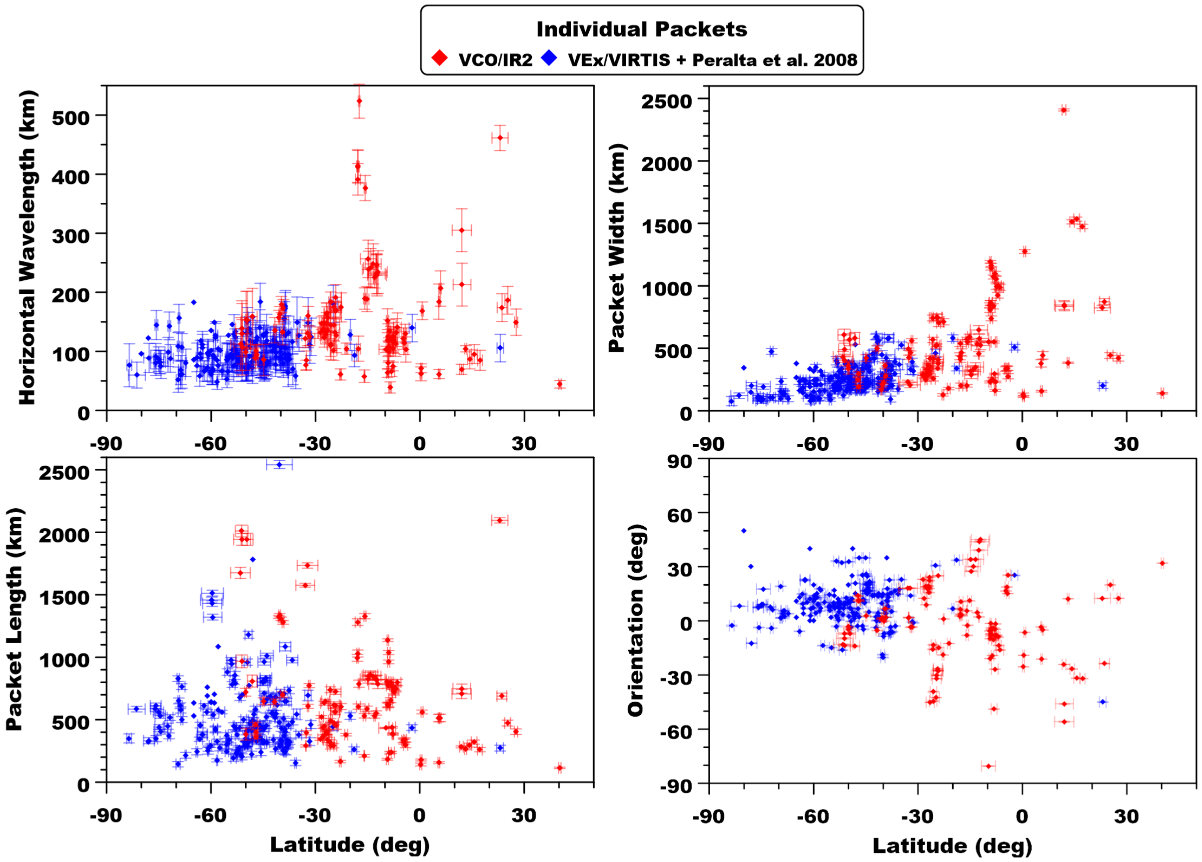

Figure 6.2.8: Distribution of morphological properties of waves with their respective latitude. Each plot point represents a wave packet detected with VIRTIS (blue) or IR2 (red).

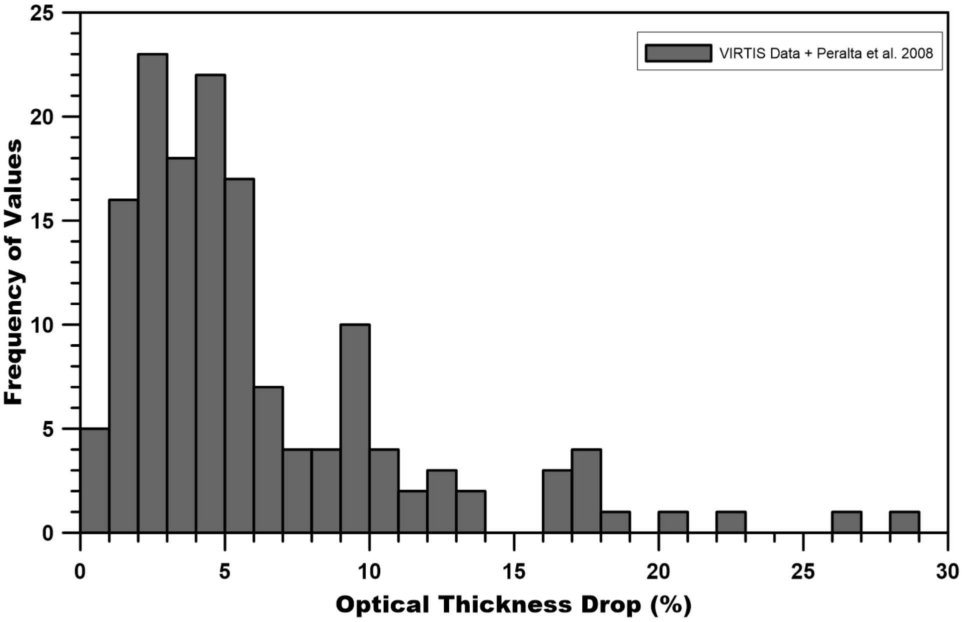

Figure 6.2.9: Histogram of the optical thickness drop ratio values for characterised packets on VIRTIS images.

crests and troughs for characterised packets. We only include data retrieved from VIRTIS because IR2 images are affected by light pollution as described in Satoh et al. [2017]. This aberration has a significant effect on the observed pixel information from which we would calculate the optical thickness, in most cases making it difficult to accurately measure the drop in optical thickness between crests and troughs with confidence.

Available data shows that for most packets the relative drop is mild, namely between 2% and 6%, with packets that have sharper differences between crests and troughs ($> 10\%$) being less frequent. However, we did not find any relation between this sharp decrease in optical thickness and any other properties or location of the wave packets. Nevertheless, there have been investigations into the relationship between optical properties of clouds and their temperature [Tselioudis et al., 1992, 1994]. Given this relation, with radiative transfer models it might be possible to derive other properties for these waves, including their amplitude and ultimately the energy they can transport.

6.2.2 Dynamical properties

With techniques akin to cloud tracking described in Machado et al. [2017], Peralta et al. [2018] and Goncalves et al. [2020], we measured the phase speed of 50 different wave packets on both instruments. Figure 6.2.10 shows the measured wave-packet phase velocity compared with the mean zonal wind profiles for the lower cloud of Venus, where these waves were detected. Each phase velocity data point represents a different packet.

Figure 6.2.11 shows the intrinsic phase velocity of measured waves. These are the values presented in Fig. 6.2.10 with the retrieved local background wind subtracted. As this calculation is performed with $\hat{c_p^x} = c_p^x$ - $\bar{u}$, where $\hat{c_p^x}$ is intrinsic phase velocity, c_p^x is the measured phase velocity, and $\bar{u}$ the local background wind, along with Venus featuring a retrograde wind flow, negative values imply a wave with its phase speed faster than the local wind and, conversely, positive values imply slower wave packets relative to the background wind.

Figures 6.2.12 and 6.2.13 show how wave packets propagate during observation. The latitude/longitude map shows the travelled distance in a straight line between the first tracked position to its last known location. Both the initial and final positions marked on the map do not necessarily represent wave generation or dissipation. The labels on each arrow represent the minimum lifetime of tracked waves as they propagate on the atmosphere of Venus. As already demonstrated in Fig. 6.2.6.D, most of the packets follow the dominant zonal wind flow along their trajectory which is further illustrated here as well as in Figs. 6.2.12 and 6.2.13.

Figure 6.2.14 presents a histogram plot of the vertical wavelengths calculated with the dispersion relation from Sect.5.3.3 (Eq.5.12). Since static stability values can change considerably with both latitude and altitude, even in such a narrow region as the lower cloud layer, the derived vertical wavelength values were obtained with corresponding static stabilities as shown in 6.2.14. In turn, these were calculated from temperature profiles retrieved with radio occultation data, whose results are summarised in Ando et al. [2020]. We considered a larger altitude range of $\sim$ 44-56 km to calculate the values for λ_z, in order to accommodate the possible variability of the altitude range where the lower cloud is estimated to be [Titov et al., 2018].

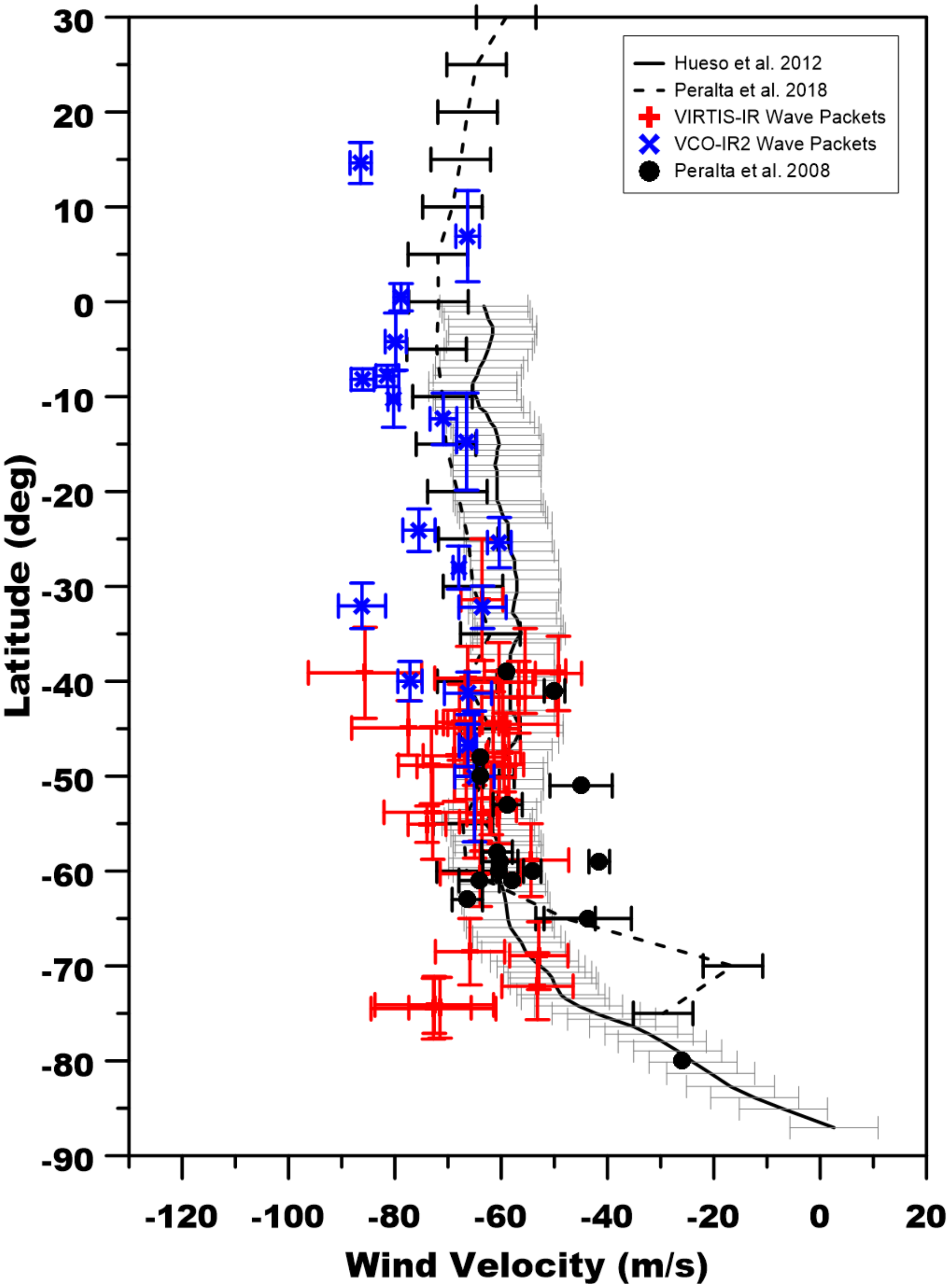

Figure 6.2.10: Zonal wind profile of Venus' lower cloud and the measured phase velocity of characterised packets from VIRTIS and IR2 data. The filled and dashed profiles in black represent the wind profiles on the lower cloud reported in Hueso et al. [2012] and Peralta et al. [2018], respectively. Blue crosses (dark grey) and red plus signs (light grey) mark the absolute phase velocity of wave packets retrieved with IR2 and VIRTIS respectively along with data from Peralta et al. [2008].

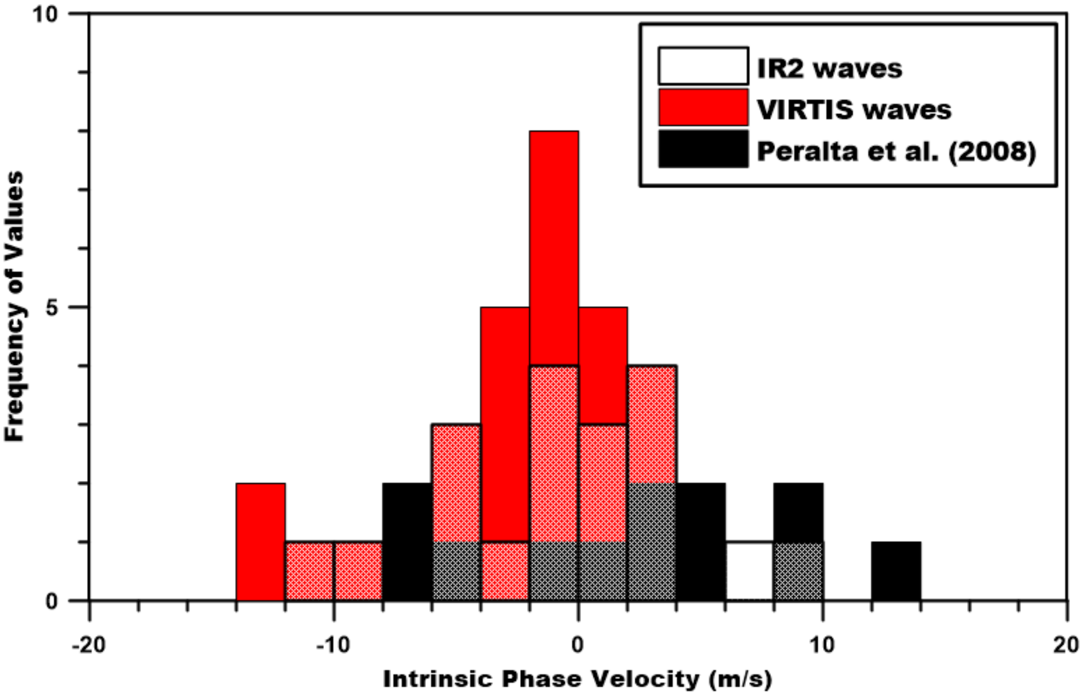

Figure 6.2.11: Histogram of intrinsic phase velocity of characterised packets. Bin size is 2 m/s and each value represents a different packet. Red (light grey) bins show values from VIRTIS data and overlaid on top with a semi-transparent pattern are values from IR2 data. Additionally, as black bins we show the data from Peralta et al. [2008].

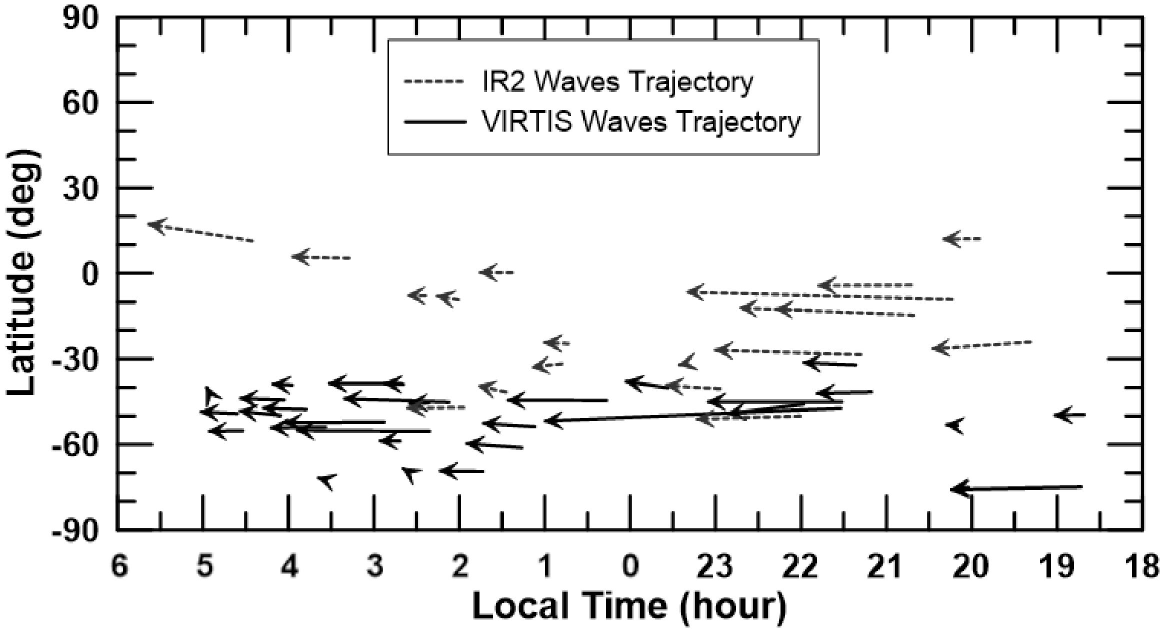

Figure 6.2.12: Trajectory of tracked wave packets from VIRTIS (filled line) and IR2 (dashed line) data on a latitude/local time map of the nightside of Venus. The length of the arrows represents the location of the first observation of the packet, following a straight trajectory to its last observed location.

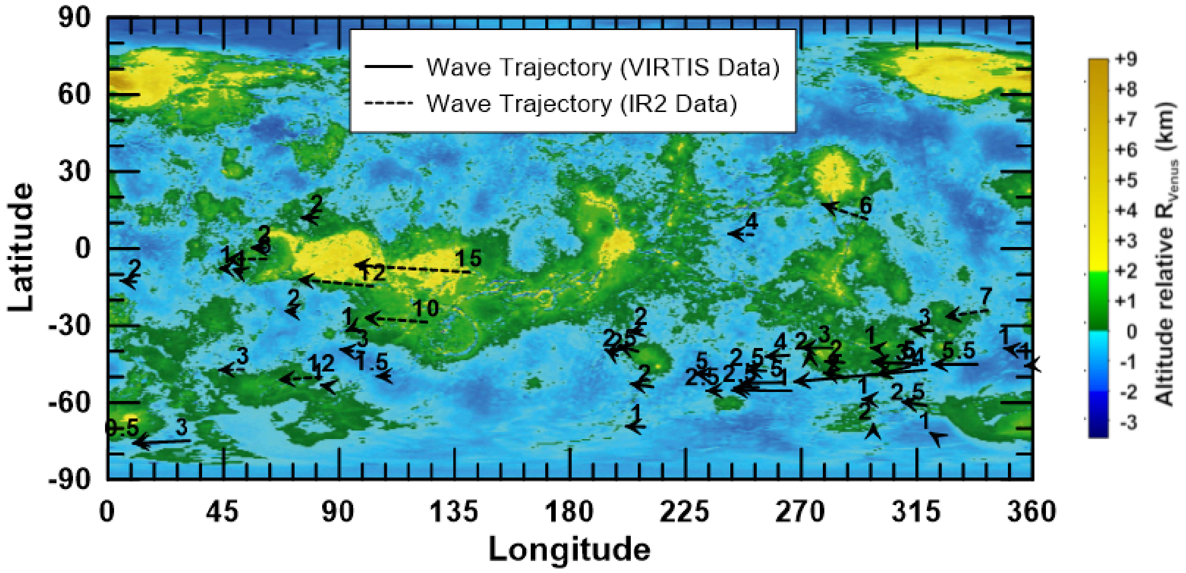

Figure 6.2.13: Trajectory of tracked wave packets from VIRTIS (filled lines) and IR2 (dashed lines) data from the location of the first characterisation to the final observed location. The labels on each arrow represent the minimum lifetime in hours of the respective packet. Topography map from Magellan probe data in the background.

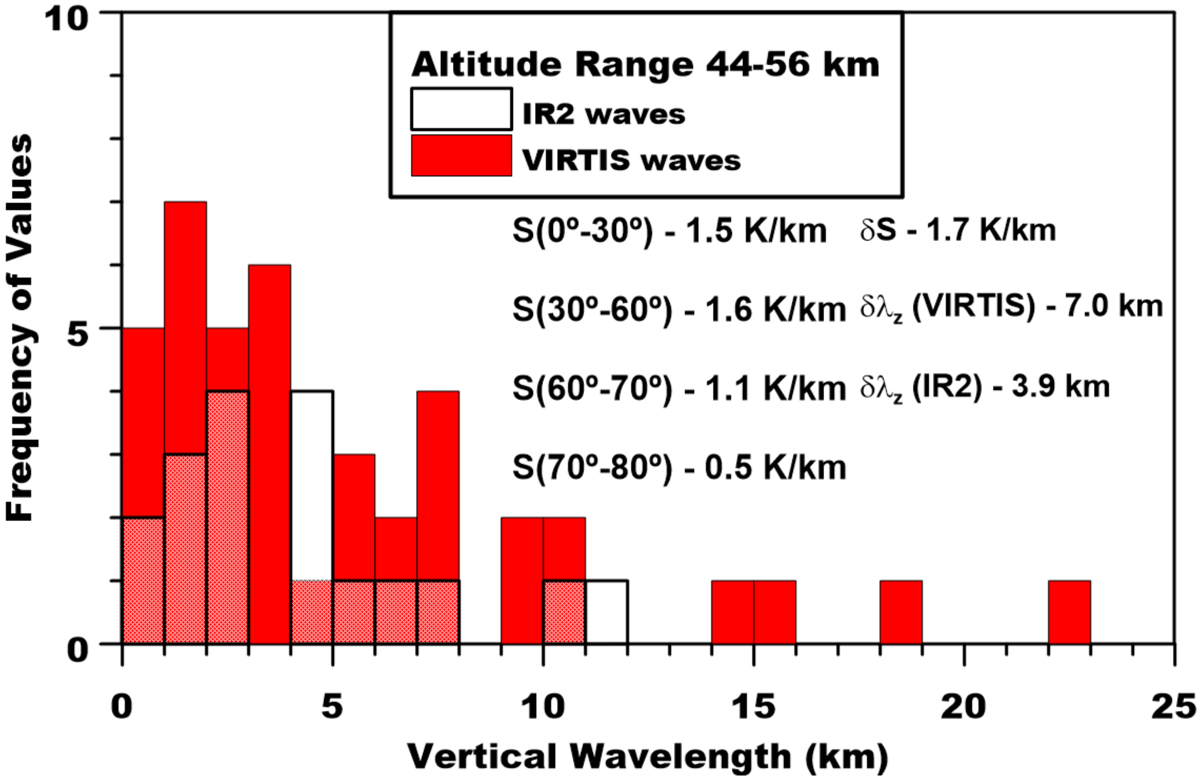

Figure 6.2.14: Histogram of the vertical wavelength of distinct characterised packets for the altitude range (44-56 km). We also present here the values of the static stability used to compute the vertical wavelengths for each latitude range (S), the mean error on the static stability (δS) from Ando et al. [2020], and the propagated errors for the vertical wavelength for both instruments ($\delta\lambda_z$). The bins are 1 km wide.

Table 6.4: Morphological characterisation precision

Instrument	Spatial resolution (km/pix)	ζ_{λ_x}	ζ_{PW} (Km)	ζ_{PL}	ζ_{θ} (°)
VIRTIS	23.9 (12.78 - 42.6)	12.23 (12.23%)	24.2 (9.68%)	18.63 (3.83%)	1.54 (17.11%)
IR2	20.6 (5.32 - 51.19)	21.95 (13.89%)	51.98 (9.86%)	36.92 (5.16%)	2.3 (76.67%)

Mean spatial resolution values followed by their respective minimum and maximum values and individual measurement errors for each morphological property measured. The percentage value is relative to the mean values retrieved for each property in Table 6.3.

6.2.3 Characterisation precision

The spatial resolution of images is the most important aspect concerning both atmospheric wave detection and their morphological and dynamical characterisation. In turn, these are highly dependent on the proximity of the spacecraft to the target location being monitored. Given the orbital characteristics of both spacecraft detailed in Svedhem et al. [2007a] for Venus Express and Nakamura et al. [2016] for Akatsuki, the mean spatial resolution obtained on images with characterised waves was ∼ 23.9 km/pix and ∼ 20.6 km/pix for VIRTIS and IR2 data, respectively, with better resolution towards higher latitudes for the former and closer to the equator for the latter.

The contents on Table 6.4 show the measurement error for each morphological property which is given directly by the spatial resolution of the image where a wave packet is detected. As discussed in Sect. 5.5.2 this resolution is highly dependent on the distance between the spacecraft and the target, controlled by its orbit around Venus. The values for ζ_{λ_x}, ζ_{PW}, ζ_{PL}, and ζ_{θ} represent the mean standard deviation between measurements of the same wave packet for each respective property. With these values, it is possible to gauge the consistency of the measuring process within each wave packet. As the error in the distance measurement calculation (see eq.5.1) is the same between measuring λ_x, PW, or PL, and since the two latter values are usually higher than the former, we expect a decrease in percentage error even if the absolute values for ζ_{λ_x}, ζ_{PW}, and ζ_{PL} rise beyond the mean spatial resolution.

The value for ζ_{θ} in Table 6.4 is remarkably higher in percentage because the mean value for orientation of packets approaches 0° (see Table 6.3). The packet length also had an observable influence on the precision of the orientation values. As such, we were able to retrieve packet orientation with greater confidence for longer waves (with larger packet length) than for shorter ones. The width of the packets also played a role in the precision of orientation measurements however, it was not as important as the packet length. Retrieved phase velocities are affected by the spatial resolution of each image and the time interval between them in much the same way as with cloud tracking, using Eq. 5.23 to calculate the error in phase speed retrieval. The average error for measured phase velocities and background wind is ∼ 6.2 m/s within the range 2.5 - 12 m/s for VIRTIS waves and ∼ 2.2 m/s within 1 - 5 m/s for IR2 waves.

6.2.4 Interpretation of Characterised Packets

The nature of characterised waves

We interpret the waves analysed in this study as internal gravity waves due to the atmospheric conditions in which they reside (static stability), as well as their combination of characteristics which are not consistent with other types of waves that could form in Venus' atmosphere [Peralta et al., 2008]. To further support this interpretation, we have built a dispersion diagram which relates different models of Venus' atmosphere, and evaluates the type of wave detected depending on their horizontal wavelength and intrinsic phase speed, as well as the latitudinal region and altitude sounded.

Figure 6.2.15 shows theoretical models for waves of various types given their respective horizontal wavelengths and intrinsic phase velocities [Peralta et al., 2014a,b]. Reference values used to build these models are detailed in Seiff et al. [1985] and Taylor et al. [1985], some of which are included in a compendium of models for the atmosphere of Venus called the Venus International Reference Atmosphere (VIRA). However, these dispersion diagrams also use more recent data from instruments onboard Venus Express for more robust modelling of the atmosphere [Piccialli, 2010, Hueso et al., 2012]. Each type of coloured line (a combination of dashes and dots) represents the analytical solution for pure waves of the appropriate type with specific vertical wavelengths. Also represented with grey lines are the Brunt Väisälä frequency (N), the centrifugal frequency (Ψ), and the centrifugal frequency modified by the meridional shear of the background zonal wind

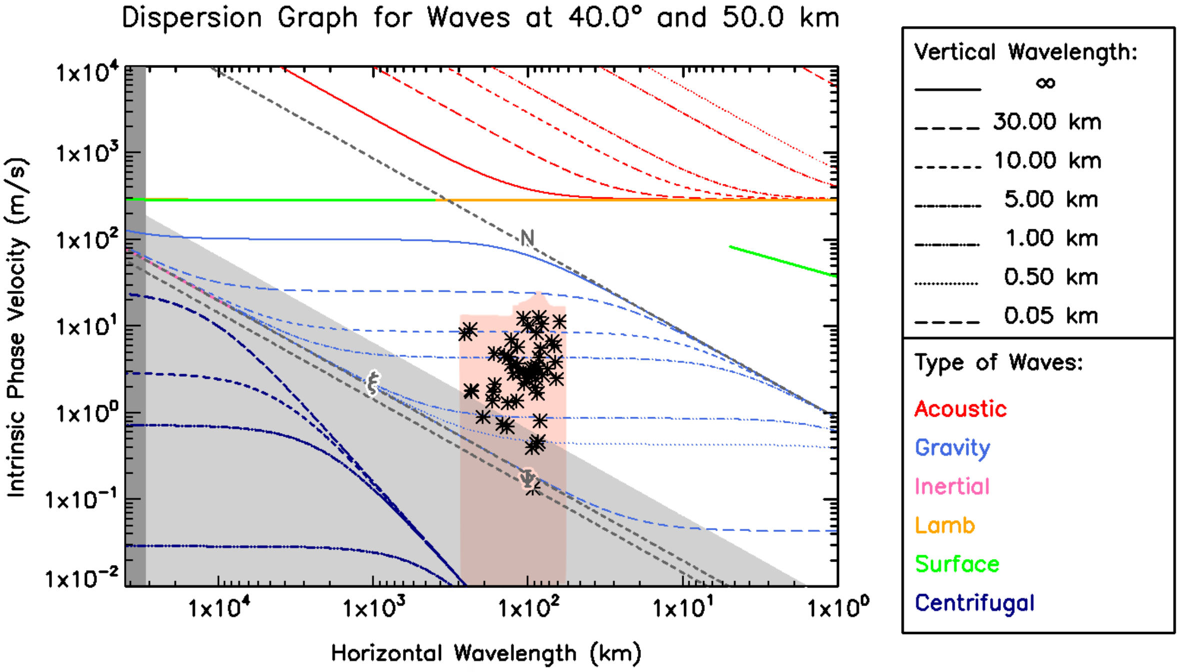

Figure 6.2.15: Dispersion diagram for dynamically characterised waves on both data sets. Each dashed coloured line represents the value of the vertical wavelength that a wave would have, given its specific horizontal wavelength and intrinsic phase velocity values according to the models described in Peralta et al. [2014a,b]. The shaded pink region over the data points represents the error on the phase velocity of the waves. Due to the logarithmic nature of this diagram, the error bars go all the way down towards the abscissa.

(ξ) [Peralta et al., 2014a,b]. Lastly, the dark and light grey shaded areas mark the limits of the maximum horizontal wavelength allowed at the respective latitude and where the usual condition in which the intrinsic frequency of waves is much greater than ξ no longer applies, respectively. In summary, these three quantities (N, Ψ and ξ) can serve as boundaries where internal atmospheric gravity waves manifest themselves and are able to propagate as such. Even though the shape of the dispersion diagram, particularly the values of N, Ψ, and ξ, are variable with latitude and altitude, we present a single dispersion diagram comprising all the data. We verified that for each of their respective conditions, most characterised packets remain within the gravity wave region and that the error bars related to the measurements are large enough to justify the use of a single mean value for latitude and altitude. As such, we used those mean values to build the dispersion diagram in Fig.6.2.15. More details on these models can be found in Peralta et al. [2014a,b].

The position of most characterised wave packets (black crosses in Fig. 6.2.15) is well within the gravity wave region. A few of these packets fall under the light grey area of the plot, where some assumptions regarding the dispersion relation used in this model are no longer valid, which makes these particular packets more difficult to interpret regarding their nature. However, with the error bars present in Figs. 6.2.15, all packets can be considered as atmospheric gravity waves. Their position in the dispersion diagram also provides an estimation of the vertical wavelength of wave packets represented by the dashed lines. The static stability used in the models, which enables the calculation of vertical wavelengths, comes from Venus Express Data and its calculation is described in Piccialli [2010] with the lowest altitude the models reach at 50 km. However, in this work we estimated the vertical wavelengths from equation 5.12, and used updated values of temperature from radio-occultation profiles from Akatsuki [Ando et al., 2020].

Vertical wavelength estimation and altitude of waves

The values for the vertical wavelength are calculated for a wider region than what is estimated to be the lower cloud of Venus (44-49 km of altitude). According to Titov et al. [2018], the altitude level for the lower cloud starts at approximately 47 km, stating that the boundary between the lower and middle cloud is not well defined, going as high as 56 km. We also know from several models of the atmosphere of Venus, such as those described in Lefèvre et al. [2018], that there is a highly convective zone above 50-51 km which makes propagation of gravity waves more difficult. Furthermore, gravity waves cannot be observed in a region where the static stability is zero [Sutherland, 2010]. We chose the larger interval, which accommodates both interpretations, as we are calculating an average result for all these altitude levels and the mean altitude value coincides exactly with the region where waves should start propagating (on the region where the static stability approaches zero, close to 50 km in altitude). Additionally, the vertical extension of these waves should not be larger than the area on which they are propagating. According to Fig. 6.2.14 we have a substantial number of waves that extend beyond 5 km (larger than the 44-49 km altitude range), and so a larger altitude interval must be considered. Regarding the convection region where we should not see gravity waves, there is a possibility, as discussed in Lefèvre et al. [2020], of transmission of gravity waves through these impossible zones, much like a quantum tunnelling effect, to upper layers of Venus' atmosphere, possibly depositing momentum and feeding the super-rotation of the upper clouds. However, we are probably seeing waves generated by the convective region between the lower and upper clouds that propagate downwards, and as the region below the supposed lower cloud ($<$ 44 km) is stable until roughly 30 km, it is possible to have waves that vertically extend down to these levels. One possible way to distinguish the altitude range within which we see waves, and whether these are propagating upwards or downwards, could be via the verification of upper cloud images at the same geographical locations as the waves in this study. With these detections we could measure cloud properties and dynamics for any possible alteration due to the waves propagating in the lower cloud.

Estimated values of the vertical wavelength do not take into account the presence of vertical wind shear of the zonal wind, or that the static stability below the cloud layer (where it can propagate) changes with altitude, which influences the form of Eq. 5.12. Considering the effects of wind shear on the propagation of waves, it is possible to verify whether or not the influence from vertical shear is great enough to produce significant changes to the vertical wavelength of characterised waves. We can use the relation $|\hat{c_p^x}| > \lambda_z.|\frac{\partial \bar{u}}{\partial z}|$ from Iga and Matsuda [2005] to determine whether or not the waves studied here are fast enough to avoid perturbation by vertical wind shear within one vertical wavelength. We took this analysis to the dynamically characterised packets and concluded that all waves are indeed fast enough for the vertical shear of the zonal wind to be insignificant. To further develop our analysis of this issue we recalculated the vertical wavelength using a more complete equation, which includes wind shear and performs the Wentzel-Kramers-Brillouin (WKB) approximation. This way, an alternate analytical formula can be obtained to compute the vertical wave number. Further details on this equation and the approximations used can be found in the textbook by Nappo [2002]:

$$m^2(z) = \frac{N^2}{\hat{c_p^x}^2} + \frac{\partial^2 \bar{u}}{\partial z^2}\frac{1}{\hat{c_p^x}} - \frac{1}{H\hat{c_p^x}}\frac{\partial \bar{u}}{\partial z} - \frac{1}{4H^2} - k^2, \tag{6.1}$$

where the partial derivative terms of the background zonal wind correspond to the vertical shear and its variability within the middle-lower cloud. Vertical profiles of the zonal wind can be found in Peralta et al. [2014a] which are based on data from Pioneer Venus probes as well as more recent cloud-tracking data of the upper and lower clouds. In Table 6.5 we present the range of values considered for the different variables at play in Eq.6.1. Wind shear values are obtained from the vertical profile of the zonal wind in Peralta et al. [2014a].

Comparing the results between estimated vertical wavelengths obtained from Eqs.5.12 and 6.1 we arrive at an approximately 4% relative difference between the results from both equations. These results, which are consistent with the verification from Iga and Matsuda [2005], allow us to conclude that the vertical shear, although present on the sounded region of the atmosphere, has insufficient influence to perturb the vertical extension of the characterised waves.

Dependence on latitude/local time and influence on wave properties

Figures 6.2.12 and 6.2.13 show that in general, the waves identified in this work mostly follow a zonal downstream propagation, and as we see in Fig. 6.2.6.D, the wave fronts are generally perpendicular to parallel lines moving the perturbation mostly westward. As gravity waves seem partially limited by ξ in terms of propagation [Peralta et al., 2014a],

Table 6.5: Variable values on the estimation of λ_z

Latitude Range	0-30°	30-60°	60-70°	70-80°
N × 10^{-3} (s^{-1})	(5.5 ± 5.2)	(5.7 ± 5.3)	(4.9±7.6)	(3.6±6.7)
$\hat{c_p^x}$ (m/s)	[-12.6 – 12.7] ± 4.4			
$\frac{\partial \bar{u}}{\partial z} \times 10^{-3}$ ($m.s^{-1}.Km^{-1}$)	-0.9 ± 2.3			
$\frac{\partial^2 \bar{u}}{\partial z^2} \times 10^{-6}$ ($m.s^{-1}.Km^{-1}$)	1.2 ± 2.4			
H (m)	6380			
k × 10^{-5}(m^{-1})	[2.7 – 10] ± 1.2			

The latitude range intervals are the same as in Ando et al. [2020]. Values for N are obtained using the equations in Sect.5.3.3 and the temperature profiles obtained from radio occultation data from Akatasuki, described in Ando et al. [2020]. We present the value and its propagated error for each entry. For $\hat{c_p^x}$ and k we present its range of values (minimum and maximum) across both VIRTIS and IR2 datasets and the mean velocity error and propagated error for the wave number across all measurements. For the wind shear and its variability we present the mean within the largest altitude range described earlier (44-56 km) along with its standard deviation across all latitude ranges as all values are within the presented error.
The Scale-height magnitude is the reference value for the cloud layer of Venus [Peralta et al., 2014a].

we investigated the relationship between morphological aspects of waves and the retrieved dynamic properties.

We can see from Fig. 6.2.16 that most of the identified waves tend towards shorter lifetimes even for the case of IR2 waves. Even though few wave packets were observed over long periods (more than 10 hours), wave packets that live the longest tend to have slower intrinsic speeds. For shorter-lived packets, intrinsic phase speed is shown to be more variable. The bottom plot compares the observed packet lifetime with their respective mean orientations from parallel. Even though most packets have small orientations (mostly zonal downstream propagation) there is no apparent influence of orientation on lifetime, as shown by the data retrieved from IR2. The top plot possibly indicates that waves tend towards equilibrium with the zonal flow when they disperse [Sutherland, 2010].

Possible mechanisms for wave generation

Surface forcing - The asymmetry of wave occurrence on Venus could suggest a forcing mechanism probably linked to either topography (non-stationary Lee waves) or any other localised features that are dependent on longitude or local time. In both bottom plots of Fig. 6.2.4, there are two areas where wave occurrence is higher, one of which corresponds to the Aphrodite Terra, a large mountain range, while the other does not appear to be linked to any remarkable topographic feature. It is also relevant to point out that we also see a higher occurrence of waves at local times not long after dusk (terminator) and before dawn. However, results supporting a clear local time dependence remain inconclusive, as already found by Peralta et al. [2008].
Even though there is a concentration of packets in the region between Helen Planitia and Lavinia Planitia this can be attributed to an observation bias, as this region features a higher number of observations, especially with VIRTIS images during the observed period.

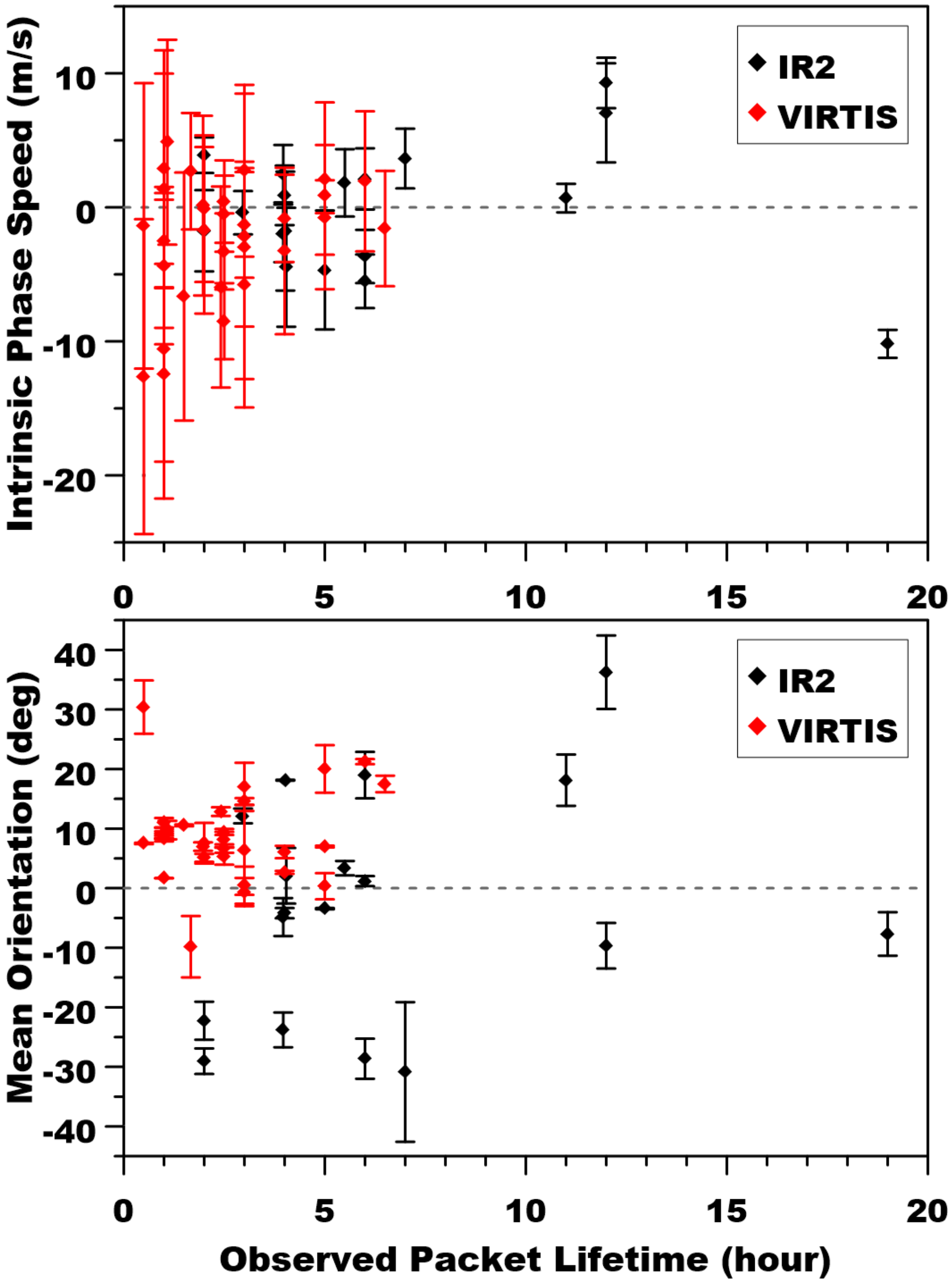

Figure 6.2.16: Observed lifetime of identified packets (whose dynamics are characterised herein) versus their intrinsic phase speed (Top) and mean orientation (Bottom). Each point represents a single packet. The error bars for intrinsic phase speed correspond to the velocity error, the calculation of which was performed with equation 5.23, while the error bars for orientation represent the standard deviation from the mean value between all orientation measurements for each specific packet.

As such, there is no clear wave dependence with any geographical location on Venus, at least for small-scale waves in the lower cloud.

The static stability profile of the lower cloud and below has been observed from entry probes (Vega 2 down to the surface and Pioneer Venus probes down to 12 km altitude) and is available in the VIRA model [Seiff et al., 1985, Zasova et al., 2007]. It shows a low (down to zero) static-stability region between roughly 20 and 30 km of altitude, and the zero-static-stability convective layer in the low and middle clouds (roughly 50-55 km altitude). This convective layer, and the stable region immediately below, is also characterised from radio-occultations from Magellan, Pioneer Venus, and Akatsuki, as recently discussed by Ando et al. [2020]. It is clear from these observations that the static-stability profile is dependent on local time and latitude.

As atmospheric gravity waves cannot propagate in unstable regions [Nappo, 2002, Sutherland, 2010], the vertical movement of waves that would be forced on the surface would be compromised through this low-static-stability region. However, Lefèvre et al. [2020] showed that stationary gravity waves generated by topographical features can indeed travel upward to the cloud deck through a type of tunnelling effect due to their large vertical wavelengths. These stationary waves are proposed to explain the presence of the large-scale bow-shaped stationary waves observed with Akatsuki [Fukuhara et al., 2017]. The transmission factor for waves with similar wavelengths to those retrieved for this study reaches 20% for the lowest unstable layer (mixed layer), and up to 45% for the cloud convective layer considering their thickness [Lefèvre et al., 2020]. Therefore, it could be possible that waves generated near the surface could be part of those seen in the lower cloud region in our work. Furthermore, the horizontal wavelength of trapped lee waves on Venus, with the mesoscale model described in Lefèvre et al. [2020], is about 150 km, which is ten times greater than what is found on Earth [Ralph et al., 1997], and consistent with the waves in this study. However, according to the simulations performed by Lefèvre et al. [2020], the vertical wavelengths of these waves should be at least three times greater than what we calculate from our estimation with radio occultation data. Additionally, such mountain-generated waves as those described in the observations performed in Kouyama et al. [2017] and the models of Lefèvre et al. [2020] seem to be preferentially generated in the afternoon, which makes observations of trapped lee waves generated by mountains on the nightside unlikely. Also, there are a significant number of waves whose location does not match any remarkable topography, and the mesoscale simulations imply that some of the estimated vertical wavelengths for the observed packet should not be allowed to propagate because of limitations from near-surface conditions. Moreover, stationary waves have not yet been reported on the nightside lower cloud [Peralta et al., 2017b, 2019], preventing confirmation of this hypothesis. Also, mesoscale simulations of orographic gravity waves might not be suitable to model the non-stationary waves presented in this work.

Convection and Instabilities - It has been argued before that the most likely source of excitation for these waves is convection, in particular from the convectively unstable region in the lower and middle cloud [Baker et al., 2000a,b, Imamura et al., 2014]. Efforts to model convection-generated waves in the lower cloud [McGouldrick and Toon, 2008] have shown that such waves could be observable in VEx/VIRTIS images. The most recent simulations done with an idealised Large-Eddy-Simulation model [Lefèvre et al., 2018] have shown that gravity waves were generated both above and below the convective layer. These latter authors also showed the strong influence of the vertical wind shear on the wavelengths and direction of propagation of the gravity waves. In this latter model, the strong convective activity induces gravity waves below the clouds over roughly 5 km, with or without wind shear. The presence of wind shear makes the wavefronts align perpendicularly to the wind direction, and increases the horizontal wavelength. This is interpreted by the authors as the consequence of an obstacle effect due to the interaction of the background wind with convective updrafts and downdrafts. This is consistent with the observed orientation measured in the present work, as well as with observations reported for the upper cloud (where the meridional wind is much stronger than below the clouds). Indeed our results are consistent with some predictions from models of convectively generated waves, namely their estimated vertical wavelength and spatial scales (morphological properties).

Some of the characterised packets might also be generated through a Kelvin-Helmholtz instability mechanism. With the estimated values of the Brunt Väisälä frequency from the static-stability profiles and the vertical profiles of the zonal wind from VIRA models presented in Peralta et al. [2014a], we calculated the Richardson number (R_i) for different latitudinal bins and heights as presented in Sanchez-Lavega [2011], but without the contribution from the vertical shear of the meridional wind as we lack the spatial resolution to retrieve reliable data for the meridional wind in the lower cloud [Hueso et al., 2012]. For an altitude range of 44-52 km, R_i is mostly between 0.001 and 0.194 in our calculations for Venus, which suits the narrow region for the generation of Kelvin-Helmholtz instabilities ($0 < R_i < 0.25$) [Sanchez-Lavega, 2011]. However, the critical value of R_i for which instabilities occur is subject to debate, because some authors suggest that the flow might be unstable for much higher values of R_i [Piccialli, 2010]. This leads to some uncertainty over the conditions where we might expect these types of instabilities to form, and whether or not these can be responsible for gravity waves such as those characterised in this paper.

Some of these waves could also be generated by shear instabilities within the lower cloud. Several packets seemingly interact with their environment and such perturbations could also be part of a wave-generator mechanism. From Fig. 6.2.17 we notice there is an increase in the vertical shear of the zonal wind at latitudes close to 60°. This not only coincides with the cold collar region but also with the highest concentration of packets observed in our study. Even though this large number of packets has been addressed as an observational bias from VIRTIS, their location might be linked to this rise in wind shear and be generated by an instability provoked from it.

One last aspect regarding wave generation and propagation that is important to clarify is that, depending on the source, waves in this cloud region travel in vertically different directions, therefore either propagating upwards into the convective layer with almost zero static stability, or to deeper layers of the atmosphere of Venus [Lefèvre et al., 2018].

Wave excitation and dispersion: Impact on circulation

Observation of apparent packet excitation and/or dissipation was possible for a small number of packets. These were registered simply as positive confirmation of the presence of a wave in a given location and, with the calculated value of its phase velocity, we can estimate its position on another image at an earlier or later date. In a very small number of cases, we were able to catch a glimpse of either small disturbances that would grow into

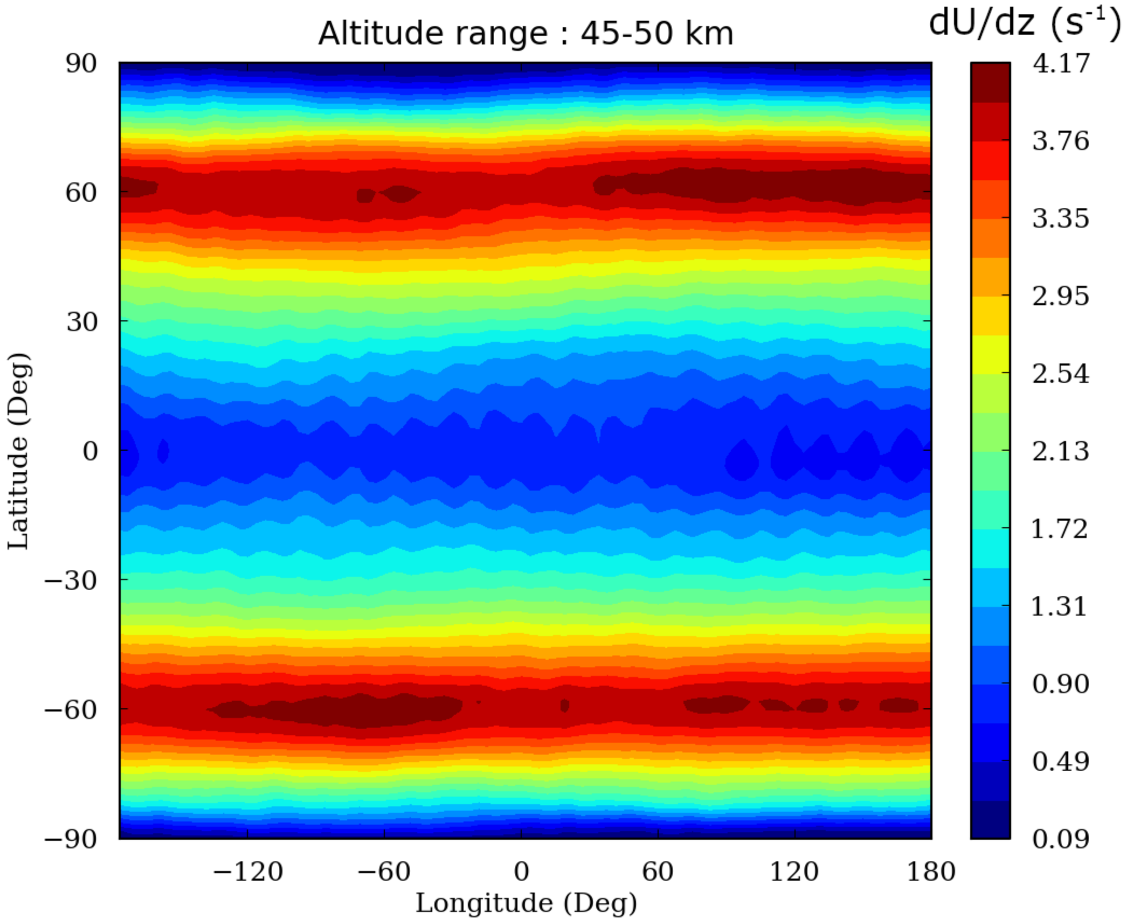

Figure 6.2.17: Latitude/longitude map of the vertical shear of the zonal wind at the altitude of the lower cloud layer. Vertical wind shear is in m.s^{-1}.Km^{-1}. An increase in the vertical shear is noticeable in the cold collar region on both hemispheres.

a wave packet that was characterised, the result of breaking or dissipation of a wave, or simply the disappearance of a packet in the time interval between two sequential images of the same location. Some of these packets are seen to lose part of their structure, and in one particular case we see a wave packet interacting with another feature in the atmosphere of Venus, and its structure being dissipated as it passes through. We analysed the influence of the wave packet dissipation on the background wind flow by taking wind tracers in the region where the wave would pass, before or when the wave packet was active, and after breaking.

Even though the breaking of gravity waves dumps energy and momentum on their respective atmospheric layer, and as such we could expect an increase in the background wind flow velocity after dissipation, we verified that for all cases the wind flow was slowed after the wave disappeared, and in four of the five cases we could see that for waves with greater intrinsic phase speed, this drop was larger (see Table 6.6).

Unfortunately, opportunities to accompany wave propagation until breaking or dissipation were extremely rare for this data set, because this has to be combined with the already limited available data of dynamically characterised waves as explained in Sect.6.2.2. Possible solutions might include more continuous observations of the nightside of Venus, such

Table 6.6: Observed appearance/disappearance of wave packets

Orbit	Date (dd/mm/yyyy)	Time (UT-hour)	Lat (deg)	LT (hour)	$\hat{c_p^x}$	δU (m/s)	ΔU
607	18/12/2007	17.48 - 22.48	-44	2.7	-1.575	11.041	14.241
r0025	04/09/2016	15.06 - 17.06	1	1.6	3.901	1.553	3.884
r0026	05/09/2016	03.56 - 05.56	-24	0.8	-1.741	3.439	14.844
r0026	05/09/2016	04.56 - 09.56	-32	23.3	-4.667	3.846	18.38
r0026	05/09/2016	04.56 - 10.56	-40	23.1	2.131	3.509	15.519

The orbit column follows the respective nomenclature norms for each spacecraft (the first entry corresponds to VEx/VIRTIS and the four remaining belong to Akatsuki/IR2); Time refers to the temporal window of observation of the wave packet; Lat, LT refer to the mean latitude and local time of the packet during propagation; $\hat{c_p^x}$ is the intrinsic phase velocity; δU is the wind measurement error and ΔU is the wind speed drop between the wave packet appearance and disappearance.

as those that could hypothetically be achieved by what is proposed in Kovalenko et al. [2020], with micro-spacecraft inserted on Sun-Venus' Lagrange point orbits. Other solutions include further model studies on the transmission of waves between layers of the atmosphere similar to Lefèvre et al. [2020], concentrating on mesoscale waves in order to distinguish exactly where these waves dissipate.

Comparison with previous wave studies

Beyond the above-mentioned study of atmospheric waves in the lower cloud [Peralta et al., 2008], very few extensive analyses of this kind have been carried out. Peralta et al. [2019] characterised a large number of cloud morphologies observed on the nightside of Venus with Akatsuki/IR2, including wave packets. Even if they were not the focus of that particular study, waves identified in Peralta et al. [2019] served as valuable confirmation of wave packets identified for this work, as well as validation of some characterisations of waves. Another study, focusing on atmospheric waves on the dayside upper clouds, was presented by Piccialli et al. [2014]. Their survey covers the northern hemisphere from 45° to polar latitudes at a latitude of approximately 66 km. Such waves are also interpreted as gravity waves, however the morphological properties of those wave packets have much smaller scales, which can be related to the narrower field of view and higher spatial resolution of VEx/VMC images during pericentric observations. The dimensions of the upper cloud waves in this latter work were reported to be about one order of magnitude smaller than what we find for wave packets in the lower cloud. The orientation of wave packets has a broader distribution than our findings, and wave packets are concentrated above the mountain range Ishtar Terra. Wave properties and the distribution of wave activity suggests that Kelvin-Helmholtz instabilities or surface forcing play important roles in generating the waves found by Piccialli et al. [2014] and [Peralta et al., 2019].
The contrast between dayside upper cloud and nightside lower cloud waves is readily apparent by their morphological properties and distribution, acknowledging that the study by Piccialli et al. [2014] was confined to a region in the north hemisphere due to an observational bias from VMC observations [Markiewicz et al., 2007]. Also, because of the

Table 6.7: Averaged Doppler winds on each band of Jupiter observed with ESPRESSO

[1] Latitude (°)	[2] Doppler Wind (m.s^{-1})	[3] Error (m.s^{-1})
0	119.30	9.07
10	99.43	10.1
-10	52.49	6.65
15	-16.8	9.17
-15	-18.4	13.36
-21	33.2	16.3

[1] Observed latitude band; [2] Zonal wind speed calculated from Doppler Velocimetry technique; [3] Average error of measurements in its corresponding latitudinal band. Negative values of the zonal wind indicate westward flow.

spacecraft orbit, these latter authors were unable to retrieve dynamical properties from waves in the upper cloud [Moissl et al., 2009].
This divergence in properties could also indicate a different forcing mechanism for gravity waves at different altitudes, or it could be that the conditions in which we find both types of wave packets (dayside upper cloud and nightside lower cloud) constrain the observable morphological properties. Future analyses of wave packets in the upper clouds in ultraviolet images from Akatsuki's Ultraviolet Imager (UVI) could help further confirm these hypotheses and possibly establish a connection between gravity waves on both cloud layers.

6.3 Analysis of the winds on Jupiter at the Troposphere

6.3.1 Doppler winds with VLT/ESPRESSO

The results presented in this section constitute a first-time retrieval of atmospheric winds on Solar System planets by the ESPRESSO instrument. Thus, given the exploratory nature of this work, we regard these as the first step to fine-tune our model of observation and techniques for the next generation of instruments and telescopes.
With our observing strategy and posterior data reduction and corrections we were able to retrieve multiple longitudinal profiles of the zonal component of the winds in Jupiter at selected band signalling the distinct flow regimes.

The changing wind flow regimes on equatorial latitudes (20°N - 20°S) on Jupiter's atmosphere is readily apparent with our results presented in Table 6.7. The values presented form an average of the Doppler winds retrieved at each latitude band. Figure 6.3.1 shows the wind velocity values retrieved along each band for each position observed with ESPRESSO. For this observing run, the winds are stable within the error bars of the retrieved data however, at the 10°N band we notice greater variability.

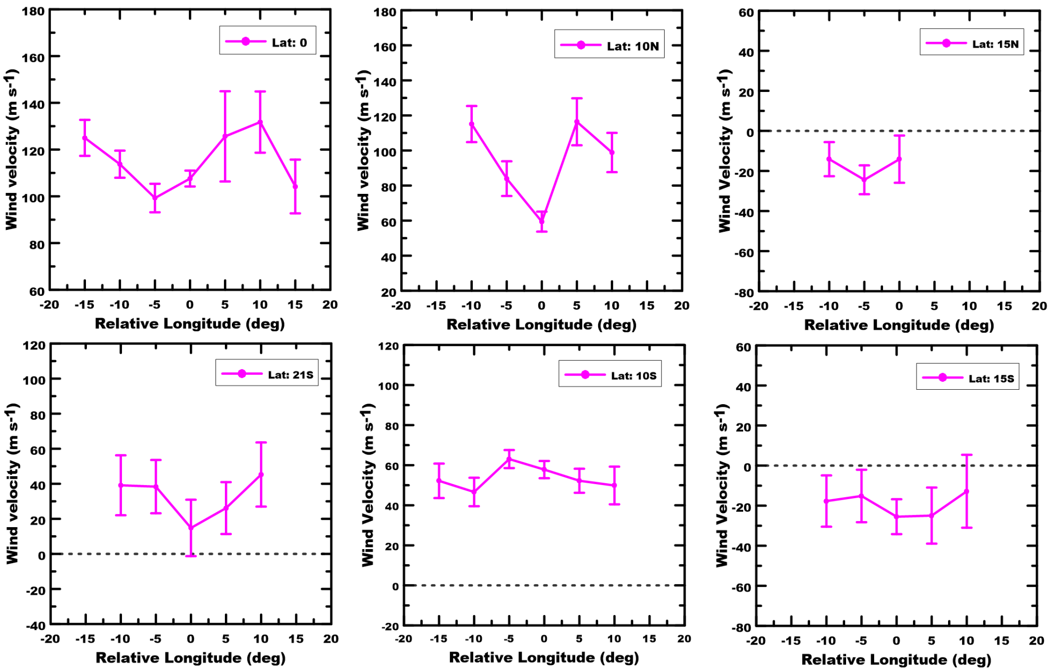

Figure 6.3.1: Longitudinal profiles of the zonal wind on each band in Jupiter with observations from VLT/ESPRESSO. The longitude in these plots has the sub-observer longitude as a reference point, hence it is not the true planetary longitude

6.3.2 Comparison with previous measurements

Cloud Tracking

Given the general stability of the zonal wind profile of Jupiter, we can compare our Doppler velocimetry retrievals with previous results, even if observations are separated by a number of years. However, some caution must be taken since, although the general variability of the wind profile stays on the order of 10 m/s, which is comparable to our error bars, episodes of increased variability have been observed Asay-Davis et al. [2011]. The magnitude of the jets at approximately 7°S and 6°N, and 24° has been noticed to change by more than 40 m/s at specific periods of observation Garcia-Melendo et al. [2011], Barrado-Izagirre et al. [2013], Johnson et al. [2018].

The general stability of the zonal wind profile of Jupiter can be verified in Fig. 6.3.2. This plot also highlights the periods of variability at specific regions on Jupiter's banded circulation. Several authors have explored the causes for these changes Garcia-Melendo et al. [2001], Asay-Davis et al. [2011], Tollefson et al. [2017], mentioning that the time intervals for these variations can range from hours to months, making it difficult to determine the average zonal wind profile and the exact culprit of many of these changes Asay-Davis et al. [2011]. For all measurements in Fig.6.3.2, a cloud tracking method was employed even if several techniques from individual Garcia-Melendo et al. [2001] and automatic tracking Salyk [2006] to 2D correlation routinesChoi et al. [2011], Galperin et al. [2014] were used.

Our cloud-tracked winds from Cassini images on Jupiter (see Table 4.5) were also used in this long term comparison, given the general stability of the profile as addressed ear-

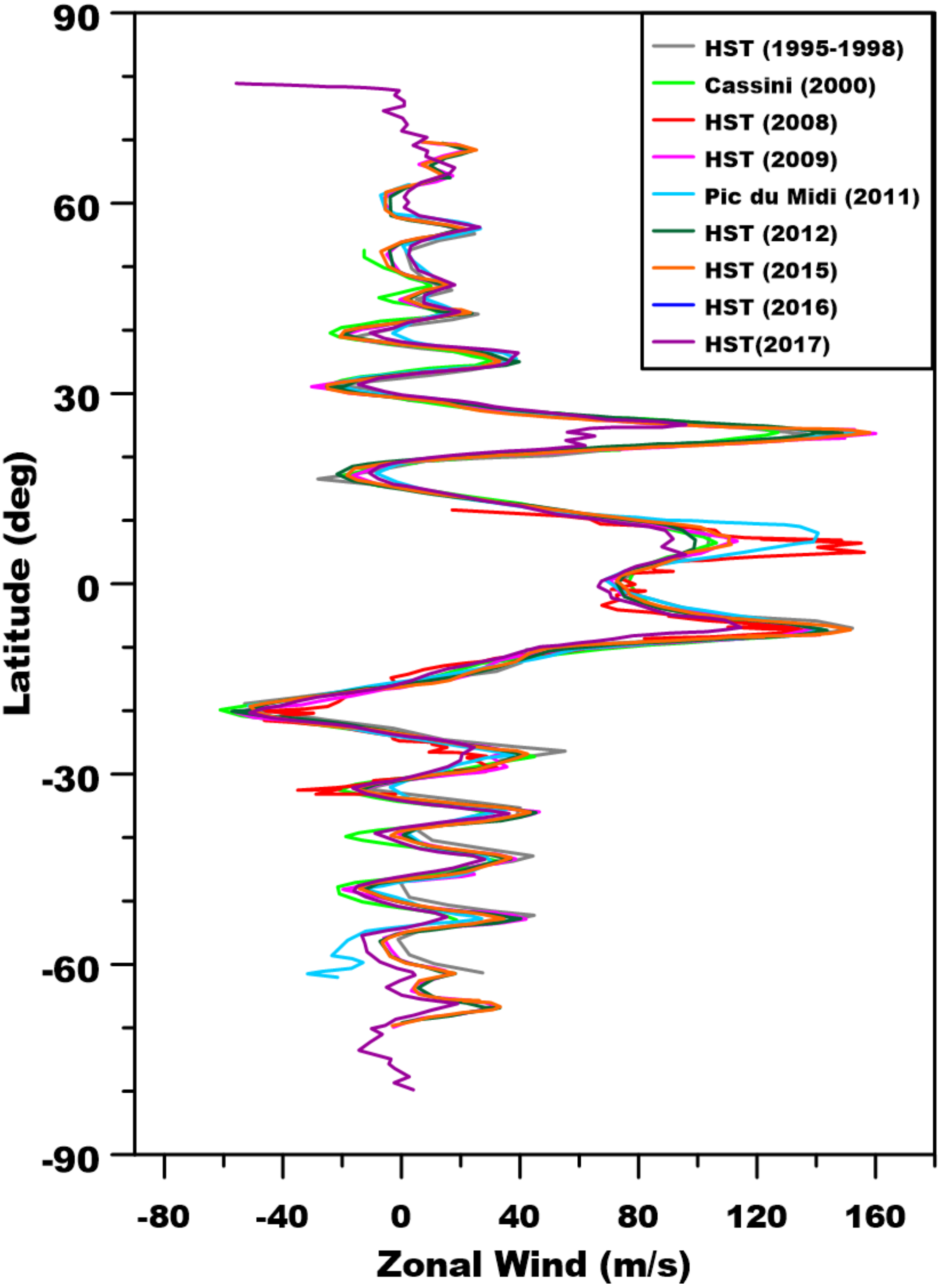

Figure 6.3.2: The zonal wind profile of Jupiter's upper tropospheric clouds at approximately 0.7-1.5 bar. The different profiles concern observations throughout approximately two decades taken with Cassini during its fly-by manoeuvre in December 2000 Galperin et al. [2014], ground observations at Pic-du-Midi Barrado-Izagirre et al. [2013] and HST Garcia-Melendo et al. [2001, 2011], Tollefson et al. [2017], Johnson et al. [2018]. The winds represented here were retrieved with cloud tracking techniques.

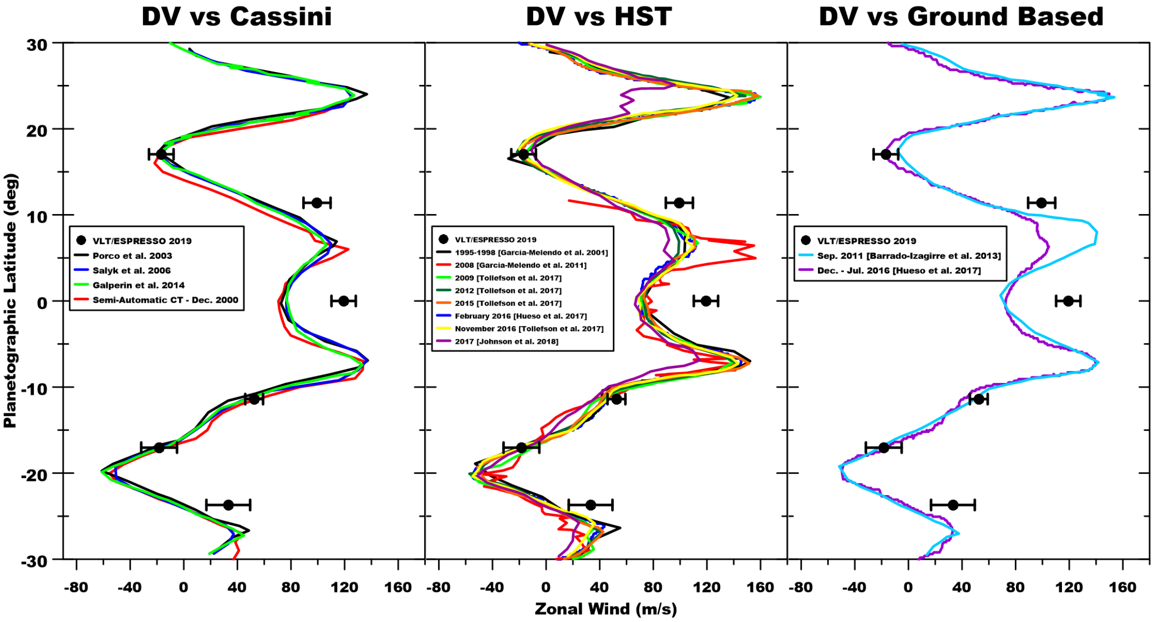

Figure 6.3.3: Comparative wind profiles retrieved from Cassini, HST and ground based observations with Doppler velocimetry results at visible wavelengths. We limit the profiles to equatorial latitudes to match the range of our ESPRESSO observations. Each of the wind profiles used for comparison is taken from a previous publications with the exception of the red profile in the leftmost panel. These are wind velocity results retrieved with 2D Semi-Automatic Correlation cloud-tracking using the PLIA tool Hueso et al. [2010].

lier. A total of 5620 wind tracers were retrieved, concentrating on the regions that were also observed with ESPRESSO. We can use these results combined with legacy data from other cloud-tracking efforts shown in Fig. 6.3.2 to evaluate the consistency of our Doppler velocimetry retrievals.

We can see our Doppler velocimetry results compared with retrieved wind velocities from different instruments in Fig. 6.3.3. The Cassini profiles feature reference data from automatic cloud tracking from two separate authors Porco et al. [2003], Salyk [2006], and an additional analysis using 2D correlation of mosaics built with Cassini/ISS images during the fly-by period between December and January 2000/2001 Galperin et al. [2014]. We also included our own cloud tracking data, taken also with Cassini with a semi-automatic effort described in Sect. 5.2.1. The middle panel feature more profiles due to the higher cadence of observations provided by HST, including an effort to continuously provide imaging data on Jupiter's atmosphere to accompany its evolving atmosphere, through the OPAL program which started observations in 2014 Wong et al. [2008] on Uranus and 2015 on Jupiter Simon et al. [2015]. The record of HST observations in Fig. 6.3.3 starts in 1995 with the study by Garcia-Melendo et al. [2001] who did not report any significant changes to the zonal wind profile during their period of observation (3 years). The next set of observations occur with Garcia-Melendo et al. [2011] which couples data from both Cassini and HST in 2008, reporting an increase on the 6°N jet by approximately 40 m/s. We include then a more extensive report of HST observations in Tollefson et al. [2017], featuring Hubble data from 2009-2016, and another observation in 2016 by Hueso et al. [2017], which was accompanied by ground-based observations. The last set of data from 2017 was explored in Johnson et al. [2018], who also analysed the zonal wind profile of Jupiter with different filters from HST.

The rightmost panel in Fig. 6.3.3 shows ground based measurements taken from observations with the Pic du Midi 1 meter telescope Barrado-Izagirre et al. [2013], and a collection of different observations from Amateur astronomers and PlanetCam UPV/EHU Sanchez-Lavega et al. [2012] mounted on the 2.2 meter telescope in Calar Alto Observatory Hueso et al. [2017].
From the three profiles we can verify that there is reasonable agreement between our Doppler retrievals and previous results however, it is interesting to note that at the equator, the Doppler winds appear to be faster than any previous measurements, by a difference that exceeds 20 m/s, double what local and temporal variations to the zonal wind predict. It is possible that this value is an outlier, but given the exploratory nature of this work, and thus lack of more substantial data, it is difficult to confirm this.

Previous Doppler Velocimetry results

Since this work explores the capabilities of ESPRESSO to perform Doppler velocimetry on planetary atmospheres of the Solar System, the volume of data of this kind to compare with our observations is relatively scarce as opposed to cloud tracking. Multiple studies Goncalves et al. [2020, 2021], Machado et al. [2012, 2014, 2017, 2021] have used Doppler velocimetry to retrieve winds on Venus at visible wavelengths and other targets have been considered with similar techniques such as Mars at submm/mm wavelengths Lellouch et al. [1991], Moreno et al. [2009] and Titan in the infrared range Kostiuk et al. [2001, 2005, 2006, 2010].
Doppler velocimetry on Jupiter at similar wavelengths than this work was achieved with success for the first time in Goncalves et al. [2019] with JOVIAL-JIVE (Jovian Oscillations through Velocity Images At several Longitudes - Jovian Interiors from Velocimetry Experiment in New Mexico) observations in 2015 and 2016. A comparison between the Doppler winds retrieved for this work and previous measurements with a similar technique are presented in Fig. 6.3.4. Even though both techniques use visible solar light reflected on Jupiter's upper tropospheric clouds, and the time separation between observations is not large when looking at previous comparisons with cloud-tracked winds, there is some discrepancy between both data sets. Although there is good agreement at 10°S and 15°S, our other average values differ from the profiles retrieved by Goncalves et al. [2019] by 5-6 σ (the error bar of our retrievals) when taking into account the other data points. Since this method measures the actual velocity of atmospheric particles, Doppler winds can be subject to variations due to wave activity Goncalves et al. [2019], which can translate to higher magnitude differences than the previously mentioned 10 m/s. However, when comparing our results with observations with HST in 2015, 2016 (see Fig.6.3.3) which Goncalves et al. [2019] have used for comparison in their Doppler velocimetry results, we do not find such significant differences. It is true that this work is exploratory and it features a single observing run, but ESPRESSO has an overall higher spectral resolution than the instrument used in Goncalves et al. [2019], which can be an alternate explanation, as ESPRESSO results should be more sensitive to the alternating jets of Jupiter.

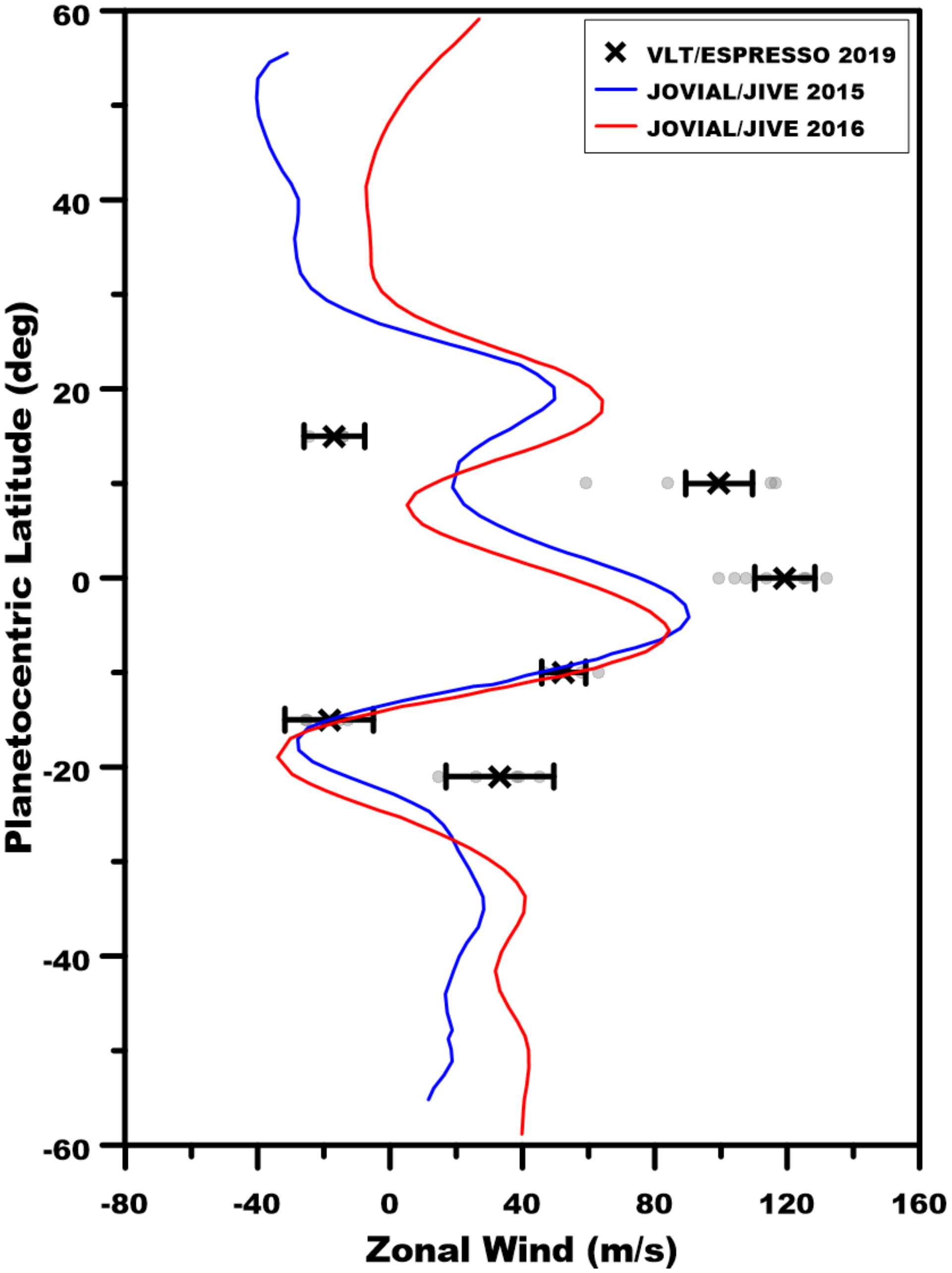

Figure 6.3.4: Zonal winds retrieved with Doppler velocimetry techniques with VLT/ESPRESSO observations (calculated average - black crosses) and the JOVIAL-JIVE retrievals in 2015 (blue profile) and 2016 (red profile). The faint gray circles are the data points of our Doppler wind retrievals from which the average was calculated, whose values are presented in Table 6.7.

6.3.3 Multiwavelength Comparison

Since ESPRESSO observations, for the purpose of this work, were performed using the full set of Fraunhofer lines in the visible part of the spectrum, it is possible that the winds retrieved with our Doppler method originate from different regions of the troposphere than the visible cloud layer observed previously with Cassini or HST. In Johnson et al. [2018], they employ a multi-wavelength analysis of Jupiter's banded structure, to study the zonal wind profile's variation as function of wavelength. In Fig. 6.3.5 we present the zonal wind profile observed at multiple wavelengths, which include both ultraviolet Li et al. [2006] and visible wavelengths Johnson et al. [2018], to compare with our Doppler results. The profile remains mostly unchanged at visible wavelengths (395-658 nm), except at the two most powerful jets at approximately 7°S and 23°N, which seem more sensitive to different wavelengths. Also, most cloud features that are identified with cloud-tracking techniques are present on many visible wavelength filters with little changes to morphology or drift rate Li et al. [2006]. Hence, the stability of the zonal wind profile across several wavelengths is also partially a consequence of the relatively large vertical structure of most tracked features. The wind profile retrieved in the ultraviolet (264 nm), tracked features that could not be observed at other wavelengths similar to the ones discussed in Johnson et al. [2018]. These higher winds at approximately 350 mbar pressure level R. West et al. [2007], appear to have less prominent jets across all latitudes and a slight increase in wind magnitude at the equator. However, it is not enough to justify the 110 m/s Doppler wind retrieved at the equator with ESPRESSO.
Longitudinal variations could also explain some of these differences between the results presented in this work and the legacy of zonal wind measurements retrieved, as these can have magnitudes that go beyond the standard deviation of our results as reported in Johnson et al. [2018].

Considerations on Altitude of Wind Velocity Tracers

Even though wind results from both our Doppler technique and cloud-tracking seem consistent, there are important differences in how these velocities are retrieved. This can have implications on their interpretation and vertical location in the atmosphere Machado et al. [2021]. The cloud-tracking method follows the movement of cloud features in the atmosphere. As such, the altitude/pressure level from which winds are extracted is directly dependent on where these features are formed and propagate, which for the case of Jupiter is roughly at the 0.7-1.5 bar level Sanchez-Lavega [2011], R. West et al. [2007]. The Doppler velocimetry method used in this work relies on back-scattered sunlight dispersed from Jupiter's atmosphere. The spectra obtained by ground-based observers is the result of a bolometric integration of this back-scattered radiation towards the observing line-of-sight. Although mostly concentrated on the region where optical depth reaches unity, which is roughly where the cloud features can form in the upper troposphere Porco et al. [2003], Asay-Davis et al. [2011], it is possible that the average radiation that arrives at the instrument's detector could include scattering from slightly higher levels. For this reason, it is reasonable to expect some fluctuations in the results from both techniques. A more extensive observing campaign of Jupiter with high resolution spectroscopy, coupled with

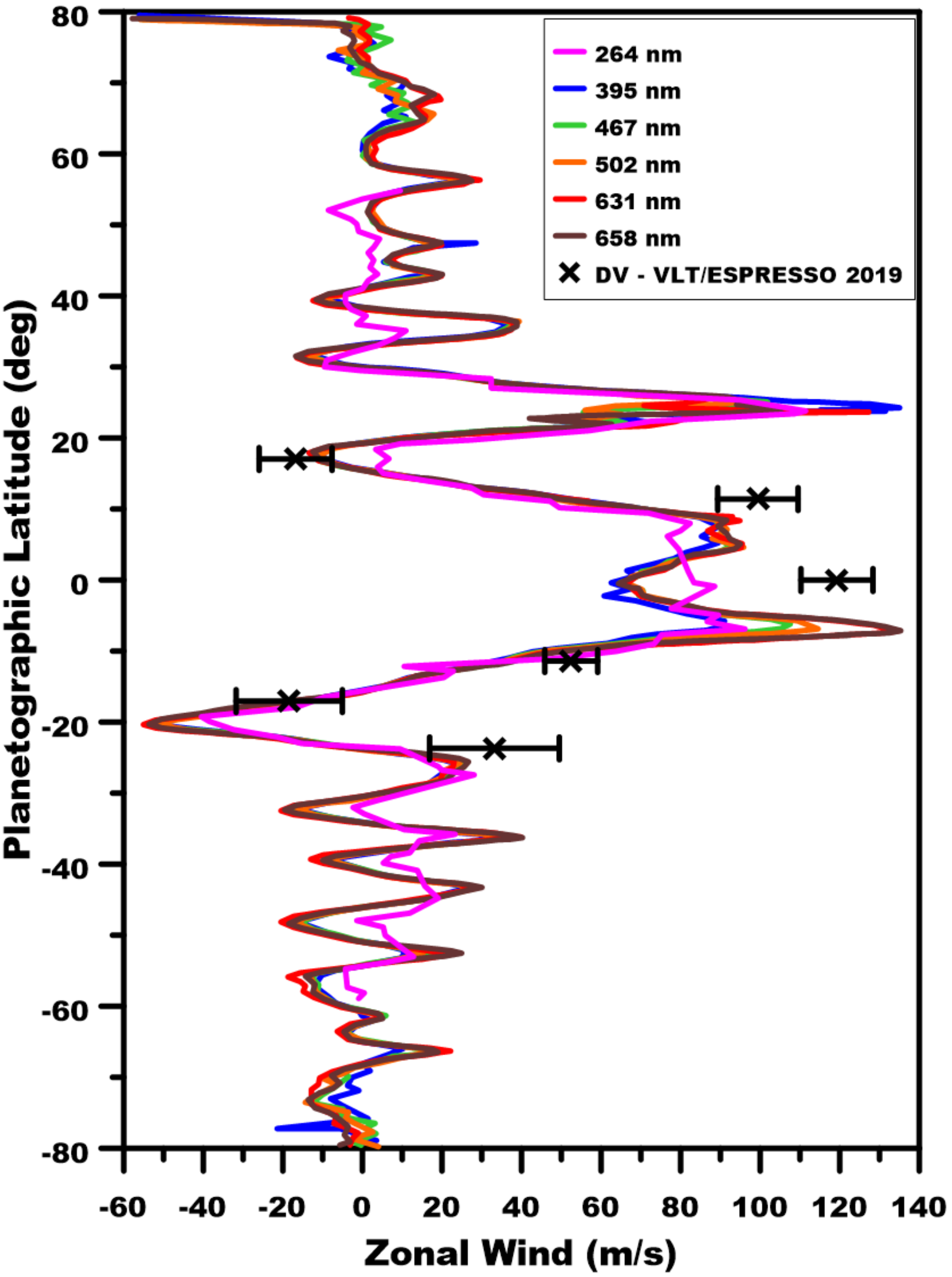

Figure 6.3.5: A multi-wavelength analysis of the zonal wind profile on Jupiter at visible and ultraviolet wavelengths to compare with the Doppler winds retrieved with VLT/ESPRESSO. The ultraviolet profile from Li et al. [2006] is the result of cloud tracking of higher altitude features than what is identified at visible wavelengths at 0.7-1.5 bar. The other five profiles were all retrieved with HST observations as described in Johnson et al. [2018].

coordinated observations to perform cloud tracking in a multi-wavelength range would allow further exploration of this subject.

Since the Doppler velocimetry method relies on solar light back-scattered on Jupiter's dayside atmosphere, the altitude of the retrieved zonal velocities ought to be located where the optical depth reaches unity [Machado et al., 2021]. Several models for the cloud properties on each band have been developed over the years which applied to the bands observed in this study show that optical thickness unity is reached in the Equatorial Zone at approximately 0.7 bar, and to slightly deeper values for both the North and South Equatorial Belts [Braude et al., 2020, Dahl et al., 2020, Simon-Miller et al., 2001]. According to these models, we can be sensing somewhere between the upper part of the cloud layer and a chromophore coating postulated by Carlson et al. [2016] to explain the red colouring of Jupiter's Great Red Spot and then expanded by Sromovsky [2017] to explain the different colourations of the belts. From this contrast between belts and zones, it is possible that features followed with cloud-tracking could be formed at different pressure levels. Also, since with our Doppler velocimetry technique we use observations in the visible wavelength range, it is possible that we might be sensing slightly different pressure levels as a function of wavelength.

Wind component entanglement

Since we are measuring winds from the radial velocity component obtained from back scattered spectra of Jupiter, the resulting wind velocity is the sum of all its components. This method has been used extensively to study Venus [Goncalves et al., 2020, 2021, Machado et al., 2012, 2014, 2017, 2021] where the zonal wind dominates atmospheric circulation at the cloud tops. For the case of Jupiter, each band can be understood as its own *Hadley* cell to the point that globally, meridional circulation is generally not measurable from Earth due to low spatial resolution [Gaulme et al., 2018]. The presence of storms, particularly in the belts, along with a high level of turbulence is evidence of vigorous convection and vertical wind shear on the upper troposphere of Jupiter, which means that the vertical component of wind velocity could be an important contributor to the overall wind velocity retrieved from the Doppler velocimetry method. Hence, there is the possibility that our method is sensitive to additional components of the wind. However, since this study covered a small region over a short time interval on the atmosphere of Jupiter, and the fluctuations between Doppler and cloud-tracking results are relatively small (5-10 m/s when not within the error bars), it is challenging to evaluate the strength of the vertical wind contribution on these results alone.

Chapter 7

Conclusions

This project concludes with the successful application of both ground and space based observing techniques to study the atmospheres of several Solar System planets. We have made an effort to cover various subjects, stringing them together with the employed methods for a comprehensive study of atmospheric behaviour. With spacecraft data from the VEx and Akatsuki missions, we have analysed the atmosphere of Venus at multiple altitude levels, gathering a three-dimensional perspective of the circulation on Earth's 'twin'. We also performed a ground-based exploration of the gas giant with ESPRESSO observations, with later comparison with the legacy of cloud-tracked data on the gas giant, including some retrievals from Cassini data performed by our team.

This analysis was performed mainly through imaging science, particularly using the cloud-tracking technique to study the general dynamics of the atmosphere, and characterisation of atmospheric waves, of which its dynamical analysis took advantage of the previously acquired proficiency with cloud-tracking. We retrieved several zonal and meridional wind profiles with this technique for both the upper and lower clouds of Venus. Our cloud-tracking effort on Jupiter was mostly complementary to other past retrievals of wind velocity in the troposphere, focusing our analysis on the same latitudinal locations observed with ESPRESSO. The data we retrieved from Cassini through cloud-tracking serve for a long-term comparison, given the 20 year separation between both observations. Ground-based observations were conducted for both cloud tracking and Doppler velocimetry purposes. With high-resolution spectra from VLT/ESPRESSO we were able to retrieve winds on Jupiter's latitudinal bands, being an exploration on the efficiency of both the instrument and the new refined method to study Solar System gas giants at visible wavelengths. The most important results from the work developed in this thesis have either been published [Silva et al., 2021], or submitted to peer-review journals [Silva et al., Submitted]. Both contribute with a step forward towards our general understanding of the underlying mechanisms at work on the atmosphere dynamics of Venus, and our ability to explore news ways to analyse the atmospheres of the outer planets, beyond the Asteroid Belt.

Atmospheric Gravity Waves

Our research on atmospheric waves in the lower clouds of Venus was motivated by the lack of a comprehensive survey for such a feature on this region of the atmosphere, while also looking for additional tools that can explain the magnitude of the superrotation in the upper clouds. Our work was oriented to follow up on the findings by Peralta et al. [2008] and Piccialli et al. [2014] on both the lower and upper clouds. Since our study of waves in the upper cloud was met by an unforeseen need for revision of the images' navigation, due to the small scale of observed waves as explained in Piccialli et al. [2014], we focussed on nightside observations to solely target the lower cloud. In conjunction with the results previously gathered, we analysed the entire VIRTIS-IR dataset at the wavelengths which target our atmospheric region of interest, and to complement these observations, we used the entire data set from the more recent IR2 camera onboard the Akatsuki spacecraft, a japanese mission which still orbits Venus. Combining both data sets was most valuable because the different orbits of both spacecraft observed Venus in high spatial resolution on different regions of the globe, contributing to a more complete characterisation of atmospheric waves.

Waves detected with VIRTIS and IR2 show similar characteristics regarding their morphological and dynamical properties, though IR2 waves show more variety even with less distinct packets. This could be attributed to waves being detected on a wider range of latitudes and local times, especially closer to equatorial latitudes. Further evaluation would be required to examine the interaction between the different flow regimes on the lower cloud of Venus and the properties of waves. However, in Silva et al. [2021] we speculate that this could be related to different forcing mechanisms at hand. Wave phase velocity and trajectory suggest that these waves are 'guided' by the background zonal wind flow, given their low intrinsic speeds and orientations. We observe a decrease in the local wind speed after waves dissipate, but the short number of data points where this was verifiable does not allow for a more robust interpretation. However, it is apparent that gravity waves are restricted by either their forcing mechanisms or the background dynamics of Venus to low intrinsic phase speed and orientations.

According to the results from this study and comparing them with suitable models, we are led to believe that convection should be the main driving force behind the generation of these waves. However, it is still not possible to rule out other sources of wave generation such as topography, wind shear, or Kelvin-Helmholtz instabilities.

The volume of this body of work amounts to the largest systematic study of atmospheric waves conducted to this day on the lower clouds of Venus, and we hope that our findings can be used to refine modern GCMs of Venus to better predict the current behaviour and its underlying mechanisms of atmospheric circulation.

Exploring Jupiter's Atmosphere with High-Resolution Spectroscopy

Already a much observed target in the Solar System, we made efforts to apply a new and refined Doppler velocimetry method to the gas giant's atmosphere, exploring the capabilities of modern instruments like VLT/ESPRESSO on the study of Solar System planet's atmospheres. We took the experience gathered in the studies described in Machado et al.

[2012, 2014, 2017, 2021], which use high-resolution spectroscopy data to employ a Doppler velocimetry method to study the dynamics of the upper clouds of Venus. Previous successes in the implementation of this technique to multiple means of data integration, whether through fibre-fed or long-slit spectroscopy across different instruments, gave us confidence to pursue other targets. Although many similarities reside between the procedures used in those studies and what has been described in this document, key differences translated into new challenges in the application and refinement of the method for Jupiter using ESPRESSO.

Given the transitory nature of the visual appearance of Jupiter as seen from Earth, as opposed to Venus at visible wavelengths, pointing accuracy was of the utmost importance in this study. The dramatic changes in circulation on latitudinal bands [Porco et al., 2003, Hueso et al., 2017, Fletcher et al., 2020] and the rapid rotation of Jupiter posed a significant challenge to retrieve winds through our Doppler velocimetry method. In spite of these difficulties, our application of the new method described in this thesis, has shown evidence that Doppler velocimetry applied to visible spectra from back-scattered solar radiation on the atmosphere of Jupiter, is efficient in retrieving wind velocity results along Jupiter's different latitudinal bands. In fact, it was the first time that a dynamical study of a Solar System planet's atmosphere was performed with observations by ESPRESSO. Our goal then was to compare with previous studies using both cloud-tracking [Choi et al., 2011, Galperin et al., 2014, Garcia-Melendo et al., 2001, 2011, Johnson et al., 2018, Salyk, 2006, Tollefson et al., 2017] and other high-resolution spectroscopy techniques [Goncalves et al., 2019], to evaluate our performance. We took advantage of the extended expertise of the team on this complementing technique and my own experience with the retrieval process from several collaborations described in section 4.4, to also contribute with additional retrieved data from Cassini.

In spite of the limited spatial and temporal coverage of Jupiter's disk allowed by the allocated observations, our results show consistency with previous cloud-tracking results, including from different observing instruments, from ground to space. Our results are in less agreement with previous Doppler velocimetry efforts [Goncalves et al., 2019], even if we display good consistency with results with other techniques from a similar period of observation [Tollefson et al., 2017], and have used an instrument with improved technical capabilities than JOVIAL-JIVE for the purposes of high-resolution spectroscopy. Despite the before mentioned consistency between the results, we do see slight fluctuations on some of bands studied with both methods and provided several hypothesis for their origin. However, given the exploratory nature of this work, our coverage was limited thus no firm conclusions could be made regarding the differences in wind velocities retrieved between both methods. With this observed agreement between the results, we intend to perform a wider observational study to cover a broader region in Jupiter. Such a campaign would make it possible to analyse more elements of the banded structure of its atmosphere, and offer greater temporal coverage, likely observing Jupiter over several days, not only to extract winds during a full rotation period, but also to investigate temporal daily variability.

Since we sense the overall visible wavelength range with the Doppler velocimetry technique and since optical depth is a function of wavelength, it is possible to explore the use of partial wavelength ranges in order to sense, at the same time, different pressure levels/altitudes simultaneously. To confirm the location of pressure levels probed with such a study, we plan to employ a modern radiative transfer suite, such as NEMESIS [Irwin et al., 2008]. Such observations, coupled with cloud-tracking results, could allows us to estimate the vertical shear of the zonal wind in the upper troposphere, where a transition between circulation regimes might be occurring [Fletcher et al., 2020].

Other Projects

While the two previous sections describe the main subjects of this thesis, as part of an active team in Solar System studies at my institute, our collaborative network allowed all of us to participate in several side-projects to broaden the topics of our research and foster teamwork within our group. While most of these collaborations eventually lead to co-authorships in publications [Goncalves et al., 2020, Machado et al., 2021], my role on each of them is varied. From aiding in the retrieval of wind measurements, to support in observing proposals, or tutoring of fellow colleagues in atmospheric waves characterisation given the more advanced stage of my career and greater expertise on the subject. Besides all other projects described in section 4.4, I will conclude this section with our involvement with the ARIEL space mission.

ARIEL is the first approved mission dedicated to the analysis of chemical composition and thermal structure of hundreds of exoplanets. The exoplanets in ARIEL's list were discovered with the transit method, where the planet passes in front of the observed star, which leads to a decrease in the flux that can be detected by modern instruments and the subsequent light curve can be used to interpret basic physical characteristics of the planetary body orbiting the star. With launch planned for 2028, we have immersed ourselves on the scientific plan of observations by integrating in working groups to anticipate the data from this instrument. Several members of the planetary sciences group at IA lead one of ARIEL's dedicated working groups "Synergies with Solar System", whose primary goal is to take the joint expertise of its members to build a bridge between Solar System planetary studies and exoplanets research. Together we proposed to coordinate several tasks including:

- Considering Solar System atmospheres a natural laboratory to understand atmospheres on planets orbiting other stars;
- Apply three-dimensional models of planetary atmospheres within the Solar System to specific exoplanet targets;
- Optimize forthcoming observations with characterisations of planets using improved GCMs;
- Use current spectroscopic and photometric data from Solar System planets observations as a template to test new tools and science cases that can be applied to exoplanets;
- Search for disequilibrium species in Solar System atmospheres to refine research protocols that could be exported for ARIEL's science cases.

In light of these propositions, in the context of our team, we are developing *PlanetWarp*, a tool that aims to provide spectrum templates of Solar System planets' reflected light in both visible and IR. The crux of this tool is to take the average spectra from known targets in our cosmic vicinity, and effectively downgrading the data to simulate how would these planets look like if they were at distances from Earth equivalent to other exoplanetary targets. Such examples can be instrumental to better interpret observed spectra from planets orbiting other stars, that might share some similarities with planets like Venus or Jupiter. Many of the spectra already obtained through previous observations with different instruments, are suitable to be used to build this tool, and we hope to gather spectra of even more planets as we develop it.

In addition to this collaborative project in the context of the ARIEL mission, I am part of the Portuguese consortium of ARIEL of which this thesis' supervisor (Dr. Pedro Machado) is Co-PI. I am also involved in the recently selected EnVision mission, a future space program dedicated to study our closest neighbour (Venus), particularly investigating the reasons why this planet has evolved so differently than our own. My involvement lays in the context of the payload instrument VenSpec-H, dedicated to nightside high-resolution spectroscopic observations of the lower clouds.

7.1 Future Prospects and Closing Remarks

The several paths followed through the work developed for this thesis are still open for further exploration. Continuous monitoring of atmosphere dynamics on Solar System planets is necessary to understand how its behaviour evolves over time, not to mention the fact that with the advent of more sophisticated instrumentation and models, our understanding of these immensely complex systems deepens with every iteration.

For the case of Venus, a complete picture of the three-dimensional nature of its massive atmosphere is yet to be assembled. We contributed here with dynamical studies on the upper cloud with different techniques and another on the lower clouds, looking for features (atmospheric waves) which might be one of the driving forces for the enhanced superrotation in the upper layers of the cloud deck. Accurate measurements of the different components of the wind [Goncalves et al., 2020] can help to reassure how the Hadley cell on Venus modulates atmospheric circulation, and how its mechanisms respond to sources of variability such as waves and thermal tides [Lebonnois et al., 2010]. Steps have also been taken to investigate how cloud deck circulation changes with altitude [Machado et al., 2021]. However, the connection between the lower and upper cloud decks, as well as the transition region from the upper cloud to the upper-mesophere and lower-thermosphere, along with both their nature, remain mostly in mystery. Our systematic study of waves in the lower cloud has also raised questions on the true role of this phenomenon within the context of atmospheric circulation, as well as their generating force. Another mirror study into the upper and middle clouds of Venus would be most helpful to understand how these structures move between layers and where exactly they dissipate, evaluating the energy and momentum introduced in the atmospheric region where they do. I would be very interested in the pursuit of such a study, making use of yet to be explored data from VMC and VIRTIS in the visible and ultraviolet range, and also UVI onboard Akatsuki. Other studies which can have a significant impact on our understanding of the atmospheric machine of Venus beyond the cloud deck and down towards the surface, include the interaction between topography and the atmosphere and how this connection can influence global circulation of Venus and the much observed cloud region [Bertaux et al., 2016].

Fortunately, greater interest on Venus has sparked recently with the tentative detection of phosphine [Greaves et al., 2021]. Although some controversy has risen from this detection, either directly or not, we look towards a bright future of Venus exploration with several space missions accepted, including ESA's EnVision on which our team is involved in.

Regarding Jupiter studies, ours was only a first step in the application of a new technique to study the gas giants, as part of a driving force to expand our current research targets, in an attempt to prove the versatility of the method. With results from Juno space mission, it is becoming increasingly clear that the banded circulation is more deeply rooted within the planet than previously thought, and that much of the chemistry and dynamics observed to this day can give contradicting evidence with respect to accepted circulation mechanisms described by models [Fletcher et al., 2020]. Nonetheless, a caveat to this conundrum may lie in a combination of new kinds of observations supporting complete GCMs for these atmospheres. Since Doppler velocimetry is able to probe back-scattered solar radiation, due to the bolometric nature of the light that reaches our observing instrumentation, it is quite possible that this method is able to capture wind velocity results at different altitudes than what has been possible with the more popular cloud-tracking technique. The refinement of this new technique applied to Jupiter and extended observations, might yield interesting results filling the gap left by conflicting models of circulation in the troposphere of Jupiter, possibly shedding some light into a previously poorly understood mechanism.

In the meantime, we look towards other targets such as Mars and Saturn, broadening the reach of this technique and of our team at the same time. We expect to publish a study on the winds on Mars brought up during the massive 2018 global dust storm [Machado et al., in prep.], and another into the clouds of Saturn and Jupiter, testing this method's efficiency at longer wavelengths (800-1000 nm). This project serves also as another statement that the underlying systems that govern various planets within the Solar System are still open for exploration, specially their mesmerizing atmospheres. Given the increasing number of space missions and ground instruments dedicated to planetary studies within the Solar System, we believe that we will be able to study these targets in supreme detail, as humanity races towards a new age of understanding.

Bibliography

C. Acton et al. A look towards the future in the handling of space science mission geometry. *Planetary and Space Science*, 150:9–12, 2017. doi: 10.1016/j.pss.2017.02.013.

A. Adriani et al. Clusters of cyclones encircling jupiter's poles. *Nature - Letter*, 555: 216–225, 2018. doi: 10.1038/nature25491.

A. Adriani et al. Two-year observations of the jupiter polar regions by jiram on board juno. *Journal of Geophysical Research: Planets*, 125(e2019JE006098):12, 2020. doi: 10.1029/2019JE006098.

M.J. Alexander et al. Recent developments in gravity-wave effects in climate models and the global distribution of gravity-wave momentum flux from observations and models. *Quarterly Journal of the Royal Meteorological Society*, 136:1103–1124, 2010.

D.A. Allen and J.W. Crawford. Cloud structure on the dark side of venus. *Nature*, 307: 222–224, 1984.

H. Ando et al. Thermal structure of the venusian atmosphere from the sub-cloud region to the mesosphere as observed by radio occultation. *Scientific Reports*, 10:3448, 2020.

J. Arregi et al. Gravity waves in jupiter's equatorial clouds observed by the galileo orbiter. *Icarus*, 202:358–360, 2009.

X. Asay-Davis et al. Changes in jupiter's zonal velocity between 1979 and 2008. *Icarus*, 211:1215–1232, 2011. doi: 10.1016/j.icarus.2010.11.018.

S. Atreya. *Atmospheres and ionospheres of the outer planets and their satellites*, volume 15. Springer-Verlag (Physics and Chemistry in Space), 1986.

S. Atreya et al. Composition and origin of the atmosphere of jupiter - an update, and implications for the extrasolar giant planets. *Planetary Space and Science*, 51:105–112, 2003.

F. Bagenal. Exploration of jupiter. 2019. URL `https://ui.adsabs.harvard.edu/abs/2019LPI....50.1352B/abstract`.

K. Baines. The visual spectrum of jupiter's great red spot accurately modeled with aerosols produced by photolyzed ammonia reaction with acetylene. *Icarus*, 330:217–229, 2019. doi: 10.1016/j.icarus.2019.04.008.

D. Baker et al. Convectively generated internal gravity waves in the lower atmosphere of venus. i: No wind shear. *Journal of Atmospheric Sciences*, 57:184, 2000a. doi: 10.1175/1520--0469(2000)057.

D. Baker et al. Convectively generated internal gravity waves in the lower atmosphere of venus. ii. mean wind shear and wave-mean flow interaction. *Journal of Atmospheric Sciences*, 57:200, 2000b. doi: 10.1175/15200469(2000)057.

N. Barrado-Izagirre et al. Jupiter's zonal winds and their variability studied with small-sized telescopes. *Astronomy and Astrophysics*, 554:A74, 2013. doi: 10.1051/0004-6361/201321201.

N. Barrado-Izagirre et al. Jupiter's third largest and longest lived oval: Color changes and dynamics. *Icarus*, 361:114394, 2021. doi: 10.1016/j.icarus.2021.114394.

K. Beisser. Pluto-bound new horizons spacecraft gets a boost from jupiter, 2015. URL `https://web.archive.org/web/20141113224828/http://pluto.jhuapl.edu/news_center/news/022807.php`.

M. Belton et al. Cloud patterns, waves and convection in the venus atmosphere. *Journal of Atmospheric Sciences*, 33:1394, 1976.

M. Belton et al. Images from galileo of the venus cloud deck. *Science*, 253:1531–1536, 1991. doi: 10.1126/science.253.5027.1531.

M. Belton et al. The galileo solid-state imaging experiment. *Space Science Reviews*, 60: 413–455, 1992.

L. Bengtsson and D. Grinspoon. *Towards understanding the climate of Venus*, volume 11. Springer, 2013.

J.L. Bertaux et al. Spicav on venus express: Three spectrometers to study the global structure and composition of the venus atmosphere. *Planetary and Space Science*, 55: 1673–1700, 2007. doi: 10.1016/j.pss.2007.01.016.

J.L. Bertaux et al. Influence of venus topography on the zonal wind and uv albedo at cloud top level: The role of stationary gravity waves. *Journal of Geophysical Research: Planets*, 121:1087–1101, 2016. doi: 10.1002/2015JE004958.

J. Blamont. Planetary balloons. *Experimental Astronomy*, 22:1–39, 2008. doi: 10.1007/s10686-008-9095-8.

S. Bolton et al. The juno mission. *Space Science Reviews*, 213:5–37, 2017a. doi: 10.1007/s11214-017-0429-6.

S. Bolton et al. Jupiter's interior and deep atmosphere: The initial pole-to-pole passes with the juno spacecraft. *Science*, 356:821–825, 2017b. doi: 10.1126/science.aal2108.

S. Bougher et al. *Venus II: geology, geophysics, atmosphere and solar wind environment*. University of Arizona Press, 1997.

A.S. Braude et al. Colour and tropospheric cloud structure of jupiter from muse/vlt: Retrieving a universal chromophore. *Icarus*, 338:113589, 2020. doi: 10.1016/j.icarus.2019.113589.

B.F. Burke and K.L. Franklin. Observations of a variable radio source associated with the planet jupiter. *Journal of Geophysical Research*, 60:213–217, 1995. doi: 10.1029/JZ060i002p00213.

R. Carlson et al. Chromophores from photolyzed ammonia reacting with acetylene: Application to jupiter's great red spot. *Icarus*, 274:106–115, 2016. doi: 10.1016/j.icarus.2016.03.008.

R.W. Carlson et al. Galileo infrared imaging spectroscopy measurements at venus. *Science*, 253:1541–1548, 1991. doi: 10.1126/science.253.5027.1541.

N.J. Chanover et al. Multispectral near-ir imaging of venus nightside cloud features. *Journal of Geophysical Research*, 103:31335–31348, 1998. doi: 10.1029/1998JE900009.

D.S. Choi et al. Power spectral analysis of jupiter's clouds and kinetic energy from cassini. *Icarus*, 216:597–609, 2011. doi: 10.1016/j.icarus.2011.10.001.

T. Civeit et al. On measuring planetary winds using high-resolution spectroscopy in visible wavelengths. *Astronomy and Astrophysics*, 431:1157–1166, 2005.

J. Connerney et al. A new model of jupiter's magnetic field from juno's first nine oribts. *Geophysical Research Letters*, 45:2590–2596, 2018. doi: 10.1002/2018GL077312.

B. Conrath et al. Thermal structure and dynamics of the jovian atmosphere 2. visible cloud features. *Journal of Geophysical Research*, 86:8769–8775, 1981. doi: 10.1029/JA086iA10p08769.

B. Conrath et al. Thermal structure and para hydrogen fraction on the outer planets from voyager iris measurements. *Icarus*, 135:501–517, 1998. doi: 10.1006/icar.1998.6000.

V. Cottini et al. Water vapor near the cloud tops of venus from venus express/virtis dayside data. *Icarus*, 217:561–569, 2012. doi: 10.1016/j.icarus.2011.06.018.

V. Cottini et al. Water vapor near venus cloud tops from virtis-h/venus express observations 2006-2011. *Planetary and Space Science*, 113:219–225, 2015. doi: 10.1016/j.pss.2015.03.012.

D. Crisp et al. Ground-based near-infrared imaging observations of venus during the galileo encounter. *Science*, 253:1538–1541, 1991. doi: 10.1126/science.253.5027.1538.

E. Dahl et al. Vertical structure and color of jovian latitudinal cloud bands during the juno era. *The Planetary Science Journal*, 2(16), 2020.

A. Dollfus. Venus: evolution of the upper atmospheric clouds. *Journal of Atmospheric Sciences*, pages 1060–1070, 1975.

P. Drossart et al. Scientific goals for the observation of venus by virtis on esa/venus express mission. *Planetary and Space Science*, 55:1653–1672, 2007. doi: 10.1016/j.pss.2007.01.003.

ESO. The very large telescope - the world's most advanced visible-light astronomical observatory. URL `https://www.eso.org/public/teles-instr/paranal-observatory/vlt/`.

L. Fletcher. Cycles of activity in the jovian atmosphere. *Geophysical Research Letters*, 44:4725–4729, 2017. doi: 10.1002/2017GL073806.

L. Fletcher et al. Mid-infrared mapping of jupiter's temperatures, aerosol opacity and chemical distributions with irtf/texes. *Icarus*, 278:128–161, 2016. doi: 10.1016/j.icarus.2016.06.008.

L. Fletcher et al. How well do we understand the belt/zone circulation of giant planet atmospheres. *Space Science Reviews*, 216(30), 2020.

T. Fukuhara et al. Lir: Longwave infrared camera onboard the venus orbiter akatsuki. *Earth, Planets and Space*, 63:1009–1018, 2011. doi: https://doi.org/10.5047/eps.2011.06.019.

T. Fukuhara et al. Large stationary gravity wave in the atmosphere of venus. *Nature - Geoscience*, 10:85–88, 2017. doi: 10.1038/NGEO2873.

B. Galperin et al. Cassini observations reveal a regime of zonostrophic macroturbulence on jupiter. *Icarus*, 229:295–320, 2014. doi: 10.1016/j.icarus.2013.08.030.

E. Garcia-Melendo et al. A study of the stability of jovian zonal winds from hst images: 1995-2000. *Icarus*, 152:316–330, 2001. doi: 10.1006/icar.2001.6646.

E. Garcia-Melendo et al. Dynamics of jupiter's equatorial region at cloud top level from cassini and hst images. *Icarus*, 211:1242–1257, 2011. doi: 10.1016/j.icarus.2010.11.020.

P. Gaulme et al. Measuring planetary atmospheric dynamics with doppler spectroscopy. *Astronomy and Astrophysics*, 617:A41, 2018. doi: 10.1051/0004-6361/201832868.

A. Del Genio and W. Rossow. Planetary-scale waves and the cyclic nature of cloud top dynamics on venus. *Journal of Atmospheric Sciences*, pages 293–318, 1990. doi: https://doi.org/10.1175/1520-0469(1990)047<0293:PSWATC>2.0.CO;2.

P.J. Gierasch and R.M. Goody. The effect of dust on the temperature of the martian atmosphere. *Journal of Atmospheric Sciences*, 29:400–402, 2020. doi: 10.1175/15200469(1972)029<0400:TEODOT>2.0.CO2.

G. Gilli et al. Venus upper atmosphere revealed by a gcm: Ii. model validation with temperature and density measurements. *Icarus*, page 24, 2021. doi: 10.1016/j.icarus.2021.114432.

R. Gomes et al. Origin of the cataclysmic late heavy bombardment period of the terrestrial planets. *Nature*, 435:466–469, 2005.

I. Goncalves et al. First measurements of jupiter's zonal winds with visible imaging spectroscopy. *Icarus*, 319:795–811, 2019. doi: 10.1016/j.icarus.2018.10.019.

R. Goncalves et al. Venus' cloud top wind study: Coordinated akatsuki/uvi with cloud tracking and tng/harps-n with doppler velocimetry observations. *Icarus*, 335:113418, 2020. doi: 10.1016/j.icarus.2019.113418.

R. Goncalves et al. A wind study of venus's cloud top: New doppler velocimetry observations. *Atmosphere*, 12:2., 2021. doi: 10.3390/atmos12010002.

D. Gorinov et al. Circulation of venusian atmosphere at 90-110 km based on apparent motions of the o2 1.27-micron nightglow from virtis-m (venus express) data. *Geophysical Research Letters*, 45, 2018. doi: 10.1002/2017GL076380.

J. Greaves et al. Phosphine gas in the cloud decks of venus. *Nature Astronomy*, 5:655–664, 2021. doi: 10.1038/s41550-020-1174-4.

D.H. Grinspoon. *Venus Revealed: A New Look Below the Clouds of Our Mysterious Twin Planet.* Helix Books, Perseus Publishing, 1997.

T. Guillot and L. Fletcher. Revealing giant planet interiors beneath the cloudy veil. *Nature Communications*, 11(1555), 2020.

T. Guillot and D. Gautier. Giant planets. *Treatise on Geophysics, 2nd edition*, pages 1–42, 2014. URL https://arxiv.org/abs/1405.3752v2.

R.M. Haberle et al. Mars atmospheric dynamics as simulated by the nasa ames general circulation model 1. the zonal-mean circulation. *Journal of Geophysical Research*, 98: 3093–3123, 1993. doi: 10.1029/92JE02946.

V.L. Hansen and I. Lopez. Mapping of geologic structures in the niobe-aphrodite map area of venus: Unraveling the history of tectonic regime change. *Journal of Geophysical Research: Planets*, 123:1760–1790, 2018. doi: 10.1029/2018JE005566.

R. Haus et al. Self-consistent retrieval of temperature profiles and cloud structure in the northern hemisphere of venus using virtis/vex and pmv/venera-15 radiation measurements. *Planetary and Space Science*, 89:77–101, 2013.

R. Haus et al. Atmospheric thermal structure and cloud features in the southern hemisphere of venus as retrieved from virtis/vex radiation measurements. *Icarus*, 232:232–248, 2014.

B. Hausler et al. Radio science investigations by vera onboard the venus express spacecraft. *Planetary and Space Science*, 54:1315–1335, 2006.

B. Hausler et al. Venus atmospheric, ionospheric, surface and interplanetary radio-wave propagation studies with the vera radio-science experiment. *ESA Scientific Publication*, 1295:1–30, 2007.

J. González Hernández et al. Espresso on vlt: An instrument for exoplanet research. *Handbook of Exoplanets*, (157), 2018. doi: 10.1007/978-3-319-55333-7_157.

J.R. Holton. *An Introduction to Dynamic Meteorology.* Elsevier Inc., 4th edition, 2004.

R. Hooke. *Micrographia.* Project Gutenberg, ebook number:15491 edition, 1664.

T. Horinouchi et al. Image velocimetry for clouds with relaxation labeling based on deformation consistency. *Measurement Science and Technology*, 28:article id. 085301, 2017a. doi: 10.1088/1361-6501/aa695c.

T. Horinouchi et al. Equatorial jet in the lower to middle cloud layer of venus revealed by akatsuki. *Nature Geoscience*, 10:646–651, 2017b. doi: 10.1038/ngeo3016.

T. Horinouchi et al. Mean winds at the cloud top of venus obtained from two-wavelength uv imaging by akatsuki. *Earth, Planets and Space*, 70:19, 2018. doi: https://doi.org/10.1186/s40623-017-0775-3.

R. Hueso. Venus cloud winds and mean albedo variability from atmospheric waves. *Journal of Geophysical Research: Planets*, 124:2681–2685, 2019. doi: 10.1029/2019JE006234.

R. Hueso et al. the planetary laboratory for image analysis (plia). *Advances in Space Research*, 2010.

R. Hueso et al. Assessing the long-term variability of venus winds at cloud level from virtis–venus express. *Icarus*, 217:585–598, 2012.

R. Hueso et al. Six years of venus winds at the upper cloud level from uv, visible and near infrared observations from virtis on venus express. *Planetary and Space Sciences*, 113-114:78–99, 2015. doi: 10.1016/j.pss.2014.12.010.

R. Hueso et al. Jupiter cloud morphology and zonal winds from ground-based observations before and during juno's first perijove. *Geophysical Research Letters*, 44:4669–4678, 2017. doi: 10.1002/2017GL073444.

S. Iga and Y. Matsuda. Shear instability in a shallow water model with implications for the venus atmosphere. *Journal of the Atmospheric Sciences*, 62:2514–2527, 2005.

N. Ignatiev. Altimetry of the venus cloud tops from the venus express observations. *Journal of Geophysical Research*, 114:E00B43, 2009. doi: 10.1029/2008JE003320.

T. Imamura et al. Radio occultation experiment of the venus atmosphere and ionosphere with the venus orbiter akatsuki. *Earth, Planets and Space*, 63:493–501, 2011. doi: https://doi.org/10.5047/eps.2011.03.009.

T. Imamura et al. Inverse insolation dependence of venus' cloud-level convection. *Icarus*, 228:181–188, 2014. doi: 10.1016/j.icarus.2013.10.012.

A. Ingersoll et al. Moist convection as an energy source for the large-scale motions in jupiter's atmosphere. *Nature*, 403:630–632, 2000. doi: 10.1038/35001021.

A. Ingersoll et al. *Jupiter*, chapter Dynamics of Jupiter's Atmosphere, page 105. Cambridge University Press, 2004.

P. Irwin. *Giant Planets of our Solar System.* Springer, Praxis Publishing Ltd, Chichester, UK, second edition, 2009.

P. Irwin et al. The nemesis planetary atmosphere radiative transfer and retrieval tool. *Journal of Quantitative Spectroscopy & Radiative Transfer*, 109:1136–1150, 2008. doi: 10.1016/j.jqsrt.2007.11.006.

N. Iwagami et al. Science requirements and description of the 1μm camera onboard the akatsuki venus orbiter. *Earth, Planets and Space*, 63:487–492, 2011. doi: 10.5047/eps.2011.03.007.

N. Iwagami et al. Initial products of akatsuki 1 micron camera. *Earth, Planets and Space*, 70:6, 2018. doi: https://doi.org/10.1186/s40623-017-0773-5.

D. Jewitt et al. Cambridge University Press, 2004.

P.E. Johnson et al. Longitudinal variability in jupiter's zonal winds derived from multi-wavelength hst observations. *Planetary and Space Science*, 155:2–11, 2018. doi: 10.1016/j.pss.2018.01.004.

S. Kane et al. Could the migration of jupiter have accelerated the atmospheric evolution of venus? *The Planetary Science Journal*, 1:10, 2020. doi: 10.3847/PSJ/abae63. URL `arXiv:2008.04927`.

I. Kanik and J.P. de Vera. Editorial: Astrobiology of mars, europa, titan and enceladus - most likely places for alien life. *Frontiers in Astronomy and Space Sciences*, 8(643268): 3, 2021. doi: 10.3389/fspas.2021.643268.

Y. Kaspi et al. Jupiter's atmospheric jet streams extend throusands of kilometers deep. *Nature*, 555:223–226, 2018. doi: 10.1038/nature25793.

W.T. Kasprzak. The pioneer venus orbiter: 11 years of data. Technical report, NASA - National Aeronautics and Space Administration, 1990.

J. Kasting. Runaway and moist greenhouse atmospheres and the evolution of earth and venus. *Icarus*, 74:472–494, 1988. doi: https://doi.org/10.1016/0019-1035(88)90116-9.

T. Kitahara et al. Stationary features at the cloud top of venus observed by ultraviolet imager onboard akatsuki. *Journal of Geophysical Research: Planets*, 124:1266–12,1281, 2019. doi: 10.1029/2018JE005842.

T. Kostiuk et al. Direct measurement of winds on titan. *Geophysical Research Letters*, 28:2361–2364, 2001. doi: 10.1029/2000GL012617.

T. Kostiuk et al. Titan's stratospheric zonal wind, temperature, and ethane abundance a year prior to huygens insertion. *Geophysical Research Letters*, 32:L22205, 2005. doi: 10.1029/2005GL023897.

T. Kostiuk et al. Stratospheric global winds on titan at the time of huygens descent. *Journal of Geophysical Research: Planets*, 111:E7, 2006. doi: 10.1029/2005JE002630.

T. Kostiuk et al. High spectral resolution infrared studies of titan: Winds, temperature, and composition. *Planetary and Space Science*, 58:1715–1723, 2010. doi: 10.1016/j.pss.2010.08.004.

T. Kouyama et al. Topographical and local time dependence of large stationary gravity waves observed at the cloud top of venus. *Geophysical Research Letters*, 44:12,098–12,105, 2017. doi: https://doi.org/10.1002/2017GL075792.

D. Kovalenko et al. Micro-spacecraft in sun-venus lagrange point orbit for the venera-d mission. *Advances in Space Research*, 66:21–28, 2020. doi: 10.1016/j.asr.2019.10.027.

V. Krasnopolsky. S3 and s4 abundances and improved chemical kinetic model for the lower atmosphere of venus. *Icarus*, 225:570–580, 2013. doi: https://doi.org/10.1016/j.icarus.2013.04.026.

S. Lebonnois et al. Superrotation of venus' atmosphere analyzed with a full general circulation model. *Journal of Geophysical Research*, 115:E06006, 2010.

M. Lefèvre et al. Three-dimensional turbulence-resolving modeling of the venusian cloud layer and induced gravity waves: Inclusion of conplete radiative transfer and wind shear. *Journal of Geophysical Research: Planets*, 123:2773–2789, 2018. doi: 10.1029/2018JE005679.

M. Lefèvre et al. Mesoscale modeling of venus' bow-shape waves. *Icarus*, 335:113376, 2020.

E. Lellouch et al. First absolute wind measurements in the middle atmosphere of mars. *Astrophysical Journal*, 383:401, 1991. doi: 10.1086/170797.

C. Li et al. The internal structure of jupiter's great red spot. American Geophysical Union, 2020.

L. Li et al. Vertical wind shear on jupiter from cassini images. *Journal of Geophysical Research*, 111:E04004, 2006. doi: 10.1029/2005JE002556.

S. Limaye and M. Rengel. Atmospheric circulation and dynamics, in: Towards understanding the climate of venus. *ISSI Scientific Reports Series*, 11:55–73, 2013.

S.C. Littleton. *Gods, Goddesses and Mythology.* Marshall Cavendish, 2005.

D. Luz et al. Characterisation of zonal winds in the stratosphere of titan with uves. *Icarus*, 179:497–510, 2005.

D. Luz et al. Characterisation of zonal winds in the stratosphere of titan with uves: 2. observations coordinated with the huygens probe entry. *Journal of Geophysical Research*, 111(E08S90), 2006.

A. Määttänen et al. Mapping the mesospheric co2 clouds on mars: Mex/omega and mex/hrsc observations and challenges for atmospheric models. *Icarus*, 209:452–469, 2010.

P. Machado et al. Mapping zonal winds at venus's cloud tops from ground-based doppler velocimetry. *Icarus*, 221:248–261, 2012. doi: 10.1016/j.icarus.2012.07.012.

P. Machado et al. Wind circulation regimes at venus' cloud tops: Ground-based doppler velocimetry using cfht/espadons and comparison with simultaneous cloud tracking measurements using vex/virtis in february 2011. *Icarus*, 243:249–263, 2014.

P. Machado et al. Venus cloud-tracked and doppler velocimetry winds from cfht/espadons and venus express/virtis in april 2014. *Icarus*, 285:8–26, 2017.

P. Machado et al. Venus atmospheric dynamics at two altitudes: Akatsuki and venus express cloud tracking, ground-based doppler observations and comparison with modelling. *Atmosphere*, 12:506, 2021. doi: 10.3390/atmos12040506.

P. Machado et al. Venus' cloud-tracked winds using ground- and space-based observations with tng/nics and vex/virtis. *Atmosphere*, 13(337), 2022. doi: 10.3390/atmos13020337.

P. Machado et al. Doppler velocimetry on mars during 2018 global dust storm. *Icarus*, in prep.

J. Margot et al. Spin state and moment of inertia of venus. *eprint arXiv:2103.01504, submitted to Nature Astronomy*, 2021. URL `arXiv:2103.01504`.

W.J. Markiewicz et al. Venus monitoring camera for venus express. *Planetary and Space Science*, 55:1701–1711, 2007. doi: 10.1016/j.pss.2007.01.004.

Marov and Grinspoon. *The planet Venus.* Yale University Press, 1998.

M. Marov et al. Preliminary results on the venus atmosphere from the venera 8 descent module. *Icarus*, 20:407–421, 1973. doi: 10.1016/0019-1035(73)90014-6.

C.H. Mayer et al. Observations of venus at 3.15-cm wave length. *The Astrophysical Journal*, 127:1–10, 1958.

T.H. McConnochie et al. Themis-vis observations of the clouds in the martian mesosphere: Altitudes, wind speeds, and decameter-scale morphology. *Icarus*, 210:545–565, 2010. doi: 10.1016/j.icarus.2010.07.021.

L.A. McFadden, P.R. Weissman, and T.V. Johnson. *Encyclopedia of the Solar System.* Second edition, 2007.

K. McGouldrick and O.B. Toon. Observable effects of convection and gravity waves on the venus condensational cloud. *Planetary and Space Science*, 56:1112–1131, 2008. doi: 10.1016/j.pss.2008.02.010.

S. Milbrath. *Star Gods of the Mayans: Astronomy in Art, Folklore, and Calendars.* University of Texas Press, 1999.

R. Moissl et al. Venus cloud top winds from tracking uv features in venus monitoring camera images. *Journal of Geophysical Research*, 114:E00B31, 2009. doi: 10.1029/2008JE003117,2009.

S. Morellina et al. Global thermodynamic, transport-property and dynamic characteristics of the venus lower atmosphere below the cloud layer. *Icarus*, 350:113761, 2020. doi: 10.1016/j.icarus.2020.113761.

R. Moreno et al. Wind measurements in mars' middle atmosphere: Iram plateau de bure interferometric co observations. *Icarus*, 201:549–563, 2009. doi: 10.1016/j.icarus.2009.01.027.

J. Moses. Photochemistry of saturn's atmosphere. i. hydrocarbon chemistry and comparisons with iso observations. *Icarus*, 143:244–298, 2000. doi: 10.1006/icar.1999.6270.

J. Moses et al. *The Stratosphere of Jupiter.* Cambridge University Press, 2007.

S. Muller et al. The challenge of forming a fuzzy core in jupiter. *Astronomy and Astrophysics*, 638(A121):11, 2020. doi: 10.1051/0004-6361/201937376.

M. Nakamura et al. Overview of venus orbiter, akatsuki. *Earth, Planets and Space*, 63: 443–457, 2011. doi: https://doi.org/10.5047/eps.2011.02.009.

M. Nakamura et al. Akatsuki returns to venus. *Earth, Planets and Space*, 68:75, 2016. doi: https://doi.org/10.1186/s40623-016-0457-6.

C. Nappo. *Introduction to Atmospheric Gravity Waves.* International geophysics series. Volume 85, 2002.

T. Navarro et al. Venus' upper atmosphere revealed by a gcm: I. structure and variability of the circulation. *Icarus*, XXX:XXX, 2021. doi: 10.1016/j.icarus.2021.114400.

F. Nimmo and D. Mackenzie. Volcanism and tectonics on venus. *Annual Review of Earth and Planetary Sciences*, 26:23–51, 1998. doi: https://doi.org/10.1146/annurev.earth.26.1.23.

R. Norris. Searching for the astronomy of aboriginal australians. *Conference Proceedings: Australia Telescope National Facility*, pages 1–4, 2007.

J.J. O'Connor and E.F. Robertson. Giovanni domenico cassini. 2003. URL `https://mathshistory.st-andrews.ac.uk/Biographies/Cassini/`.

K. Ogohara et al. Overview of akatsuki data products: definition of data levels, method and accuracy of geometric correction. *Earth, Planets and Space*, 69, 2017. doi: https://doi.org/10.1186/s40623-017-0749-5.

F. Pepe et al. Espresso: The next european exoplanet hunter. *Astronomische Nachrichten, Vol.335, Issue 1, p.8*, 335:10–22, 2014. doi: 12.1002/asna.201312004.

F. Pepe et al. Espresso@vlt - on-sky performance and first results. *Astronomy and Astrophysics*, 645(A96), 2021.

J. Peralta et al. Characterization of mesoscale gravity waves in the upper and lower clouds of venus from vex-virtis images. *Journal of Geophysical Research*, 113:E00B18, 2008. doi: 10.1029/2008JE003185.

J. Peralta et al. Analytical solution for waves in planets with atmospheric superrotation. i. acoustic and inertia-gravity waves. *The Astrophysical journal, supplement series*, 213:17:18pp, 2014a. doi: 10.1088/0067-0049/213/1/17.

J. Peralta et al. Analytical solution for waves in planets with atmospheric superrotation. ii. lamb, surface and centrifugal waves. *The Astrophysical journal, supplement series*, 213:18:15pp, 2014b. doi: 10.1088/0067-0049/213/1/18.

J. Peralta et al. Overview of useful spectral regions for venus: An update to encourage observations complementary to the akatsuki mission. *Icarus*, 288:235–239, 2017a.

J. Peralta et al. Stationary waves and slowly moving features in the night upper clouds of venus. *Nature - astronomy*, page 187, 2017b. doi: 10.1038/s41550-017-0187.

J. Peralta et al. Nightside winds at the lower clouds of venus with akatsuki/ir2: Longitudinal, local time and decadal variations from comparison with previous measurements. *Astrophysical Journal Supplement Series*, 239(29):15pp, 2018. URL `arXiv:1810.05418v2`.

J. Peralta et al. New cloud morphologies discovered on the venus's night during akatsuki. *Icarus*, 333:177–182, 2019. doi: 10.1016/j.icarus.2019.05.026.

J. Peralta et al. A long-lived sharp disruption on the lower clouds of venus. *Astrophysical Research Letters*, 47:11, 2020.

A. Piccialli. *Cyclotrophic wind in the mesosphere of Venus from Venus Express observations*. PhD thesis, Technische Universitat Braunschweig, 2010.

A. Piccialli et al. Dynamical properties of the venus mesosphere from the radio-occultation experiment vera onboard venus express. *Icarus*, 217:669–681, 2012. doi: 10.1016/j.icarus.2011.07.016.

A. Piccialli et al. High latitude gravity waves at the venus cloud tops as observed by the venus monitoring camera on board venus express. *Icarus*, 227:94–111, 2014.

C.C. Porco et al. Cassini imaging of jupiter's atmosphere, satellites and rings. *Science*, 299:1541–1547, 2003. doi: 10.1126/science.1079462.

C.C. Porco et al. Cassini imaging science: instrument characteristics and anticipated scientific investigations at saturn. *Space Science Reviews*, 115:363–497, 2004.

A. Friedson R. West, K. Baines et al. *Jupiter: The Planet, Satellites and Magnetosphere*. 2007.

B. Ragent et al. Particulate matter in the venus atmosphere. *Advances in Space Research*, 5:85–115, 1985. doi: 10.1016/0273-1177(85)90199-1.

K. Rajendran et al. Enhanced super-rotation before and during the 2018 martian global dust storm. *Geophysical Research Letters*, 48:e2021GL094634, 2021. doi: 10.1029/2021GL094634.

F. Ralph et al. Observations, simulations and analysis of nonstationary trapped lee waves. *Journal of the Atmospheric Sciences*, 54:1308–1333, 1997.

H. Ravier. *Dictionarium latino-annamiticum completum et novo ordine dispositum: cui accedit appendix praecipuas voces proprias cum brevi explicatione*. ex typis missionis Tunquini occidentalis, 1880.

S. Raymond et al. The grand tack model: a critical review. Number 310. IAU Symposium, 2014.

P. Read et al. The dynamics and circulation of venus atmosphere. in towards understanding the climate of venus. *ISSI Scientific Reports Series*, 11:73–111, 2013.

A. Riddle and J. Warwick. Redefinition of system iii longitude. *Icarus*, 27:457–459, 1976. doi: 10.1016/0019-1035(76)90025-7.

P. Rosenblatt et al. Accurate mars express orbits to improve the determination of the mass and ephemeris of the martian moons. *Planetary and Space Science*, 56:1043–1053, 2008. doi: https://doi.org/10.1016/j.pss.2008.02.004.

W. Rossow et al. Cloud-tracked winds from pioneer venus ocpp images. *Journal of Atmospheric Sciences*, 47(10):2053–2084, 1990.

C.T. Russel et al. Planetary magnetospheres. *Reports on Progress in Physics*, 56:687–732, 1993.

A. Sachs. Babylonian observational astronomy. *Philosophical Transactions of the Royal Society of London*, 276:43–50, 1974. doi: 10.1098/rsta.1974.0008.

C. Salyk. Interaction between eddies and mean flow in jupiter's atmosphere: Analysis of cassini imaging data. *Icarus*, 185:430–442, 2006. doi: 10.1016/j.icarus.2006.08.007.

A. Sanchez-Lavega. *Introduction to Planetary Atmospheres*. CRC Press, Taylor and Francis group, 2011.

A. Sanchez-Lavega et al. Variable winds on venus mapped in three dimensions. *Geophysical Research Letters*, 35:L13204, 2008. doi: 10.1029/2008GL033817.

A. Sanchez-Lavega et al. Planetcam upv/ehu: a simultaneous visible and near infrared lucky-imaging camera to study solar system objects. *Ground-based and Airborne Instrumentation for Astronomy IV - Proc. SPIE*, 8446:article id. 84467X, 2012.

A. Sanchez-Lavega et al. The rich dynamics of jupiter's great red spot from junocam: Juno images. *The Astronomical Journal*, 156(162):9, 2018. doi: 10.3847/1538-3881/aada81.

T. Satoh et al. Performance of akatsuki/ir2 in venus orbit: the first year. *Earth, Planets and Space*, 69:154, 2017. doi: https://doi.org/10.1186/s40623-017-0736-x.

A. Seiff et al. Models of the structure of the atmosphere of venus from the surface to 100 kilometers altitude. *Advances in Space Research*, 5(11):3–58, 1985.

A. Seiff et al. Thermal structure of jupiter's atmosphere near the edge of a 5-micron hot spot in the north equatorial belt. *Journal of Geophysical Research*, 103(E10):22857–22889, 1998.

A. Showman and I. de Pater. Dynamical implications of jupiter's tropospheric ammonia abundance. *Icarus*, 174:192–204, 2005. doi: 10.1016/j.icarus.2004.10.004.

J.E. Silva et al. Characterising atmospheric gravity waves on the nightside lower clouds of venus: a systematic study. *Astronomy and Astrophysics*, 649(A34):15, 2021.

J.E. Silva et al. Jupiter's atmospheree dynamics based on vlt/espresso and cassini's data. *Universe*, Submitted.

A. Simon et al. First results from the hubble opal program: Jupiter in 2015. *The Astrophysical Journal*, 812(55):8, 2015. doi: 10.1088/0004-637X/812/1/55.

A. Simon et al. Historical and contemporary trends in the size, drift and color of jupiter's great red spot. *The Astronomical Journal*, 155(151):13, 2018. doi: 10.3847/1538-3881/aaae01.

A. Simon-Miller et al. Color and the vertical structure in jupiter's belts, zones, and weather systems. *Icarus*, 154(2):459–474, 2001.

A. Simon-Miller et al. Jupiter's atmospheric temperatures: From voyager iris to cassini cirs. *Icarus*, 180(1):98–112, 2006.

C. Sonett. A summary review of the scientific findings of the mariner venus mission. *Space Science Reviews*, 2:751–777, 1963.

L. Sromovsky. A possibly universal chromophore for modeling color variations on jupiter. *Icarus*, 291:232–244, 2017. doi: 10.1016/j.icarus.2016.12.014.

D. Stevenson. Jupiter's interior as revealed by juno. *Annual Review of Earth and Planetary Sciences*, 48:465–489, 2020. doi: 10.1146/annurev-earth-081619-052855.

E. Stofan. Themis regio, venus: Evidence for recent (?) volcanism from virtis data. *Icarus*, 271:375–386, 2016.

B. R. Sutherland. *Internal Gravity Waves*. Cambridge University Press, 2010.

H. Svedhem et al. Venus express—the first european mission to venus. *Planetary and Space Science*, 55:1636–1652, 2007a. doi: https://doi.org/10.1016/j.pss.2007.01.013.

H. Svedhem et al. Venus as a more earth-like planet. *Nature*, 450:629–632, 2007b. doi: doi:10.1038/nature06432.

M. Taguchi et al. Longwave infrared camera onboard the venus climate orbiter. *Advances in Space Research*, 40(6):861–868, 2007. doi: https://doi.org/10.1016/j.asr.2007.05.085.

M. Takagi et al. Three-dimensional structures of thermal tides simulated by a venus gcm. *Journal of Geophysical Research*, 123:335–352, 2018. doi: 10.1002/2017JE005449.

Y. Takahashi et al. Lightning detection by lac onboard the japanese venus climate oribter, planet-c. *Space Sci Rev*, 137:317–334, 2008. doi: https://doi.org/10.1007/s11214-008-9400-x.

Y. Takahashi et al. 4-years lightning hunt in venus. 2020. URL `https://www.epsc2020.eu/`.

F. Taylor and D. Grinspoon. Climate evolution of venus. *Journal of Geophysical Research*, 114(E11):E00B40, 2009. doi: 10.1029/2008JE003316.

F. Taylor et al. Temperature structure and dynamics of the middle atmosphere of venus. *Advances in Space Research*, 5(9):5–23, 1985. doi: 10.1016/0273-1177(85)90266-2.

S. Tellmann et al. Small-scale temperature fluctuations seen by the vera radio science experiment on venus express. *Icarus*, 221:471–480, 2012. doi: http://dx.doi.org/10.1016/j.icarus.2012.08.023.

D. Titov et al. Clouds and hazes of venus. *Space Science Reviews*, 214(126):126, 2018.

J. Tollefson et al. Changes in jupiter's zonal wind profile preceding and during the juno mission. *Icarus*, 296:1263–178, 2017.

G. Tselioudis et al. Global patterns of cloud optical thickness variation with temperature. *Journal of Climate*, 5:1484–1495, 1992.

G. Tselioudis et al. Global, multiyear variations of optical thickness with temperature in low and cirrus clouds. *Geophysical Research Letters*, 21(20):2211–2214, 1994.

S. Uppalapati et al. Dynamics of lithospheric overturns and implications for venus's surface. *Journal of Geophysical Research: Planets*, 125(11), 2020. doi: https://doi.org/10.1029/2019JE006258.

S. Wahl et al. Comparing jupiter interior structure models to juno gravity measurements and the role of a dilute core. *Geophysical Research Letters*, 44:4649–4659, 2017. doi: 10.1002/2017GL073160.

K. Walsh et al. A low mass for mars from jupiters early gas-driven migration. *Nature*, 475:206–209, 2011. doi: 10.1038/nature10201.

T. Widemann et al. New wind measurements in venus lower mesophere from visible spectroscopy. *Planetary and Space Science*, 55:1741–1756, 2007. doi: 10.1016/j.pss.2007.01.005.

T. Widemann et al. Venus doppler winds at cloud tops observed with espadons at cfht. *Planetary and Space Science*, 56:1320–1334, 2008. doi: 10.1016/j.pss.2008.07.005.

T. Widemann et al. Venus twilight experiment: Observation and analysis of the aureole during the 2012 transit. volume 7, 2012.

A. Wilson. Technical report, NASA - National Aeronautics and Space Administration, 1987. URL https://web.archive.org/web/20140414120546/http://solarsystem.nasa.gov/missions/profile.cfm?MCode=Vega_02&Display=ReadMore.

A. Wilson. *Mars Express: The Scientific Payload.* ESA Publications Division, 2004. ISBN 92-9092-556-6.

M. Wong et al. Hubble's long-term opal (outer planet atmospheres legacy) program observes cloud activity on uranus. 2008.

R. Yadav et al. Deep convection-driven vortex formation on jupiter and saturn. *Science Advances*, 6(46):eabb9298, 2020. doi: 10.1126/sciadv.abb9298.

A. Yamazaki et al. Ultraviolet imager on venus orbiter akatsuki and its initial results. *Earth, Planets and Space*, 70:23, 2018.

R. Yelle and S. Miller. *Jupiter's Thermosphere and Ionosphere.* Cambridge University Press, 2007.

A.T. Young. Is the four-day "rotation" of venus illusory. *Icarus*, 24:1–10, 1975. doi: 10.1016/0019-1035(75)90152-9.

L. Young et al. Gravity waves in jupiter's stratosphere, as measured by the galileo asi experiment. *Icarus*, 173:185–199, 2005.

L.V. Zasova et al. Structure of the venus atmosphere. *Planetary and Space Science*, 55:1712–1728, 2007.